3-D Travel Time Tomography of the Gas Hydrate Area Offshore Vancouver Island Based on OBS Data

by

Mikhail Mikhailovich Zykov
B.Sc., Saint-Petersburg State University, 1998
M.Sc., Saint-Petersburg State University, 2000

A Thesis Submitted in Partial Fullfillment of the
Requirements for the Degree of
DOCTOR OF PHILOSOPHY
in the School of Earth and Ocean Sciences

3-D Travel Time Tomography of the Gas Hydrate Area Offshore Vancouver Island Based on OBS Data

by

Mikhail Mikhailovich Zykov

B.Sc., Saint-Petersburg State University, 1998

M.Sc., Saint-Petersburg State University, 2000

Supervisory Committee

Dr. N.R. Chapman, (School of Earth and Ocean Sciences)

Supervisor

Dr. R.D. Hyndman, (School of Earth and Ocean Sciences)

Departmental Member

Dr. G.D. Spence, (School of Earth and Ocean Sciences)

Departmental Member

Dr. S.E. Dosso, (School of Earth and Ocean Sciences)

Departmental Member

Dr. R. Illner, (Department of Mathematics and Statistics)

Outside Member

Supervisory Committee

Dr. N.R. Chapman, (School of Earth and Ocean Sciences)
Supervisor

Dr. R.D. Hyndman, (School of Earth and Ocean Sciences)
Departmental Member

Dr. G.D. Spence, (School of Earth and Ocean Sciences)
Departmental Member

Dr. S.E. Dosso, (School of Earth and Ocean Sciences)
Departmental Member

Dr. R. Illner, (Department of Mathematics and Statistics)
Outside Member

Abstract

This dissertation presents results from a complex seismic study using Ocean Bottom Seismometers (OBS) conducted at a site of deep sea gas hydrate occurrence. The site is located on the accretionary margin of the northern Cascadia subduction zone offshore Vancouver Island, Canada.

The major objectives for this study were the construction of a 3-D velocity model around the Bullseye vent zone by the means of travel time inversion tomography and the analysis of the amplitude data for reflections from the water-sediment interface and the bottom simulating reflector (BSR). Secondary objectives included the integration of the results from this study with previous knowledge about the vent zone for further clarification of its structure and evolution.

The OBS seismic data set consisted of 22 parallel lines at 200 m spacing with three perpendicular crossing lines recorded on five OBS stations. Multichannel and single channel conventional seismic data along these lines were also acquired. The OBS experiment geometry required corrections for the coordinates of sources and receivers initially obtained in the field. A new comprehensive source and receiver localization technique was developed for the case of stationary hydrophones and multiple seismic lines.

The horizontal size of the created 3-D velocity model is 3 $km \times 2.7$ km. The modelled volume is limited by the seafloor at the top and by the BSR at the bottom.

The size of a grid cell is 50 $m \times 50\ m \times 20\ m$. The uncertainty for the velocity value of individual cells was as low as 20 m/s, although the resolution of the model was reduced by the sparse receiver geometry.

The inversion results indicate a fairly uniform velocity field around and inside the vent zone. Velocities are nearly equal to values expected for sediments containing no hydrate, which supports the idea that the bulk concentrations of gas hydrates are low at the site. The largest velocity anomaly with an amplitude of +25 m/s is spatially associated with the limits of the blank zone. The anomaly suggests greater gas hydrate concentrations inside the vent zone than outside. Low vertical resolution of the model did not provide information on the depth distribution of the hydrate. However, the combination of the information from the velocity inversion with previous studies suggests that the zone of high hydrate concentration (15–20% of the pore space) associated with a hydrate lens, located at the top of the sediment section.

The vent site is characterized by a negative anomaly of the seafloor reflection coefficient, outlined by a high amplitude rim. The low reflection coefficient is believed to be the result of the processes taking place above the hydrate lens, methane venting in particular, and the high amplitude rim to be the effect of carbonate formation. The seafloor reflection coefficient zonation appears to be correlated with the distribution of low magnetic susceptibility zone in the first 8 m of the sediment section. Both phenomena can be related to the distribution of upward fluid flow at the vent site.

The cause of the blanking phenomena is likely different for different frequencies of the seismic signal. The blanking at high frequencies is an effect of near-surface disturbed sediments due to active venting and, possibly, free gas presence at the top of the vent zone. The blanking for the middle range of seismic frequencies is mostly the effect of reduced impedance contrast between the sediment layers inside the blank zone due to local presence of gas hydrates in small concentrations (2–3%).

It is concluded that the Bullseye vent zone, which shows very low activity presently, was probably much more active in the past (similar to a mud volcano). The past activity may have led to the formation of the bathymetric expression of the vent site (a

mound), together with the hydrate lens and authigenic carbonates.

Table of Contents

List of Tables

List of Figures

Acknowledgements

First of all I would like to thank my supervisor, Dr. Ross Chapman, for all his support: financial, but most importantly, his moral support and mentoring. I am also thankful to all my committee members for their continuous support through my PhD program — I was always able to get exhaustive response to all my questions and problems. I would like to deliver special thanks to Dr. Stan Dosso for all his time he dedicated to me discussing inversion problems and for providing his inversion codes that were used in my work.

Furthermore, I would like to say thanks to Dr. Michael Riedel for his help and discussions that benefited my work and also Dr. Warren Wood for all the productive discussions we had at different meetings.

A special gratitude I would like to give to Dr. Sergei Pavlovich Maschenkov (my supervisor in my Master program at the Saint-Petersburg State University, Russia) and Dr. Valery Alekseevich Soloviev (the head of the gas hydrate group at the All-Russia Research Institute for Geology and Mineral Resources of the Ocean, S.-Petersburg, Russia) , who, unfortunately, are no longer among us, and whose close involvement resulted in my entering the PhD program at the University of Victoria.

to the memory of Valery Alekseevich Soloviev

A method is more important than a discovery because a correct method of investigation leads to new and more significant discoveries.

Lev Landau

Chapter 1

Introduction

1.1 General overview

This dissertation presents results of comprehensive analysis of 3-D seismic survey data using Ocean Bottom Seismometers (OBS) over a site of proposed active venting associated with deep sea gas hydrate occurrence. The study area is located offshore Vancouver Island on the accretionary wedge in a region where extensive Bottom Simulating Reflectors are observed. The largest blank zone in the area, the Bullseye vent, was the focus of the experiment.

The area received close attention after seismic data showed blanking features, especially after massive hydrate was recovered from the vent site. The site was the target of numerous multi- and single-channel seismic surveys and various other experiments including piston coring, electromagnetic studies, and scientific drilling (ODP 146 in 1993 and IODP 311[1]).

[1]IODP 311 was ongoing as this dissertation was written. Brief and preliminary results were available from weekly reports published on-line, as well as a preliminary report (Expedition 311 Scientists, 2005).

The main objectives of this work include:

1. establishing the processing methods for unconventional seismic data recorded with ocean bottom receivers,
2. creation of a 3-D velocity model around the Bullseye vent site with travel time tomography using a combination of OBS and conventional single channel seismic data sets to determine the distribution and quantity of hydrates
3. performing amplitude studies using data recorded by OBS to create a map of the seafloor reflection coefficient of the area and to conduct an inversion of amplitude variation with angle, and
4. integration of new results with previous information for further characterization of the blank zone structure.

The main data set was collected in 1999 using a 40 in^3 sleeve gun source recorded on five OBS stations placed around the Bullseye vent. During the same cruise, conventional single- and multichannel seismic data were recorded over the same area. The OBSs recorded shots from 22 parallel seismic lines that were 200 m apart and three cross lines. The geometry of the experiment allowed creation of a 3-D velocity model with horizontal dimension of 3.0 $km \times 2.7$ km around the vent site.

The first chapter of this work provides a general overview of gas hydrates and associated issues. Chapter 2 provides more details on the gas hydrate occurrence offshore Vancouver Island with a review of previous information on the Bullseye vent site. Chapter 3 gives technical details on the 1999 COAMS seismic cruise. A comprehensive technique for localization of source and receivers developed for the purpose of the study is introduced in chapter 4. Chapter 5 is dedicated to the results of the travel time tomography studies, followed by the results of amplitude studies presented in chapter 6. Comprehensive analysis of the new information combined with the results of previous studies is given in chapter 7. Finally, a short summary, conclusions, and recommendations for future studies provided in chapter 8 completes the dissertation.

1.2 Gas hydrates — general information

Gas hydrates are a subgroup of a wider class of rigid substances known as clathrates, which are defined as compounds formed by the inclusion of molecules of one kind within cavities in the crystal lattice of another (Webster, 1994)(Fig. 1.1). There is a long list of possible host molecules that can form the crystalline structure, as well as a list of guest molecules to be dissolved in it (Pellenbarg and Max, 2000). However for gas hydrates, molecules of water act as the host and various gases act as guest molecules. Typical hydrate forming gases are CH_4 and other higher hydrocarbons, CO_2, and H_2S (Englezos, 1993).

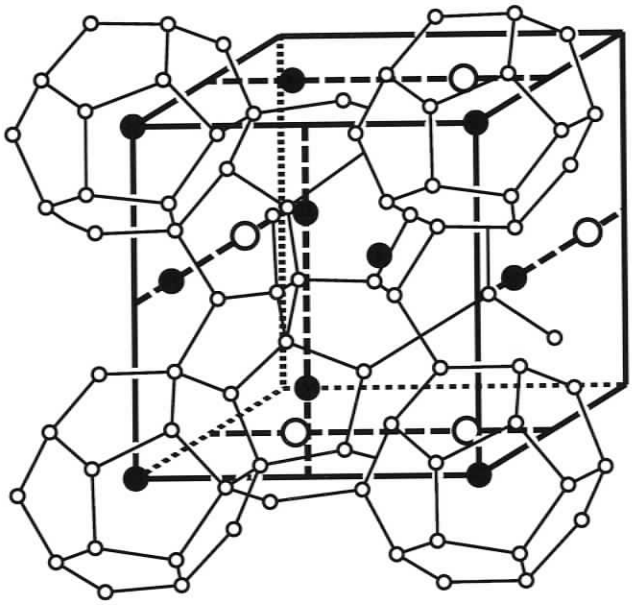

Figure 1.1: Gas hydrate Structure I (from Collett, 2000).

The discovery of clathrates took place in 1810 when Sir Humphry Davy observed formation of a precipitate while passing chlorine gas through cooled water. The interest in gas hydrates remained purely academic until the 1930's when the growing oil industry met an unsuspected problem of plugged natural gas pipelines. It was gas hydrates that were found responsible for clogging the conduit (Hammerschmidt, 1934). The formation of gas hydrates was also an issue during the exploitation of gas wells in the northern territories of USSR (Degtyarev, 1969). For three decades the study of clathrates was primarily targeted on finding ways to prevent undesired

hydrate formation.

All of the above mentioned occurrences of gas hydrates are caused by human activity and it was not until late 1960's when the first evidence of *naturally* occurring gas hydrates were observed by scientists of different countries (Vasiliev et al., 1970; Markl et al., 1970). The first documented recovery of a gas hydrate took place in 1972 at a drill site on the North Slope of Alaska (Collett, 1993). The sediment sample was collected using a pressure core barrel and tests showed that a hydrate had been recovered, but was not observed at this time. Nit until 1974 did scientists have the first chance to set their eyes on a naturally formed gas hydrate, when a core taken from the bottom of Black Sea brought it to the surface (Yefremova and Zhizhchenko, 1974). The majority of the observed naturally occurring gas hydrates are methane hydrates with small fractions of higher hydrocarbons.

1.2.1 Properties of gas hydrates

Gas hydrates are non-stoichiometric chemical compounds; that is, their chemical formula is not fixed. The ratio of water and gas molecules can vary. In other words, it can be written as $CH_4 \cdot xH_2O$ for a methane hydrate, where x is called a hydration number. The maximum amount of the methane captured in a gas hydrate structure is defined by the number of available cages to be occupied and comes to approximately one methane molecule per 5.75 molecules of water (Seo and Lee, 2002). However, gas hydrates can still be formed with only partial occupation of the available cages in the crystalline structure. Handa (1990) showed that at minimum suitable pressure the gas hydrate formation process leaves about 12% of the cages empty (Kvenvolden, 1998). The dissociation of a volume of the hydrate with such occupational rate yields about 150 volumes of the gas at standard conditions (Fig. 1.2). The occupation rate is predicted to increase with increasing pressure (Handa, 1990).

Basic physical properties of a pure gas hydrate, with minor exceptions, do not differ greatly from those of ice (Table 1.1). However, five times lower thermal conductivity and 10 times greater heat of fusion for gas hydrates are worth noting.

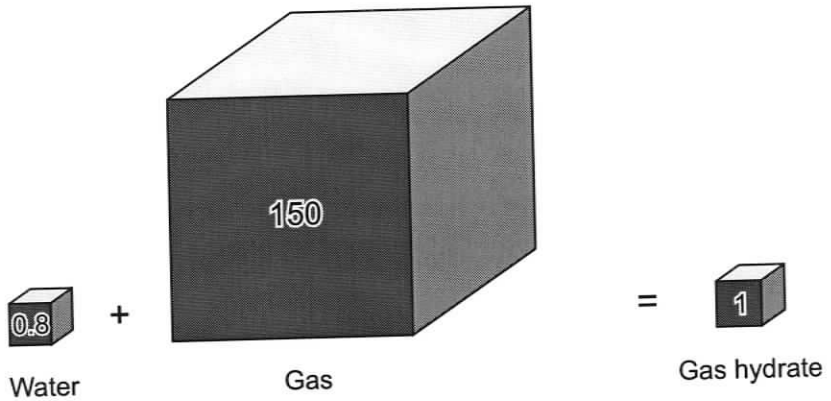

Figure 1.2: Composition of gas hydrate. 0.8 volumes of water and 150 volumes of gas form one volume of gas hydrate with 88% occupational rate (volumes measured under normal conditions).

Table 1.1: Comparison of physical properties for water ice and methane hydrate (from Pellenbarg and Max, 2000)

Property	**Ice**	**Hydrate**
Bulk density (gm/cm^3)	0.916	0.912
P-wave speed (km/s)	3.8	3.3
Velocity ratio Vp/Vs	1.88	1.95
Poisson's ratio	0.33	~ 0.33
Bulk modulus (at 272 $^\circ K$)(GPa)	8.8	5.6
Shear modulus (at 272 $^\circ K$)(GPa)	3.9	2.4
Thermal conductivity (at 263 $^\circ K$)$(W/m\cdot^\circ K)$	2.25	0.49 ± 0.02
Heat of fusion (kJ/mol)	6	54-57

The crystalline lattice of gas hydrates can be formed in a cubic system (Structure I and II) or in a hexagonal system (Structure H). Structures I and II differ by the packing, with Structure II having cages of larger size. Typical gases to form Structure I gas hydrate are methane, ethane, and carbon dioxide. The presence of propane, butane, or other gases with similar molecule size, leads to the formation of hydrates with Structure II lattice. Having the largest cages, Structure H hydrates can incorporate even higher hydrocarbons (Sloan, 1998b). In natural conditions, gas hydrates with Structure H were inferred from analysis of hydrocarbon composition in hydrates found on the seafloor in the Gulf of Mexico continental slope (Sassen and

MacDonald, 1994).

One of the greatest differences of gas hydrates from ice is in the P-T stability conditions. The temperature at which ice can exist is quite constant (0 °C) and is almost independent of pressure. The temperature of stability for gas hydrates changes dramatically (Fig. 1.3). Under pressure of 10 atm, gas hydrates are stable at -15 °C. With increasing pressure, the stability temperature also increases, reaching $+15$ °C at 100 atm (pressure equivalent of 1000 m below sea surface), and even higher temperatures for greater pressures.

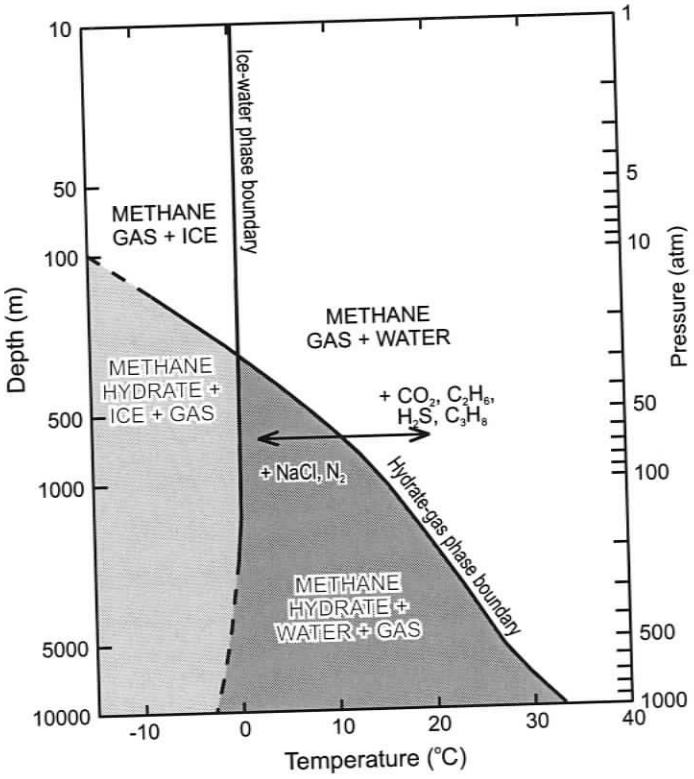

Figure 1.3: Phase diagram for pure water–pure methane system. Effect of other components on the stability field is also shown (redrawn after Kvenvolden, 1998).

The presence of different admixtures in the water-methane system can affect the stability field, either decreasing or increasing it. Such factors as salinity or presence of N_2 can shift the methane hydrate P-T curve to the left. On the contrary, presence of CO_2, H_2S, or higher hydrocarbons increases the stability (Kvenvolden, 1998). The changes to the stability field promoted by other components can be as high as several degrees. For instance, average sea water salinity reduces the equilibrium temperature by 1–2 °C, while the presence of 1% of ethane stretches the stability field to higher

temperatures approximately by the same number (Clennel et al., 1999). Also, the type of molecular packing plays a role. Structure II gas hydrates are generally more stable than Structure I hydrates (Sloan, 1998b).

1.2.2 Gas hydrates in sediments

The extent of the Gas Hydrate Stability Zone (GHSZ) in sediments is primarily defined by the pressure and temperature conditions. Naturally occurring gas hydrates are typically found in marine sediments where the water depth exceeds 300 m. This depth represents a theoretical upper limit of gas hydrate occurrence calculated using P-T diagram and assumes a bottom water temperature of 0 °C (Arctic areas) (Kvenvolden, 1993); in warmer regions the water depth usually should exceed 500 m for gas hydrates to be stable in the sediment (Dillon and Max, 2000). In the areas of permafrost development, the upper limit of GHSZ can be as shallow as 150 m below the ground surface. The lower limit of GHSZ is defined by the intersection of the phase boundary with the local temperature profile and theoretically can reach depths about 2000 m below the sea bottom, although reported hydrate occurrence depths are typically less than 1000 m (Kvenvolden and Lorenson, 2001).

Methane Source

The source of hydrocarbon gases that form gas hydrates can be either microbial or thermogenic in origin. The differentiation of sources is performed with carbon-isotopic composition studies. Microbial methane is lighter and has a carbon isotopic ratio ($\delta^{13}C$) less than $-60‰$ (Shoell, 1988). Methane produced from fossil organic matter under high temperatures has heavier isotopic composition. In addition, the hydrates formed with thermogenic methane usually contain higher hydrocarbon fractions.

Given suitable pressure and temperature conditions, gas hydrate is formed if the concentration of methane exceeds the local solubility (Sloan, 1998a). The methane solubility ranges from 40 to 200 $mMole$ per liter for typical gas hydrate sites (Davie et al., 2004). A sufficient supply of methane can be produced either *in situ* (Paull et al., 1994) or has to be brought into hydrate stability zone by upward fluid migration

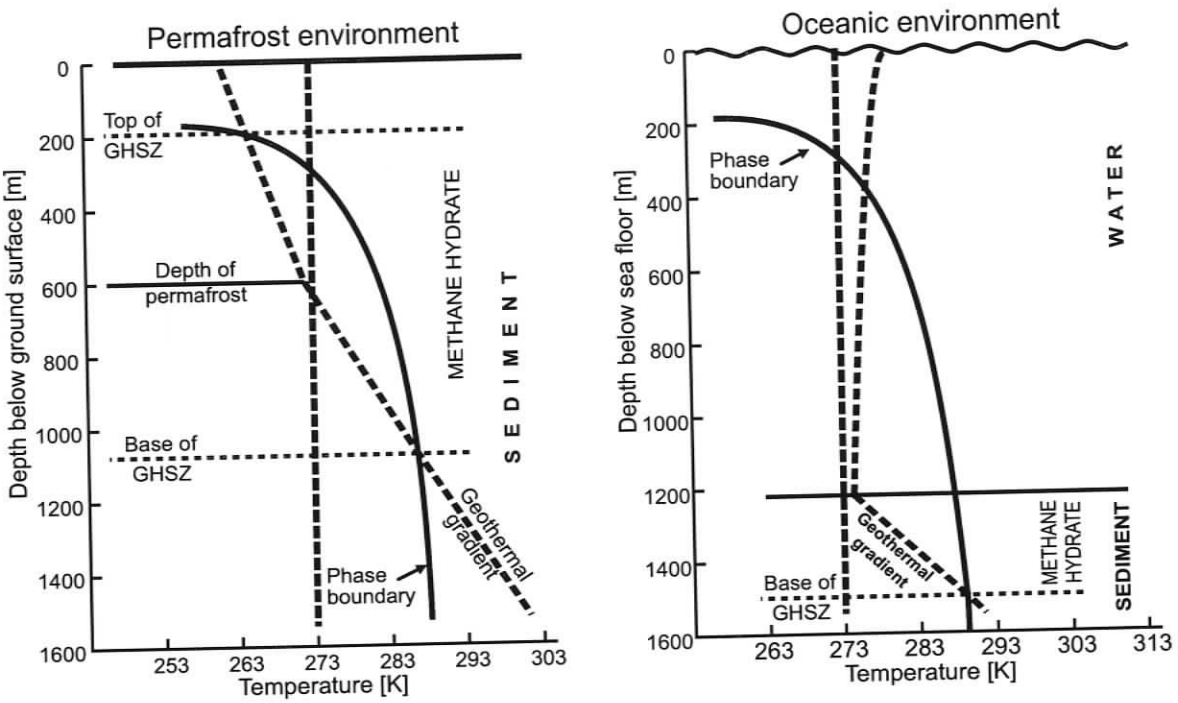

Figure 1.4: Arbitrary examples of hydrate stability regions for permafrost and oceanic environments (redrawn after Collett, 2000).

(Hyndman and Davis, 1992).

Under the *in situ* production model, the methane supply depends only on the gas produced from the organic material enclosed in the host sediments. Thus, in order to form gas hydrates, the amount of the organic content has to be sufficient. With the organic material concentration being about 1%, the amount of methane produced on-the-site will be enough to fill approximately 6% of the pore space (or 2.4% of the sediment volume) (Paull et al., 1994). Under this model, the mobility of the gas is quite limited. The gas hydrates are being formed through all the GHSZ, with the concentrations depending on the initial concentration of the organic matter.

While this model is sustainable for the sites with low gas hydrate concentrations, it is difficult to explain higher clathrate concentrations in the sediments with only the local methane supply. Paull et al. (1994) suggested that sediments containing more than nominal amounts of biogenic methane hydrates are not closed systems. Their calculations showed that concentrations of gas hydrate more than 3% of the sediment

volumes are unlikely to be achieved with methane produced *in situ*. Thus, methane has to be delivered into the gas hydrate stability zone from the outside.

Hyndman and Davis (1992) proposed a fluid expulsion mechanism that supplies additional gas required for clathrate formation (Fig. 1.5). In this model, methane and other gases are carried by fluid flow to the GHSZ from their original place of generation. While the methane-rich fluids travel upwards, the methane solubility, which depends on pressure, decreases and free gas is discharged. Consequently, the free gas phase is involved in gas hydrate formation.

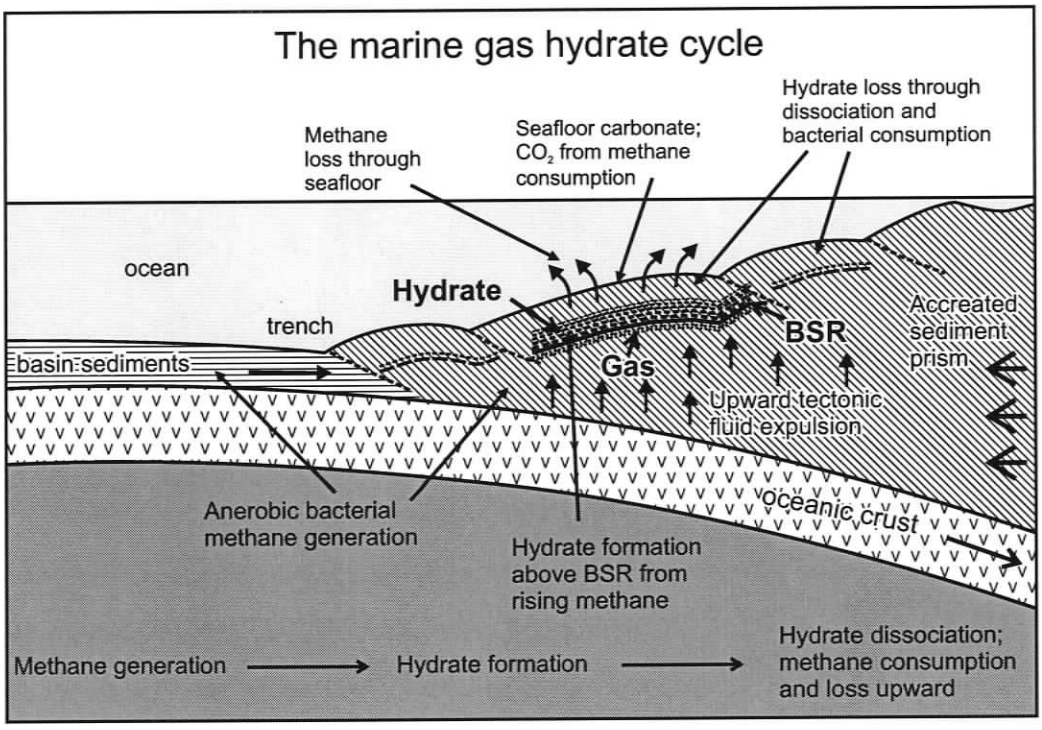

Figure 1.5: Fluid expulsion model incorporated into the marine gas hydrate cycle (after Hyndman et al., 2001).

The largest amounts of the hydrate are expected to be in close proximity to the base of GHSZ, gradually decreasing towards the seafloor. This model is able to explain the concentrations several times higher than *in situ* production model. Because the mechanism requires a driving force to provide the fluid movement, this model is more likely to be applicable at the subduction zone accretionary wedges and in areas with rapid deposition settings resulting in underconsolidation (Hyndman and Davis, 1992).

Gas hydrate interaction with sediment

Examination of the sediment samples that contain gas hydrate is very difficult, as the clathrates tend to dissociate very quickly under normal laboratory conditions. Thus, the original *in situ* structure of the gas hydrate is often perturbed.

The available data show that hydrates occur in the sediments in different forms. They are found acting as a cement, and also in various forms such as nodules, lenses, or veins (Booth et al., 1996; Ginsburg and Soloviev, 1998). Cores retrieved by deep ocean drilling revealed occurrences of layers with thicknesses of up to several metres and consisting of almost pure gas hydrates.

As noted by many researchers, the way the hydrates are present in the sediment depends on the sediment type. In course-grained sediments (sands, silts), the hydrate tends to form microcrystals in the pore spaces or play the role of a cement. On the contrary, in fine-grained sediments (clays), hydrates more often occur as localized macro bodies (lenses, veins) (Clennel et al., 1999). Similar conclusions were made from observations of a controlled hydrate growth experiment (Brewer et al., 1998).

Transformation of the liquid pore fluid into crystalline hydrate alters the bulk physical properties of the host sediment. First of all, porosity decreases, as a part of the pore space is being occupied by newly formed clathrates. Also the compressional (P) and shear (S) wave velocities change, as the newly formed crystalline substance replaces pore water.

The extent of the effect of gas hydrate formation on the acoustic properties of the sediment depends on the way the clathrates are incorporated into the sediment matrix. Three basic types of incorporation can be isolated (Dvorkin et al., 2000), in which the gas hydrate either is formed in the pore space, becomes a part of the framework, or acts as a cement (Fig. 1.6).

Even a small concentration of gas hydrates acting as cement can result in substantial increase of both P and S velocities. The amount of clathrate in the pore space needed to achieve the same velocity increase as in hydrate cemented sediment may be 2–3 times larger (Helgerud et al., 1999; Holbrook, 2001). An extended theory

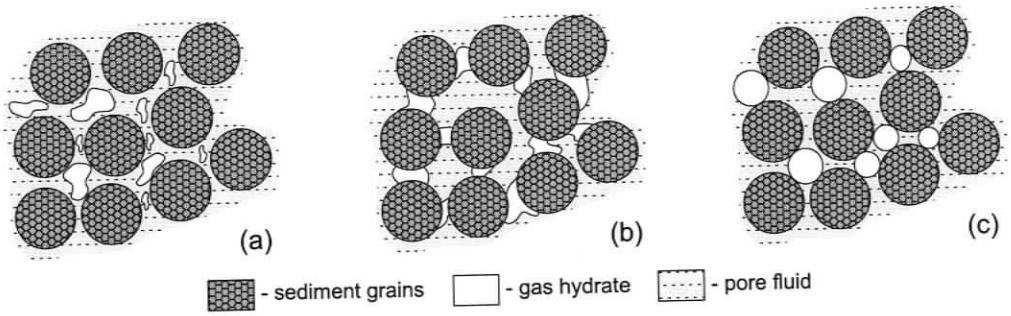

Figure 1.6: Three basic gas hydrate formation models: inside the pore space (a); as a cement for the sediment grains (b); and as a part of the solid phase (c)

was developed that allowed calculations of the effect of gas hydrate presence on the velocity of seismic wave propagation (Dvorkin et al., 2000). The calculations can provide an estimate of the gas hydrate concentration, if the reference velocity is given for the sediment without clathrates.

1.3 Detection of Gas hydrates

Direct observation

In order to have 100% confidence that gas hydrates are present at a given site, visual observation of hydrate samples is needed. The observation can be done on the samples retrieved by a drill core from the deep sediment sections (e.g., Shipboard Scientific Party, 1996) or from the near seafloor sediments sampled by piston coring devices (e.g., Spence et al., 2000). Also, there was a rare reported case of the gas hydrates being brought to the surface in a fishnet to the great surprise of the fishermen (Spence et al., 2001). *In situ* observation of gas hydrates deposited directly on the seafloor can be achieved with video devices installed on submersible vehicles (Chapman et al., 2004).

The gas hydrates in cores are described as an ice-like crystalline substance. The colour may range from the pure white to white-yellowish, if impurities of higher hydrocarbons are present (Chapman et al., 2004). The hydrate samples are cold to

the touch, dissociate quickly, and may be ignited.

The problem of preservation of the gas hydrates in samples exists. The hydrate starts dissociating as soon as it leaves its stability zone, and small samples can completely disappear by the time the core is brought on the deck of the ship. Moreover, piston coring is not very effective as it can sample only up to 10 m below the seafloor, and the drilling is extremely expensive. Hence, in most cases scientists must rely on indirect evidence of gas hydrate presence.

Indirect evidence

Remote sensing of gas hydrates is primarily done by two methods: seismic and electromagnetic surveys. The primary seismic evidence of gas hydrate occurrence includes the presence of a bottom-simulating reflector (BSR) and increased P-wave velocities compared to a sediment with no hydrate.

The BSR is thought to mark the bottom of the GHSZ. The reflection is characterized by a reversed polarity compared to the seafloor reflection. As the density is not expected to change significantly, the reversed polarity of the seismic reflection from this boundary is due mostly to the negative velocity contrast at the boundary. The velocity changes due to the presence of gas hydrates in the sediments above the BSR and no-hydrate sediments or sediments with free gas below it. Another important property of the BSR is that it follows the configuration of the seafloor, as the depth of the bottom of the GHSZ inside the sediments is primarily defined by the temperature field. The reflection cross-cuts reflections from the lithological strata.

The question of whether the BSR is the result of the hydrates on top or free gas below is still under consideration. Evidence in favor of both theories has been found (e.g., Tinivella and Lodolo, 2000; Yuan et al., 1996). This fact leads to the conclusion that for different gas hydrate sites different causes explain the BSR.

If the BSR depth coincides with the theoretical depth of the bottom of the GHSZ, there is greater confidence that this event is actually a BSR. In areas with layered sediment structure parallel to the seafloor, identification of the BSR is difficult.

While there are no reported cases of the absence of gas hydrates with the presence of the BSR, the existence of BSR is a sufficient but not a required condition for the presence of clathrates.

The P-wave velocity measurement is not very accurate, as the information about no-hydrate reference velocity is required, yet still operative method of detecting gas hydrates. Higher than predicted seismic velocities can be an indicator of hydrate presence. The velocities can be estimated by multichannel interval velocity analysis, vertical seismic profiling, or travel time tomography methods.

The replacement of the higher conductive matter (pore water) with a substance with a higher resistivity (gas hydrate) results in a change of the bulk electrical properties of the sediments. Yuan and Edwards (2000) described an electrical remote sounding method using bottom dipole-dipole systems for the assessment of gas hydrate presence.

Multiple downhole measurements can provide insight on gas hydrate existence at the site. These include the neutron porosity logs (as the formation of gas hydrates reduces the porosity), the resistivity logs, and the sonic velocity logs. Density logging is not sensitive to gas hydrates as the density of hydrates does not differ much from the density of the pore water.

Gas hydrates may be present in the cores at the seafloor, but due to the time necessary to deliver the cores to the deck of the ship, they may completely disappear through dissociation. However, the evidence of such dissociation can be detected later on.

Indirect detection based on salinity measurements can be very effective. On formation, hydrates exclude salts from the pore water. Salt dissolved in the water remains in the pore fluid and increase its salinity. Subsequently, the salinity is brought back into equilibrium by diffusion or fluid flux. Dissociation of hydrates during the core recovery process injects nearly pure water back into the system causing pore water freshening. The amount of the dissociated clathrates can be inferred from the degree of freshening.

Besides the fresh water, the clathrate dissociation produces great volumes of free gas that destroys the initial structure of the core. Cracks and cavities appear, and the sediments can become "soupy". The core material can be pushed out from the core liner by the excessive pressure.

The dissociation of gas hydrates is an endothermic reaction, that is, it consumes heat. The core areas of former gas hydrate existence are marked with negative temperature anomalies. Scanning the core with infrared cameras is a very useful tool in gas hydrate detection (Shipboard Scientific Party, 2003).

1.4 Distribution of gas hydrates on Earth

While the conditions for hydrate generation and preservation exist on 90% of the total area of the World ocean (Trofimuk et al., 1983), the number of known sites with gas hydrate presence is limited (Fig. 1.7). Nevertheless, gas hydrates are found on the slope of every continent as well as on the continents in permafrost areas. With such widespread distribution gas hydrate can with no doubt be called a global phenomenon.

Gas hydrate sites cluster close to the continents and convergent plate boundaries, which highlights the importance of sufficient methane supply for the clathrate formation. Ginsburg and Soloviev (1998) noted that all known oceanic gas hydrate sites occur on the continental and insular slopes or rises, or in the abyssal part of intracontinental and marginal seas. Such conditions are present on approximately 10% of the total Earth oceanic area (Fairbridge, 1966).

Estimates of the total volume of methane trapped in the gas hydrate accumulations on Earth vary greatly. The minimum and maximum values differ by several orders of magnitude. This kind of difference indicates, in the first place, the lack of information about the local and global distribution of gas hydrates, which leads to the employment of a number of assumptions.

Some estimates, made shortly after the discovery of natural presence of gas hydrates in sea sediments were very optimistic. The number derived by Dobrynin et al.

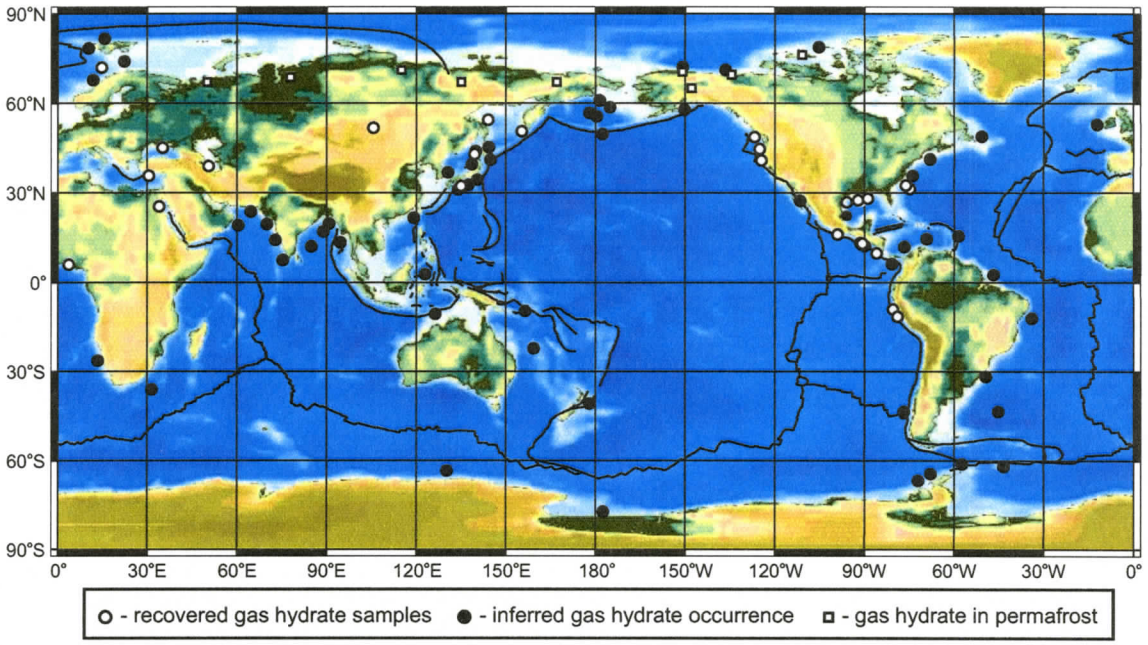

Figure 1.7: Global occurrences of gas hydrates (after Kvenvolden and Lorenson, 2001). The inferred occurrences are based on BSR presence and well log indicators.

(1983) ($7600 \times 10^{15}\ m^3$ of CH_4) is a representative example. In order to make the estimation an assumption was made that hydrates are present in the sediments anywhere that the P-T conditions favour stability. After that an average concentration of gas hydrates was multiplied by the volume of the sediments and enormous numbers appeared.

Subsequent estimations were more cautious. It became evident that gas hydrates are not formed anywhere that the physical conditions allowed, as the methane supply at the site is a vital component. Also, the inability to estimate the volume of the accumulations with confidence even at the well-studied sites, leads to a much greater uncertainties, when scaled to the whole globe.

Ginsburg and Soloviev (1998) summarized some of the methods used in calculations of quantities of methane stored in gas hydrates. At present, the consensus value of $4.8 \times 10^{18}\ g$ of carbon stored in the geological systems associated with hydrates (Buffett and Archer, 2004) is widely used.

1.5 Why study gas hydrates

Among many reasons for studying gas hydrates there are three major ones. The methane stored in clathrates can: (i) represent a future energy source; (ii) play a role in global climate change; (iii) may represent a potential geological hazard.

1.5.1 Gas Hydrates as a Potential Energy Resource

Considering the total volume of methane stored in hydrates globally, gas hydrates are a very attractive source for hydrocarbons in the future. The comparison of the amount of methane with conventional energy reserves may be quite impressive (up to 100 times more (Kvenvolden, 1998)), but such estimates should be treated with a great care, as the overwhelming majority of the gas hydrates may not be recoverable. Nevertheless, some of the well-studied gas hydrate sites have high economical potential, e.g., structural gas hydrate accumulations in Northwestern Gulf of Mexico (Milkov and Sassen, 2002).

Harvesting gas hydrates for methane is associated with certain complications. Mainly they are (i) technical difficulties of dissociating gas hydrates, (ii) economical effectiveness compared to other hydrocarbon resources, and (iii) ecological impact.

In order to dissociate gas hydrates they either have to be removed from their stability zone or, for in-situ dissociation, the stability conditions have to be changed. In the former method, gas hydrates can be mined at the seafloor. *In situ* dissociation of gas hydrates can be done by several methods. They include (i) thermal stimulation of the sediments containing gas hydrates, which can be done through injection of either hot water or steam, (ii) local depressurization at the site below the pressure of hydrate stability, (i) injection of an inhibitor into the reservoir. The most environmentally unfriendly is considered the third one, yet it was proven to be economically effective (Sloan, 1998a).

At present, only two cases of the methane production have been reported, both of them from permafrost gas hydrates. The first one dates back to 1969 from the Messoiakh gas hydrate field (Makogon, 1984). The hydrate dissociation was performed

through injection of an inhibitor (a mixture of methanol and calcium chloride) into the well. Over 17 years of production, $5 \times 10^9\ m^3$ of gas were released from the hydrate phase (Makogon, 1984). The other case of methane recovery refers to the Mallik Gas Hydrate Production Research Well Program in MacKenzie River delta. At the Mallik site, the methane production was only for research. Several methods were tested, primarily depressurization and thermal stimulation (Dallimore et al., 2002).

1.5.2 Gas Hydrates and Global Climate

Shine et al. (1990) estimated that methane has a global warming potential 20 times greater than an equivalent weight of carbon dioxide. The amount of methane stored in gas hydrates is perhaps 3,000 times the amount in the atmosphere (MacDonald, 1990). Thus, natural gas hydrate could be a potential major agent of global climate change.

During a global warming period, two major processes can occur on the Earth. (I) The ocean level rises as melting ice-fields contribute extra water. This would increase pressure at the seafloor, expanding the GHSZ. (II) The water temperature in the oceans increases, depleting the GHSZ. For the deeper parts of the ocean, the increasing pressure would outweigh the increase in temperature leaving more stable conditions for gas hydrates; in the shallow regions (300–500 m), temperature changes might prevail. In this case the base of the GHSZ rises and may even disappear completely in some areas (Fig. 1.8). The methane from destabilized hydrates is released into ocean water and, eventually, may reach the atmosphere.

The rising or lowering of the bottom of the GHSZ can produce a feature called a double BSR. In this case, two reflectors with the characteristics of the BSR can appear on a seismic section. One represents the present position of the bottom of the GHSZ and the other its relict (Bangs et al., 2005). The gas hydrate sites at Nankai Trough (Foucher et al., 2002) and Hydrate Ridge offshore Oregon (Bangs et al., 2005) are examples of places where a double BSR was observed.

Permafrost hydrates are also subject to the influence of warmer climate. The

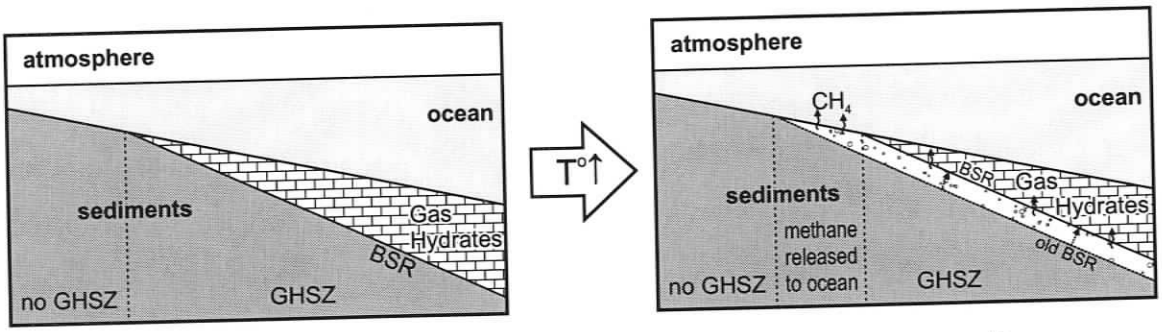

Figure 1.8: Example of the GHSZ retreat under warming conditions. In the areas where the GHSZ completely disappear methane is released to the ocean.

increasing sea level can cause flooding of low-lying permafrost areas, warming them by the oceanic water. Under the new conditions, hydrates will dissociate releasing methane (Dillon and Max, 2000).

In both cases global warming increases the intake of methane into atmosphere. The additional methane causes more warming, and therefore positive feedback may be established.

Conversely, a global cooling period leads to the decrease of the atmospheric temperature and, consequently, the temperature of the World ocean. The ocean level also decreases, reducing the pressure at the seafloor. Paull et al. (1991) suggested that in this situation the destabilization effect of the depressurization due to lower sea level would prevail and more methane would be delivered into atmosphere, limiting the level of atmosphere cooling.

No theory has been tested yet against all available evidence, and thus the exact role of gas hydrates in the global climate change is not known (Kvenvolden, 1999). Also the ocean can act as a buffer for the methane flux, as only as little as 1% of the methane released into the ocean may actually reach the atmosphere, while the rest is oxidized (Kastner, 2001). Nevertheless, methane from gas hydrates is definitely part of the global climate change system, whether as an initiator or a response (Nisbet, 2002).

1.5.3 Gas hydrates as a Geohazard

As the oil industry improves its technology, the ability to advance to deeper sea water increases. Thus, human made structures are now entering the areas where the gas hydrates may be present in the sediments. These structures interact with the sea bottom in one way or another, and thus are subject to various geohazards that come from the sediment masses, such as land slides, slumps, or cratering (Hovland and Gudmestad, 2001).

The role of gas hydrates in geohazards originates from the fact that the water and gas mixture contained in the pore space, greatly changes the mechanical properties of the sediment (shear strength in particular) when it converts into the solid state. The mechanical strength, in turn, is vital for the physical stability of the sediments.

The usual scenario of gas hydrate formation requires an external supply of methane into the stability field. Without formation of clathrates, that additional methane would pass through the sediments and be released into the water. Generation of gas hydrates leads to the local retention of the gas. Gas hydrates become a compressed spring, which remains so as long as the pressure-temperature conditions remain the same.

If the gas hydrate acts like a cement for the sediment grains, the particles are no longer cemented after dissociation. The shear strength of the sediments degrades greatly. Water that was in a solid state due to clathrate formation transfers into a liquid state, increasing the porosity and the water saturation of the sediment. Finally, the fact that the volume of released gas can be up to 160 times greater than the initial volume occupied by the hydrate leads to pore fluid overpressure. Thus, the mechanical strength of the sediment may become even lower than it was initially (before the formation of gas hydrates).

McIver was first to recognize the possible connection between the boundaries of gas hydrate stability zone and submarine slides and slump surfaces (McIver, 1977). Later this was supported by studies of surficial slides and slumps on the continental slope and rise of West Africa, slumps on the U.S. Atlantic continental slope, large

submarine slides on the Norwegian continental margin, sediment blocks on the seafloor in fjords of British Columbia, and massive bedding-plane slides and rotational slumps on the Alaskan Beaufort Sea continental margin (summarized by Kvenvolden, 1999).

Drilling sediments that contain gas hydrates may lead to dangerous situations such as the collapse of casings under increased pressure, loss of mud control, and loss of stability of the rig after a large gas release. These are serious concerns, as they can lead to a loss of expensive equipment and represent a safety threat to the drilling crew (Hovland and Gudmestad, 2001).

Chapter 2

Gas hydrates in Northern Cascadia Region

2.1 General Tectonic Setting

The area of interest is 43 nautical miles (80 km) offshore Vancouver Island, on the accretionary wedge of the Cascadia subduction zone (Fig. 2.1). The convergent margin separates the Juan de Fuca and North American plates. The Juan de Fuca plate subducts in the NE direction almost orthogonally to the plate boundary, with the present rate about 45 $mm/year$ (Riddihough, 1984). The water depths on the shelf are about 200 m, and they increase over the 60 km width of the accretionary prism to 2500 m in the oceanic basin. The crustal age of the subducting plate is 4.5 Ma. The oceanic crust is covered with 3.1 km, on average, thick sediments. The basin fill consists of of two units: pre-Pleistocene, fine-grained hemipelagic sediments (1.4 km), and rapidly deposited, considerably coarser Pleistocene turbidites (1.7 km)(Davis and Hyndman, 1989).

Very young, buoyant oceanic crust produces a well-coupled interface with the overriding plate. Complete offscraping of the oceanic basin sediments produces a large accretionary prism along the Cascadia margin (Davis and Hyndman, 1989). An abrupt transition from the oceanic basin to the accretionary wedge occurs at a prominent landward-dipping frontal thrust fault. More thrust faults are revealed landward, with major ones penetrating most of the basin section (Hyndman, 1995).

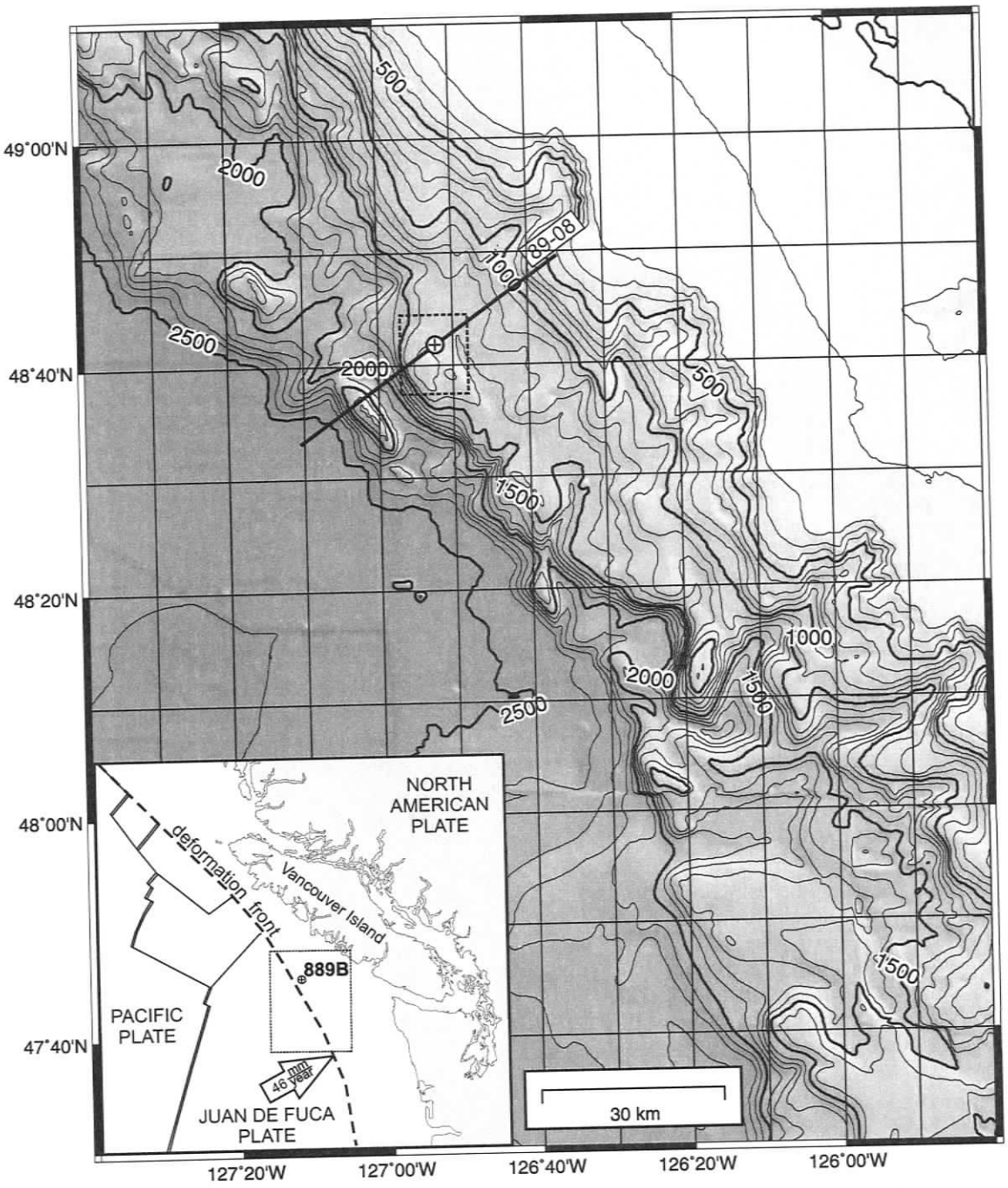

Figure 2.1: Bathymetry of the Cascadia margin in the vicinity of the ODP 889/890 drill site. General tectonic setting is shown on the insert.

The top of the oceanic crust under the accretionary wedge deepens towards the shore with a slope of 3° to 4° increasing to 10° under the outer edge of the shelf (Hyndman, 1994). Accreted sediments are folded into anticlinal ridges with fold axes approximately parallel to the margin. The ridges rise as much as several hundred metres above the adjacent seafloor (Hyndman, 1995). The seismic reflection continuity in the accreted sediments is significantly reduced compared to that for the abyssal plain sediments.

Half way up the continental slope, the accretionary prism forms a 15–20 km wide bathymetric bench with water depths of 1300–1500 m. The area of the investigation is located closer to the seaward side of the bench near two topographic highs, which are 3 km apart and rise about 200 m above the adjacent seafloor (Fig. 2.2). The sediment thickness is approximately 4.5 km at this location (Westbrook, 1994).

The accreted sediments are covered with slope sediments, which show strong continuous reflectivity. The thickness of the slope sediment unit varies from a few 10's of metres at the top of local ridges to several 100's of metres in between the ridges and in the large slope basin just landward of these ridges (Fig. 2.3).

The age of the sediments from the cores at the ODP drill sites 889 and 890 was identified using micropaleontology methods (Caulet, 1995). Analysis of the radiolarian assemblages provided a constraint on the minimum age for only a few depth points of the 889 well. The first conclusive age determination occurred at a depth of 38 m, and was defined as not younger than 0.4 Ma. Other age-depth information for the 889 site is presented in Table 2.1. At the 890 site the only age identification refers to a depth of 3.7 $mbsf$, and is defined as 0.55 Ma to present (Caulet, 1995).

depth ($mbsf$)	age (Ma)
38	> 0.4
82	0.8
89	0.9
101	> 1.0
168	> 1.7
207	< 2.0

Table 2.1: Age-depth information for the ODP 889 site (Caulet, 1995).

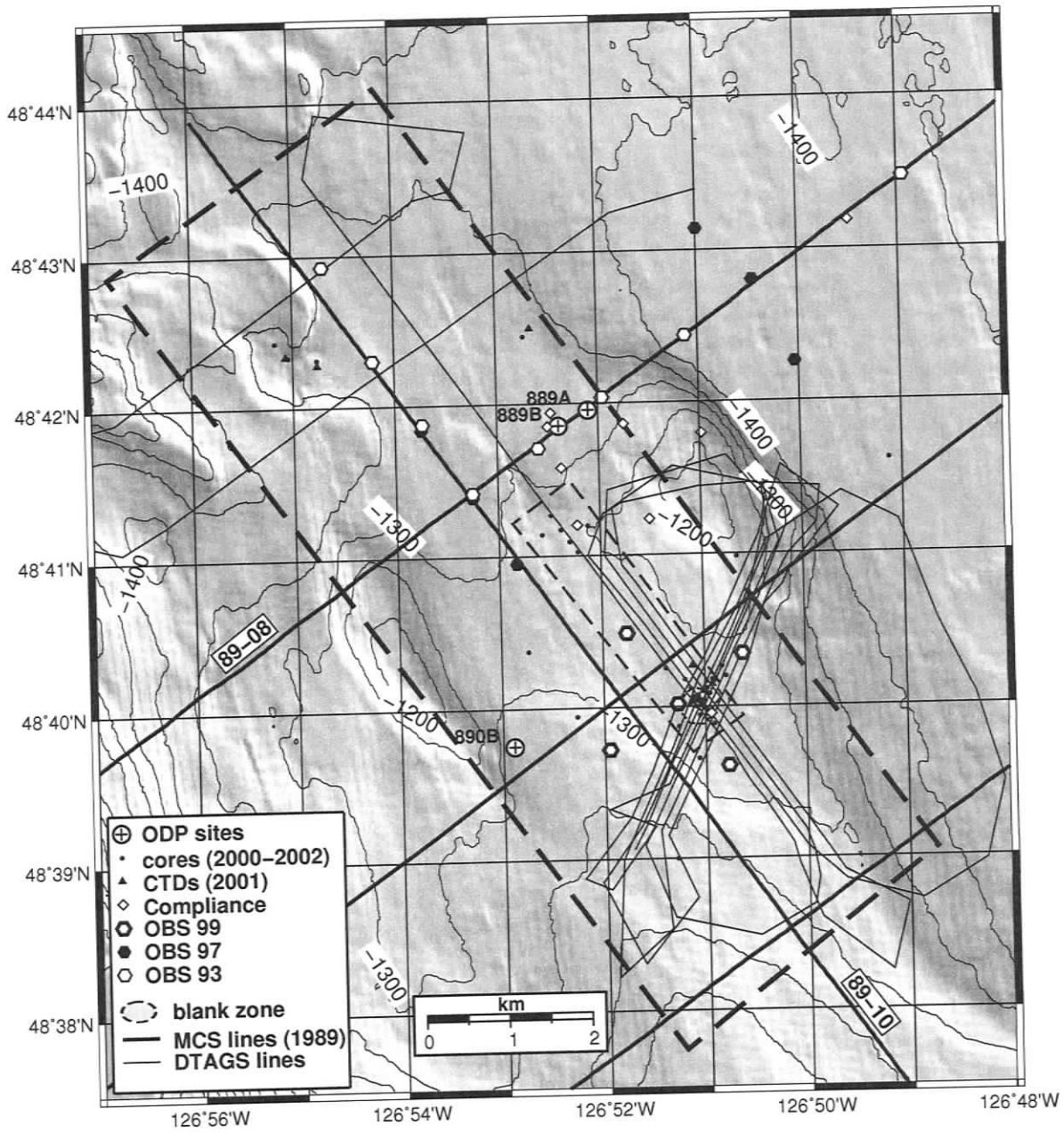

Figure 2.2: Bathymetry map around the site of interest. Major geophysical and coring studies are also indicated. Thick dashed box outlines the area of COAMS-99 multichannel seismic experiment, thin dashed box represents the limits of COAMS-99 high resolution single channel experiment.

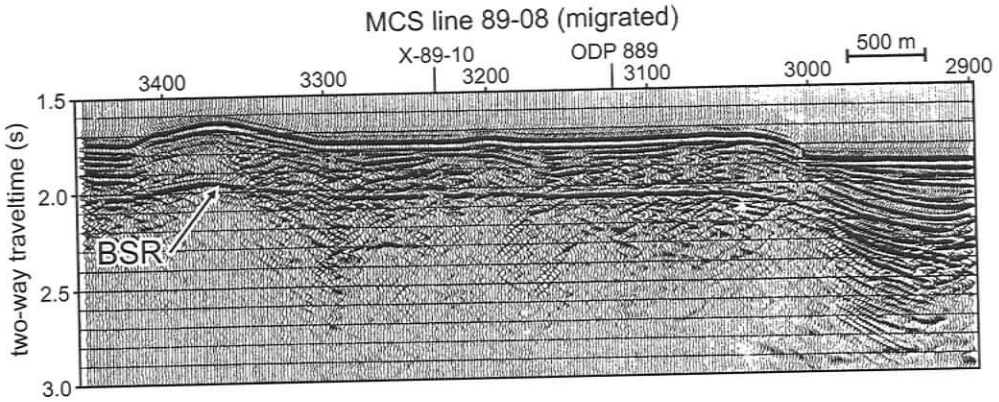

Figure 2.3: Multichannel seismic line 89-08. BSR is clearly visible over the accreted sediments. A ridge structure can be observed on the left side of the profile section (after Yuan et al., 1996).

2.2 Geophysical studies of hydrates

After the discovery of gas hydrates in the Cascadia region in 1985, the area became a focus of many detailed geophysical surveys targeted on the study of the natural gas hydrate in the deep-sea environment. The presence of the clathrates was inferred from the presence of the BSR in multichannel seismic sections collected in 1985 (Davis and Hyndman, 1989). In 1989, new seismic lines provided additional insight into the distribution of the BSR across the Cascadia margin (Hyndman, 1995). In 1992 ODP Leg 146 drilled at sites 889 and 890 in this gas hydrate region, as well as at site 888 in the deep ocean basin for the no-hydrate/gas reference (Westbrook et al., 1994).

A wide variety of geophysical studies have been carried out in the vicinity of the site of interest. These include multiple conventional single and multichannel seismic surveys (single profiles and grids of lines), deep-towed high-resolution seismic surveys using Deep Tow Acoustic Geophysics System (DTAGS), seismic surveys using Ocean Bottom Seismometers, high-resolution high frequency echosounder sub-bottom profiling, electrical surveys, seafloor compliance studies, and heat flow measurements. Several research cruises were dedicated to the sampling of the seafloor with piston coring devices. Video images of the seafloor together with the seafloor carbonate samples were collected using a submersible remotely operated vehicle. The locations

of the major studies mentioned above are shown on Figure 2.2.

2.2.1 Spatial distribution of the BSR and its properties

As indicated previously, the presence of gas hydrates and their distribution over the northern Cascadia region was inferred primarily from the presence of BSRs on seismic sections. Due to the apparent seismic transparency of the accreted sediments, the BSR was clearly recognizable where the bottom of the GHSZ was located within this sediment unit. The bedded slope sediments obscured the BSR, though in such areas (e.g., right hand side of the seismic section on Figure 2.3) substantial concentrations of gas hydrates were inferred from multichannel interval velocity analysis (Yuan et al., 1996) and controlled-source EM measurements of electrical resistivity (Yuan and Edwards, 2000).

The most seaward appearance of the BSR occurs a few kilometres landward of the deformation front (Fig. 2.4). The BSR disappears in the areas with water depth less than 800–900 m. The depth of the BSR below the seafloor in the region varies over the range of 175–400 m depending on water depth.

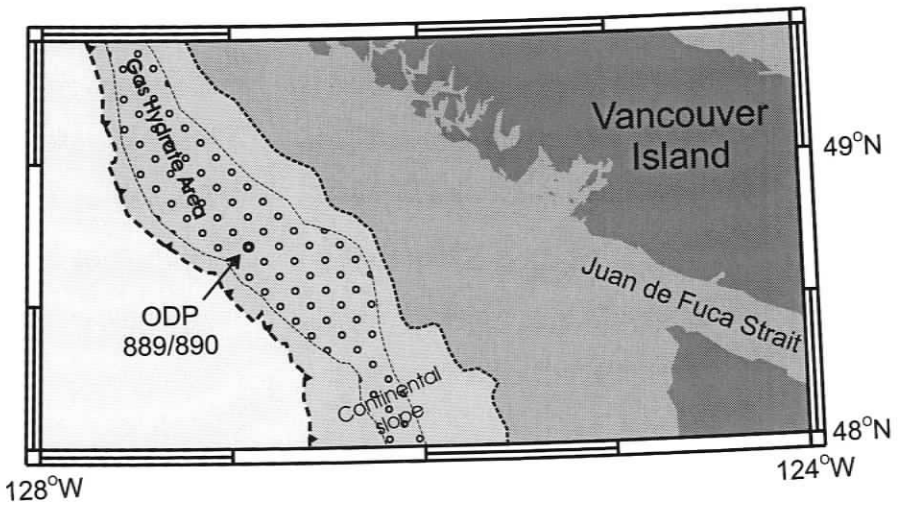

Figure 2.4: Distribution of the BSR over the northern Cascadia region (after Hyndman et al., 2001). Deformation front indicated by a thick dashed line ticked with triangles.

On the seismic sections recorded using a low frequency seismic source (20–30 Hz),

the BSR reflection is generally observed as a single pulse, similar to a reflection from a simple interface. The reflection coefficient is about 50% that of the seafloor (0.1–0.15) (Hyndman and Spence, 1992). Although the wavelength of such low frequency signals is about 60–80 m, any gradual impedance changes at the BSR that occur over as much as half this distance would produce a seismic signature of a simple interface.

Subsequent seismic surveys with different seismic sources revealed a strong frequency dependence of the BSR signature in the Cascadia area. Fink and Spence (1999) compared three seismic profiles shot over the same line but with seismic sources of different frequencies (30, 75, and 150 Hz for dominant frequency). The BSR reflection coefficient was found to be much lower for the higher frequencies. The amplitude of the BSR signal for the 30 Hz recording was as much as 40% higher than for 150 Hz source. At the even higher frequencies provided by DTAGS (250–650 Hz), the BSR reflection is very weak or even absent for the areas where it is strong in the lower-frequency data (Chapman et al., 2002).

The variation of the BSR strength with frequency can be explained by the fact that the decrease of the impedance occurs over some depth range rather than as a sharp change. That is, physically the BSR can be approximated not by a single interface but by a layer of finite thickness with negative velocity gradient. Modelling of the BSR response for different frequencies gave the range of 4–8 m as an estimation for the thickness of the layer producing the BSR (Chapman et al., 2002).

As the change in the acoustic impendence of the sediments at the BSR is mostly due to velocity contrast, three possible scenarios were considered for the origin of the BSR in the region (Fig. 2.5)(e.g., Yuan et al., 1999). First, the decrease in the P-wave velocity can be the result of transition from gas-hydrate-containing sediments above the BSR to no-hydrate sediments below the BSR (Fig. 2.5a). Also, the possibility exists that the BSR is caused by a layer with bubbles of free gas in the pore space (Fig. 2.5b). Finally, a combination of the above mentioned scenarios can be present (Fig. 2.5c), that is, the layer of sediments with gas hydrate is underlaid by sediments with free gas. The contrast of the P-wave velocity at the BSR is estimated at a value

of 250 m/s (Chapman et al., 2002). Such contrast can be provided by gas hydrates occupying 20–30% of the pore space or by 1% of free gas.

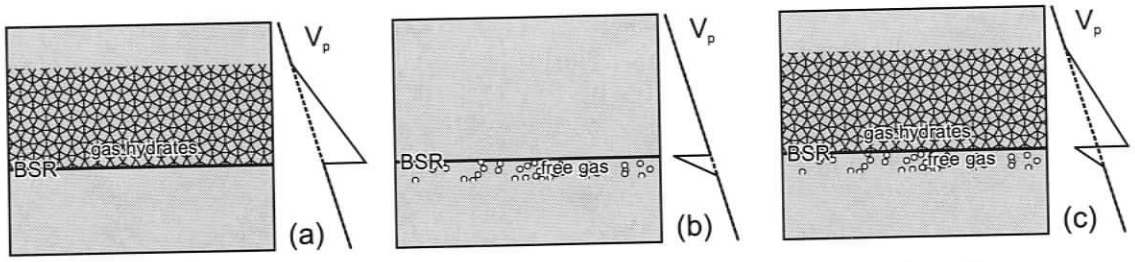

Figure 2.5: Models for the BSR producing environment (see description in the text).

Analysis of the reflection amplitude data was performed in an attempt to distinguish between the three probable models (Hyndman, 1992). Unfortunately, the amplitude studies were not able to provide a definite answer (Yuan et al., 1999; Riedel, 2001), primarily because of the insufficient quality of the available data combined with relatively small velocity contrasts compared to those for conventional hydrocarbon deposits, for which the AVO analysis normally is successful.

2.2.2 Sediment velocity and gas hydrate concentrations

The information about the velocity in the sediments around the ODP 889/890 well site is available from many different methods. These include the sonic well log, vertical seismic profiling (VSP), core physical property measurements, multichannel seismic interval velocity analysis, and travel time tomography (Fig. 2.6).

The variability of the velocity values is quite high when the results from the different methods are compared. This can be explained by uncertainty limitations of the different techniques. Also, it should be pointed out that different surveys were carried out at different sites. Although all surveys are separated by only a few kilometres, the thickness of sediment units may vary significantly even over that distance.

The most detailed vertical velocity profile is available from the sonic well log for the ODP 889a/b wells. According to Westbrook et al. (1994), the sediment section in

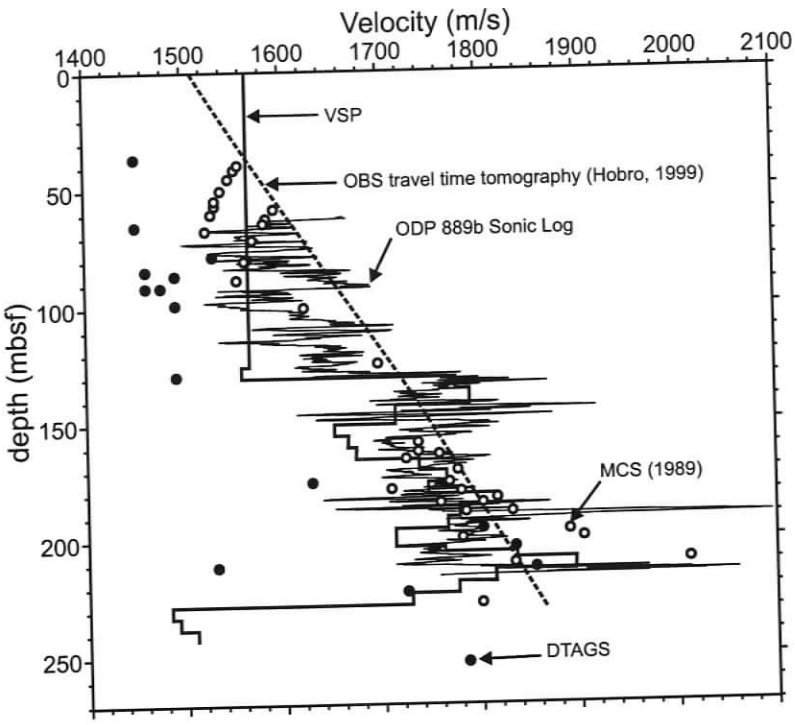

Figure 2.6: Results of previous velocity studies in the vicinity of ODP 889/890 well site (after Chapman et al., 2002).

the depth range from the top to the BSR can be subdivided into into two units. The first unit is represented by slope and slope basin sediments consisting of clayey silts and fine sands. The boundary between the units occurs at 128 m below the seafloor. The lower unit is similar in composition to the top one, but is more consolidated and highly fractured. It is interpreted as sediments that have undergone an accretion process.

The shallowest sonic logging data was at 60 $mbsf$ where the velocity measurements were about 1600 m/s. The transition between the sediment units was marked with a jump in velocity. The sonic log velocities immediately above the BSR are about 1800 m/s if averaged over the depth range of 20 m. Although the wells penetrated the BSR, the sonic log failed to record a low velocity zone immediately below the BSR. This can be explained by the fact that the drilling process might have flushed away the gas phase (Westbrook et al., 1994). In contrast, the VSP profile showed velocities as low as 1490 m/s below the BSR.

Another highly reliable source for the velocities in the sediments above the BSR at the site is the results of travel time tomography performed by Hobro (2000a). Veloc-

ities were 1500 m/s for the sediments just below the sea bottom. Velocity increases smoothly, almost linearly, down to the BSR reaching values of 1800–1850 m/s for the sediments above the BSR. However, the tomography inversion did not provide the fine structure of the velocity profile because of its resolution limitations.

The most important feature of a gas hydrate site is the concentration of gas hydrates in the sediment. This information is important for all gas hydrate issues, especially related to energy resource and climate change.

The concentration of gas hydrates in the sediment has been estimated from the effects of the dissociation, such as degree of pore water freshening or temperature decrease, and from the way in which the physical properties of the sediment are changed by the presence of hydrate. The most important physical properties that can be affected by the presence of gas hydrate are P- and S-wave velocities, resistivity, and porosity. Confident estimations for the gas hydrate concentration can be made if the background value for a property and the mechanism of gas hydrate influence on that property are known.

The expulsion model for gas hydrate formation suggests that the maximum concentration is just bove the BSR, with a gradual decrease up to the seafloor.

The estimation of gas hydrate concentrations from P-wave velocity was performed using the reference velocity from a general trend estimated with multichannel interval velocity analysis (Yuan et al., 1996). According to this study, the hydrate occupies 0–5% of the pore space in the depth range from the seafloor to approximately 130 $mbsf$. The concentration abruptly increases downward after that depth to 15–20% and reaches its maximum of about 35% at the BSR.

From the pore-water freshening calculations, the estimates of hydrate concentration are higher, about $35 \pm 10\%$ for the layer 100 m thick immediately above the BSR (Hyndman et al., 1999). In these calculations, the background or reference salinity of the pore fluids was derived from the site 888 well where salinity varied little from the seawater values.

The resistivity well log data provided values for the hydrate concentration that

were lower than those from the salinity data, but higher than those from the velocity studies. According to the resistivity log, almost no gas hydrate can be found close to the seafloor. The hydrate occupies 10% of the pore space for the depth around 130 m, and on average 28% for the deeper sediments. As for the salinity data, the background resistivity was derived from site 888 (Hyndman et al., 1999).

Electrical remote sounding surveys were performed in the area around the ODP 889 drill site in 1999(Yuan and Edwards, 2000). These experiments utilized a seafloor electric dipole-dipole array that produced average resistivity estimates for different depths depending on the source-receiver separation and estimated the resistivity of the sediments. Results indicated hydrate concentrations of about 17–26% of the pore space for the 100 m sediment layer above the BSR (Yuan and Edwards, 2000).

The concentrations of gas hydrates provided by all the different methods are quite high. However, the greater uncertainty is associated with the choice of background reference profile, which is selected from a location about 60 km away. Moreover, the reference site ODP 888 was located seaward of the deformation front, which is in a different tectonic environment.

Recently, the method for calculating the hydrate concentration was re-evaluated. Riedel et al. (2004) tried to establish a different background reference for the sediment properties. The new calculations showed that the concentration of gas hydrates can be as small as 5–10% of the pore volume for the 100 m thick layer above the BSR.

2.2.3 Blanking and carbonate pavement

In 1997 the survey with DTAGS discovered an unexpected phenomenon in the vicinity of the ODP drill sites. The seismic sections showed vertical zones in the sediment with much reduced amplitudes (Fig. 2.7). The features were called wipe-out zones or blank zones. The coherent reflected signal is significantly reduced or completely lost inside the blank zones. The attenuation of the seismic signal increases with frequency. Wherever the reflectors can be traced through the feature, a small pull-up of several milliseconds is generally observed on the normal incidence seismic sections.

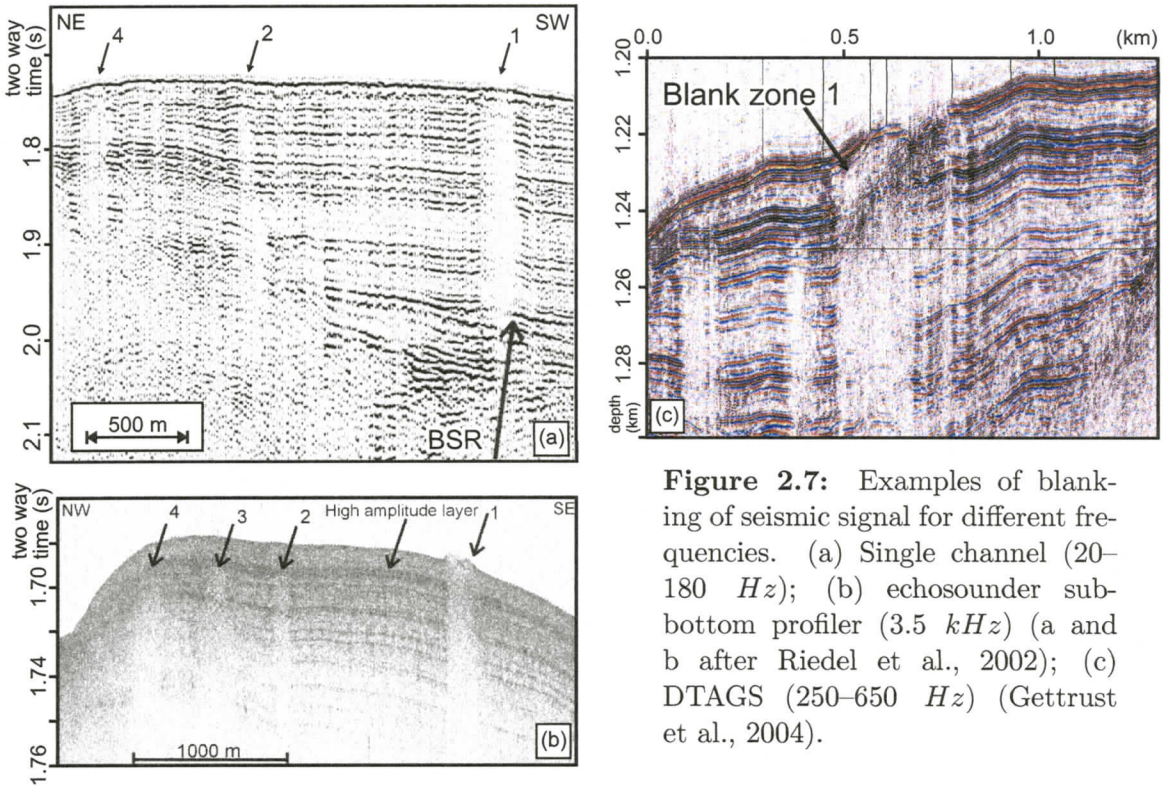

Figure 2.7: Examples of blanking of seismic signal for different frequencies. (a) Single channel (20–180 Hz); (b) echosounder subbottom profiler (3.5 kHz) (a and b after Riedel et al., 2002); (c) DTAGS (250–650 Hz) (Gettrust et al., 2004).

The blank zones occur mainly above the BSR, and the vertical extent of the zones varies from site to site. They may penetrate the whole sediment section between the BSR and the seafloor or only part of the distance above the BSR. In the horizontal plane the zones have circular or elliptical shape and sizes of several hundred metres. That is, their width might be up to several times greater than their height, which is not always obvious on seismic sections with an exaggerated vertical scale. The vertical borders may be vertical or slightly tilted (Riedel, 2001).

In the vicinity of the ODP 889/890 drill site, several prominent blank zones were observed. The largest one (1 on Figure 2.7) was named "Bullseye" (Riedel, 2001). It lies in line with three other similar features. The shape of the Bullseye blank zone is elliptical with areal dimensions of 400 $m \times 600$ m (as determined by 3-D seismic survey) with the longest axis being almost perpendicular to the imaginary line joining the the four blank zones. As the largest discovered blank zone feature in the area, the Bullseye feature was the target of multiple geophysical surveys, including heat flow measurements, piston cores, and direct video observation.

A pseudo 3-D seismic survey revealed the presence of a high amplitude ring around the blank zone #1 (Hyndman et al., 2001). Also diffraction features were observed at the edges of the blank zones (Fig. 2.8).

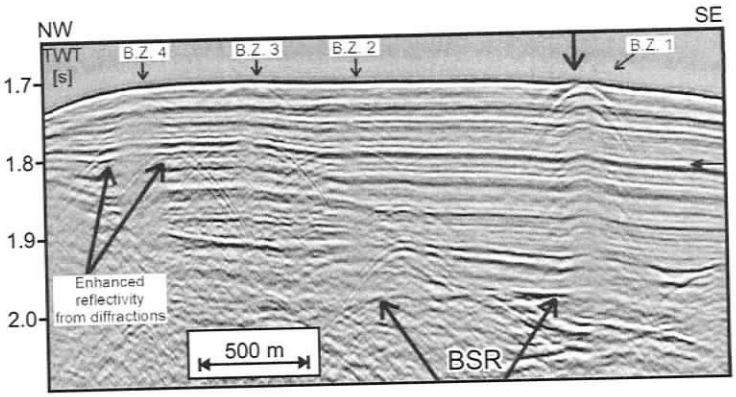

Figure 2.8: Example of diffractional features associated with the blank zones. Multichannel seismic line, unmigrated (after Riedel et al., 2002).

Samples of massive gas hydrate were found in the cores taken within the blank zone (Novosel et al., 2005). In the coring survey massive hydrate was sampled down to a depth of about 8 $mbsf$ (maximum penetration of the coring device)(Novosel, 2002). However, video observations made with a remotely operated submersible vehicle discovered only very small, isolated colonies of diverse marine biota associated with methane seeps (Riedel, 2001).

Carbonate outcrops were also found in the vicinity of the blank zone #1. The carbonates form plates several centimetres thick and cover significant areas of the seafloor. The isotopic analysis of the carbonates suggested their formation by oxidation of biogenic methane (Riedel et al., 2006).

The collected evidence suggests an active venting site associated with the blank zone (Novosel et al., 2005). The venting occurs through small vent outlets. The methane flux within the Bullseye vent is estimated to be 32–60 $mol{\cdot}m^{-2}{\cdot}k.y.^{-1}$ (3–6 times higher than outside the vent) using the depth of sulfate-methane interface (Riedel et al., 2006).

Despite the extensive investigation there is no agreed-upon mechanism to explain the origin of blanking at the Bullseye vent site. Scattering of seismic energy is likely. Suggested mechanisms include bodies of massive gas hydrates formed by increased fluid and methane flow (Riedel, 2001), and free gas inside the zone due to shallowing

of the GHSZ as a result of focused flow of warm fluids (Wood et al., 2002).

Among the unresolved questions are: (1) What is the velocity inside the vent zone relative to the outside? (2) How does the velocity relate to the distribution of gas hydrates through the vent site? (3) Is there any presence of free gas inside the blank zone? and (4) Is a single mechanism responsible for the blanking, or are different mechanisms required to produce separate effects at different seismic frequencies?

Chapter 3

COAMS-99 cruise

The data sets used in this work were obtained during the COAMS-99 cruise that took place from July 26 until August 11 of 1999 in the vicinity of ODP drill site 889/890. The main target was the group of blanking zones discovered in an earlier survey using the DTAGS system in 1997 (e.g., Chapman et al., 2002). The goal of the experiment was to acquire extensive data to help understand the sediment structure and migration regime of fluids and gas around the blank zones (Riedel et al., 1999).

The experiment was carried out from the research ship C.C.G.S. John P. Tully (length: 68.9 m; gross tonnage: 2021 t). The main acquisition systems were:

- multichannel Canadian Ocean Acoustic Measurement System (COAMS) hydrophone array, with active length 1140 m;
- single channel Teledyne array;
- Ocean Bottom Seismometers (OBSs);
- on-board high frequency systems (3.5 kHz subbotom profiler; 12 kHz echosounder).

The collected data included:

- pseudo 3-D multi-channel seismic, covering an area of 12 $km \times 4$ km with 41 lines at 100 m separation and 8 cross-lines with 1 km separation (Fig. 3.1);
- single channel seismic along the same tracks;

- 5 OBS recordings for the half of the multichannel seismic tracks (22 lines at 200 m separation and 3 cross-lines) (Fig. 3.2);
- single channel seismic over the area of 3.7 $km \times 0.75$ km that covered the blank zones with 25 parallel lines at 25 m separation;
- 3.5 and 12 kHz echo sounder data recordings for the whole period of the survey;
- navigation and depth to the seafloor.

Navigation information was obtained using a GBX GPS/Beacon Receiver produced by Communication Systems International. It is a Differential Global Positioning System (DGPS) that utilizes a correctional signal from beacons to achieve an accuracy of 2–5 m for estimates of positions. The satellite receiver antenna for the system was placed at ship's aft mast.

Multichannel and single channel seismic data sets were analyzed thoroughly by Michael Riedel in his thesis work (Riedel, 2001). For easier correlation, the cross-reference information for the seismic lines from different data sets is presented in Table 3.1.

3.1 Seismic systems

The disposition of the on-board and towed instruments during the COAMS-99 experiment is shown on Figure 3.3. The important distance measurements between the systems are indicated on the diagram.

3.1.1 Seismic source

For the purpose of producing a controlled acoustic impulse, a single airgun source was used. The volume of the work chamber was 40 in^3 (0.655 l). The airgun had a wave-shape kit that performed a two-stage air release (50% of the volume or 20 in^3 at each stage) with an interval of few milliseconds in order to reduce the bubble collapse energy.

Table 3.1: Crossreference nomenclature for COAMS survey track-lines.

in cruise	streamer grids	OBS grid	heading
Crl-01	Inl-01	Grl-01	S - N
Crl-02	Inl-09	Grl-05	N - S
Crl-03	Inl-05	Grl-03	S - N
Crl-04	Inl-17	Grl-09	N - S
Crl-05	Inl-13	Grl-07	S - N
Crl-06	Inl-25	Grl-13	N - S
Crl-07	Inl-21	Grl-11	S - N
Crl-08	Inl-33*	Grl-18	S - N
Crl-09	Inl-29	Grl-16	S - N
Crl-10	Inl-41	Grl-22	N - S
Crl-11	Inl-37	Grl-20	S - N
Crl-12	Inl-39	Grl-21	N - S
Crl-13	Inl-31	Grl-17	S - N
Crl-14	Inl-35	Grl-19	N - S
Crl-15	Inl-23	Grl-12	S - N
Crl-16	Inl-27	Grl-15	N - S
Crl-17	Inl-15	Grl-08	S - N
Crl-18	Inl-19	Grl-10	N - S
Crl-19	Inl-07	Grl-04	S - N
Crl-20	Inl-11*	Grl-06	N - S
Crl-21	Inl-03*	Grl-02	S - N
Crl-22	Inl-06*	n/a	N - S
Crl-23	Inl-02*	n/a	S - N
Crl-24	Inl-14*	n/a	N - S
Crl-25	Inl-10*	n/a	S - N
Crl-26	Inl-22	n/a	N - S
Crl-27	Inl-18*	n/a	S - N
Crl-28	Inl-30*	n/a	N - S
Crl-29	Inl-26	Grl-14	N - S
Crl-30	Inl-38*	n/a	N - S
Crl-31	Inl-34*	n/a	S - N
Crl-32	Inl-40*	n/a	N - S
Crl-33	Inl-32*	n/a	S - N
Crl-34	Inl-36*	n/a	N - S
Crl-35	Inl-24*	n/a	S - N
Crl-36	Inl-28*	n/a	N - S
Crl-37	Inl-16*	n/a	S - N
Crl-38	Inl-20*	n/a	N - S
Crl-39	Inl-08	n/a	S - N
Crl-40	Inl-12*	n/a	N - S
Crl-41	Inl-04*	n/a	S - N
Crl-42	Xl-01	n/a	W - E
Crl-43	Xl-02	n/a	E - W
Crl-44b	Xl-03	n/a	W - E
Crl-45	Xl-04	n/a	E - W
Crl-46	Xl-05	n/a	W - E
Crl-47	Xl-06	Xl-01	E -W
Crl-48	Xl-07	Xl-02	W - E
Crl-49	Xl-08	Xl-03	E - W

* - indicates lines for which good shotpoint hydrophone data are available

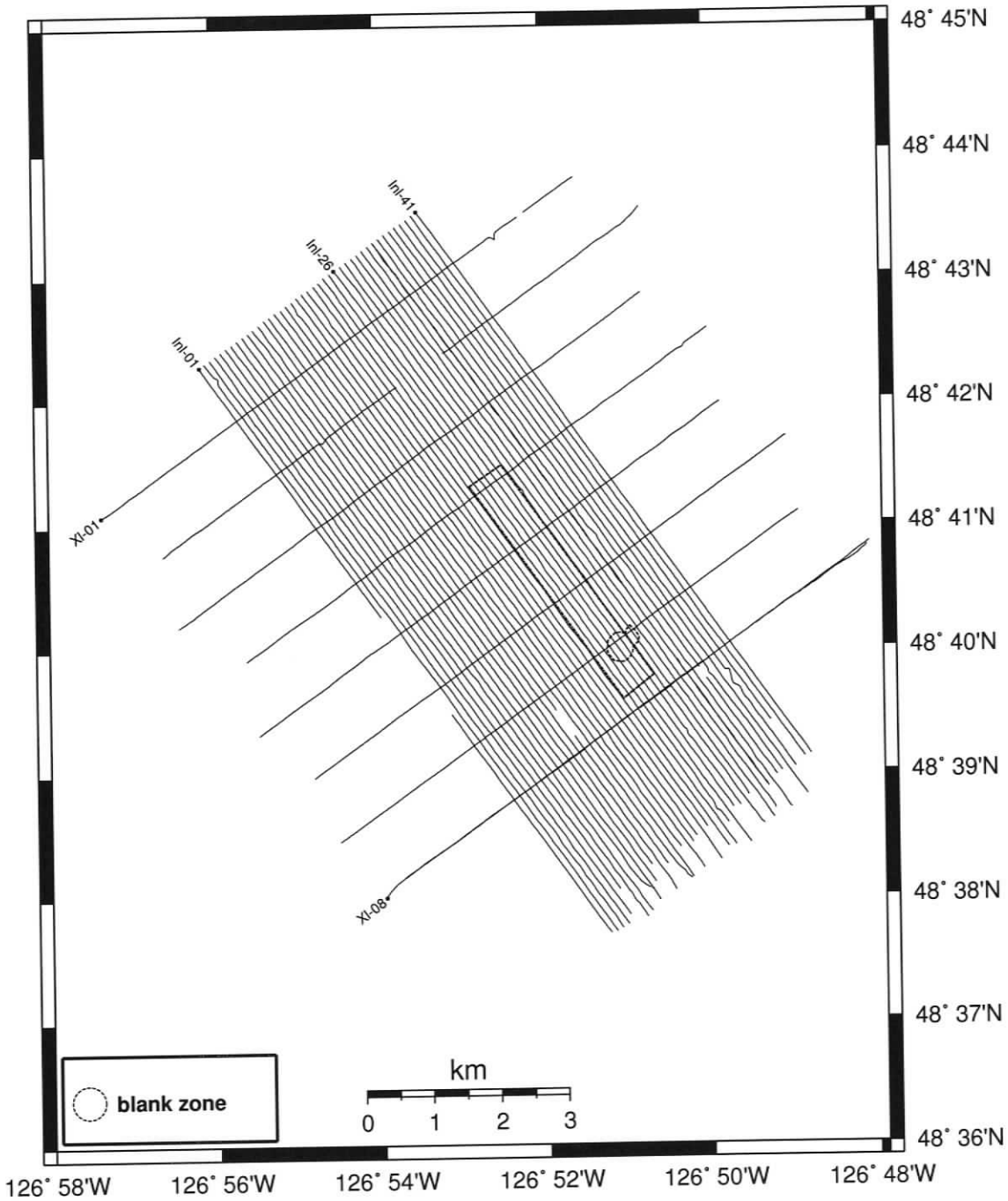

Figure 3.1: Tracklines for which both multi- and single-channel seismic data were obtained. Dash-dotted line outlines the area covered by 25 m lines spaced grid of single channel seismic survey. Limits of the main blank zone are shown (within the SE part of the 25 m grid).

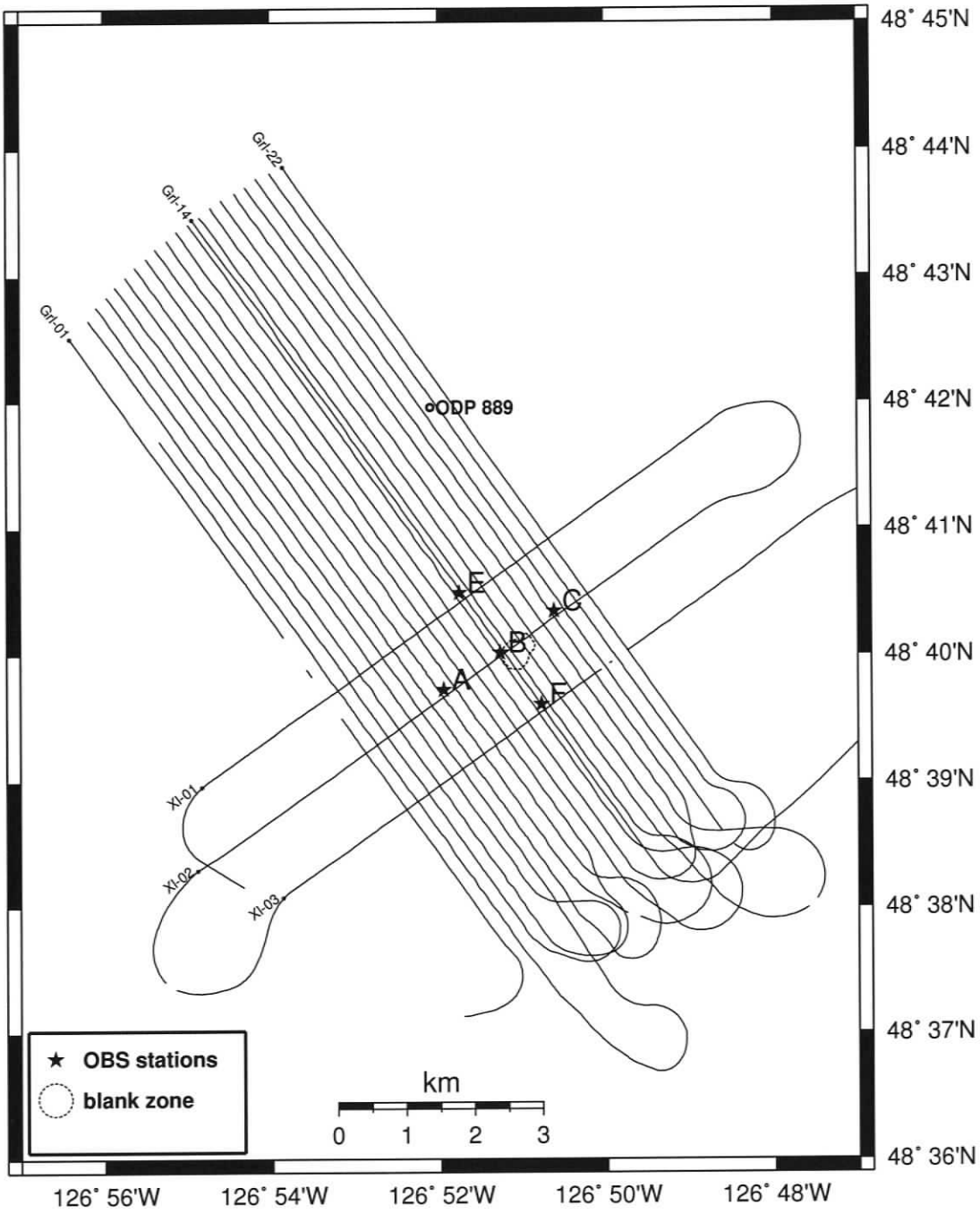

Figure 3.2: Shots recorded by OBS stations. Limits of the Bullseye vent zone and the location of ODP 889 drill well are also shown.

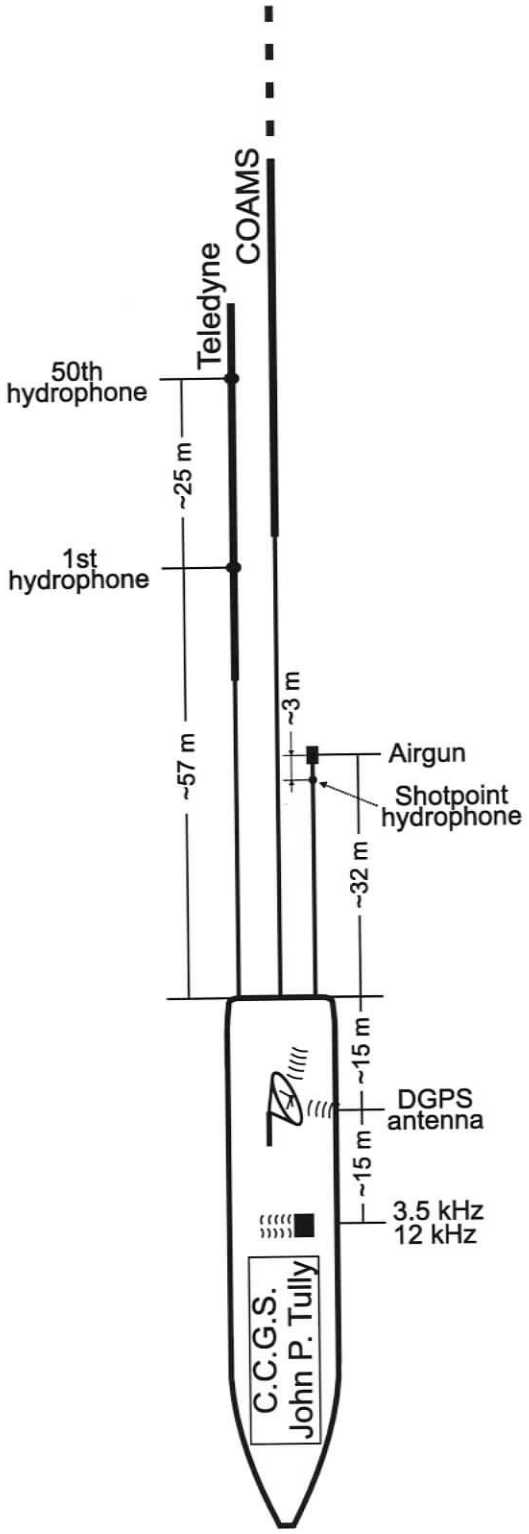

Figure 3.3: Geometry and placement of onboard and towed systems used during COAMS-99 cruise.

The seismic source was recorded by a shot point hydrophone. The hydrophone was placed in the vicinity of the airgun with an estimated position 3 m in front and 3 m below. This sensor was used for controlling the time of the air release and recording the source signature. The shape of the signal can be used to improve the quality of seismic data processing operations (e.g., deconvolution) and modelling (e.g., full waveform inversion). The signal from the shotpoint hydrophone was digitized with a time step of 39 μs. Figure 3.4 shows an example of the airgun initial impulse for four shots. The shape of the first peak was consistent (with rare exceptions) along the survey, with the arrival time after the trigger pulse being 20 ± 1.5 ms. Based on the known distance between source and receiver, the delay of the airgun system to the trigger signal can be estimated at 18 ± 1.5 ms.

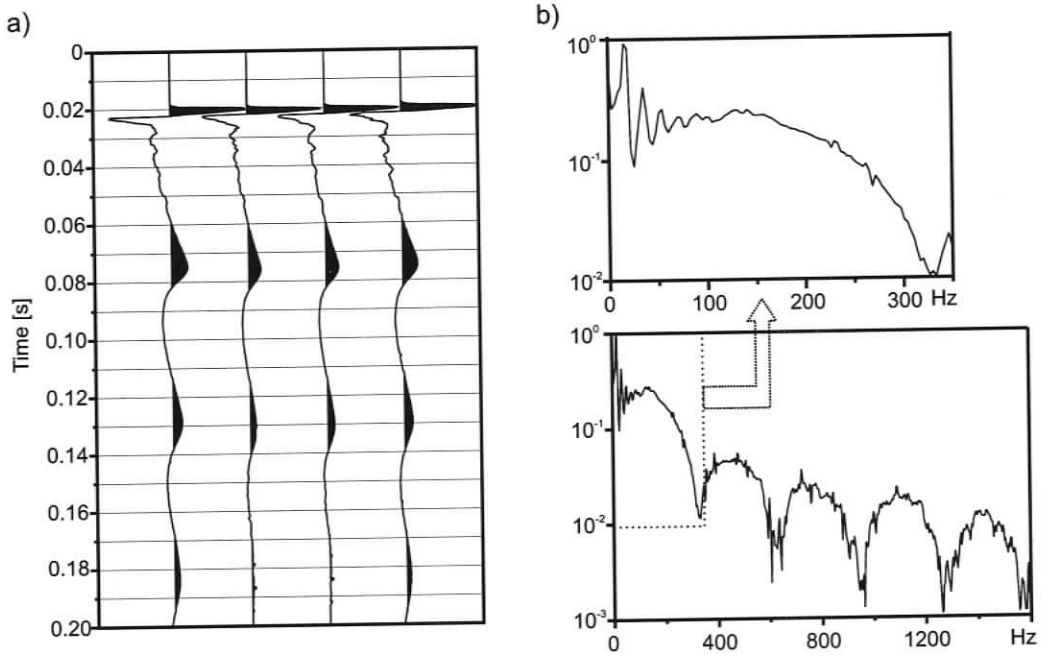

Figure 3.4: Seismic source signature. Time domain data (a) and amplitude spectrum (b)

The released air bubble generates an oscilating "bubble pulse" signal with a period of about 50 ms, and a duration of 3–4 oscillation cycles (Fig. 3.4a). The bubble pulse generates a strong low frequency signal with a maximum frequency of 25 Hz. While this signal was almost undetectable in the raw single channel data (likely due to

pre-digitize high-pass filtering), the bubble pulse was very strong in the OBS data. Unfortunately, the shotpoint hydrophone was not operated at all times during the cruise, so the initial shot impulse signature was retrieved for less than half of the shots.

The airgun was towed approximately 32 m behind the stern. A flotation device was used to sustain the device at a constant depth which was estimated at ≈ 2 m. For the purpose of modelling and data processing the depth of the seismic source was fixed at that value.

Originally, it was planned to trigger the airgun every 19 m, so the shot points were equally spaced along the track. However, some difficulties arose with prediction of the ship position. Thus, the actual distance between shot points varied from 10 to 32 m.

3.1.2 OBS

An OBS is an autonomous seismic recording device designed for use in seismic surveys in areas with water depth up to several kilometers. It is deployed on the seafloor and remains fixed at the site for the period of experiment. For the COAMS-99 cruise six Dalhousie OBSs (Fig. 3.5) were obtained from the Dalhousie Seismic Group, Dalhousie University.

The instrument itself has a positive buoyancy in the water that is provided by three hollow glass spheres. In order to deliver the device to the seafloor a heavy weight (anchor) is attached to its bottom. The link between the OBS and its anchor is detachable. The release mechanism is activated by an acoustic message, after which the instrument floats up to the surface where it emits radio and visual signals for easier spotting and recovery.

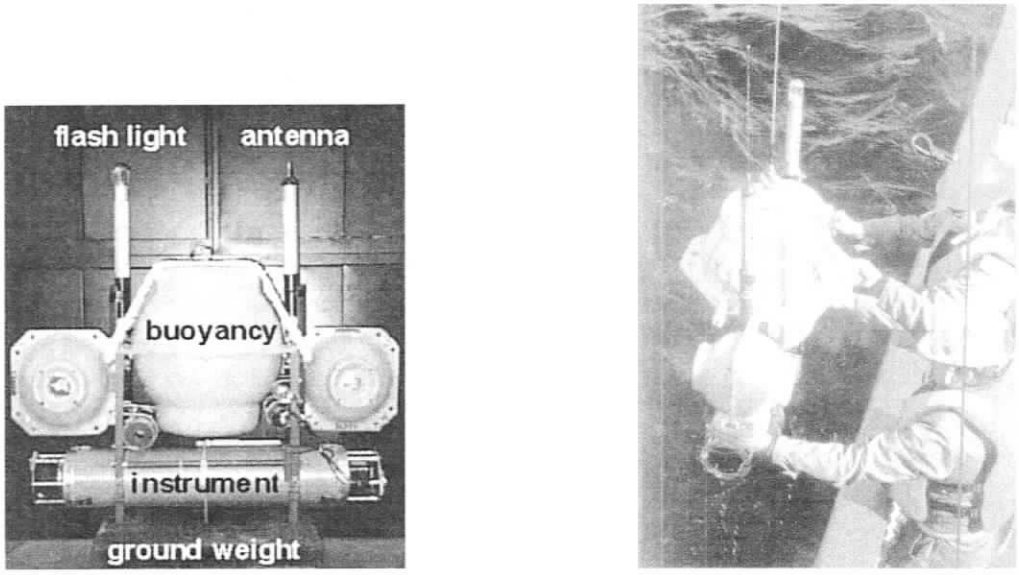

Figure 3.5: Dalhousie OBS instrument (left) (*photograph from Dalhousie Seismic Group website*) and device recovery moment (right).

Each OBS includes four essential systems:

1. sensor system
2. data storage
3. timing
4. communication

The communication system has very limited capabilities and is used only at the recovery stage at the end of the survey, as described earlier.

The seismometer sensing system consisted of one pressure sensor (hydrophone) and a 3-component geophone package. The analog signals from the four sensors were filtered using an anti-alias filter with corner frequency of 200 Hz, and then were digitized with 1.433 ms sampling interval (698.8 Hz) and 16-bit dynamic range ($\pm$32768). The temporary storing of data was implemented in a 2 MB RAM. Upon filling the contents of this memory, the data were dumped into a 1 GB hard drive as a separate file each time. Detection was not performed during the data dumping process, which took approximately 20 seconds. This resulted in having about two

Table 3.2: OBS deployment/recovery information (all times are in UT: day:hour:minute).

OBS	Deployment time	recovery time	Clock set time	Clock check time	Set - check period (hrs.)	drift (ms)	drift rate (ms/day)
A	214:06:00	221:05:02	213:19:24	221:05:23	178	68.2	9.2
B	214:06:20	221:04:09	213:20:08	221:04:38	176.5	29.5	4.0
C	214:04:40	221:07:08	213:20:21	221:07:53	179.5	4.4	0.6
E	214:07:03	221:06:10	213:22:41	221:06:34	175.9	26.5	3.6
F	214:07:02	221:03:12	213:20:35	221:03:52	175.3	-44.6	-6.1

dead time series per 40 recording. The active operational period with the system parameters used was limited by the storage capacity to approximately 2.5 days.

The recorded seismic data were tied to an absolute timescale using a precise clock (Austron 1115 OCXO 5 MHz) with an expected time drift rate less than 1 ms per day. On the ship, the time instants of air gun releases were determined using two Dalhousie GPStar Odetics receivers which were separately. The Odetics receivers were also used to set the time for the OBS internal clocks before deployment and later to check after recovery. Despite the small expected drift rate, the actual average drift for the internal timing systems was up to 10 ms per day (see Table 3.2). Besides having larger values, the clock drift rates for stations A and F were not steady, as discovered during the data processing, and this resulted in non-linear drift function (see Chapter 4).

All six instruments were labelled by letters from A to F. During the predeployment test, one (D) was found to be inoperable and was excluded from the array. The remaining five were deployed at the site, four at the corners of a square with sides of 1.4 km and one in the centre. The minimum distance between adjacent OBSs was 1 km. The diagonals of the square were aligned along the directions of the survey track lines (Fig. 3.2). The configuration of the instruments provided two lines with three stations in each line.

In this study only data recorded by the hydrophone were used for analysis and modelling. Examples of the seismic data recorded by the hydrophone sensor of the OBSs are provided in Appendix B

3.1.3 Teledyne single channel streamer

The Teledyne system is a 50 m long oil-filled single channel streamer. It consists of three parts: two vibration isolation modules in front and at the end of the streamer of lengths 15 and 10 m respectively, and a 25 m long active section with 50 hydrophones equally spaced at 0.5 m. The signals from all hydrophones were summed to form one channel. The head of the streamer was towed 42 m from the stern of the ship.

The streamer had a built-in preamplifier with a high-pass filter set at 60 Hz. Before digitizing at a sampling time interval of 1.433 ms (698.8 Hz), the signal was further filtered with a Krohn-Hite filter set at 70–2000 Hz (Riedel et al., 1999).

3.1.4 High frequency systems

Two high frequency systems, a 3.5 kHz subbottom profiler (ORE Model 140 transceiver) and 12 kHz echosounder (Simrad EA-500), were used during the COAMS-99 cruise. They were installed in the hull of the vessel, amidships.

The subbottom profiler transmitted a signal with a 4 s repetition rate, and the received signal was digitized at a 39 μs sampling period. The device consisted of 16 individual transceivers combined into an array of size 82 $cm \times 82$ cm. The transmitting beam width was 30°.

The data from the echosounder were not digitized. They were immediately plotted using colour inkjet printer using the colour scale to grade the strength of the reflected echo. Also, the received signal was subject to real time processing in order to determine the arrival time of the seafloor reflection and hence to calculate the depth to the sea bottom at given point. The time-to-depth conversion was done using a fixed mean water velocity of 1492.6 m/s.

Water sound speed profiles were measured at the end of the cruise with a velocimeter (Applied Microsystems Ltd.)and are shown in Fig. 3.6.

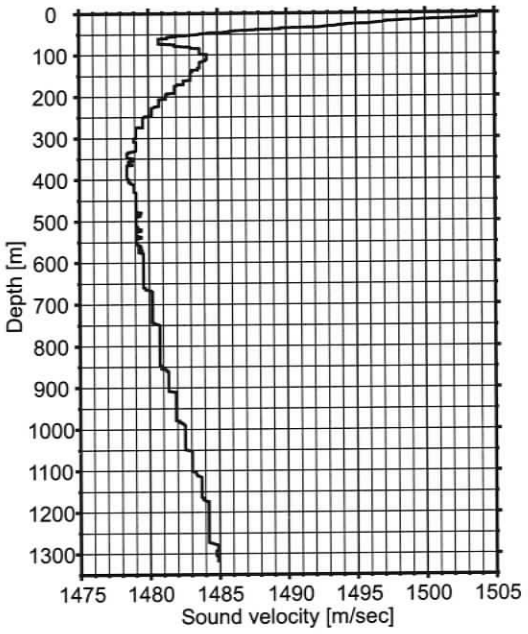

Figure 3.6: Vertical sound speed profile for August 9, 1999 at 48° 41.3806', 126° 52.3661'

Chapter 4

Localization of sources and receivers

The first step in the seismic data processing after recovering raw data is the definition of the survey geometry. The initial assessment of coordinates for the sources and receivers made in the field sometimes is sufficiently accurate for further processing. On the other hand, it might be the only available way to determine the positions. For present data set, improved localization and timing were vital for meaningfully inverting the data.

For the surveys that involve fixed instruments (either sources or receivers), it is possible to improve the initially evaluated geometry greatly through a localization approach (Dosso et al., 1998; Barlee et al., 2002). The basic concept uses the signal travel times for each pair of source-receiver to obtain more accurate estimation of the true geometry of the experiment. Also there might be other values besides the position coordinates that need to be adjusted (e.g., water column velocity profile bias, internal clock drift, etc.). Hence, the sources and receivers localization (SRL) problem can be formulated as the recovery of the position coordinates of the sources and receivers along with other correctional parameters using the travel times of acoustic waves.

In order to solve the inversion problem correctly, possible types and origin of errors have to be evaluated, and then the mathematical approach has to be developed and applied.

4.1 Types of errors in the OBS survey

4.1.1 Positioning errors

While the coordinates of the deployment point on the sea surface for the recording instrument can be obtained with high accuracy, the actual resting point on the seafloor is not well known. The uncertainty in the position may increase for deep water deployments of greater than 1 km, where the horizontal drift of the descending device may be large depending on the currents and the physical shape of the instrument. In addition, the depth of the recording device is obtained using a bathymetry map, the accuracy of which may be much lower than the desired accuracy for the survey geometry.

The positions of the seismic sources are better constrained but can still be unacceptably large. During the survey the receiver antenna for the GPS system used for navigation is placed on the top of the mast, approximately in the centre of the ship, a few tens of metres from the stern. On the other hand, the seismic source is being towed a few tens of metres behind the stern (Fig. 3.3). This adds up to a distance of several tens of metres between the point of coordinates determination and the point which coordinates need to be known (47 m for the COAMS-99 cruise geometry). The correction for this distance can be done through interpolation along the ship's track line, but the trajectory of the airgun may lie a few tens of metres to one side of the antenna's track, especially in strong side winds or currents, or if the ship is turning.

These issues indicate that despite the use of very precise DGPS with an accuracy of up to ± 2 m, the actual accuracy of the seismic source coordinates may be worse than ± 10 m, which may be unacceptable.

4.1.2 Timing errors

For a conventional seismic survey with airguns, the firing device sends the firing signal to the seismic source and at the same instant the recording device starts writing data. The system makes use of the relative time and the only correction that has to be made is for the response time of the source to the firing signal. However, for surveys that

utilize autonomously recording sensors a timing problem exists.

For those types of surveys in which geometry does not allow the direct delivery of the firing signal to the recording device, absolute time must be employed. In this case the source system records the absolute time instant of the firing signal, and the recording device operates independently in a continuous writing mode while putting time stamps throughout the record.

The requirements for the accuracy of time determination at any given instant during the survey are very high. The GPS clock is the source for the accurate timing of the firing system on the ship. Unfortunately, the satellite signal cannot reach the seafloor instruments through the water and precise clocks must be incorporated into the recording devices in order to sustain the time consistency of the seismic data.

To satisfy the purpose of the survey, the precision of the OBS clocks must be in the range of few milliseconds for the period of the survey. The standard procedure includes the clock calibration using the GPS clock before the deployment, and subsequently obtaining the time difference between the internal clock and GPS time after recovery of the instrument. The basic correction is then made assuming a linear clock drift between check points. In this experiment the analysis showed that the clock drift can reach values of several tens of milliseconds over the period of the survey, and it is not always linear.

4.2 Mathematical inversion approach

In general any modelling procedure can be described by a vector equation:

$$\mathbf{d} = \mathbf{D}(\mathbf{m}) \tag{4.1}$$

where $\mathbf{m}$ is the parameter vector of the model, $\mathbf{D}$ the response function, and $\mathbf{d}$ is the model response (data). Provided any two out of three are known, it is usually possible to obtain the third one. The most trivial procedure is obtaining $\mathbf{d}$, and is called forward modelling. The recovery of $\mathbf{D}$ is the most difficult task and probably never used in geophysics. Recovery of the model parameters from the response, called

the "inverse problem", is in widespread practice, although in many cases it is not a straightforward problem particularly if $\mathbf{D}$ is a non-linear function.

In the case of SRL, $\mathbf{d}$ incorporates all known data (travel times) and $\mathbf{m}$ all unknown parameters that need to be recovered (coordinates, clock drift, etc.). The SRL problem is non-linear, but a local linearization can be achieved by expanding $\mathbf{D}(\mathbf{m}) = \mathbf{D}(\mathbf{m_0} + \delta\mathbf{m})$ to first order about an arbitrary starting model $\mathbf{m_0}$. This yields

$$\mathbf{d} = \mathbf{D}(\mathbf{m_0}) + \mathbf{J}\delta\mathbf{m} \tag{4.2}$$

Further substitution of $\delta\mathbf{m} = \mathbf{m} - \mathbf{m_0}$ into (4.2) and rearranging terms leads to

$$\mathbf{Jm} = \mathbf{d} - \mathbf{D}(\mathbf{m_0}) + \mathbf{Jm_0} \equiv \check{\mathbf{d}} \tag{4.3}$$

where $\mathbf{J}$ is a Jacobian matrix, that consists of partial derivatives $J_{ij} = \partial t_i(\mathbf{m_0})/\partial m_j$ and $\check{\mathbf{d}}$ may be defined as the modified data (Dosso et al., 1998).

Since the higher order terms of the Taylor series were neglected during the linearization step, the solution for (4.3) will not necessarily fit the data. An iterative approach has to be employed in which the starting model $\mathbf{m}_0$ is updated after each step, to be used in the next iteration

All measured data are contaminated by some level of noise. To solve the inverse problem with noisy data, a standard assumption is made that the error n_i on datum d_i is due to an independent, Gaussian-distributed random process with zero mean and standard deviation σ_i. In this case, instead of an exact solution, a maximum-likelihood solution is obtained to fit the measured data most closely (least-squares technique). The data misfit function, which must be minimized, is introduced as

$$\chi^2 = |\mathbf{G}(\mathbf{Jm} - \mathbf{d})|^2 \tag{4.4}$$

where $\mathbf{G}$ is a weighting matrix, which is diagonal with ith element representing the reciprocal of the uncertainty $(1/\sigma_i)$ of the ith measured datum. By setting $\partial\chi^2/\partial\mathbf{m} = 0$, the solution becomes

$$\mathbf{m} = [\mathbf{J}^T\mathbf{G}^T\mathbf{GJ}]^{-1}\mathbf{J}^T\mathbf{G}^T\mathbf{Gd}. \tag{4.5}$$

However, the least-squares method fails if the matrix to be inverted is singular. This occurs when the problem is under-determined. Also, an unstable solution of the inversion may be present due to an ill-conditioned Jacobian matrix, for which small variations in data lead to very large variations in the solution.

Ill-conditioning is a common problem for long-offset surveys with bottom-moored instruments. This problem may arise for certain types of geometries, in particular, when all receivers are grouped in the middle of the survey area with the longest distance between two instruments being several times smaller then the longest shot offset. In this case the azimuths at the far offset shotpoints to the recorders are concentrated in a narrow sector and as a result there is a great instability in the solution for coordinates of those shots.

The difficulties with under-determined or ill-conditioned problems can be overcome by using a regularized inversion technique. In this case, *a priori* information is included into the inversion. As (4.3) is expressed in terms of the model and not as the model perturbation, this information can be added easily.

A priori information can be of different types. First, a simple example is independently estimated values for the model parameters. These values form the initial model ($\hat{\mathbf{m}}$). Second, in case of shooting along the track lines, the expectation of the seismic source trajectory being a smooth line is reasonable. With the *a priori* information used, the function to be minimized takes the form of

$$\phi = |\mathbf{G}(\mathbf{J}\mathbf{m} - \mathbf{d})|^2 + \mu_1|\mathbf{H}_1(\mathbf{m} - \hat{\mathbf{m}})|^2 + \mu_2|\mathbf{H}_2(\mathbf{m} - \hat{\mathbf{m}})|^2 \tag{4.6}$$

where μ is a trade-off parameter that controls the relative importance of fitting the measured data compared to maintaining the *a priori* model. Based on the number of different types of *a priori* information, additional regularization terms can be added to the function. In the case of only one regularization term, the regularized solution becomes

$$\mathbf{m} = \hat{\mathbf{m}} + [\mathbf{J}^T\mathbf{G}^T\mathbf{G}\mathbf{J} + \mu_1\mathbf{H}_1^T\mathbf{H}_1 + \mu_2\mathbf{H}_2^T\mathbf{H}_2]^{-1}[\mathbf{J}^T\mathbf{G}^T\mathbf{G}\mathbf{d} - \mathbf{J}\hat{\mathbf{m}}]. \tag{4.7}$$

For the purpose of using the prior estimate of the model as a regularization term,

the matrix $\mathbf{H}_1$ takes the form of a diagonal matrix with each element equal to the reciprocal of the uncertainty of estimation for the corresponding model parameter:

$$\mathbf{H}_1 = \mathrm{diag}[1/\xi_j]. \tag{4.8}$$

The smoothing regularization uses the fact that the second derivative is a measure for the smoothness of the function. The second derivative of a discreet function m at point j is defined as

$$\left.\frac{d^2m}{du^2}\right|_j = -\frac{m(u_j)}{(u_{j+1}-u_j)^2} + \frac{m(u_{j+1})(u_{j+2}-u_j)}{(u_{j+2}-u_{j+1})(u_{j+1}-u_j)^2} - \frac{m(u_{j+2})}{(u_{j+2}-u_{j+1})(u_{j+1}-u_j)}, \tag{4.9}$$

where u is an independent variable. By letting $\hat{\mathbf{m}} = 0$ and $\mathbf{H}_2$ be a tridiagonal matrix with non-zero elements given by

$$\mathbf{H}_2 = \mathrm{tridiag}\left[\frac{-1}{(u_{j+1}-u_j)^2}, \frac{(u_{j+2}-u_j)}{(u_{j+2}-u_{j+1})(u_{j+1}-u_j)^2}, \frac{-1}{(u_{j+2}-u_{j+1})(u_{j+1}-u_j)}\right], \tag{4.10}$$

the term $|\mathbf{H}_2\mathbf{m}|^2$ provides a measure of the curvature of the model.

For every iterative algorithm, conditions for the convergence have to be defined. Among several possibilities, two convergence criteria that control the inversion process in the most effective way can be defined: (i) the RMS misfit with the measured data is equal or less than the number of data ($\chi^2 = N$ or $\bar{\chi}^2 = \chi^2/N = 1$, defined as a statistically appropriate level of data fitting (Dosso et al., 1998)); (ii) the RMS change of the model elements from one iteration to another is less than a certain value, chosen accordingly to the desired uncertainty of the solution.

In order to satisfy the first criterion to achieve convergence of the inversion and at the same time use the *a priori* information to its full potential, the trade-off parameter (or parameters) μ requires a fine tuning (Dosso et al., 1998). Generally, the minimization of the regularization term in (4.6) leads to an increase of data misfit and vice versa. An adequate value for μ prevents overfitting the data, that is, fitting noise that is present. If it is impossible to satisfy the first criterion, the accuracy of measured data may be overestimated and require reconsideration.

The above approach for solving the inversion problem is very flexible in terms of model parameters that may be included. If a parameter affects the model response data through the response function and the respective derivative can be defined analytically, the parameter can be included into the model and successfully recovered.

4.3 Application to the problem

4.3.1 Unknowns

Any measured value is subject to a measurement error. The accuracy is different for different parameters, so is the influence on the modelling results.

The following model parameters were included in the inversion as unknowns for the localization problem:

- x, y, z coordinates for the receiver positions
- x, y coordinates for the source positions
- constant bias of the measured sound speed profile
- coefficients for the linear drift function of the internal clocks of the recording instruments

The following definitions were used to provide derivatives for the parameters being resolved. The sound-speed profile is set by a series of depth-velocity pairs ($\{(z_k, c_k)\}$). The corresponding sound-speed gradient is $\{c'_k\}$, where $c'_k = (c_{k+1} - c_k)/(z_{k+1} - z_k)$. The ray parameter is calculated as: $p = \cos\theta(z)/c(z)$. The horizontal range r between source and receiver is obtained using $r = \sqrt{(x_s - x_r)^2 + (y_s - y_r)^2}$. An auxiliary parameter $w_k = \sqrt{1 - p^2 c_k^2}$ is introduced for more compact representation of the equations. The detailed derivation of the derivatives can be found in Dosso and Collison (2001)

Receiver and source coordinates

The depth of the air gun was assumed to remain constant during the survey. Possible deviation from the shot plane may have been due to the waves on the sea surface and can be considered to be negligible. Hence, in order to reduce the number of unknowns and reduce the size of the matrices, only two horizontal coordinates of the source position were chosen for inversion. All three coordinates for the receivers were included in the model vector.

The partial derivatives of the travel time with respect to horizontal coordinates of sources and receivers are

$$\begin{array}{ll} a) \ \frac{\partial T}{\partial x_s} = p(x_s - x_r)/r & b) \ \frac{\partial T}{\partial y_s} = p(y_s - y_r)/r \\ c) \ \frac{\partial T}{\partial x_r} = p(x_r - x_s)/r & d) \ \frac{\partial T}{\partial y_r} = p(y_r - y_s)/r \end{array}, \tag{4.11}$$

while the partial derivative for the vertical coordinate of receivers is

$$\frac{\partial T}{\partial z_r} = -\frac{1}{\sqrt{c(z_r)[1 - p^2 c^2(z_r)]}}. \tag{4.12}$$

Sound-speed profile bias

Due to different factors, the measured sound-speed profile for the water column is subject to bias. The uncertainty for the bias can be up to $\pm 2\ m/s$ (Vincent and Hu, 1997). For the shots with offsets around 4 km, this error in sound-speed profile can lead to travel time errors of up to $\pm 4\ ms$ and significantly affect the results of the localization. The correction value for the bias of sound-speed profile (c_b) is inserted into the model vector and the partial derivative is calculated using following equation:

$$\frac{\partial T}{\partial c_b} = \sum_{k=j}^{i-1} \frac{1}{c'_k} \left[\frac{w_{k+1}}{c_{k+1}} - \frac{w_k}{c_k} \right] \tag{4.13}$$

Variable drift of internal clocks of the instruments

The initial inversion attempts to recover the true survey geometry using the travel times failed to converge. It was impossible to achieve a desired fit ($\pm 1.5\ ms$) of

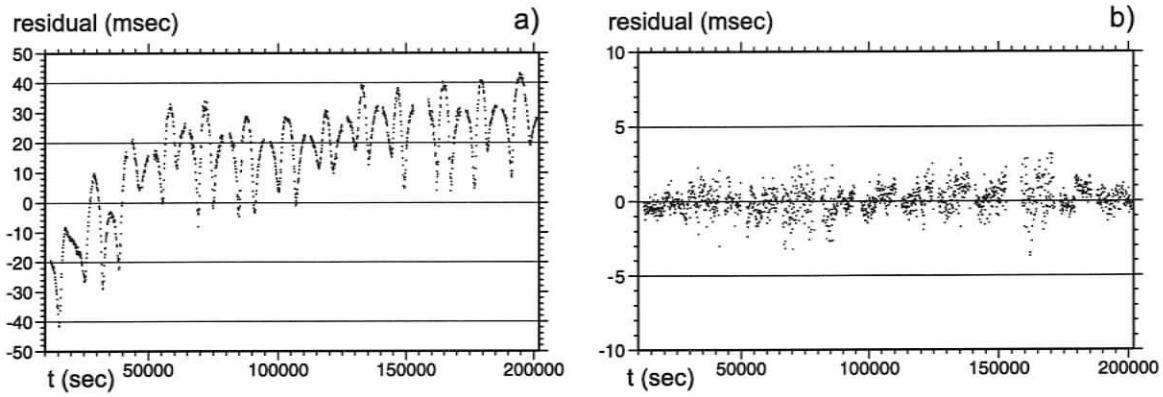

Figure 4.1: Residuals of travel times vs. shot time from the beginning of the survey. For station A (a) presence of a trend is obvious, which can be explained by uncorrected drift of the internal clock. For station C (b) the residuals after inversion fall into desired range (± 2 ms).

the measured data inverting a model that included only coordinates of sources and receivers as unknowns.

The calculated residuals revealed that OBS A and F had the largest mismatch in the modelled travel times. For the test purposes they both were excluded from the inversion. The subsequent runs of the inversion using data from three stations succeeded. Thus, in order to be able to use seismic data from the two excluded OBSs special treatment for localization was needed.

In order to investigate the matter, first the uncertainty of the measured travel times for these two instruments was increased. The inversion was able to achieve convergence with an uncertainty set to ± 10 ms. Then the residuals of the travel times for all five stations were plotted versus the time of the shot from the start of the survey. Figure 4.1 represents two of these plots. Very large residuals of up to ± 40 ms as well as a trend in the residuals for the station A (Fig. 4.1a) is obvious. Closer investigation reveals a change in the slope of the trend approximately at 70000th second (the oscillation of the residuals with the period of shot interval for two lines is due to poor recovery of the true coordinates for the station).

The following assumptions were made: (i) the internal clocks of some OBS had a large (≈ 40 m/s for the shooting period) uncorrected drift; (ii) without any additional

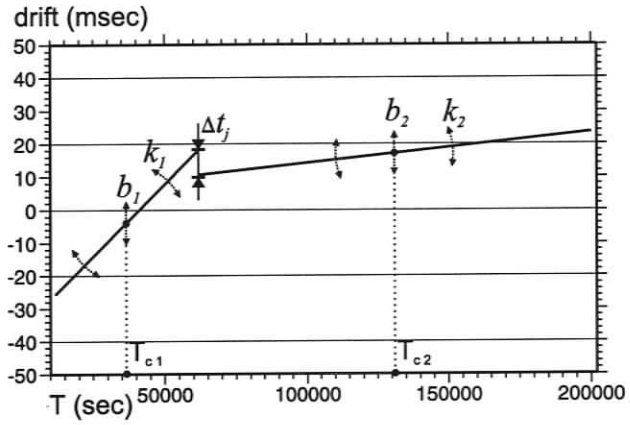

Figure 4.2: Approximation of the drift function with a series of linear functions.

information on the drift function pattern it can be approximated by a linear function; and (iii) the drift rate is likely to have changed during the survey.

Thus, the drift function for the whole time period of the survey can be represented by a linear function $t_{drift} = b + kT$ if the drift rate is constant, where T is the shot instant time after the beginning of the survey. If the drift rate is suspected to have changed, the drift function can be represented by a series of linear functions (legs), each function referring to a part of the time line during which the drift rate is supposed to remain constant:

$$t_{drift} = \begin{cases} b_1 + k_1\hat{T} & \text{if } T_0 \leqslant T < T_1 \\ b_2 + k_2\hat{T} & \text{if } T_1 \leqslant T < T_2 \\ \dots & \dots \end{cases} \tag{4.14}$$

where $\hat{T}$ is the time with respect to the centre of the leg ($\hat{T} = T - T_c$) (Fig. 4.2).

The coefficients of the linear functions ($b_1, b_2, ..., k_1, k_2, ...$) are unknowns and are included into the model vector. The partial derivatives with respect to these model parameters are

$$\frac{\partial T}{\partial b} = 1 \qquad \frac{\partial T}{\partial k} = \hat{T} \tag{4.15}$$

For the instruments with just one leg in the drift function this technique works well. However, for the drift functions with more than one leg additional problems arise. As each leg is represented by an independent linear function, shifts in the

overall drift function can appear at the joint points (Fig. 4.2, Δt_j). While the rapid shifts in the clock running may be quite natural for some systems (e.g., adjustments of the clock through calibration with an external time source at some points during the survey), for the general case the assumption can be made that the drift function is continuous. Thus, while inverting for the drift function, the discrepancy at the joint points must be set equal to zero. In other words, it can be referred to the category of input data (knowns).

As a known, the Δt values (zeros) for each joint point are inserted into the data vector with the modelling function being

$$\Delta t_i = b_i + k_i(T - T_{c_i}) - (b_{i+1} + k_{i+1}(T - T_{c_{i+1}})). \tag{4.16}$$

The uncertainty for these values needs to be set very small (several orders less than uncertainty for the travel time data), so they have greater priority in fitting of the input data during the inversion. Partial derivatives to be inserted into the Jacobian matrix are

$$\begin{aligned} &a)\ \frac{\partial \Delta t_i}{\partial b_i} = 1 \qquad && b)\ \frac{\partial \Delta t_i}{\partial b_{i+1}} = -1 \\ &c)\ \frac{\partial \Delta t_i}{\partial k_i} = T - T_{c_i} \qquad && d)\ \frac{\partial \Delta t_i}{\partial k_{i+1}} = -(T - T_{c_{i+1}}). \end{aligned} \tag{4.17}$$

Using this approach in the localization inversion, the complicated drift function was recovered for stations A and F, achieving the same fitting quality for the direct water wave travel time data as for the other three instruments. The final residuals along with the drift function for the OBS A are presented on Fig. 4.3

4.3.2 Smoothness regularization

The derivatives used in the matrix for a regularization term that controls smoothness of the tracks have to be taken with respect to some independent variable. There are suggestions of using the offset of the sources (receivers) from the beginning of the track (array) (e.g., Barlee et al., 2002) and this is reasonable provided the offset values are measured or calculated by any other method rather than using coordinates of the sources/receivers. Otherwise the offset cannot be considered as an independent

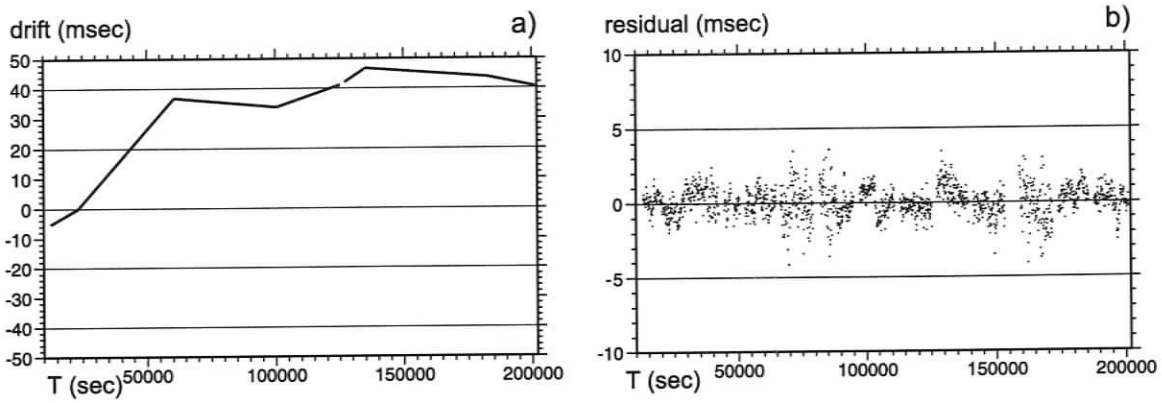

Figure 4.3: Recovered drift function of the internal clock for OBS A (a) and achieved travel time residuals using correction for the drift (b)

variable with respect to the coordinates and its utilization can lead to some undesired effects.

For localization of the airgun shot coordinates for shots fired in track lines such as in the COAMS-99 survey, the ideal independent variable is the time of the shot. The time is truly an independent variable. Moreover, the whole survey can be treated as one continuous track and the matrix $\mathbf{H}_2$ does not need to contain rows of zeros to separate the elements belonging to one track line from another.

The other advantage of using time as a variable for calculating the second derivative is the ability to restore the approximate position of the shot if both the coordinates and the exact time of the shot are estimated with a large uncertainty. This can happen if at some point during the survey the signal from all satellites was lost. In this case the regularization helps to place the shot using the positions of the adjacent shots, for which the travel time is defined with appropriate accuracy, and the time of the shot. In other words, interpolation is being performed.

An example of smoothness regularization effect on the results of survey geometry refining is shown in Fig. 4.4. Without smoothness regularization applied, the track line simulates a saw tooth pattern, which is unrealistic for the seismic source to follow. It is explained by the fact that the inversion fits the travel time data containing noise. When the roughness measure was minimized together with travel time misfit, the

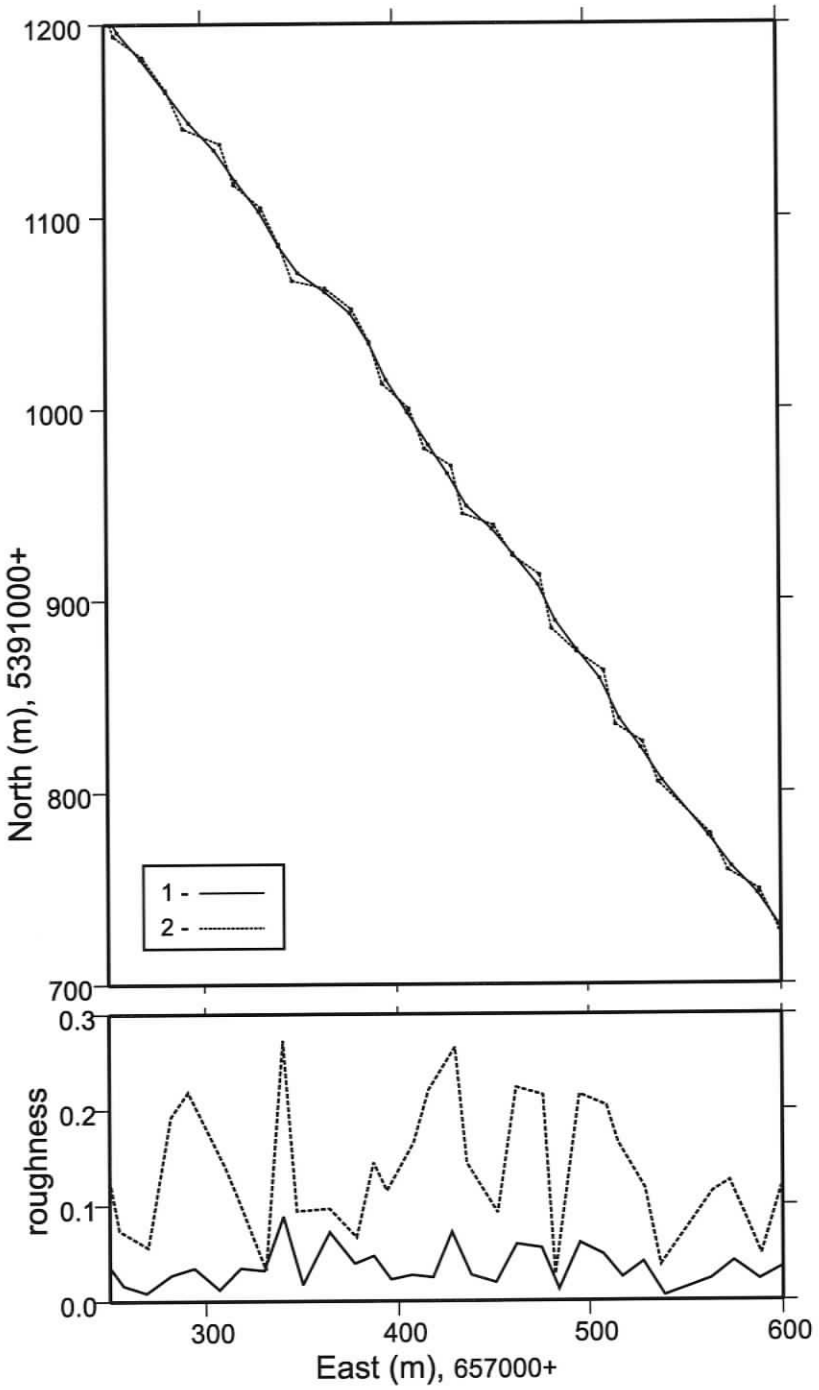

Figure 4.4: Example of the recovered track line (upper) with (1) and without (2) smoothness regularization applied. Quantitative comparison of the roughness factor ($|\mathbf{H}_2\mathbf{m}|^2$) for each method is also shown (lower).

trajectory of the air gun becomes a more practical smooth curve. The regularization prevents the inversion from fitting the noise rather than data.

4.3.3 Code, input data, and results

The seismic data set, subject to geometry refining, consisted of 5 OBSs and 15,305 shots. The time of the direct water wave arrival was picked for each source-receiver pair and a data vector was formed consisting of 76,525 elements. The model vector consisted of 30,651 elements. The uncertainty for the travel time picks (0.75 ms) was assigned as a half of the sampling rate of the recording device (1.433 ms), and estimated uncertainty for the seismic source response time (± 1.0 ms).

The estimated uncertainties for the parameters of the initial model (*a priori* information) are shown in the Table 4.1

Table 4.1: Uncertainty for the initial model parameters estimation.

parameter	uncertainty
x and y shots	± 15 m
x and y OBSs	± 200 m
z OBSs	± 5 m
c_b	$\pm 2 m/s$

The code, used for performing localization, was a modified code originally written by Dr. Stan Dosso (Dosso and Sotirin, 1999). While the main parts of the algorithm were preserved (raytracing, matrix inversion, adjusting the regularization weighting parameter μ), new features were added, such as solving for the drift of the internal clocks, and utilization of the sparse matrix technique.

The code was developed using Matlab and has shown a good performance efficiency. The convergence for the inversion problem was achieved after three iterations with the running time approximately five minutes.

The resulting χ^2 achieved was 76,104, or, when normalized ($\bar{\chi}^2 = \chi^2 / N_{data}$), 0.99. The RMS change of the shot positions was found to be about 6.7 m. Figure 4.5 shows the results of localization inversion.

Table 4.2: Comparison of the recovered depth of the instruments with the depth according to the bathymetry map

OBS	depth [m] localization	depth [m] bathymetry	mismatch Δ [m]
A	1327.1	1325.9	-1.2
B	1266.4	1266.6	0.2
C	1257.9	1257.5	-0.4
E	1260.9	1262.2	1.3
F	1281.3	1280.6	-0.7

As a quality control procedure, the recovered depths of the instruments were compared to the depth of the seafloor at their recovered locations according to the high resolution bathymetry map, which was specially constructed for the site area (see Section 5.3.1). The results of comparison are shown in Table 4.2. The mismatch of the depths is less than 1.3 m. Thus, the accuracy of depth recovery for the instruments is better than 0.1%, considering an average depth of 1300 m. The recovered drifts over time for the internal clocks of OBSs are shown on Figure 4.6. These are excess drifts, since all the instruments have undergone the basic drift correction based on the discrepancy of the internal clock readings and the GPS clock time.

The refined coordinates for the shot and receivers were inserted into the headers of seismic traces. The residuals for the measured travel times after the inversion were considered as residual statics. Correctional shifts in seismic traces for each shot were performed according to the residual value for the shot.

4.4 Discussion and conclusion

To investigate improvements of the new technique the results for different approaches have to be compared. Three modes of the inversion were tested. In mode I all three stations were assigned the same uncertainty for the travel times. It corresponds to an assumption, that the clock drift at every station is in its normal limits according to the specification. Mode II suggests that an unusually high drift was discovered for the clocks of instruments A and F and the uncertainty of the travel time was assigned

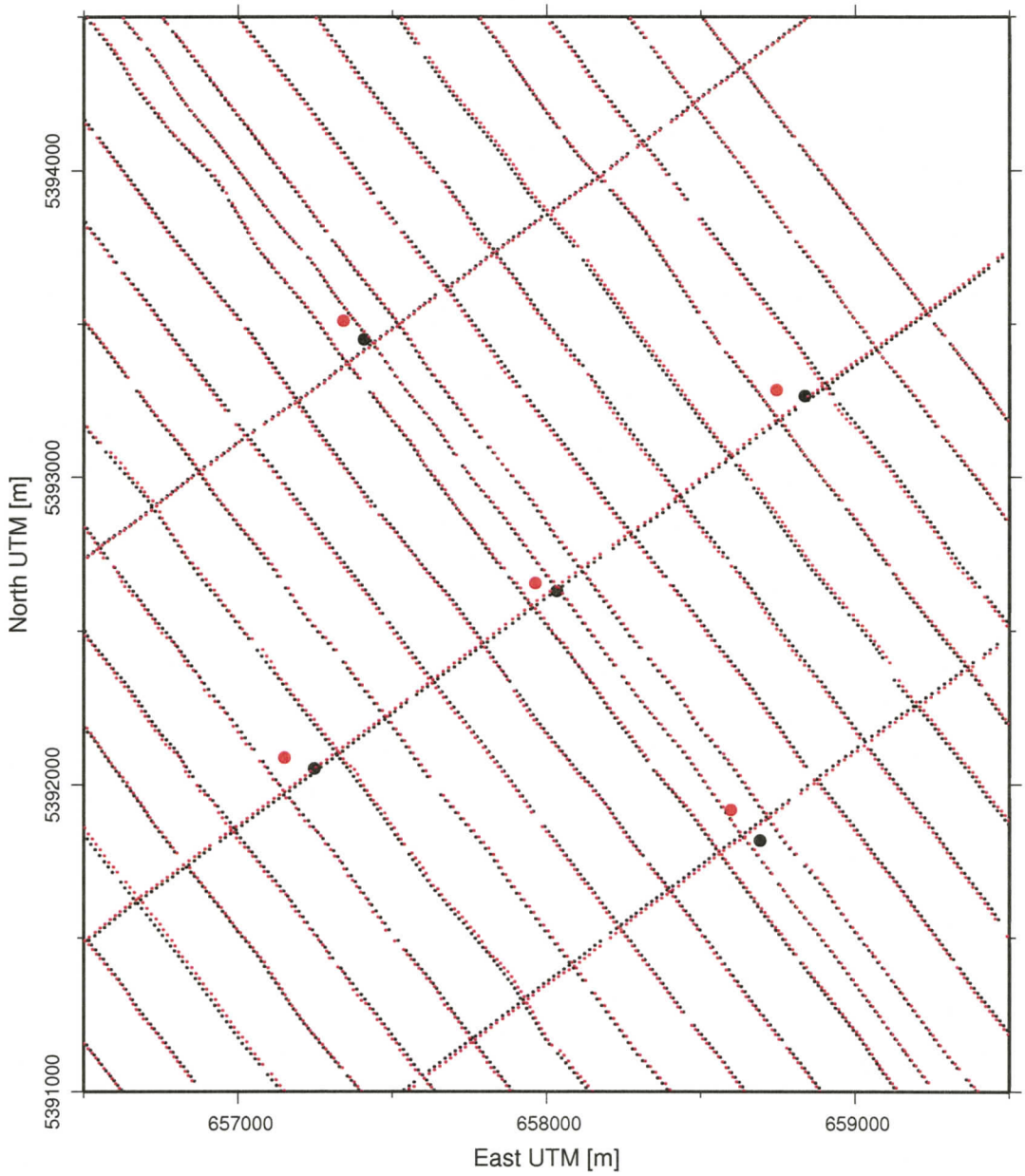

Figure 4.5: Results of the localization inversion. Starting estimation model (black) and final model (red) are shown both for shots (small circles) and OBSs (large circles).

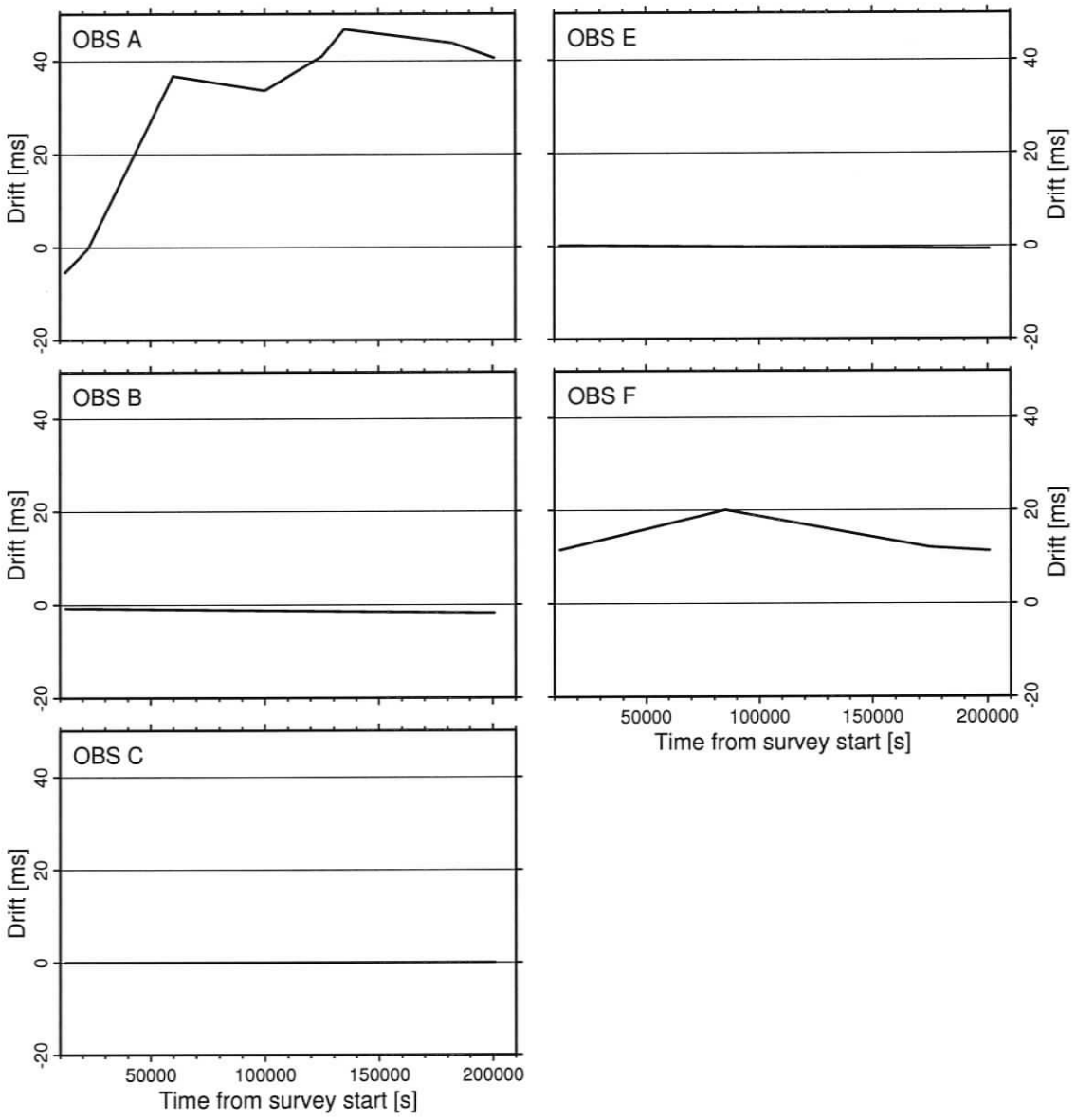

Figure 4.6: Recovered drift functions over time for internal clocks for five OBSs.

accordingly. Modes I and II were solved without estimating the drift of the clocks. Mode III utilizes the ability of the inversion technique to resolve the drift of the instrument clocks. The parameters that were different for different modes together with the achieved fit quality and the RMS residuals for the input data are shown in Table 4.3. The standard set of unknowns (coordinates of sources and receivers, and bias of the sound speed profile) is solved for in all three of them.

Table 4.3: Data fit quality for different modes of inversion.

Mode	drift solved?	travel time uncertainty		fit quality $\bar{\chi}^2$	RMS residual [ms]
		A and F	B, C, and E		
I	No	±1.5 ms	±1.5 ms	12.3	5.24
II	No	±10 ms	±1.5 ms	0.99	11.59
III	Yes	±1.0 ms	±1.0 ms	1.01	1.01

The third type of inversion was used to obtain the final results for localization. The other two were compared to it for the evaluation of improvements in the localization and input data fit. Figure 4.7 shows the horizontal locations for the shots and receivers obtained using three types of inversion. Table 4.4 provides estimated instrument depths obtained with the different inversion types for comparison to the depth of the sea bottom at the instrument location given by the bathymetry map.

Table 4.4: Comparison of the recovered depth of the instruments with the depth according to the bathymetry map for different types of inversion.

OBS	depth $[m]$	I		II		III	
	bathymetry	depth $[m]$	$\lvert\Delta\rvert$ $[m]$	depth $[m]$	$\lvert\Delta\rvert$ $[m]$	depth $[m]$	$\lvert\Delta\rvert$ $[m]$
A	1325.9	1399.2	75.3	1375.8	49.9	1327.1	1.2
B	1266.6	1249.8	16.8	1264.8	1.8	1266.4	0.2
C	1257.5	1257.6	0.1	1259.7	2.2	1257.9	0.4
E	1262.2	1245.3	16.9	1262.3	0.1	1260.9	1.3
F	1280.6	1311.4	30.8	1301.9	21.3	1281.3	0.7

The results show that the autonomous instruments are subject to timing errors due to unstable drift in the internal timing system. The drift with unstable rate is impossible to correct by means of the basic correction using the discrepancy of the

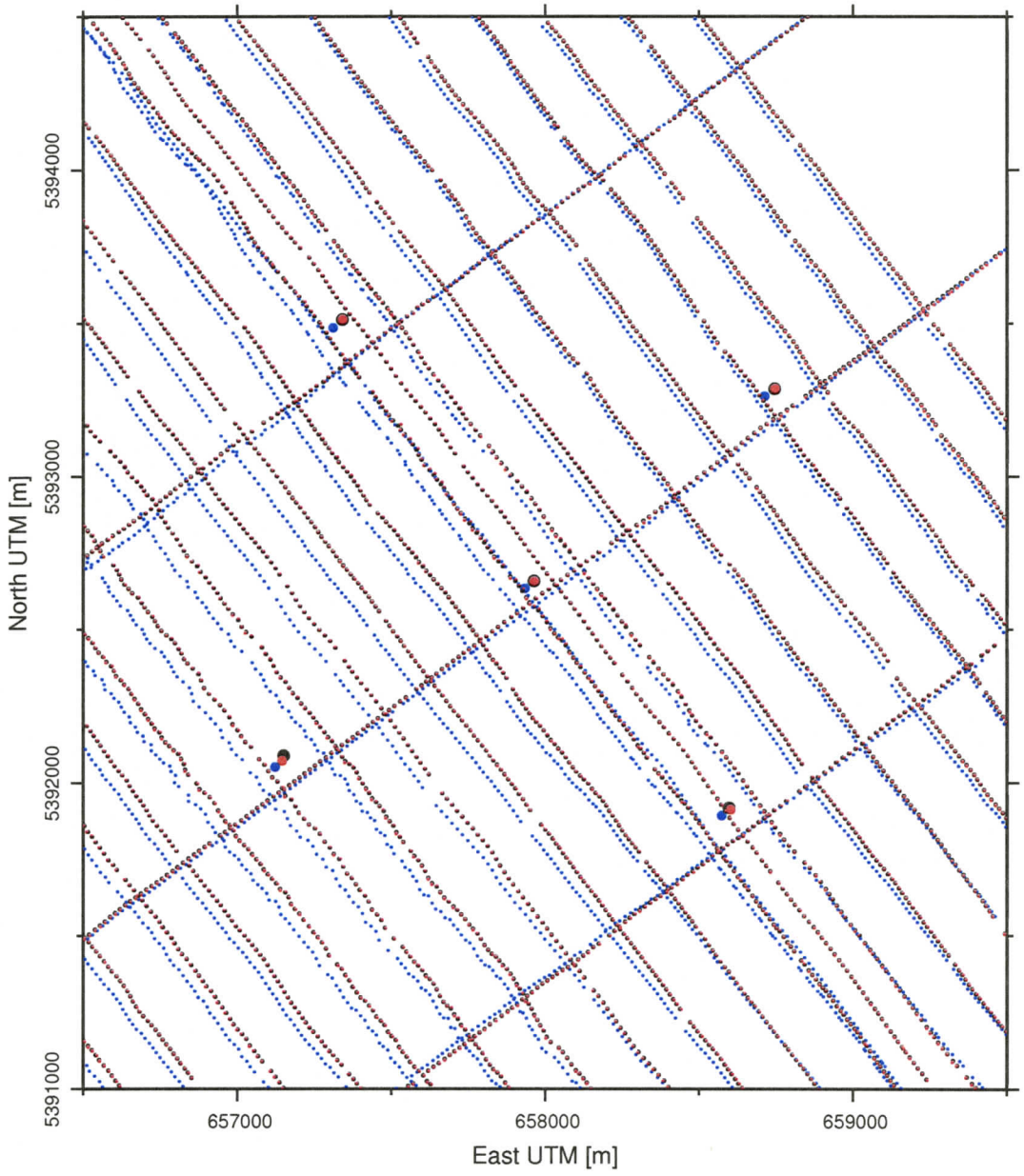

Figure 4.7: Comparison of the results obtained by different modes of inversion (blue – I; red – II; black – III). Horizontal positions of shots (small circles) and OBSs (large circles) are shown.

internal and GPS clock readings at the end of survey. This drift produces an error for the travel time picks and it has a non-Gaussian distribution, and hence cannot be corrected through the averaging of a large number of data.

The results for mode I show that if the uncertainty of the travel time data corrupted by the internal clock drift are set equal to the uncertainties for the other travel time data, the inversion fails to converge and the results of localization violate the initial estimate model. By increasing the uncertainty for those faulty travel times it is possible to achieve inversion convergence. In this case the locations for the shots are estimated primarily using the information from the other instruments. While this approach provides a good estimation of the true geometry for the shot positions and a part of the instruments, the seismic data from the instruments with unstable clock drift is still unusable due to bad localization for those instruments (see Table 4.4) and large residuals for the travel times (Fig. 4.8).

By approximating the unstable drift of the internal OBS clocks for the instruments by a series of linear functions and including the coefficients of those functions in the inversion it is possible to recover the drift function and successfully solve the overall localization problem. The seismic data recorded by the instruments with faulty clocks can be used in the subsequent data processing.

The developed technique can be used for solving the localization problem for any type of survey that includes autonomous instruments and the shooting is performed in a track-by-track fashion. It is able to recover the internal clock drift function that is impossible to correct by any other means.

The approximation of the drift by a series of linear functions provides a more physically reasonable way to make corrections for the drift rather than by introducing a constant time correction for each individual seismic line such as in the localization technique introduced by Hobro (1999).

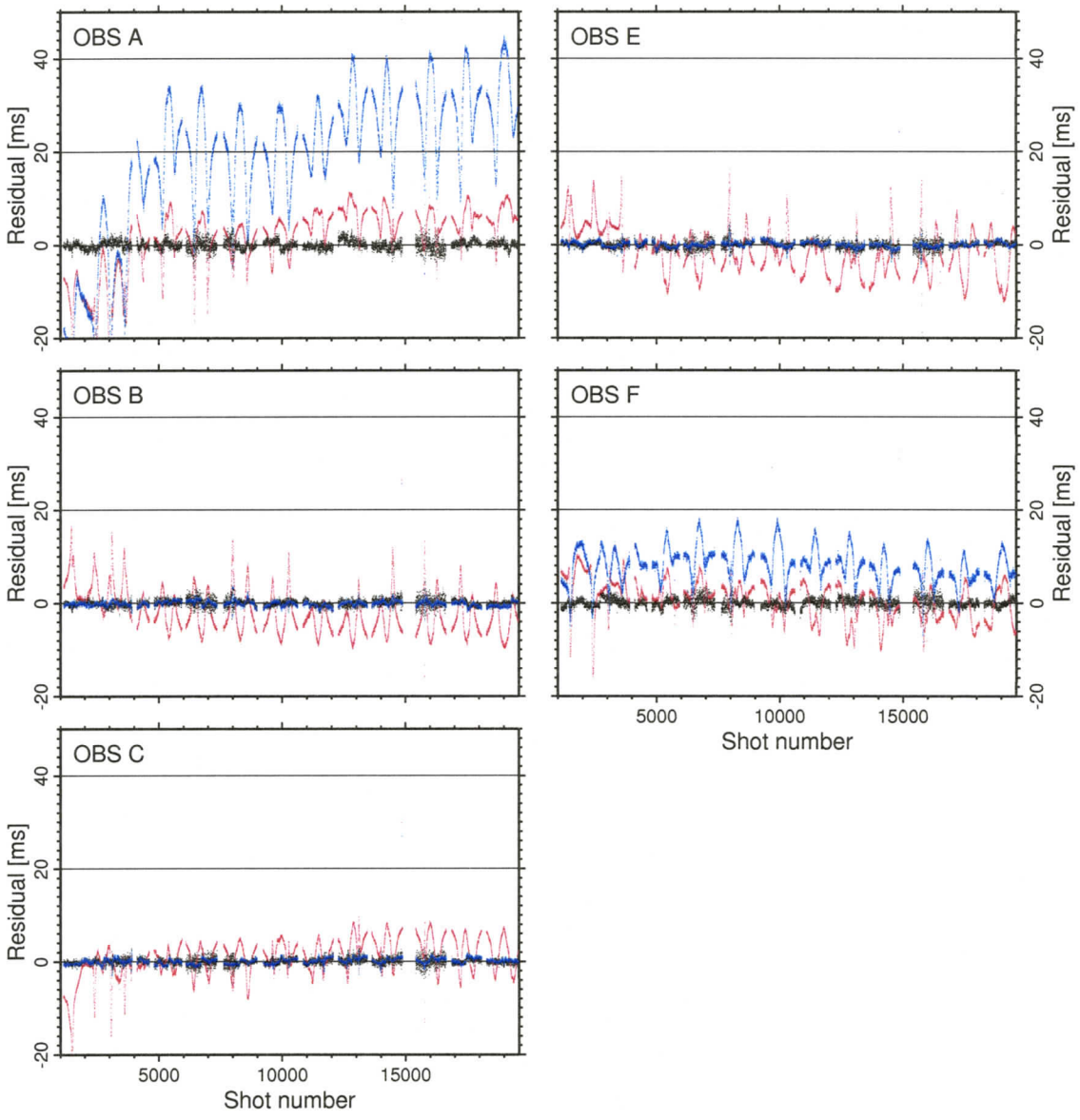

Figure 4.8: The final travel time residuals for different inversion modes (I–red; II–blue; III–black).

Chapter 5

Travel time tomography

5.1 Background

The word *Tomography* comes from Greek words *tomo*, meaning 'slice' or 'cut', and *graph* that means 'describing'. This term is used for methods that provide a model for the internal structure of an object by making observations on its surface. Tomographic methods are generally applied when there is a need for a non-destructive way to examine the object (e.g., human head), or when sampling methods are prohibited or extremely ineffective (e.g., earth crust) in describing large volumes of the object. The applications include medicine, engineering, construction, and physical sciences. Of course, the subject matters are different, as well as the technical details of the implementation, but the main idea of tomography as a non-invasive investigation approach stays the same.

In geophysics seismic tomographic inversion methods are widely accepted. They differ by the type of the seismic signal used (P- or S-waves), by the data for modelling (travel time, full waveform, amplitudes), by the number of dimensions in the model (1-D, 2-D, 3-D), by the type of signal paths (reflection, refraction, first arrival), or by the geometry of the seismic experiment (normal incidence, wide angle, cross-well). Also the physical properties of the object of interest that are modelled vary: P- or S-wave velocity, attenuation.

The tomographic inversion used in this study can be described as 3-D, P-wave, wide angle, reflection, travel time tomography. It was conducted to obtain a model

of the P-wave velocity structure of the Bullseye vent site.

5.1.1 Parameterization of the model - options and differences

Parameterization of a model is the key step in obtaining meaningful results from the tomographic data inversion. The ability of the inversion code to generate a model with specific structural features primarily depends on the parameterization.

For reflection seismic data, the usual practice is to model the medium by one or more layers separated by interfaces that are supposed to produce the reflections. The way an object is parameterized has to be chosen very carefully taking into consideration the expected structure of the modelled medium.

The method for parameterizing the variation of velocity with depth requires careful consideration of the expected structure of the modelled medium. That is, the inclusion of *a priori* information into the inversion process starts at the earliest stage — the parameterization. Options for parameterizing the medium are described below.

One parameter fixed

The travel time of a ray depends on two parameters — distance travelled and velocity in the medium. It is impossible to resolve them separately with only one type of ray, such as normal or close-to-normal incidence rays in conventional seismic surveys. Nevertheless it is possible to estimate one parameter of this pair by fixing the other one, usually the one which is expected to be least variable or have lower spatial variation frequency. It is then assumed that all variations in travel time are due to the parameter that is allowed to change.

Though this method introduces a very strong bias into the model at the earliest stage of modelling, it still has its place. Sometimes it is the only way to achieve stable results for estimates of the parameters of the model in the situation of limited data availability. In this case the fixed parameter is controlled by independent measurements (e.g., velocities from well-log data) (Spence et al., 1995).

Full inversion

For models with both velocity and depth to the interfaces as variable parameters, there are two major options for parameterization. In the first one, the velocity is kept constant in the vertical direction inside a layer, though it can change with the transition to another layer (lateral variation of the velocity is also allowed). In the second, the velocity of the layer is allowed to change according to an unknown gradient sought in the inversion. The gradient can be linear and defined by two velocity nodes at the top and at the bottom of the layer, or it can be defined by the grid cells. Both methods have advantages and disadvantages.

The positive aspect of the model with constant vertical velocity in the layer is that it introduces fewer parameters — only one velocity parameter per layer in the vertical dimension. Hence, the computational requirements are significantly lower for this inversion compared to the inversion of the model that includes velocity gradient. Also, fewer unknowns provide less complexity and better conformity to the Occam's razor principle of simplicity[1], especially in the case of limited data.

On the other hand, the fewer model parameters approach may not provide the required vertical resolution for the velocity, particularly if the layer thickness is large and there is an expected variation of the velocity inside the layer. In addition, with this type of parameterization, identification of a vertical velocity anomaly with vertical extent less than that of the layer thickness is impossible. Finally, if the layer thickness is changing greatly in the presence of a strong vertical velocity gradient, a false lateral velocity anomaly may appear as shown in Fig. 5.1. In this figure, both sections represent the same uniform environment with the vertical velocity gradient and produce equivalent travel time data. The explanation of this phenomena is simple: the velocity parameter represents the average velocity in the vertical cell; for the parts of the layer with increased thickness the average velocity will be higher, as the layer includes deeper parts of the sediment section with the higher velocities; the

[1]Between two models that describe given data equally well, the simpler one is most probably correct

visualization of such a model (Fig. 5.1) shows a false lateral variation of the velocity in the layer.

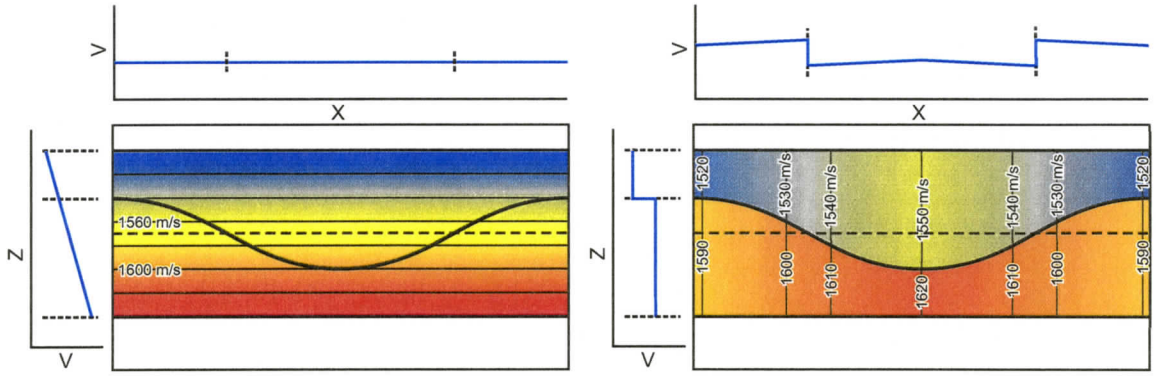

Figure 5.1: Appearance of "false" lateral velocity anomaly (right pannel). Horizontal velocity slices taken at dashed line are provided for each model. Vertical velocity profiles are also shown. Thick line represents an interface.

In the second parameterization method, the advantages and disadvantages are reversed. The greater number of velocity nodes allows more accurate modelling of the vertical velocity variation, but at the expense of larger number of parameters and greater computational requirements. However, the presence of multiple velocity nodes for the vertical direction inside the layer allows localization of anomalies with greater accuracy, and the size of an anomaly can be independent of the size of layers.

It can be concluded that constant velocity parameterization is more suitable for cases in which the vertical velocity function is mostly controlled by the different sediment types that form the layered structure, rather than by the depth (e.g., the increase of the velocity due to compaction). That is, the vertical velocity gradient inside the layer is negligible in comparison to the change of the velocity at the interfaces between layers. The gradient still can be correctly revealed if the medium is represented by a stack of many thin layers. However, this requires reflection data from all interfaces, which is often impossible to obtain.

Velocity change at the interface

A velocity change at the interface is the only way to vary the velocity parameter with depth for the constant-velocity layer parameterization. For the velocity-gradient parameterization, there is an option to bind the nodes of the velocity grid at the bottom of one layer to the velocity at the top of layer below it smoothly together. That is, no discontinuity of the velocity function is allowed during the transition from one layer to another, achieving a smooth velocity profile with depth. It is justified if the vertically-averaged velocity is not expected to change at the interface more than it would change from cell to cell in the layer (Fig. 5.2). In this figure, all three velocity profiles give the same travel time for a ray over the covered distance. The real velocity profile (thin solid line) has finely detailed structure, which usually cannot be resolved by seismic travel time tomography. Although it is the fine-layered structure that generates the reflections (for instance, at 150 m the velocity contrast is more than 400 m/s), the structure is averaged over the cell size in the inversion to yield a smooth profile (thick solid and dashed lines). In this case, the separation of the sediment section into the layers is arbitrary, rather than a representation of the different sediment types with different compressional wave velocities.

Therefore, unless the modelled sediment section is composed of packages of different type of sediments that are bounded by specific reflectors, there is no compelling reason to introduce a velocity discontinuity at the layer boundaries. Moreover, in modelling a uniform section of non-compacted sediments where the reflection events are produced by thin layers of velocity contrasts which are randomly distributed over the section, the parameterization with no velocity discontinuity is justified.

5.2 Inversion code — Jive3D

In this thesis the Jive3D tomogrphic inversion code was applied. The name of the tomography inversion code stands for Joint interface-velocity estimation in 3-D. It was written by James Hobro as a part of his PhD thesis (Hobro, 1999) and was

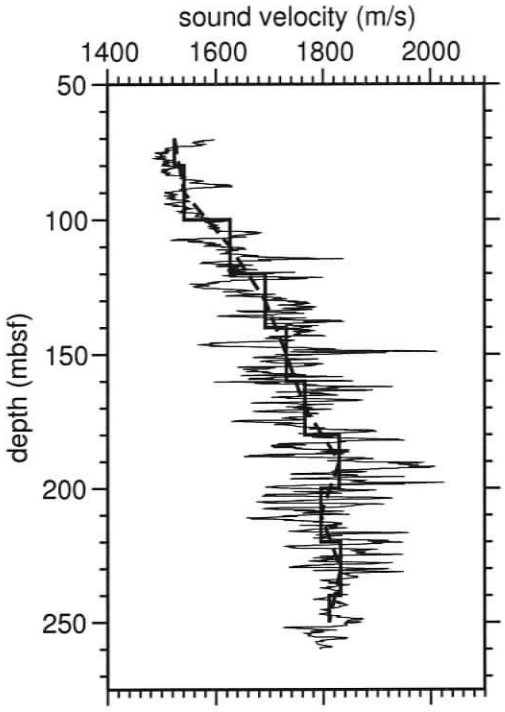

Figure 5.2: Example of parameterization of a measured velocity profile (thin solid line) by constant-velocity-in-the-layer model (thick solid line) and by model with velocity gradient with depth (thick dashed line).

tested using synthetic and real travel time data (Hobro, 2000a). The code is a 3-D extension of a 2-D algorithm by McCaughey and Singh (1997).

Jive3D is a well known and powerful tool for performing an inversion of travel time data (e.g., Evangelidis et al., 2004; Funck et al., 2000). It has been included into a standard package of the research tools of several seismic groups (e.g., Dalhousie Seismic Group, LITHOS group). The code was previously applied to obtain a low-resolution velocity structure of a gas hydrate site in the Cascadia region by inverting reflection and refraction travel time data recorded by OBSs offshore Vancouver Island (Hobro, 1999; Hobro et al., 2003)

The Jive3D tomographic code allows combined inversion of refractions and reflections and is implemented in the layer interface formalism. The parameterization of the model uses equally spaced grids both for interface surfaces and velocity grids (Fig. 5.3). The actual surfaces and the velocity function in the layer for the ray tracing are calculated using the result of the convolution of the values at the grid nodes with a cubic B-spline (Hobro, 1999). This allows a velocity gradient inside cells and, consequently, true refraction with depth (compared to a simple grid parameterization

with no cell gradients in which refractions of rays can occur only at the cells borders).

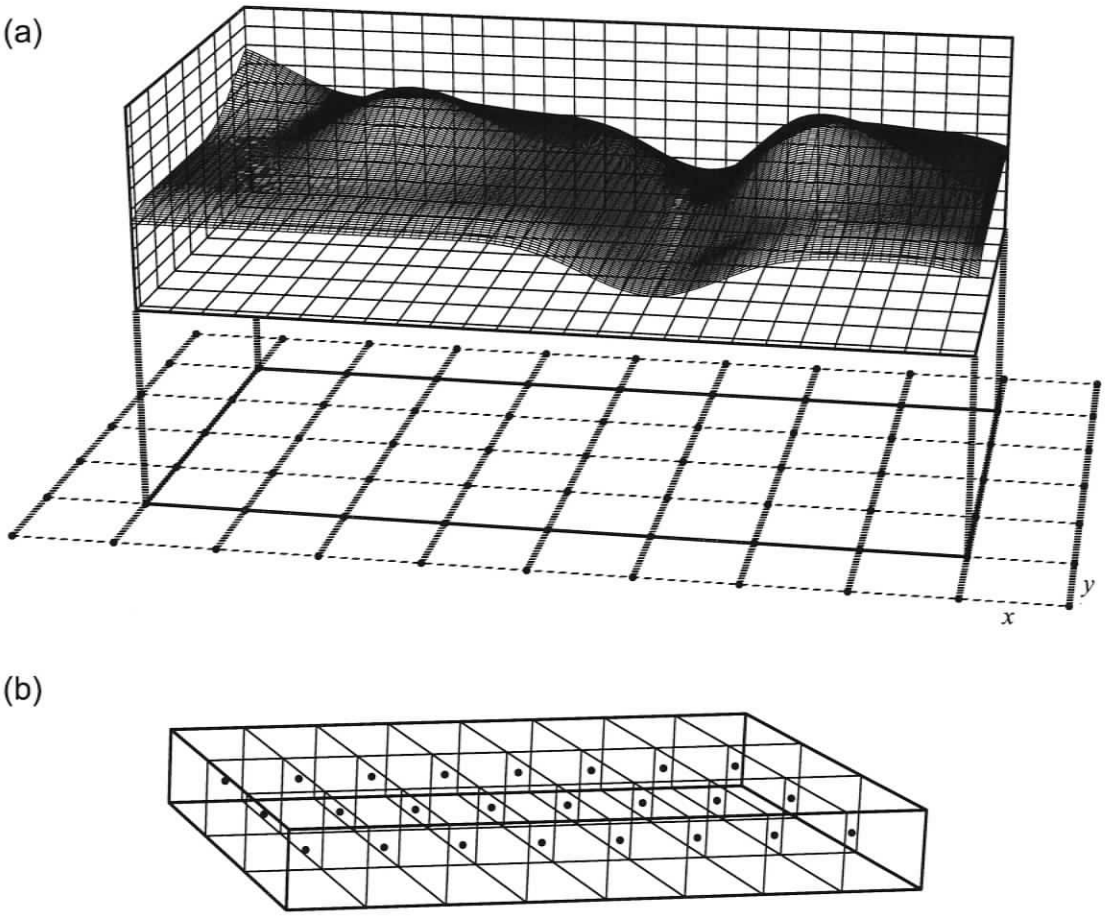

Figure 5.3: Interfaces (a) and velocity in the layers (b) are defined in Jive3D by grids (From Hobro, 1999).

The cell size is allowed to vary from layer to layer, which provides flexibility in choosing the number of cells required for simulating different layers. For example, the ocean can be approximated by a layer with one velocity cell, reducing the total number of cells.

The inversion method uses a linearized iterative approach (similar to the one used for the experiment geometry inversion, see section 4.2) for the travel time inversion. The final model that provides a satisfactory fit to the data is obtained through a series of refinements of a starting model.

The algorithm produces a minimum-structure model that fits the given travel-

time data to a required accuracy using the simplest model possible for given input parameters. The desired simplicity of the model (amount of structure) is controlled by a smoothing factor, which is a trade-off parameter between the accuracy of fitting of the input data and the smoothness of the generated model. The code allows the user to specify different smoothing parameters separately for each interface or layer. In addition, the smoothing factor in each dimension (X, Y, or Z) is controlled separately.

The code is implemented in Fortran 95 using a sparse matrix technique that compresses matrices by storing only non-zero elements. This allows a substantial reduction of the computational resources needed for inversion, and increases the allowable size of the model (number of grid nodes).

Along with the final model, the code produces output that can be used in the evaluation of the quality of the result, such as ray tracing to determine ray coverage in the model and travel time residuals information. Although these can be considered only as an indirect measure for the reliability of the final model, they still can be used for general evaluation of the final model.

Finally, the code allows an uncertainty analysis to be performed on the resultant model to obtain explicit uncertainty values for each model parameter. Unfortunately, this examination requires an extremely large amount of computer memory as it involves the construction of a full covariance matrix of the model, the size of which is equal to the square of the number of unknowns. The results of the uncertainty analysis still may be obtained through either a layer stripping method, or by reducing the the size of the model. The layer stripping method was tested but it provided unsatisfactory results. Thus for the purpose of the uncertainty analysis the physical size of the model was reduced to include only central part of the model and the horizontal cell size was increased by a factor of two.

5.3 Inversion procedure

5.3.1 Seafloor model

Unfortunately, there is no high quality bathymetry data set for the area of interest. The only available map was created based on the swath echosounder data collected during the SO 111 cruise in 1996 (Villinger, 1996). This data set did not receive a proper level of processing, and consequently contains artificial linear features. The express comparison of the swath bathymetry with the grid produced by simple gridding of the echo sounder data reveals that the depth discrepancy could be up to 5 m. Thus, a new bathymetry map had to be created.

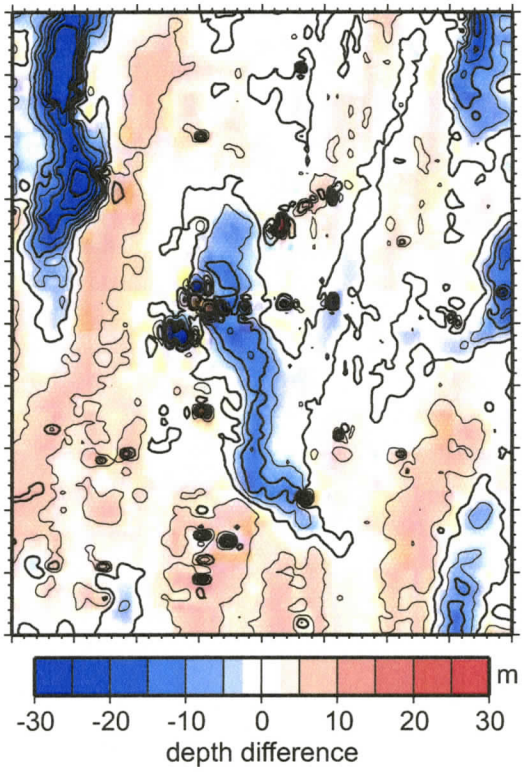

Figure 5.4: The difference between the available swath bathymetry data and gridded echo sounder data from COAMS-99 (no prior processing). The linear features of the SW–NE direction coincide with the direction of the ship tracks for swath bathymetry, and thus they are believed to be artificial.

During the cruise, the depth to the seafloor information was collected using a 12kHs Simrad EA500 echo sounder. The time of the bottom reflection arrival was automatically picked and converted to depth using a nominal constant sound velocity of 1492.6 km/s (Riedel et al., 1999). The measurements were done every 10 seconds or approximately every 20 m along the profile (ship velocity 4 knots). These data

were used to create a new bathymetry grid for the site area.

First of all, the depth measurements were converted back to the sea bottom reflection travel times. Then the quality of the data was checked. Some individual samples were found to be corrupted and gave unrealistic values, supposedly due to failure of the automatic picker to recognize the correct peak, or to the presence of air under the hull of the ship at the device location. These points produced very local highs and lows (see Fig. 5.4, where the local positive and negative spikes on the map are the results of such faulty data points) and were easy to identify by simple comparison with the adjacent data samples. The total number of outliers was relatively small (less than 0.2%) and they were eliminated from the data set with no loss of resolution.

The next step included a cross check of the profile data. The differences at the cross points were calculated for the main grid lines and cross-lines. The discrepancies were manually minimized by adding or subtracting a constant value from the travel times for each profile. The equivalent depth values for the time corrections applied for different profiles were in the range of $\pm 3\ m$.

The travel path for the echo sounder signal is not always strictly vertical, e.g., in the areas where the seafloor is not perfectly horizontal, the sea bottom location of the reflection point of the shortest ray migrates from its vertical projection from the sea surface of the shot point. For this reason, it is incorrect to use simple gridding of the data points according to the sea surface navigation. Instead, the bathymetry map was created using the tomography code with the travel time reading used as input data. A single layer model was constructed for this purpose with the node of the layer representing the water and the bottom interface being the seafloor. The grid for the seafloor has the cell size of $50\ m \times 50\ m$. The sound velocity in the water was obtained from a profile measured in the experiment (see Fig. 3.6), and an average value, 1481.5 km/s, obtained by integration of the profile was used.

The results from the OBS localization were used to establish a datum for the resultant grid. The depths of the grid were corrected by a constant value so the OBSs were 1 m above the seafloor.

5.3.2 Travel time data

The travel times of rays were obtained using single channel seismic data (normal incidence) and data recorded by OBSs (the complete range of angles from normal incidence to wide angle). Examples of seismic sections are shown in Figure 5.5.

Due to the high frequency seismic source, and consequent high vertical resolution of the seismic data, about 20–25 events can be recognized on the single channel seismic data between the seafloor reflection and the BSR and even more events on the sections recorded by the OBSs (see Fig. 5.5). The selection of the events for the tomographic inversion was based on certain criteria. First of all, the event must be traceable through the whole modelling area, i.e., on every seismic section. Not all events satisfied this criterion. Some of them, especially the weakest ones, disappear in certain parts of the modelled area. Second, the chosen events must be distributed evenly throughout the seismic section.

The model that was constructed for this inversion contains 5 layers and 5 interfaces. The top layer (or, strictly speaking, half-space) represents water column, and the top interface simulates the sea bottom. The bottom of the model or the deepest interface represents the BSR. There was no possibility to model any deeper layers, as there was no continuous deeper reflector present throughout the modelled area.

The following events were chosen (two way travel time relative to the seafloor reflection is given for the single channel data in the vicinity of the OBS B):

1. 90 ms
2. 180 ms
3. 235 ms
4. 280 ms (BSR)

The event #3 was not traceable in the vicinity of the OBS C, as the layered structure of the slope sediments is strongly disturbed there and the accreted sediments package lies closer to the sea surface. All other events were observed (sometimes weakly) in all seismic sections on both single channel and OBSs.

The chosen events were traced from one single channel seismic line to another using the cross lines. The events for picking on the seismic data recorded by OBSs were identified with the help of the single channel seismic data. For that, the printed seismic sections were aligned along the same shot trace (with the minimum offset for the OBS) such that the seafloor reflection for the normal incidence data coincided with the direct water wave arrival on the OBS section, and then compared (e.g., Fig. 5.5).

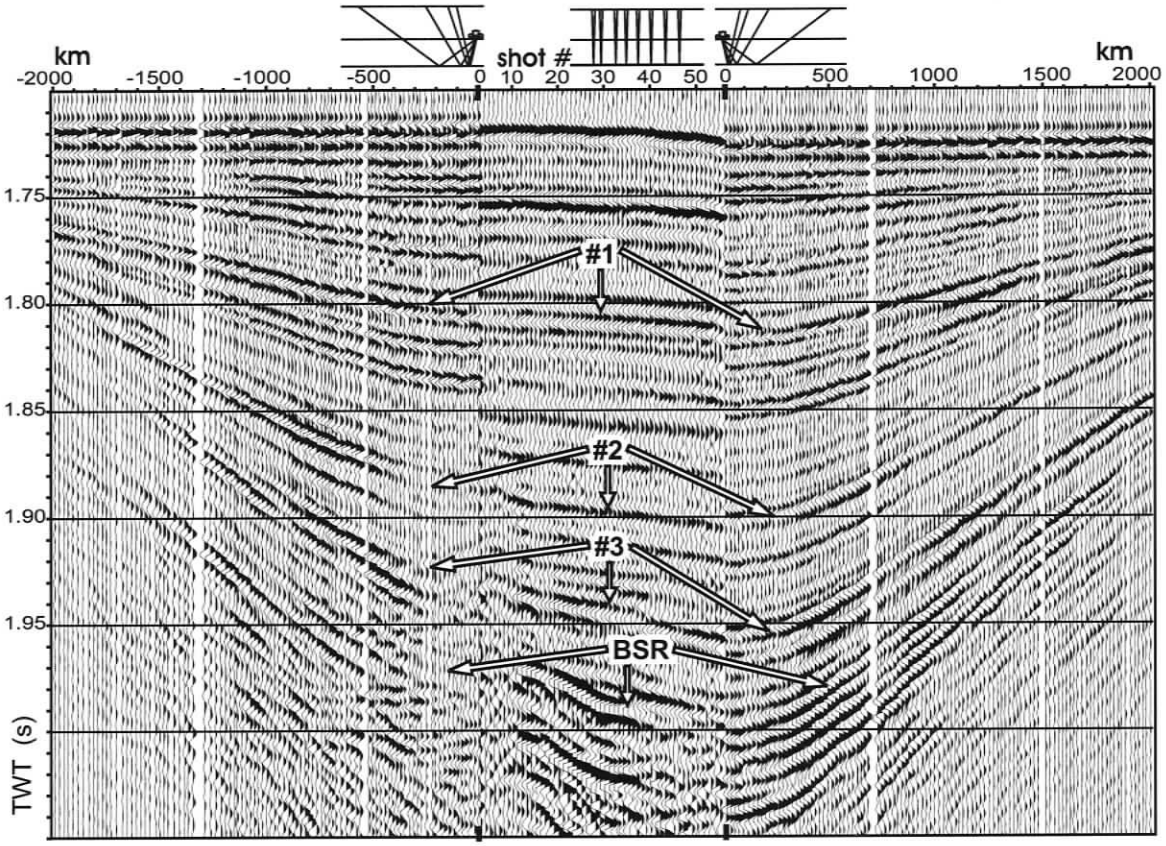

Figure 5.5: Example of the seismic sections (Grl-14) aligned for picking. The middle panel presents single channel seismic data. It helps to trace reflection events from OBS B recording (left panel) to OBS F recording (right panel). The direct water-wave arrival is flattened on the OBS data. Time is given in two-way travel time (TWT).

The single channel normal incidence data were taken from the channel four of the COAMS recordings. they did not receive any processing prior to picking except for

datum correction. The vertical position of the group #4 on COAMS streamer varied through the survey in the range of 15–23 m below the sea surface mainly as a result of different ship velocity. The picked times were brought to a datum 2 m below the sea surface using the seafloor reflection arrival. For that the picked time of the seafloor reflection was compared to the calculated time from ray tracing. The geometry for the forward model assumed that the source and receiver were both at 2 m depth and used the newly created bathymetry data. The correction times were calculated for each shot separately. The differences were used to correct the travel time data for the later arrivals. The correction values were in the range of ± 3 m/s.

The OBS sections were processed by F-K filtering prior to picking. The F-K filter was found to be able to effectively suppress the bubble pulse signal and at the same time be least destructive for the useful signal. With the direct water wave arrival flattened, the bubble pulse forms a horizontal bands across the seismic sections. In the F-K domain it is possible to remove the events of certain dipping angle (0° in case of the bubble pulse). Other seismic events have different dipping and are not affected by the filter significantly.

The time of picks were adjusted using the residual times from the source-receiver localization inversion.

While examining the OBS seismic section, it was difficult to identify the exact offset at which the transition from the reflected phase to the refracted phase occurred. In fact, the reflection phase gradually changes to the refraction phase over a span of offsets, approximately 100–150 m. The use of the travel time data with the wrong phase assigned can have a very negative effect on the reliability of the tomography results, and introduce a strong bias into the input data. Thus, to be on the safe side, it was decided to use only the reflected signal for tomography.

The cut-off offset for the reflected phase was determined for each seismic line individually, using an estimated transition offset from the ray tracing procedure and, mainly, by visual detection of the waveform shape change on the seismic section. The furthest offset varied for different events. It was shortest for the BSR event (3–3.5 km)

and longest for interface #1 (4.5–5 km).

The uncertainty values for the travel time picks were evaluated based on several factors. First, it was the quality of the data (e.g., signal-to-noise ratio). The signal-to-noise ratio for the picked events was 25 dB for the OBS recordings and 4 dB for the normal incidence data. Second, the wavelength of an event was taken into consideration. For example, the BSR reflection has lower frequency content, hence longer wavelength and lower vertical resolution.

Also the interference of the chosen reflection with other events on the seismogram increases the uncertainty of the picking. The vertical resolution of the seismic data decreases downwards on the OBS seismic section, so does the accuracy of the travel time picking. Thus, the uncertainty assigned for the travel time data was different for different events and laid in the range from 0.75 ms for the uppermost event to 3.0 ms for the BSR travel time (see Fig. 5.1).

The uncertainty in the survey geometry, in turn, also introduced uncertainty to the travel time data. The high quality localization for the OBS data gives an uncertainty less than 1 ms. It was not possible to provide the same localization accuracy for the single channel data, thus uncertainty due to geometry consideration for the single channel normal incidence data was estimated to be about three times higher than for OBS data.

In the OBS data, the uncertainty for the travel times was estimated to be 0.75 ms for event #1, 1.5 ms for event #2, 2.5 ms for event #3, and 3.0 ms for the BSR. For the single channel data, events #1, #2, and #3 were assigned 3.0 ms uncertainty and for the BSR event, 4.5 ms. When time picking was complicated by increased signal-to-noise ratio or interference with other events, uncertainties were up to two times higher.

Except for a few minor cases, the identification and picking of the event was distinct. The picking was performed manually.

5.3.3 Model parameterization

Coordinate system transformation

In order to optimize the geometry of the experiment for the tomographic inversion the coordinate system had to be adjusted. The following procedures were done:

1. Geographical coordinates were translated into UTM coordinates using World Geodetic System 1984 (WGS84) ellipsoid with central meridian -129°.
2. The coordinate system was turned by 36.765°counter-clockwise around the point with coordinates 657964E, 5392656N (position of the OBS B). After this operation the direction of the main grid lines became N–S.
3. The origin of the coordinate system was moved to the point with coordinates 656500E, 5391000N.

All the calculations, plots, and other operations were done in the new coordinate system.

The modelled area is 3 km × 2.7 km with OBS B at approximately the centre. The vertical span of the model is from -1220 m (the highest seafloor point) to -1620 m (the lowest point of the BSR). The thickness of the inverted portion varied according to the depth of the BSR below the seafloor and was about 220–240 m. The cell size for the interface grid was 50 m × 50 m and for the inverted velocity grids 50 m × 50 m × 20 m, so the horizontal dimensions of the model were 60×54 cells with about 20 cells in vertical direction (Fig. 5.6). With the chosen cell size the targeted blank zone (600 m × 400 m in horizontal dimensions) is represented by 12×8 cells.

Parameterization and control parameters

Before the method of parameterization and other control parameters were chosen the characteristics of the medium proposed for modelling were studied. Based on the available geological and geophysical information (see Chapter 2) the following characteristics of the modelled object were revealed:

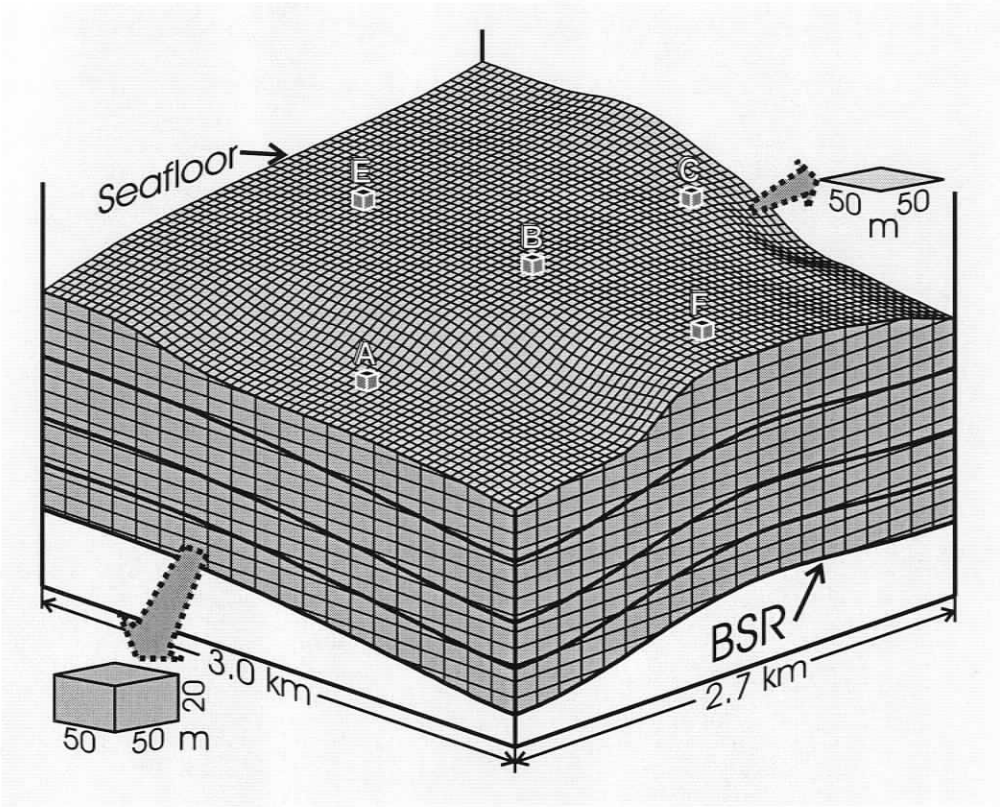

Figure 5.6: Parameterization of the model.

- The modelled section is composed of slope sediments with low compaction, similar mineral content and grain size;
- The velocity gradient with depth is about 1–1.5 m/s per m. The velocity increases due to increasing compaction and possible rise in gas hydrate concentrations with depth, rather than with the change of sediment type;
- The reflection events are produced by thin layers;
- The only change of the sediment lithological structure occurs at the boundary between slope sediment and accreted sediments. No strong reflection event suitable for picking is associated with this transition;
- The thickness of the layers varies spatially. The interfaces do not conform to the sea bottom and their depth below the seafloor varies greatly over the region;

- The curvature of the BSR is expected to be less than that for other interfaces, as it is mostly controlled by P-T field rather than tectonic processes.

Based on these observation the following parameters were used while inverting the model:

- The chosen parameterization type allowed the presence of a velocity gradient in the layer;
- No velocity jump was allowed with the transition to another layer;
- The smoothness factor for the BSR was larger than for other interfaces;
- The smoothness factor for the velocity grid was less than the one for the interfaces.

5.3.4 Starting model

A proper starting model is a vital necessity for rapid convergence and also for the overall ability of the inversion to converge to a reasonable final model.

The starting model for the velocities was constructed based on the sonic log and VSP data at the ODP 889 site. The velocity gradient in the sediments was assumed to be about 1 m/s per 1 m of depth below the seafloor with 1500 km/s P-wave velocity for the sediments at the sea bottom. The layer velocities were specified accordingly. No specific anomalies were introduced into starting model.

The positions of interfaces in the starting model were estimated using the normal incidence travel time data. In the beginning, the interfaces were introduced as flat horizontal planes. A preliminary inversion step was done to obtain the configuration of the reflectors that satisfies the normal incidence data better. During this inversion step the velocities were held constant, letting the depth to the interfaces be adjusted according to the travel time data. The model obtained from this preliminary inversion was used as a starting model for the full inversion, using all available travel time data and inverting for both velocities and depth to the interfaces.

5.3.5 Convergence criteria

For the linearized iterative inversion several criteria can be used to make the decision to stop the inversion process. These are:

- the number of iterations performed;
- the χ^2 misfit for the travel time data;
- the stability of the solution.

The convergence of the inversion can be considered satisfactory only when the last two criteria are met. The model obtained after the last step is considered to be the final model.

Any value of χ^2 less than unity is supposed to indicate that the model satisfies the input travel time data with given uncertainties. The stability of the solution is evaluated by comparing the results produced by two consecutive iterations. The RMS value of perturbations of all model parameters has to be small.

The situation when only one out of the last two criteria is met may indicate that a problem exists in the inversion settings. In particular, if only the third one is satisfied, it is an indication that the uncertainties for the input travel time data might be underestimated (i.e., they were set to be too small), or the smoothness constraints that are put on the model are too large.

It may also occur that the appropriate fit of the input data is achieved, but the solution is unstable. This might be an indication that the available input data do not constrain the model strictly enough. Introduction of a greater smoothness parameter might help to overcome this problem.

5.4 Synthetic tests

Prior to inverting the measured data it is required to perform some synthetic test in order to establish the limitations and abilities of the method with the available experimental geometry and chosen parameterization.

For these purposes, several synthetic models were created that simulated reasonable physical models for the observed acoustic features in the seismic data. Two most probable models that try to explain the blanking phenomenon were considered (Fig. 5.7). The proposed anomalous zone associated with the blank zone is assumed to have ellipsoidal shape with horizontal dimensions of 600 $m \times 400$ m.

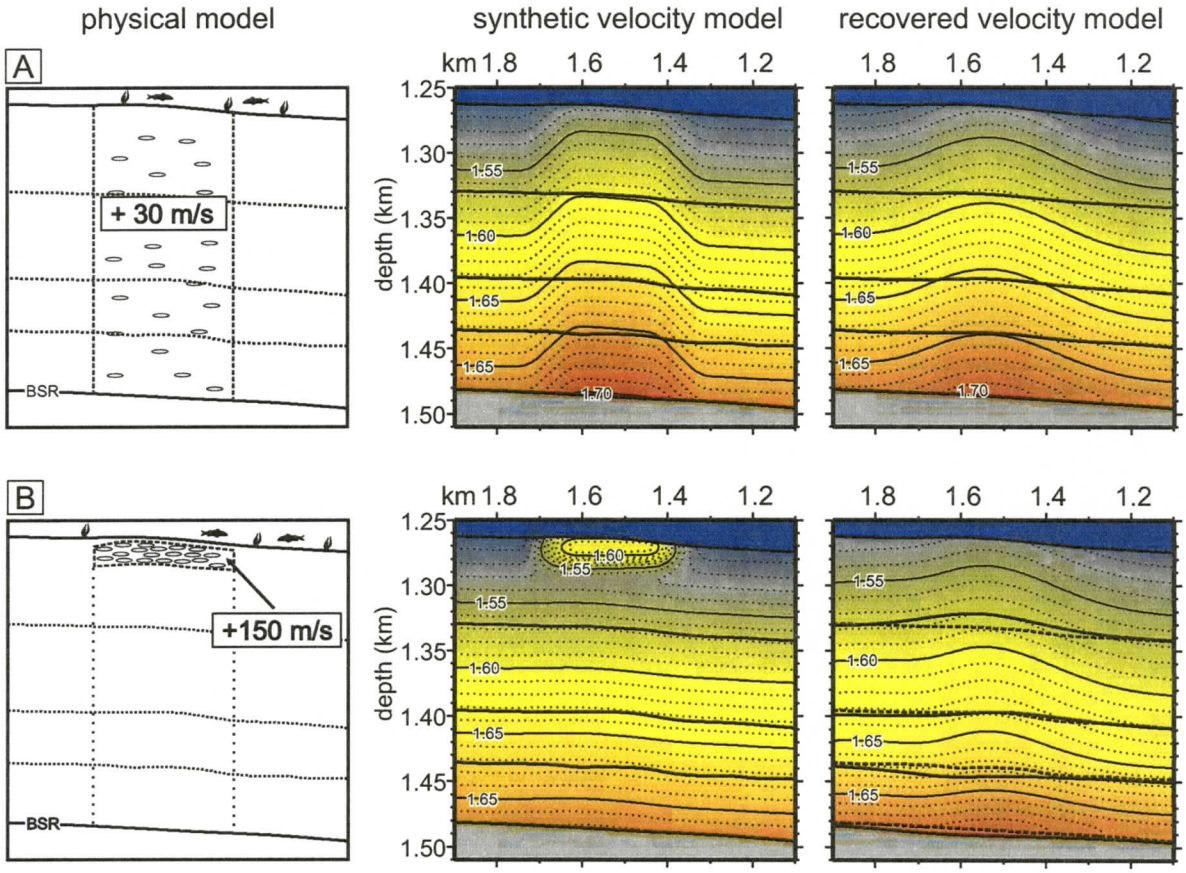

Figure 5.7: Synthetic test of the inversion. The possible physical models (*left column*), their expressions in the velocity field (*middle*) and results of the inversion of the synthetic travel time data (*right*) are shown.

The first model (A) assumes increased velocity in the whole volume of the blank zone, which might be the result of the presence of gas hydrate in greater concentrations compared to the outside of the blank zone. To model this situation, a positive velocity anomaly with a magnitude of 30 m/s was introduced to the background velocities within the blank zone over the whole vertical span of the modelled sediment section.

Such a small value for the magnitude does not necessarily represent the actual velocity increase due to anomalous gas hydrate presence, but was chosen mainly to test the method sensitivity.

The other hypothesis (B) assumes the presence of a localized volume of sediments (15–20 m in thickness) with significantly higher P-wave velocities. This body is located close to the sea surface and does not extend deeper; that is, the velocity under it is the same as the velocities outside of the blank zone. This model is consistent with the hydrate cap model.

As a part of simulation, noise was added to the synthetic travel time data samples. The noise had a Gaussian distribution and standard deviation equal to the uncertainty of the travel time data.

The geometry and parameterization of the model and control parameters for the inversion of the synthetic data were the same as for the following inversion of the measured travel time data.

The results of the inversion of the synthetic travel time data set are shown in the third column of Figure 5.7. The test showed that the inversion cannot localize a thin body velocity anomaly near the seafloor (model B). It tends to spread the region of the increased velocity vertically. Most likely this is the result of the sparse OBS geometry of the experiment. The results for the two different physical models are almost undistinguishable from each other. However, the anomaly tends to decrease with depth for the thin body case, while for the vertical anomaly the increase of the velocity reaches the same level for all depths in the resulting velocity field.

From the model A results, it can be noted that the limits of the anomaly are not so well determined and the true anomalous velocity (+30 m/s) was not fully recovered by the inversion (only +20 m/s). This can be explained by the need to use a large smoothness factor in the inversion. This parameter acts as a trade off between higher resolution and reliability in the inversion results. For the sparse OBS geometry in this experiment, a large smoothness factor is required. Otherwise, false anomalies due to noise in the data may appear in the poorly constrained areas.

In order to check the sensitivity of the inversion, that is the minimum velocity anomaly that produces sensible differences (compared to the uncertainty) in the travel time data, the travel time residuals for the model A were examined (Fig. 5.8).

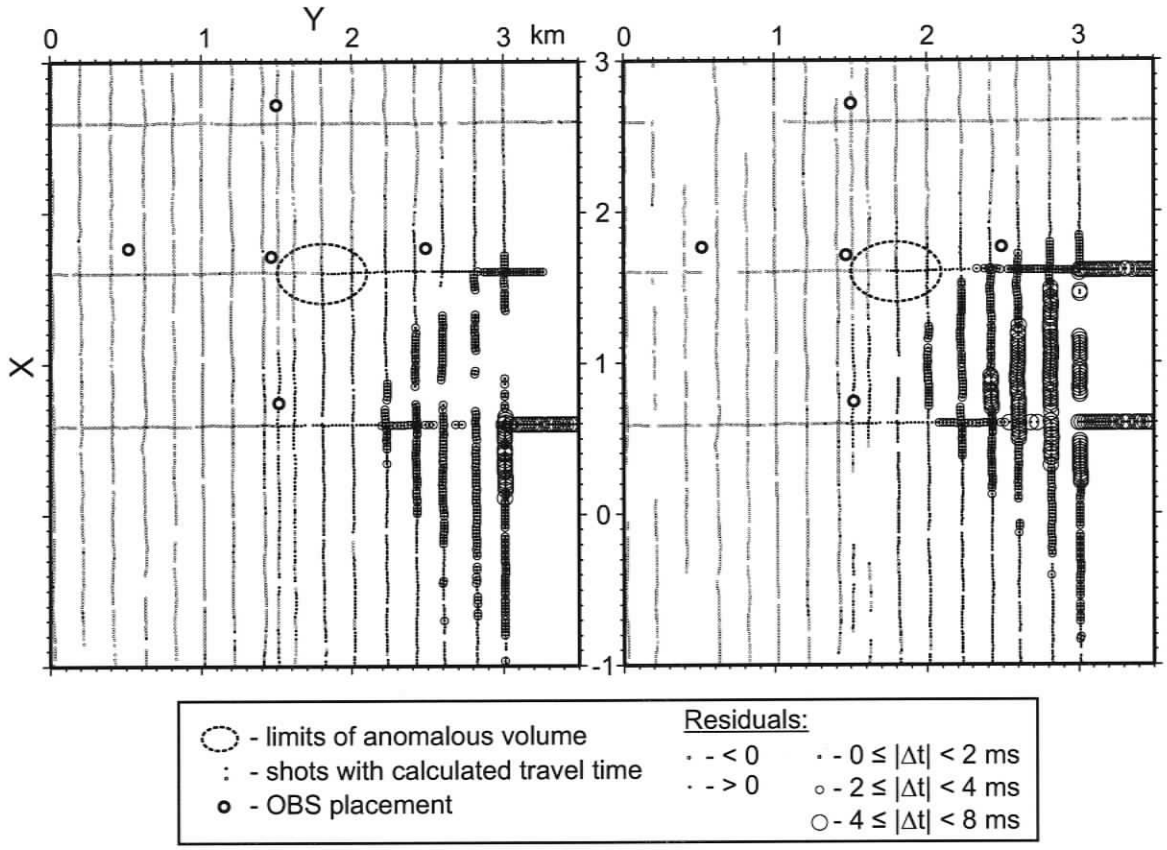

Figure 5.8: Travel time residuals for the anomalous model A. The partial data set are shown for the wide-angle reflections recorded by OBS B from interface #2 (left) and BSR (right).

The shown residuals are the reduction in travel times due to presence of a positive velocity anomaly of 30 m/s in the volume with the ellipsoidal shape in the horizontal plane and the vertical extent from sea bottom to the BSR. For the same shots, residuals are greater for the BSR reflection than for the shallower interface, since the travel path in the anomalous media is greater for deeper reflections. By the same reason, the wider angle rays also feature larger residuals.

The estimated travel time differences due to increased velocity in the anomalous

region for the normal incidence rays are $-5\ ms$ for the BSR reflection.

The examination of the residuals reveals that the wide angle data are quite sensitive even to the small velocity change. The travel time difference due to the $+30\ m/s$ anomaly are up to two times greater than the uncertainty of the travel time data. Thus, the conclusion can be drawn that the sensitivity of the experiment with respect to the velocities is about $\pm 15\ m/s$.

The synthetic case modelling was also used to estimate the ray coverage of the model volume. The example diagram is shown on Figure 5.9. Shown by this figure, the best coverage (in terms of diversity of the ray types) for the experiment geometry occurs in the region between OBSs, since every volume unit is sampled by three types of rays: normal incidence and wide-angle rays from two different OBSs. The worst coverage is in the vicinity of each OBS, for only normal incidence rays from the single channel conventional seismic and near-normal incidence rays from OBSs are available in those regions.

While the inversion is not very sensitive to random noise, systematic error on the input data may affect the results greatly. The systematic error may appear due to picking the wrong event or due to interference of two different events. To avoid this situation, the picking was done with great care and with multiple cross-checking using the cross-profiles. An event was picked and the travel time sample was included into the data set in case of high confidence only. The large number of shots allowed partial exclusion of arrivals with little effect on the ray coverage.

The results of the synthetic experiment can be summarized as follows:

- The final velocity models inverted for the two different physical models of a thin anomalous body and an anomaly with a large vertical extent are almost indistinguishable from each other in the case of small anomalous values.
- The horizontal limits of small amplitude anomalies cannot be accurately determined but are smoothed over distances of 1 to 2 cell sizes.
- The maximum anomalous velocity increase tends to be underestimated.

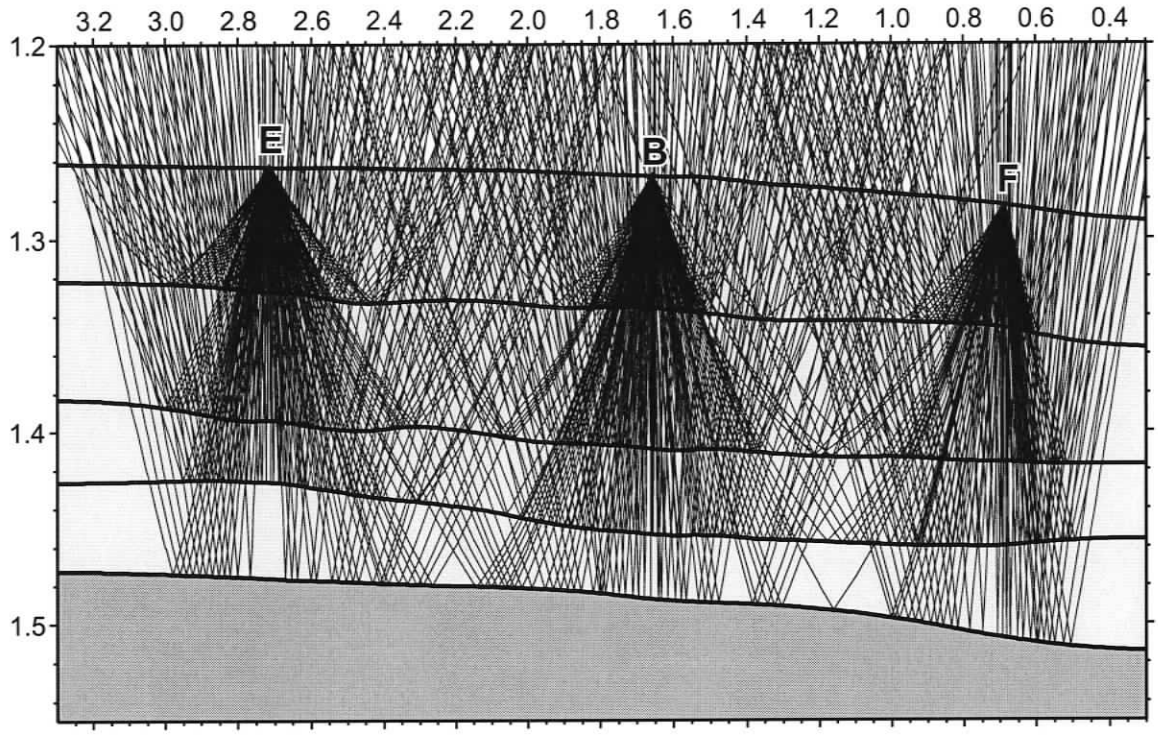

Figure 5.9: Ray coverage of the model volume. Shots for only one seismic profile (Grl-14) are shown. Only every fifth ray is plotted. The normal incident rays are not shown (they go approximately every 20 m along the profile).

5.5 Results of the travel time tomography inversion

5.5.1 Final model

Presentation of a 3-D model is usually done through a 2-D slice method (e.g. Zelt et al., 1996; Hobro, 2000a). Two types of slices cutting the 3-D cube were produced. Lateral velocity variation is shown in slices cutting the model cube at constant depths below the seafloor (Figs. 5.10–5.12). Also, a series of vertical slices in N–S and E–W directions were created (Figs. 5.13 and 5.14). Since a vertical velocity gradient is present at the site as well as bathymetry variations, slices at constant sub-seafloor depth represent the anomalous variation of the velocity field better than plane horizontal slices.

The slices are shown for constant depths of 1 m, 50 m, and 190 m below the

seafloor. The slice at 1 m (Fig. 5.10) practically represents the velocity of the model at the sea bottom. The 50 m slice (Fig. 5.11) provides the horizontal distribution of the velocity function for the upper part of the sediment section. Finally, the 190 m slice gives the velocities for the sediments close to the BSR.

The vertical slices are made parallel to the model axes in the North–South (Fig. 5.13) and West–East (Fig. 5.14) directions. Three slices in each direction serve the goal of highlighting the main features of the model, especially those that are associated with the blank zones (Fig. 5.15).

The layers are also presented in a 3-D perspective view (Fig. 5.16) together with the limits of the main blank zone at the site. The configuration of the reflectors does not follow the shape of the seafloor. The deeper interfaces (#2 and #3) outline a well pronounced depression extending in the N–S direction that does not have an expression either in the bathymetry, or in the shape of the BSR. The elevation of the flanks over the central part of the depression are over 50 m. The deeper parts of the section are more affected by the flexure. The blank zone does not coincide with the centre of the feature, but is located on the east flank of it.

Examination of the tomography inversion results focused on the central part of the model, the portion that is better constrained by the data. The uncertainty here can be as low as ± 30 m/s. In general, the well constrained area is defined as a region in which the uncertainties for the velocity are less than 100 m/s. The reliability of the velocity values outside this area is poor, and might be subject to numerical anomalies not supported by the data but instead may be artificial outcomes of the algorithm as a result of the sparse receiver geometry of the experiment.

The average velocity profile for the central part of the model is compared with the previous studies for the area (Fig. 5.17), in particular, with the velocity measurements obtained at the drill site 889. The recovered average variation of the velocity with depth corresponds well with the previously known values, especially for the upper part of the profile.

Just below the seafloor, velocities are 1500–1520 m/s, which are just slightly

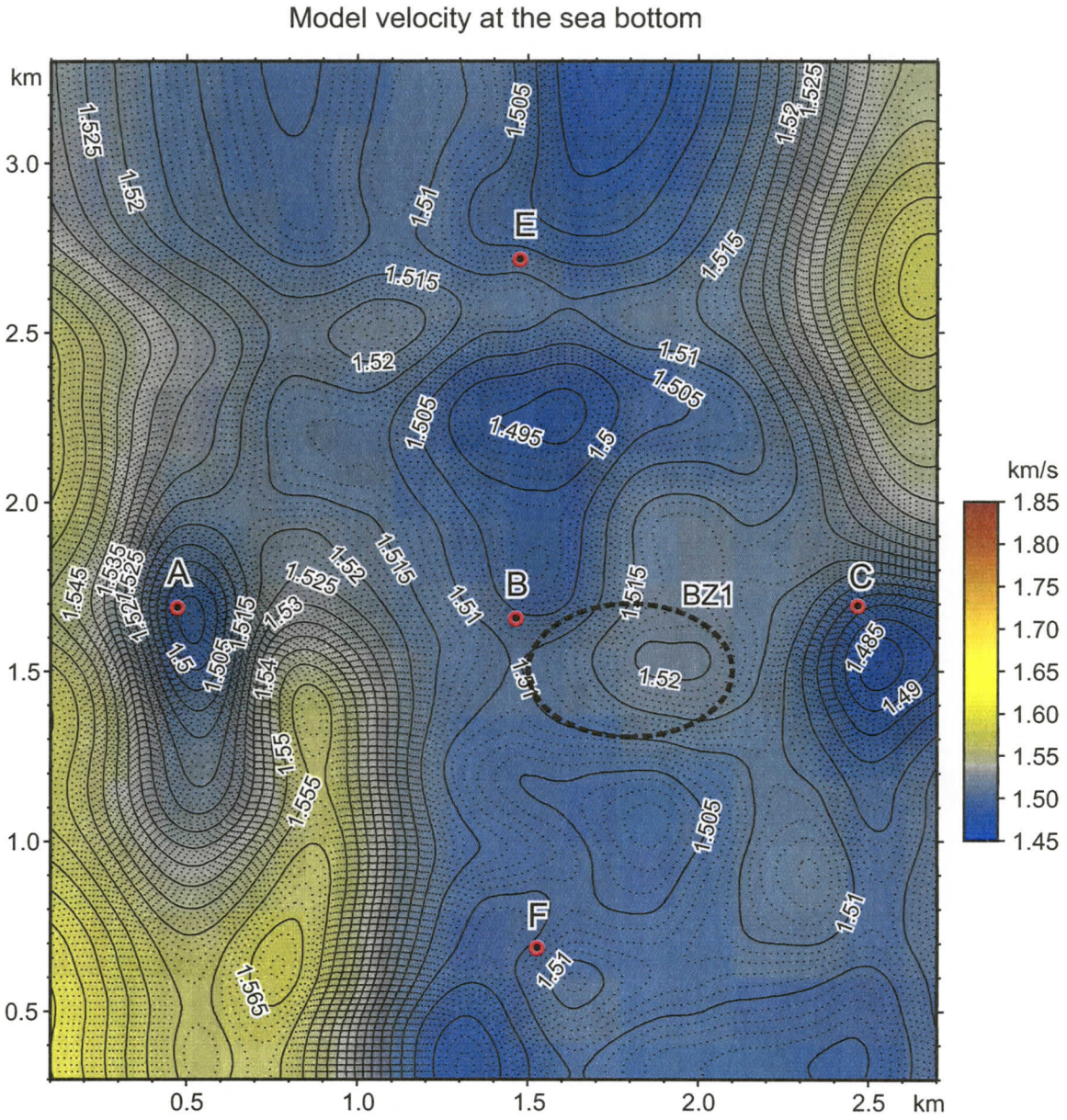

Figure 5.10: Final model velocities at the sea bottom. Black dashed line outlines the limits of the main blank zone. Velocity contours are in km/s. OBS locations are shown by red dots.

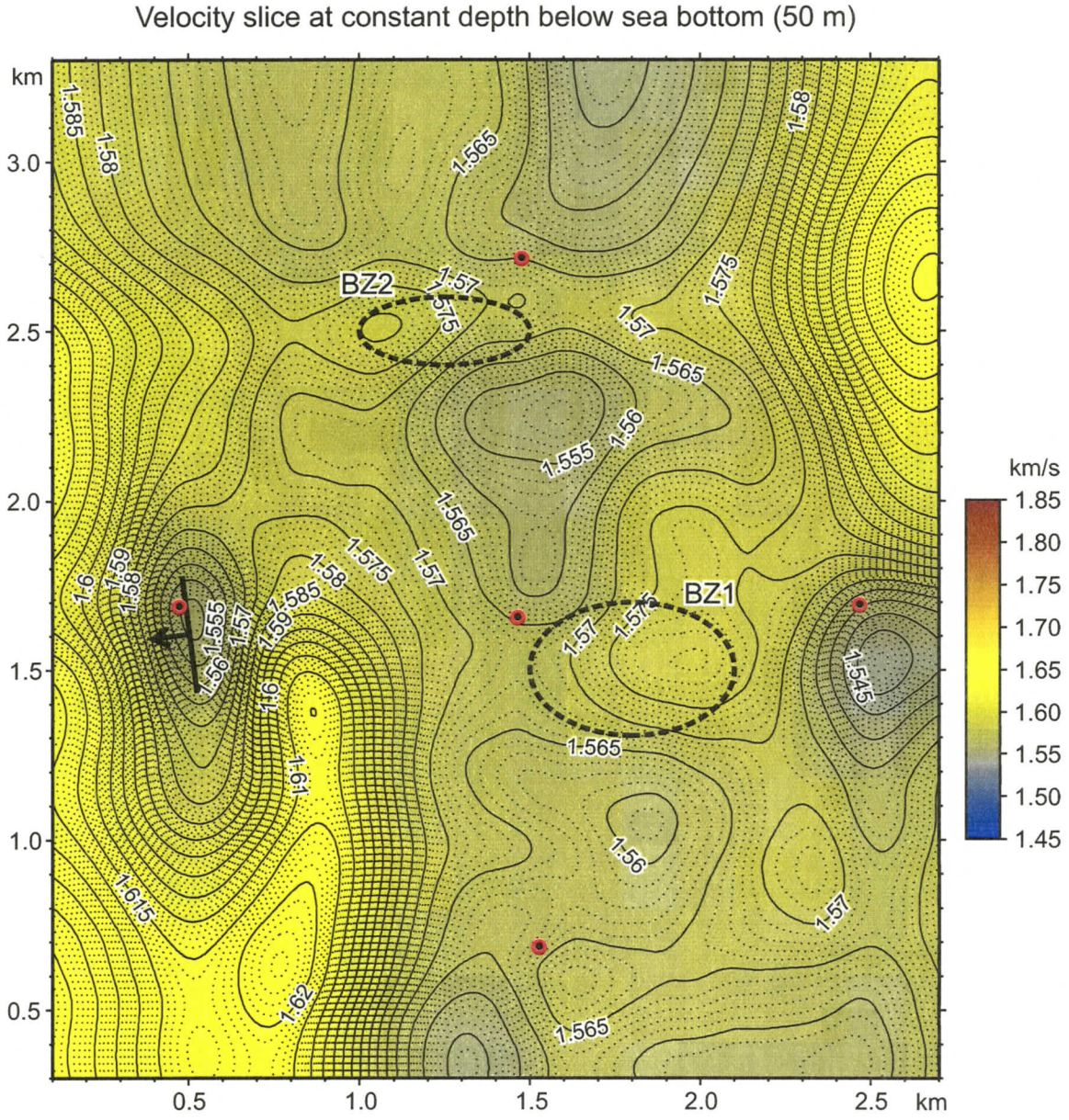

Figure 5.11: Final model velocities. Slice at 50 m constant sub-bottom depth. Black dashed lines outline the limits of the blank zones. Velocity contours are in km/s.

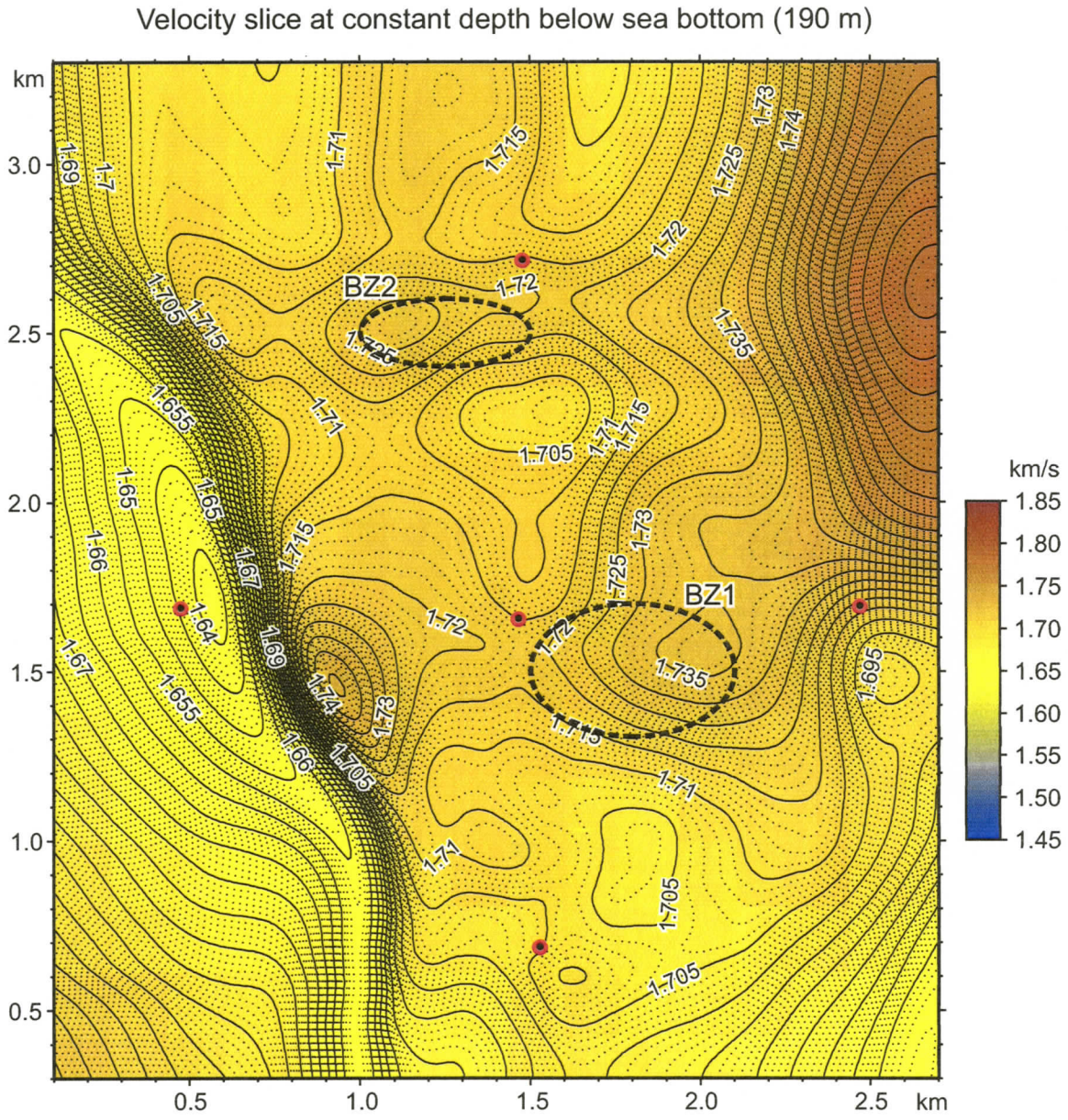

Figure 5.12: Final model velocities. Slice at 190 m constant sub-bottom depth. Black dashed lines outline the limits of the blank zones. Velocity contours are in km/s.

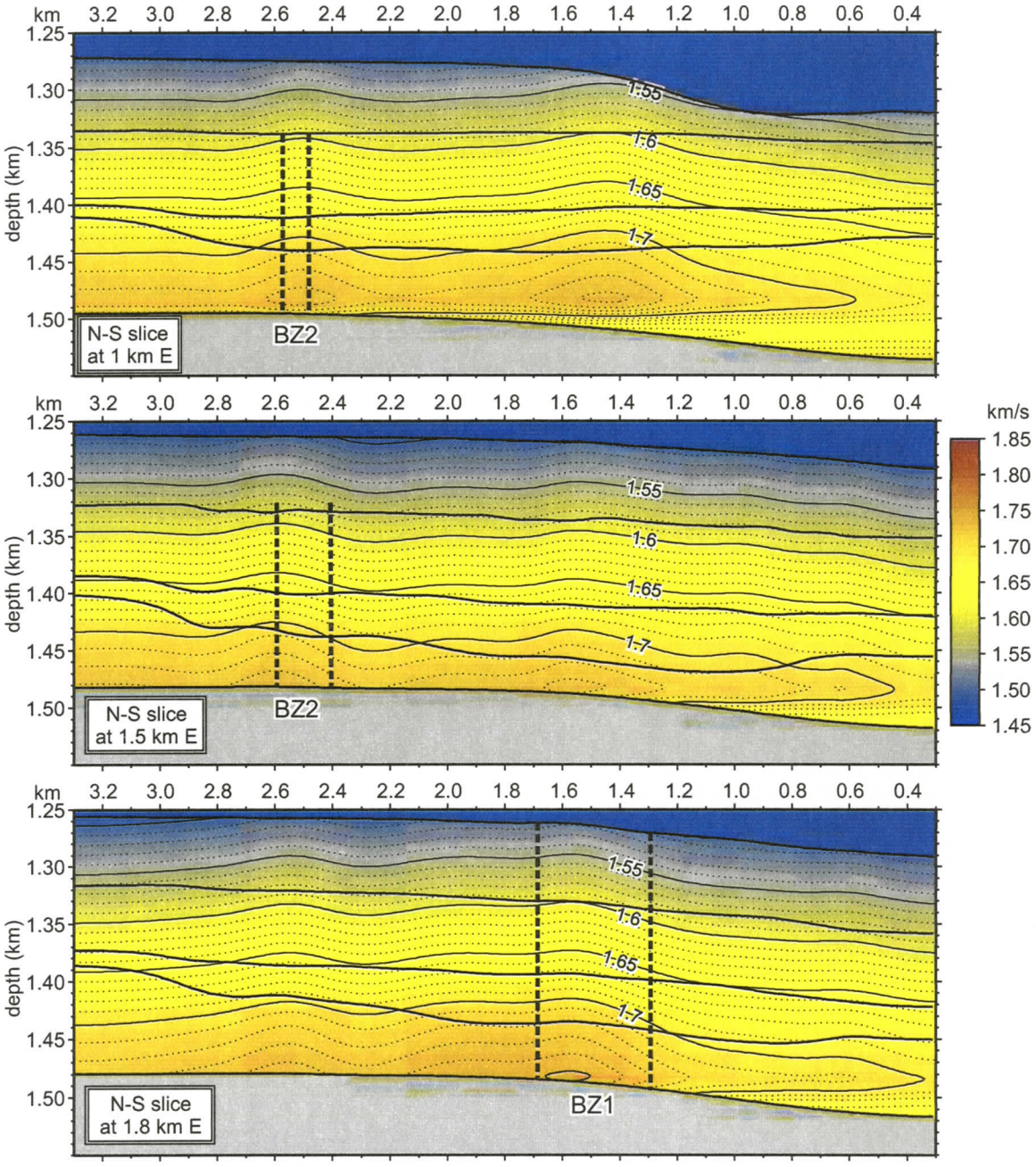

Figure 5.13: Final model velocities. Vertical slices in N–S direction. Black dashed lines outline the limits of the blank zones. Velocity contours are in km/s.

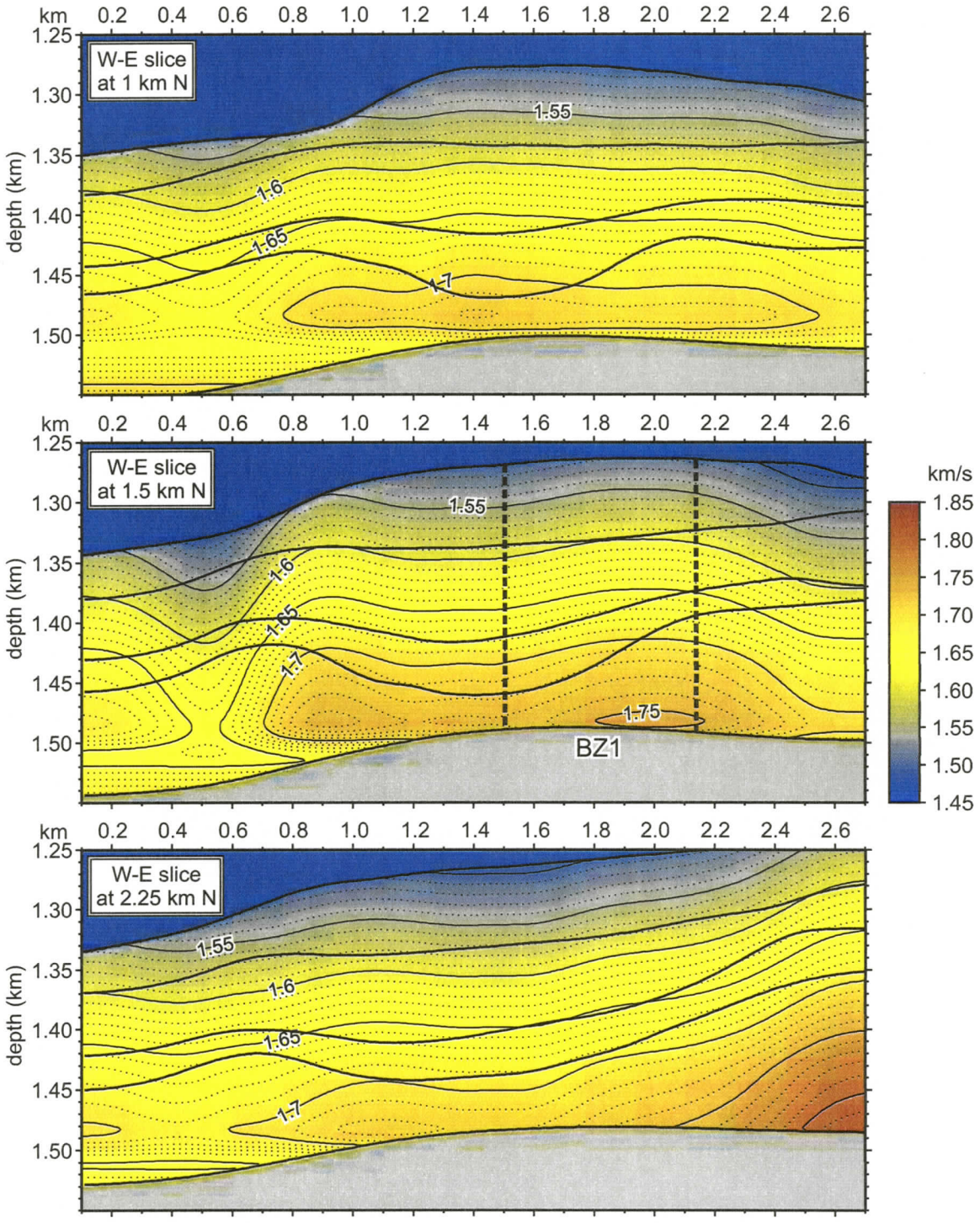

Figure 5.14: Final model velocities. Vertical slices in W–E direction. Black dashed lines outline the limits of the blank zones. Velocity contours are in km/s.

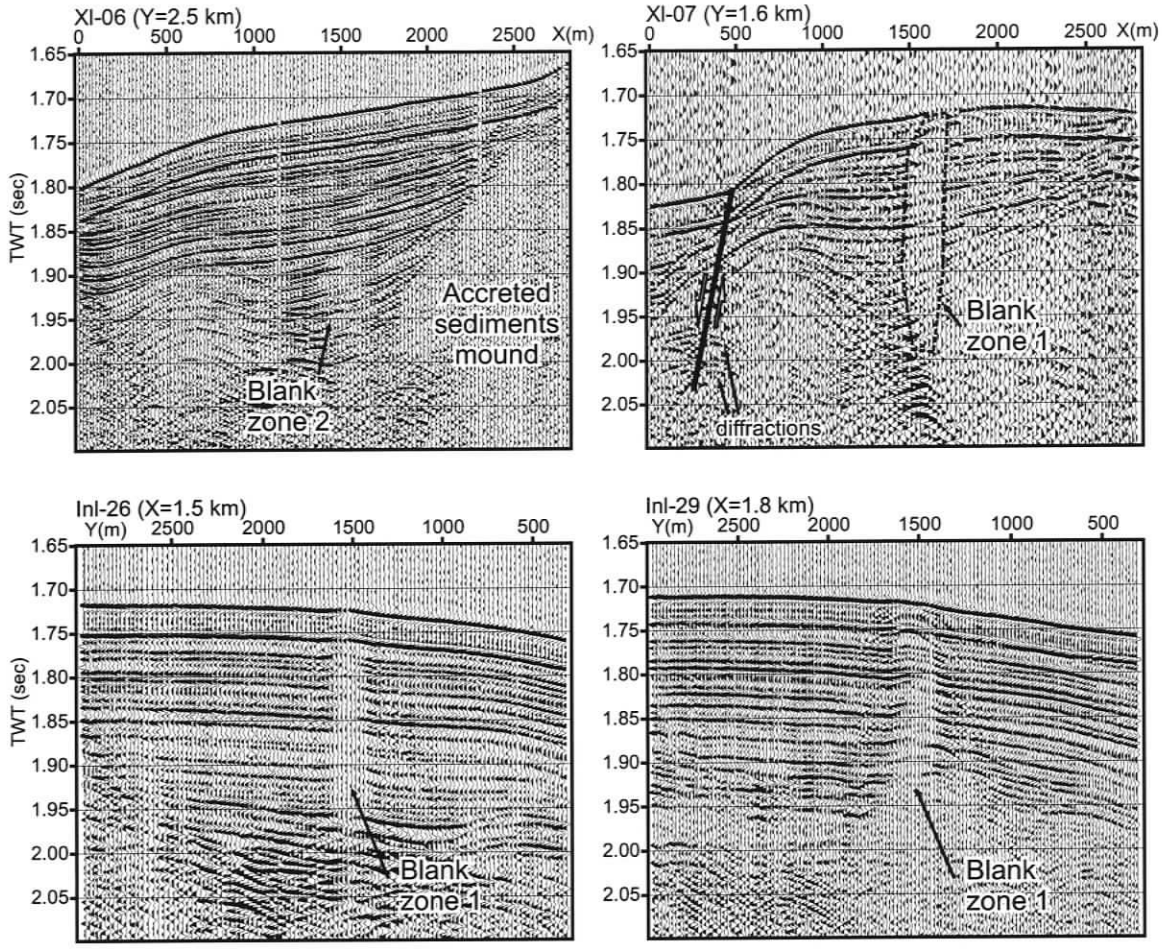

Figure 5.15: Single-channel data. Nomenclature given as per single-channel profile grid (Fig. 3.1, Table 3.1). The coordinates are given in the model coordinate system.

greater than the P-wave velocity in the water (1481 m/s). Velocity increases almost uniformly down to the BSR with a gradient about 1 m/s per 1 m, reaching values of 1700–1750 m/s immediately above the BSR. The gradient is slightly lower for the lower part of the model and does not change greatly over the modelled area.

The spatial variations of the velocities are best recognizable on the slices with constant depth below seafloor (Figs. 5.10–5.12). All positive anomalies correspond well with the bounds of the blank zones identified from the single channel seismic profiles. Though the overall increase does not exceed +20 m/s, it indicates that the sediments inside blank zones have higher velocities than those outside, but the

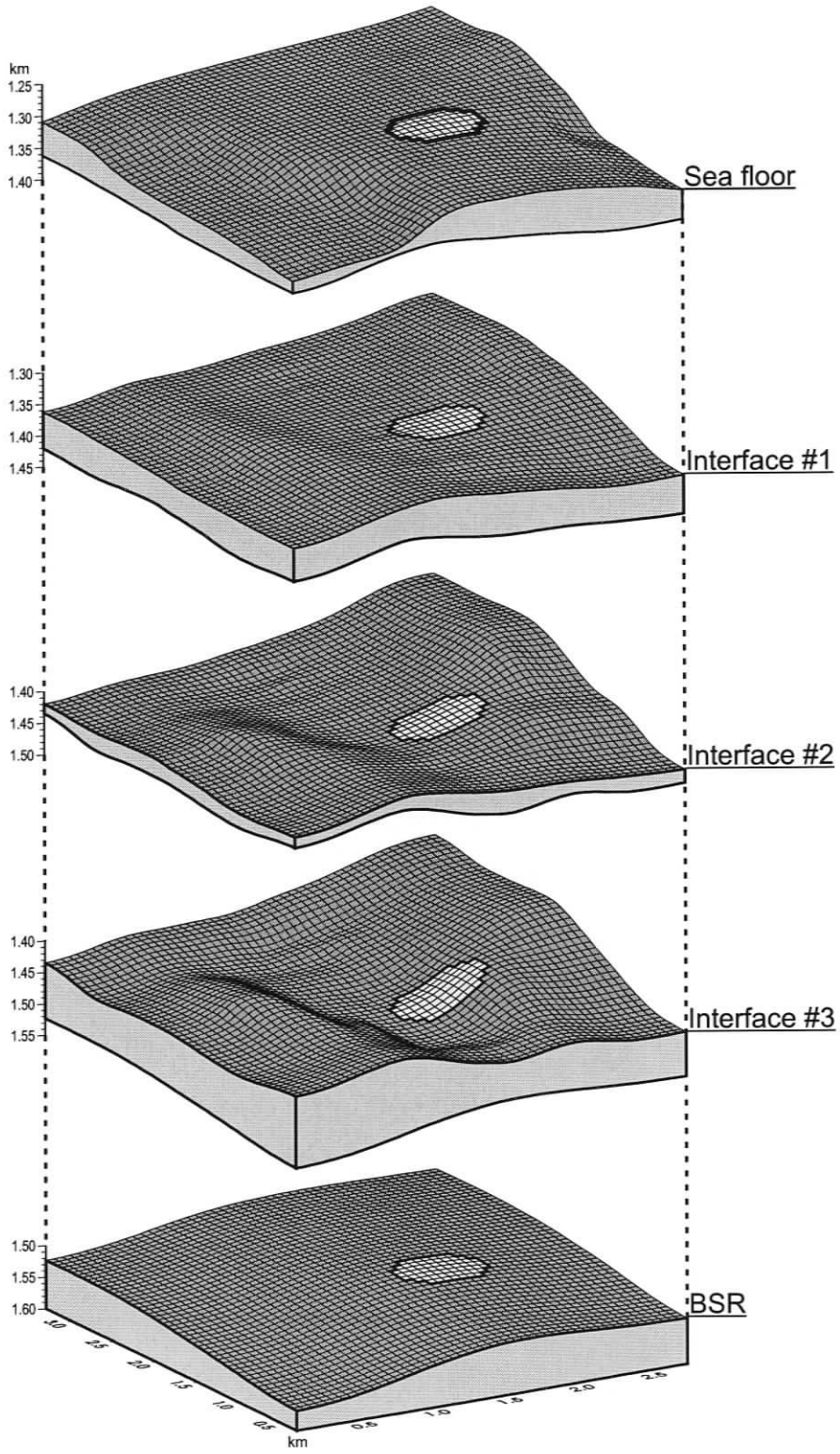

Figure 5.16: The 3-D perspective view of the interfaces of the final model. The limits of the main blank zone are outlined.

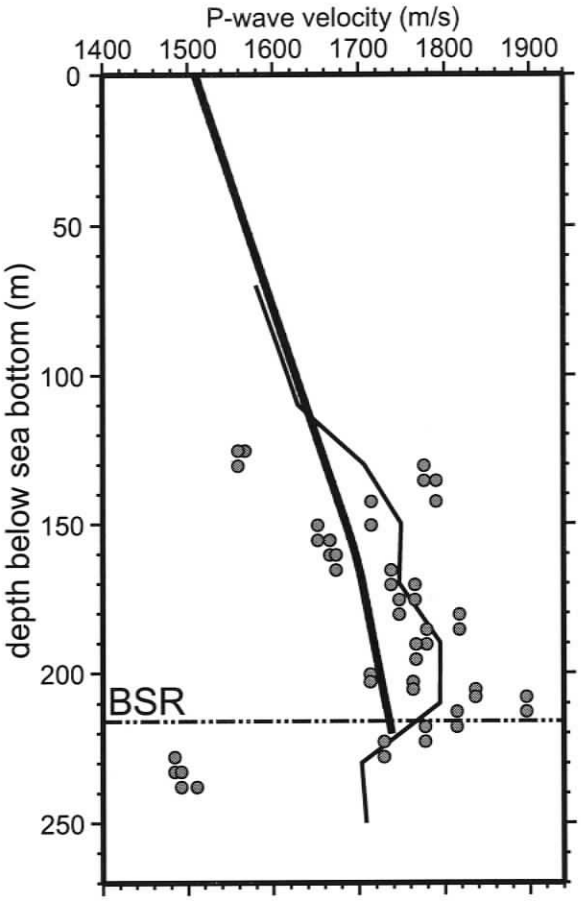

Figure 5.17: Velocity vs. depth profiles for the final model (thick line) and the sonic log profile (thin line) for the drill site 889 (averaged over 20 m depth intervals). The results of VSP profiling are also shown (grey circles). The position of the drill site is approximately 3 km to the North from OBS C.

difference is not large.

A pair of positive and negative anomalies in the vicinity of the OBS A (0.5E, 1.7N, and 0.8E,1.4N on Figs. 5.10–5.12) spatially corresponds to a normal fault seen on the single seismic section (Fig. 5.15, Xl-07).

Vertical slices, in general, reveal a good spatial agreement between the limits of the blank zones and regions with elevated velocity values, although the width of the velocity anomalies may be up to 2 times wider than the actual width of the blank zone (e.g., N–S slice at 1 km E, left zone). The W–E slice at 1.5 km N (Fig. 5.14) cuts through the middle of the main blank zone and the anomalies associated with the normal fault. It shows that the highest velocity at the BSR (1750 m/s) is inside the blank zone.

The negative velocity gradients located a few tens of metres above the BSR seen on the vertical slices in the peripheral parts of the model are believed to be artificial

features and are not reasonably explainable by any geological phenomenon. Unfortunately, this degrades the value of the inferred velocities at the BSR at the extremities of the grid.

The high positive anomaly in the N–E corner of the model is believed to be real (Figs. 5.10–5.12; Fig. 5.14bottom), though its position is outside of the high confidence region. The increase of velocity can be associated with the accreted sediments that form a mound which approaches the seafloor (Fig. 5.15, Xl-06).

In summary, the good quality results obtained by the travel time tomography inversion are in good agreement with the general knowledge of the region and they provide more details about the velocity distribution and interface geometry for the site. No extreme anomalies were revealed, and this indicates that the velocity field over the site is more or less uniform.

5.5.2 Quality assessment of results

The assessment of the final model quality, i.e., its reliability, can be performed using direct and indirect techniques. The direct assessment provides an ultimate measure of the final model quality by providing the uncertainty values for each parameter that was involved into the inversion.

Indirect techniques provide general information on the reliability of the final model, giving an answer to the question: for what regions of the model can the results not be trusted? They do not address the question of which specific feature of the model can be trusted. The indirect assessment technique involves travel time residual statics, ray coverage of the model, resolution tests and others as described by Zelt (1999).

Indirect

The ray coverage of the model volume was discussed earlier for the synthetic case (Fig. 5.9). Since the ray coverage is mostly defined by the geometry of the experimental survey, that is by positions of the shots and receivers, it is not significantly different for the real model.

The modelling statistics for the final model that includes the number of travel time picks used, hit rate (the number of connecting ray paths that actually were traced by the ray tracing routine), and the χ^2 values for each particular ray phase are given in Table 5.1.

Table 5.1: Modelling statistics for the final model.

Source	phase	Picks	Hit rate	Data uncertainty	χ^2
OBS A	1	6377	97.3%	0.75 ms	0.66
	2	4402	97.8%	1.5 ms	0.35
	3	1831	99.8%	2.5 ms	0.25
	4	3794	97.5%	3.0 ms	0.63
OBS B	1	8448	97.8%	0.75 ms	0.96
	2	6609	98.3%	1.5 ms	0.27
	3	5283	98.2%	2.5 ms	0.27
	4	5172	97.7%	3.0 ms	0.33
OBS C	1	6662	98.0%	0.75 ms	0.75
	2	2885	99.4%	1.5 ms	0.27
	4	2687	99.3%	3.0 ms	0.55
OBS E	1	7725	98.4%	0.75 ms	0.93
	2	5106	98.6%	1.5 ms	0.42
	3	3886	99.0%	2.5 ms	0.35
	4	2998	98.7%	3.0 ms	0.42
OBS F	1	6458	98.7%	0.75 ms	0.77
	2	5677	99.0%	1.5 ms	0.25
	3	4255	99.0%	2.5 ms	0.20
	4	2816	98.7%	3.0 ms	0.45
Normal incidence	1	2109	100%	3.0 ms	0.30
	2	1700	99.9%	3.0 ms	0.44
	3	1540	99.9%	3.0 ms	0.47
	4	1689	100%	4.5 ms	0.61
	Total:	**100,109**	**98.0%**	–	**0.55**

The χ^2 was about 2 times less than unity, which suggests that the estimations of the uncertainties of the travel time data for some phases were conservative. Also it showed that the chosen smoothness factor allowed a satisfactory fit of the input data.

The stability of the final solution was checked by calculating the difference between the final model and the model obtained at the previous iteration. Figure 5.18 presents

the results of the test. The absolute perturbation of a single velocity parameter is less than 1 m/s for the most of the model. It increases up to 3 m/s in the poorly constrained areas. The overall stability of the final model can be described as very good. The RMS of the model parameter perturbations for the entire model volume was 0.45 m/s.

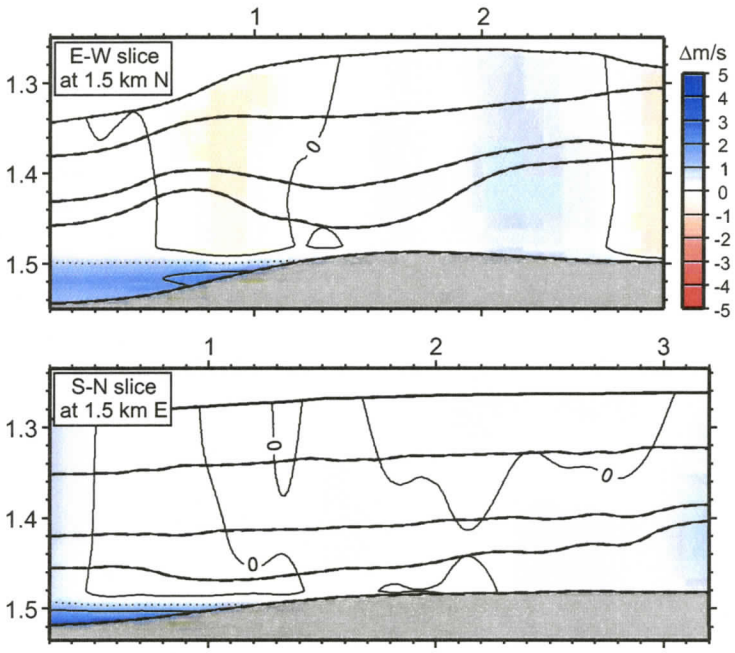

Figure 5.18: Differences of the models obtained at two consecutive iterations. Vertical slices of the 3-D model were created in perpendicular directions through the centre of it. The interfaces are shown in solid and thick dashed lines for these two models (they almost perfectly coincide with each other).

Direct

The direct quality assessment of the inversion results involves calculation of the uncertainty value for each model parameter. Instead of the mostly qualitative analysis provided by indirect assessment, the direct one provides a quantitative measure, the calculation of which is based on the combined numerical evaluation of different control parameters.

The uncertainty analysis package for Jive3D estimates uncertainties based on: (i) the estimated travel-time uncertainties of the input data, and (ii) the correlations introduced between neighbouring parameters as a result of smoothing regularization (Hobro, 2000b). The inclusion of the smoothing regularization into uncertainty analysis biases the uncertainty estimation and makes them smaller by assuming that

the true model actually has the same amount smoothness as it was introduced by the smoothness regularization term during the inversion. The values produced by uncertainty analysis represent one standard deviation in the Gaussian model.

The uncertainty calculation process involves inversion of the full Hessian matrix that consists of a square of the total number of the model parameters elements. Unlike the matrices involved in the model inversion, it is not sparse; that is, all its elements must be stored in the computer memory. This fact greatly reduces the maximum possible number of parameters in the model that is suitable for the uncertainty analysis. The commonly used layer-stripping method fails to provide adequate results. Therefore, the uncertainties of the final model had to be calculated for the entire model simultaneously.

In order to be able to perform the uncertainty analysis, the model size was reduced to 2 $km \times 2.1$ km and the horizontal cell size was increased to 100 m for both interface and velocity grids. Multiple tests showed that the increased size of the grid cells did not introduce significant difference into the results of the uncertainty analysis. For the test the uncertainties were calculated for smaller parts of the 50 m cell model and compared to those for the complete 100 m cell model. The uncertainties for the model with smaller cell size were at least not worse than for those the model with larger cell size.

The spatial distribution of calculated uncertainties for two different depths below the seafloor and the uncertainties for the vertical slices of the model are provided in Figures 5.19 and 5.20 respectively.

As expected, the central part of the model is better resolved than its flanks. The smallest values for the uncertainties are located in the planes going through three OBSs. The N–S direction (along the depression) is better resolved than W–E (across the depression); this might be associated with the configuration of the interfaces and the lower accuracy of picking for the parts of the interfaces with large dips.

The minimum uncertainty value for the velocity achieved for the model was as low as 20 m/s. In order to evaluate the distribution of the uncertainty values, a

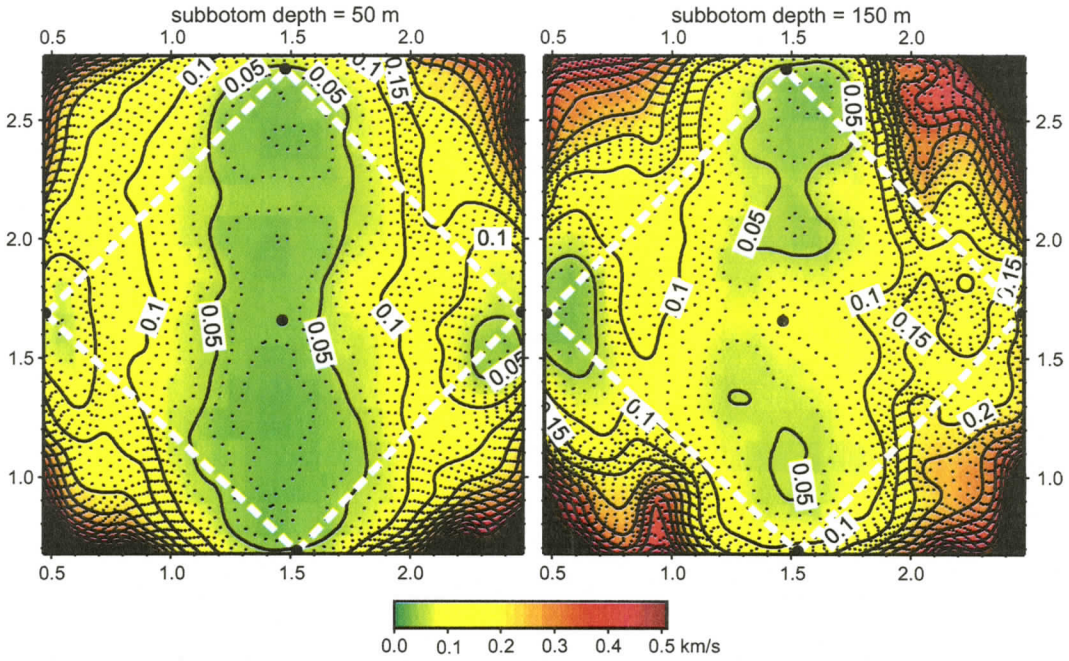

Figure 5.19: Subhorizontal slices of uncertainty values for the final model. Slices created for the surfaces of constant depth below the sea bottom (50 and 150 m). Black dots indicate OBS positions. White dashed line outlines the horizontal limits of the volume used in the volumetric percentile calculation of uncertainties.

statistical analysis was performed on the volume of the model limited on the sides by four vertical planes drawn through the OBSs (Fig. 5.19), with sea bottom at the top, and by the BSR at the bottom. The analysis shows that almost 1/3 of the volume of this portion of the model has the uncertainty better than 50 m/s. The complete volumetric results are presented in Table 5.2. The uncertainty for the depth to the interfaces can be as low as 1 m. In the central part of the model the average uncertainty of the vertical interface position is 4 m.

The results of the inversion showed much greater reliability than that obtained by Hobro et al. (2003) for the adjacent region. In that work the velocity values were pronounced well-constrained if they had uncertainty less than 600 m/s. The use of a higher frequency seismic source, travel time data for four reflectors instead of one, and closer spaced recording stations are the primary reasons for the lower uncertainties

Table 5.2: Volumetric statistical analysis of the uncertainty values for the velocity model.

uncertainty (m/s)	< 50	< 100	< 150
amount of model parameters with specified uncertainty	32%	77%	94%

and overall better quality of the results.

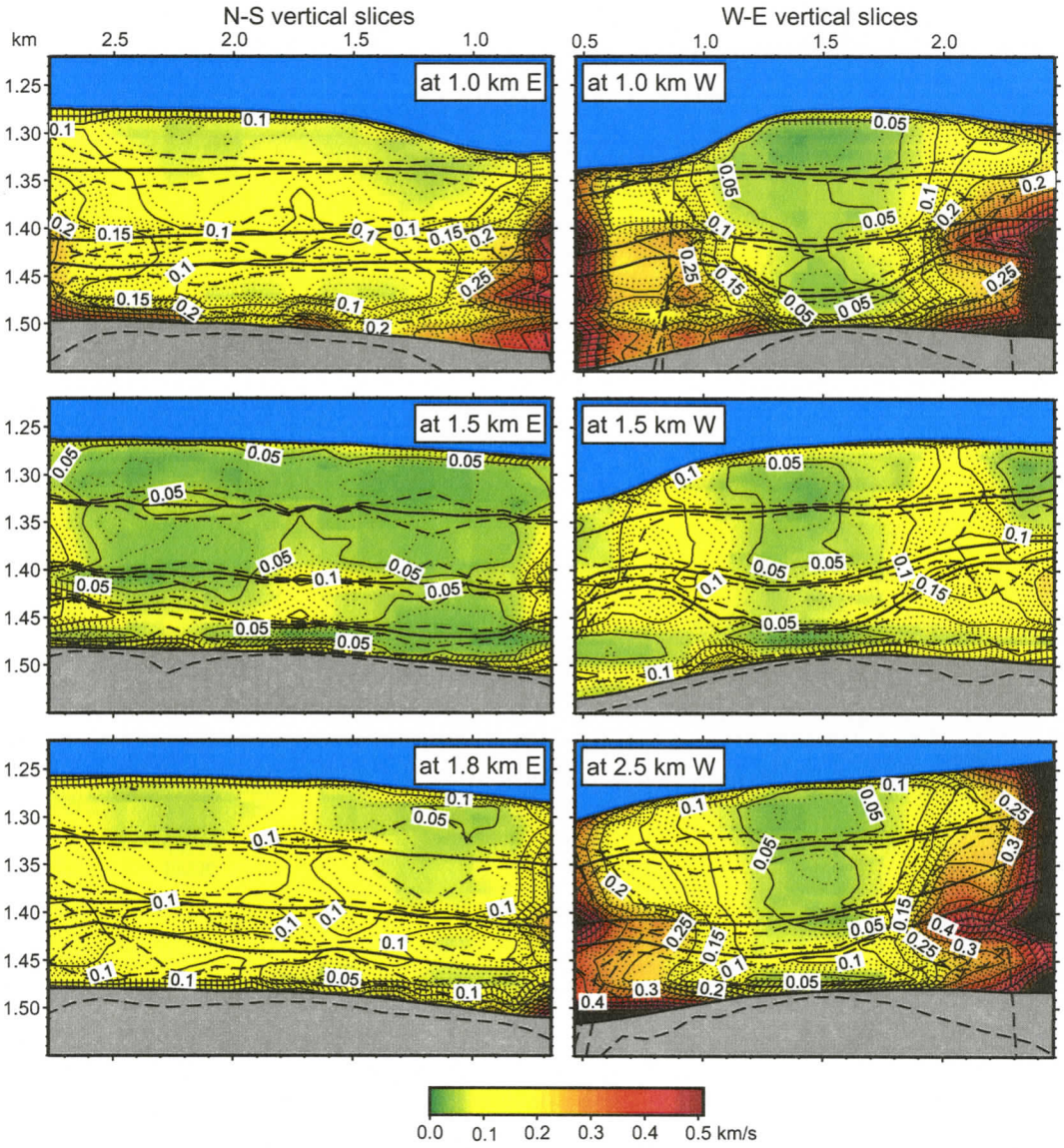

Figure 5.20: Vertical slices of uncertainty values for the final model. Thick solid lines show position of the interfaces. Thick dashed lines outlines uncertainty for the interface depth parameters.

Chapter 6

Amplitude analysis

6.1 Theory

When a plane wave reaches an interface at which acoustic properties change, a portion of the incoming energy is reflected back into the upper medium and the remainder is transmitted into the lower one. In addition, waves of different types are generated at the point of incidence (wave conversion). In the case of a P-wave with incident angle greater than 0° the following four waves are generated (see Fig. 6.1):

- reflected P-wave
- reflected S-wave (vertical polarization)
- transmitted P-wave
- transmitted S-wave (vertical polarization)

This is true only for a solid-solid interface. For liquid-solid boundary (e.g. the sea bottom) no energy is reflected as an S-wave, because S-waves cannot propagate in liquid phase media. In the simplest case of a wave at normal incidence, there is no wave phase conversion at the interface.

The angles of the propagation vectors for the waves with respect to the normal to the interface at the point of incidence satisfy Snell's law:

$$\frac{\alpha_1}{\sin\theta_0} = \frac{\alpha_1}{\sin\theta_1} = \frac{\beta_1}{\sin\psi_1} = \frac{\alpha_2}{\sin\theta_2} = \frac{\beta_2}{\sin\psi_2} \tag{6.1}$$

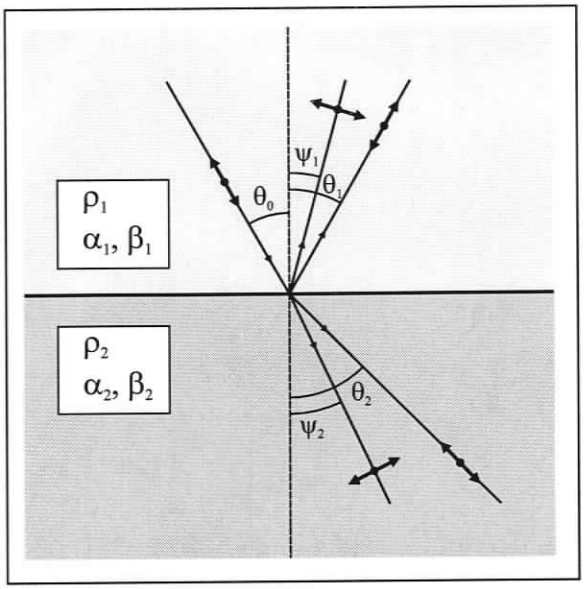

Figure 6.1: Reflection and refraction of an incident P-wave at a layer boundary.

where the index refers to the parameter either to the upper (1) or lower (2) half space, and α and β, and θ and ψ are the velocities and incidence angles of the P- and S-waves respectively. For waves of the same type, the incidence angle is equal to the reflection angle.

The amount of energy that is reflected back from the interface is defined by equation:

$$E_{rfl} = R \cdot E_0 \tag{6.2}$$

where E_0 is the incoming energy and R is the reflection coefficient for the specific wave phase. For the normal incidence geometry, the reflection coefficient is defined as:

$$R = \frac{\rho_2\alpha_2 - \rho_1\alpha_1}{\rho_2\alpha_2 + \rho_1\alpha_1} \tag{6.3}$$

where ρ is the density of the media and α is the wave propagation velocity. The product of density and velocity for the medium is called impedance. The physical meaning of the impedance is defined as a measure of the amount of resistance to particle motion (Aki and Richards, 1980).

The reflection coefficient becomes more difficult to estimate for incidence angles that are different from normal to the interface, as the amount of energy carried away from the reflection point by each type of wave depends not only on the media properties on each side of the interface, but also on the incident angle of the incoming wave. Zoeppritz in 1919 derived a set of equations, now commonly referred to as the Zoeppritz equations, that can be used to calculate the amplitudes and energy of the resulting waves (Yilmaz, 2001):

$$\begin{aligned}
A_1\cos\theta_1 + B_1\frac{\alpha_1}{\beta_1}\sin\psi_1 + A_2\frac{\alpha_1}{\alpha_2}\cos\theta_2 - B_2\frac{\alpha_1}{\beta_2}\sin\psi_2 &= A_0\cos\theta_1 \quad (6.4)\\
-A_1\sin\theta_1 + B_1\frac{\alpha_1}{\beta_1}\cos\psi_1 + A_2\frac{\alpha_1}{\alpha_2}\sin\theta_2 + B_2\frac{\alpha_1}{\beta_2}\cos\psi_2 &= A_0\sin\theta_1\\
-A_1\cos 2\psi_1 - B_1\sin 2\psi_1 + A_2\frac{\rho_2}{\rho_1}\cos 2\psi_2 - B_2\frac{\rho_2}{\rho_1}\sin 2\psi_2 &= A_0\cos 2\psi_1\\
A_1\sin 2\theta_1 - B_1\frac{\alpha_1^2}{\beta_1^2}\cos 2\psi_1 + A_2\frac{\rho_2\beta_2^2\alpha_1^2}{\rho_1\beta_1^2\alpha_2^2}\sin 2\theta_2 + B_2\frac{\rho_2\alpha_1^2}{\rho_1\beta_1^2}\cos 2\psi_2 &= A_0\sin 2\theta_1
\end{aligned}$$

where A and B are the amplitudes for the P- and S-waves respectively.

The exact solution for the amplitudes can be obtained by solving the system of linear equations (6.4). Figure 6.2 provides an example of the amplitudes for the reflected, transmitted and converted phases depending on the incident angle.

An exact solution exists for the amplitude of each phase. The following is an example of the P-to-P reflected wave (from Aki and Richards, 1980):

$$A_1 = \frac{\left[\left(b\frac{\cos\theta_1}{\alpha_1} - c\frac{\cos\theta_2}{\alpha_2}\right)F - \left(a + d\frac{\cos\theta_1}{\alpha_1}\frac{\cos\psi_2}{\beta_2}\right)Hp^2\right]}{D} \quad (6.5)$$

where

$$\begin{aligned}
D &= EF + GHp^2,\\
E &= b\frac{\cos\theta_1}{\alpha_1} + c\frac{\cos\theta_2}{\alpha_2}, \qquad F = b\frac{\cos\psi_1}{\beta_1} + c\frac{\cos\psi_2}{\beta_2},\\
G &= a - d\frac{\cos\theta_1}{\alpha_1}\frac{\cos\psi_2}{\beta_2}, \qquad H = a - d\frac{\cos\theta_2}{\alpha_2}\frac{\cos\psi_1}{\beta_1}\\
a &= \rho_2(1-2\beta_2^2p^2) - \rho_1(1-2\beta_1^2p^2), \qquad b = \rho_2(1-2\beta_2^2p^2) + 2\rho_1\beta_1^2p^2,\\
c &= \rho_1(1-2\beta_1^2p^2) + 2\rho_2\beta_2^2p^2, \qquad d = 2(\rho_2\beta_2^2 - \rho_1\beta_2^1),\\
p &= \frac{\alpha_1}{\sin\theta_0} \quad (6.6)
\end{aligned}$$

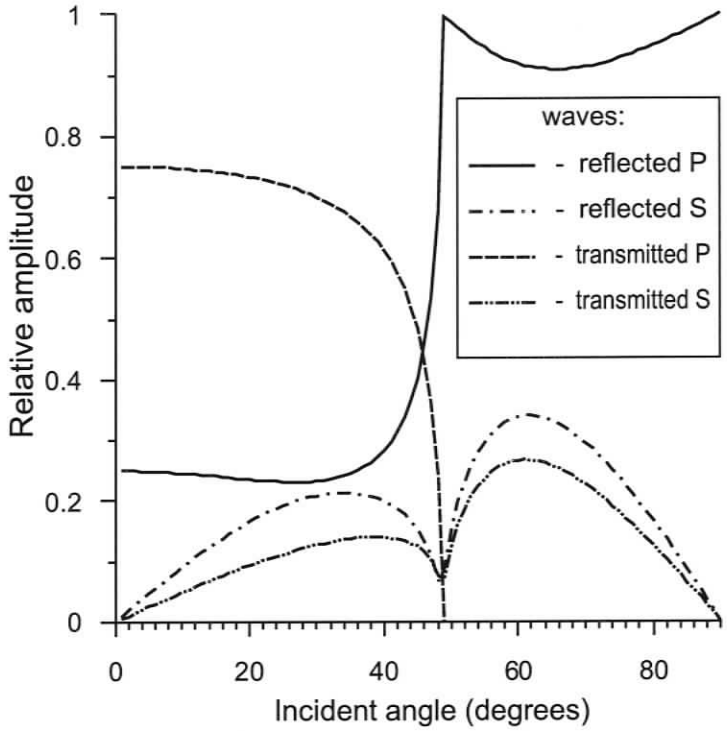

Figure 6.2: Incident angle dependence of the amplitudes of the outgoing ray phases. Media properties used in calculations: $\alpha_1 = 1500\ m/s$; $\beta_1 = 500\ m/s$; $\rho_1 = 2000\ kg/m^3$; $\alpha_2 = 2000\ m/s$; $\beta_2 = 800\ m/s$; $\rho_2 = 2500\ kg/m^3$;

The changes in the parameter values of the media alter the amplitude curve. However, changes of different parameters affect different parts of the curve (e.g., Riedel and Theilen, 2001). Therefore, by observing the variation of the reflection amplitude with the incidence angle it is possible to infer the acoustic properties of the media on the both sides of the interface. This method is called AVA (Amplitude Variation with Angle), or, since the true angle of incidence is usually unknown and is estimated using the offset between source and receiver, it is commonly referred to as AVO (Amplitude Variation with Offset).

The exact computation of the reflection coefficient requires many mathematical operations to be performed and analytical analysis is complicated. The first issue was important several decades ago, when the computational capabilities were limited and efficient solutions had to be found even at the expense of exactness.

To address the complexity problem, a number of approximations to the Zoeppritz equations were offered by different scientists (Aki and Richards, 1980; Shuey, 1985, etc.). In addition to not being exact, the approximate solutions have certain limitations, such as the maximum incident angle, maximum or minimum parameter

contrast, and others.

In this study the choice was made in favor of the exact solution and Equation 6.5 is used for forward modelling of the amplitude of the reflected P-wave.

6.2 Amplitude data processing

Before the amplitude analysis can be performed, a number of issues have to be addressed. They refer to the preparation of the seismic data for the amplitude analysis, actual amplitude picking, and post-picking amplitude data processing.

6.2.1 Amplitude recovery

Seismic data preparation

While preparing the seismic data for amplitude analysis, it is important to preserve true amplitude relationships (Yilmaz, 2001). Therefore, the processing steps were kept to a minimum:

1. Resampling with 0.5 ms sampling rate
2. Time correction to flatten the first arrival
3. F-K filtering

The Nyquist theorem states that during the conversion of the analog signal to a digital form with sampling frequency f_{smpl}, frequency components up to $f_{smpl}/2$ are preserved. That is, two signals, analog and its digitized version, will be equal in the frequency domain for frequencies less than $f_{smpl}/2$. In the time domain, the waveform has to be restored using the individual samples.

The waveform reconstruction is usually done by fitting a spline function to the existing data samples followed by re-sampling of the function at a greater sampling rate. The standard resampling routine in the CLARITAS seismic package utilizes quadratic spline. Figure 6.3 provides an example on how resampling affects a waveform.

The resampling procedure does not and cannot add new information. Both original and resampled signals are identical in the frequency domain, but it does approx-

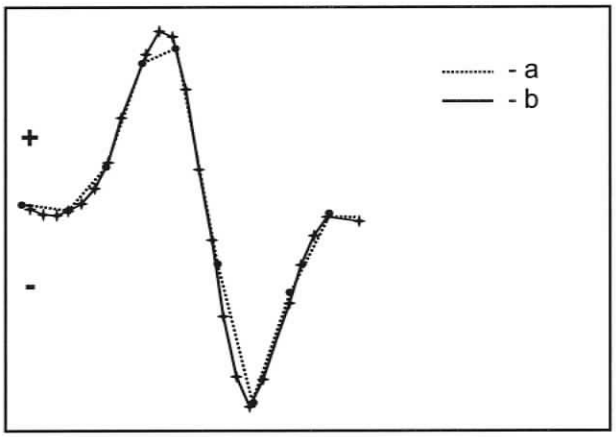

Figure 6.3: Recovery of the wave shape through resampling using cubic spline. a - original data (1.433 *ms* sampling rate); b - signal resampled with 0.5 *ms* sampling rate; Note the difference in the maximum amplitude for the positive peak.

imately reconstruct the original form of the analogous signal in the time domain.

In a data set with many traces, the average value of the maximum amplitude for the first break should increase with the increase of the re-sampling rate, as the samples will interpolate the peaks more closely. The value for the new sampling rate was determined empirically. The traces with original 1.43 *ms* sampling time were resampled at a series of smaller sampling times and maximum values of the samples were picked for the same arrival. The choice was made in favor of the frequency after which no significant change of the amplitudes was observed (Table 6.1).

Table 6.1: Average peak amplitude change for the restored signal with the change of the resampling rate.

Sampling time	1.433	1.00	0.75	**0.50**	0.25
% change	0	-0.2	2.5	0.32	0.33

The choice was made in favour of 0.5 *ms* sampling time.

The F-K filter tool was used to suppress the bubble pulse signal. The chosen filter was successful in significant reduction of the bubble pulse amplitudes on the seismic sections, while only slightly affecting the usable seismic events. The greatest degree of amplitude corruption due to application of the filter occurred for the shots with the smallest offset. This fact was taken into consideration in the subsequent analysis. The filter was applied only when picking amplitudes of the reflected signal. The amplitudes of the direct water wave arrival and its water column multiple were

picked using original seismic traces.

Amplitude picking

The amplitude picking was performed in a semi-automatic manner.

A software program was written for the automatic part. Seismic traces in *SeismicUnix* format were provided for the input, along with the file containing the list of trace numbers and time of a particular event (the arrival times used for travel time tomography). The program then looked for a maximum (or minimum, in case of the BSR) amplitude value in the specified time window around the time of the event, outputting the amplitude and actual time of the picked sample.

After that a manual sifting of the picked data samples was performed to reject bad data samples. The times of the amplitude picks were plotted on top of the seismic section and the quality of picking was evaluated. The data samples for which the amplitude was believed to be corrupted by interference of two events or by other means were eliminated from the data set.

Binning of data samples

The picked amplitudes, when plotted against offset or angle, represent a cloud of points. However, for the purpose of amplitude analysis, it is more convenient to operate with a discrete representation of data with an assigned uncertainty for the value of each element.

In order to obtain a single curve, an amplitude binning procedure was performed. It consisted of two steps. First, the X-axis was divided into bins of constant offset width and the mean amplitude value and standard deviation were calculated for data points in each bin. Second, the data samples that did not fall within the two standard deviations around the mean value (the so called "outliers") were removed from the data set and a new average value and standard deviation were obtained. Average amplitude values were then assigned to the center of bins and the standard deviations used as uncertainties for the values. For the cases for which the number of points in a bin was too small (< 5), which led in some cases to insupportable small

uncertainty, the uncertainty value was taken from the adjacent bin. An example of the initial data and the result of data sample binning is shown in Figure 6.4.

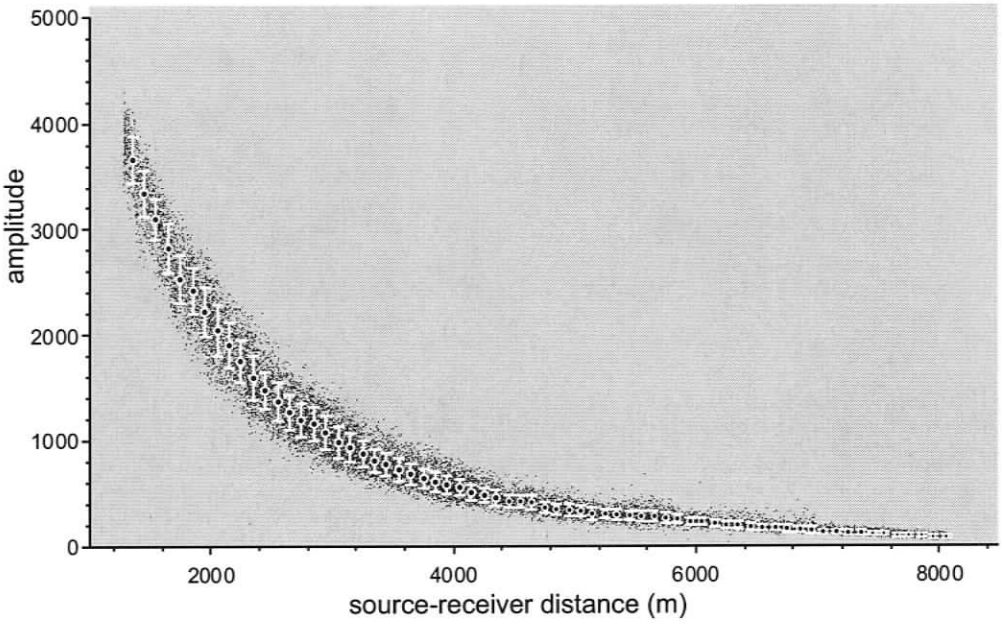

Figure 6.4: Example of the initial amplitude data and the result of binning. Amplitudes (uncorrected) of the direct water wave for OBS F are shown

The binning procedure served several purposes. First of all, it reduced the number of data points and provided simplified amplitude versus offset function. Second, it worked as an averaging operator. Third, and probably most important, it allowed evaluation of the uncertainty for the data points of the amplitude curve.

The size of the bins has to be chosen carefully. On one hand, it must be big enough that the number of points in each bin is sufficiently large to obtain legitimate statistical results; on the other hand, it must be small enough to represent the variations of the amplitude properly.

For this study, in case of variation with offset, the size of a bin was chosen to be 100 m; for the variation with angle, the data samples were averaged over 2° bins.

Amplitude correction for spherical spreading

We first assume that the airgun is a point source, so seismic energy propagates as a spherical wave through the body of the media. The area of the the wave front increases with distance from the source proportionally to R^2; therefore the energy delivered to a point depends inversely on the square of the distance. The wave amplitude is related to the energy density as the square root; thus, in theory, the decay of the wave amplitude is proportional to $1/R$.

For conventional seismic surveys, the distance travelled by a particular ray is usually not known and is estimated using travel time, so that the amplitudes are corrected for the geometrical decay by multiplying by the time of the arrival. For the work in this thesis ray paths were estimated using the ray tracing technique, and the actual path lengths were used to derive corrections for spherical spreading.

In order to verify how the theory corresponds with the observations, the corrections were applied to the amplitudes of the direct water-wave arrival event (Fig. 6.5) for which spherical spreading should in principle produce the only amplitude variation. OBS F was chosen for the test since all others experienced amplitude clipping of the water-wave arrival for the near-offset shots.

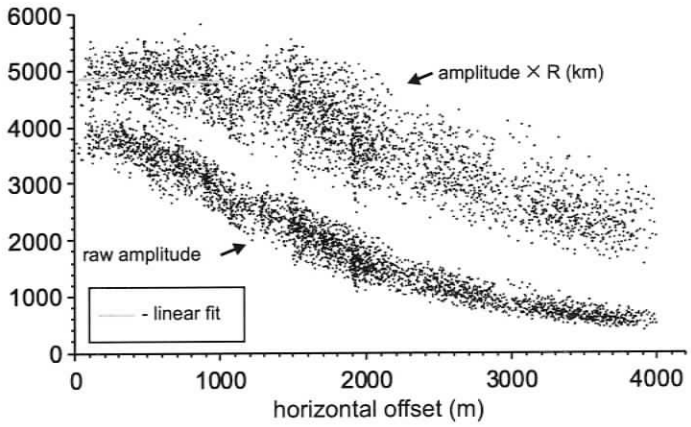

Figure 6.5: Amplitude correction for spherical spreading. Direct arrival recorded by OBS F used. Correction was done by multiplying the picked amplitudes by the ray path lengths in km. Note the linear fit of the corrected amplitudes is nearly flat for the shots with horizontal offset less than 1000 m

As can be seen in the figure, the amplitudes are fully corrected for the shots with horizontal offset less than 1000 m (emerging angles $< 33°$) and under corrected by less than 5% for the shots closer than 1500 m to the station (emerging angles at the

source $< 50°$). It is clear that for the shots with greater horizontal offset other means of correction are required, for example, correction for the interaction of the source impulse with its sea-surface ghost (Papenberg, 2004). Since the emerging angles of most of the rays used in the amplitude studies were less than 50°, the decision was made that the simple correction for distance was satisfactory and the rays with emerging angles greater than 50° had to be excluded from the calculations. The offset limit varied for different ray phases depending on the depth of the reflection point and the dipping angle of the reflector.

As the seismic source was a single air-gun and the receiver was a single hydrophone, it was assumed that no additional correction was required for the source or receiver directivity.

6.2.2 Source signature stability

The quality of any analysis depends on the quality of the input data. For the AVA studies it is important to eliminate or suppress any other variations in the signal amplitude other than those influenced by the parameters of the media. Instability of the seismic source signature is one of the amplitude noise factors that contributes to the uncertainty in the amplitude data. The effort was made to isolate and subtract the variation of the source impulse energy from the amplitude readings used in the AVA analysis.

As described in section 3.1.1, the waveform of the initial impulse was recorded using a hydrophone placed in close proximity to the air-gun. Unfortunately, the portions of useful seismic recordings for this hydrophone were available only for the last two track lines recorded by the OBSs. Nevertheless, this overlap in the records made it possible to evaluate the overall consistency in the source impulse amplitude.

First of all, the amplitude of the positive and negative peaks were picked using the automated picker that searched for a maximum/minimum sample value in a specified time window. As the time of the first break recorded by the shot point hydrophone was approximately the same for the entire survey (± 2 ms) and the event was not

corrupted with other events, the manual sifting of the data values was not required.

The amplitudes were plotted versus shot number (Fig. 6.6a and b). The clouds of points representing different profiles are visibly separated on the graphs by a gap, as the recording of the signal from the hydrophone was stopped as the ship advanced to the next seismic line. The wider gap marks the time when the gun was pulled out for service.

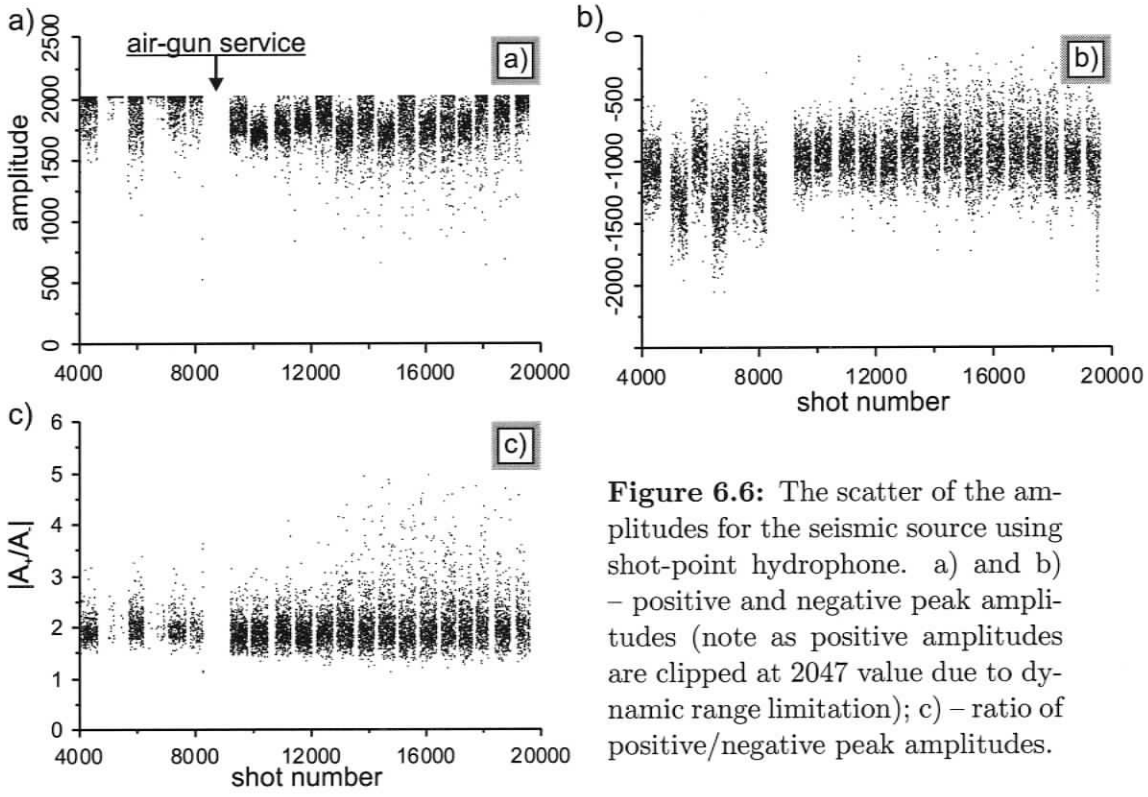

Figure 6.6: The scatter of the amplitudes for the seismic source using shot-point hydrophone. a) and b) – positive and negative peak amplitudes (note as positive amplitudes are clipped at 2047 value due to dynamic range limitation); c) – ratio of positive/negative peak amplitudes.

Since the analog signal from the shot-point hydrophone was digitized with a 12-bit dynamic range, the positive peak of the wavelet for approximately 20% of shots was clipped due to the high gain setting for acquisition and recording systems.

Statistical analysis showed that the mean value of the negative amplitude for different track lines varied by ~15–20%, while the standard deviation of the amplitude for the shots of a single track varied by about 10–15%. For further investigation, the absolute value of the ratio of maximum and minimum amplitudes for each shot was calculated (Fig. 6.6c). Only those shots for which neither peak was clipped were

included into calculations. The overall mean value for that ratio was estimated to be 2.04 with a standard deviation of 60%, which indicates a rather large dispersion.

Two processes were suspected to contribute most to the measured amplitude variation of the initial impulse. These are: the actual variations in the impulse due to inconsistency in the gun firing, and variations due to change of the relative position of the hydrophone and gun. The latter case can be explained by the fact that for each point in close proximity to the source there is a different degree of interference between the direct wave and the wave reflected from the sea surface. Hence, the signal is different if measured at different points even if the measurements are taken for the same shot.

In order to investigate the problem, the variation of the amplitudes recorded by the shot point hydrophone were compared to the variations in the signal for the direct water wave arrival recorded by OBSs (more details on the direct water wave arrival are provided in the next section). The comparison was done by calculation of the cross-correlation function. The distinctive peak in the cross-correlation function was observed for zero lag, i.e., when the amplitude sequences were aligned with the same shot numbers corresponding to each other. The average correlation coefficient was calculated 0.37.

That is, some degree of correlation in the amplitude variation for the signals recorded in the close field and in the far field was revealed, providing evidence that the signal recorded by the shot-point hydrophone can be used for corrections for the variation of the amplitude of the initial source impulse.

Unfortunately, this could not be implemented in this study, since the shot-point hydrophone recordings were available only for the last two seismic lines recorded by OBSs. Also the fact that the some amplitudes were clipped significantly degraded the value of the data provided by the shot-point hydrophone. However, the available data gave important information on the average variation of the amplitude of the initial pulse.

6.3 Direct water-wave arrival

Among all the events recorded on the seismic sections, the direct water-wave is the signal least affected by the propagating medium. The analysis of this signal can provide estimations on source signature instability (also discussed earlier).

The amplitude of the first break was picked for all available shots recorded by all five OBSs. Then the bin average values were plotted against the distance between source and receiver (Fig. 6.7).

The figure shows that despite the fact that gain was set the same for all OBSs, the effective gain was different for OBS C and F. The actual origin of this phenomenon is unknown. OBSs A, B, and E give almost identical curves.

As mentioned before, the amplitudes were clipped at a value 32,768 due to 16-bit digitizing limitation. Nevertheless, the curves extend higher than that value because the amplitudes were picked on the resampled seismic traces. Having the higher gain, OBSs A, B, and E suffered the most from clipping and the direct water-wave signal is not usable for the amplitude analysis from the shots with the offsets less than 2.1 km. Due to lower gain, more shots data can be used for OBS C, but unfortunately the most important near zero-offset shots have to be excluded. Fortunately, the gain for OBS F was low enough to provide unclipped amplitudes for shots over the entire range of offsets.

In order to estimate the similarity of the amplitude variation in the signals recorded by OBSs, the cross-correlation functions were obtained for each possible pair out of 5 OBSs. All shots that were available simultaneously for each OBS and for which the signals were not clipped at either station were used in the calculations. The correlation functions had very distinctive maximum peaks at the zero lag. The correlation coefficients are presented in Table 6.2.

The coefficients indicate that an overall moderate level of correlation (according to the scale provided by Franzblau (1958)) is present between the signals. The only source of variations that can influence all OBS simultaneously in the same manner is the seismic source, and the analysis demonstrates that it contributes to the overall

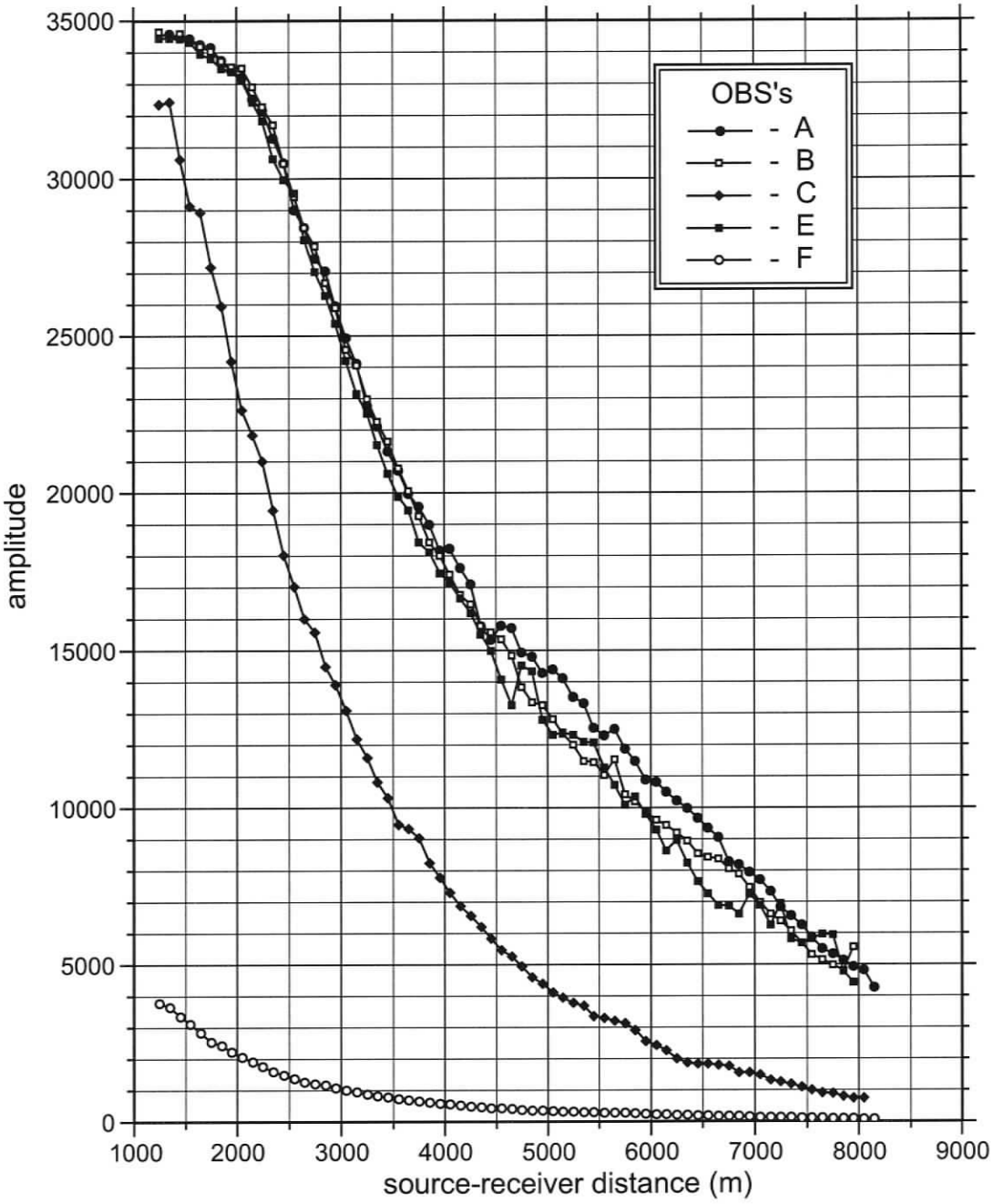

Figure 6.7: Direct water-wave amplitude variation with distance. Bin average values plotted (bin size 100 m).

Table 6.2: Correlation coefficients of the direct water-wave arrival amplitudes for each OBS pair.

	A	B	C	E	F
A	1	0.69	0.46	0.51	0.32
B	0.69	1	0.52	0.52	0.41
C	0.46	0.52	1	0.38	0.56
E	0.51	0.52	0.39	1	0.25
F	0.32	0.41	0.56	0.25	1

amplitude variation.

It may be possible to localize and suppress the amplitude noise due to source signature instability. For that a correction coefficient was calculated as a ratio of the amplitude of the direct arrival to the average value of the bin it falls in. This was done for each shot and for each OBS separately and averaged over five OBSs producing one correction value for each shot. These coefficients, assigned for each shot, were used to correct other reflection amplitudes picked for later events in the subsequent processing.

6.4 Sea bottom reflection coefficient

The analysis of the sea bottom reflection coefficient provides a means to study the spatial variation of acoustic properties for the sediment immediately below the seafloor. It can be useful considering the fact that these sediments may be influenced by the physical and chemical processes that take place deeper in the section, such as gas seepage due to gas hydrate dissociation.

6.4.1 Bottom reflection coefficient using near normal incidence rays

The OBS survey geometry is not able to provide a primary bottom reflection as the sensor sits virtually on the seafloor. Thus in this study, the amplitude of the direct water-wave was compared with the water column multiple signal that was reflected from the seafloor and then from the sea-surface (Fig. 6.8).

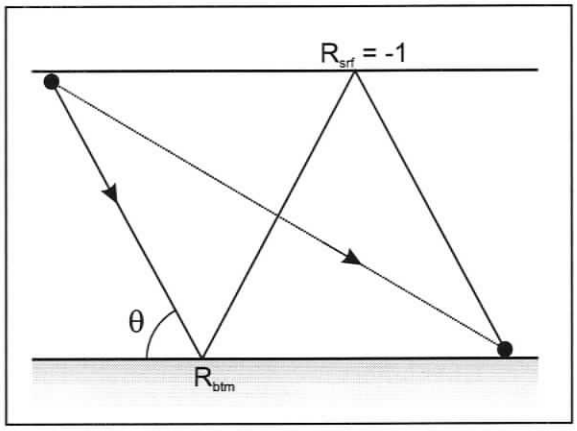

Figure 6.8: The paths of the rays used in evaluation of the sea bottom reflection coefficients. Perfect reflection was assumed at the sea surface with phase reversal ($R_{surface} = 1$).

The amplitude of the direct water-wave (A_{direct}) can be expressed as the initial amplitude of the impulse at the source multiplied by the decay function with distance ($D(d) = 1/d$), while the expression for the amplitude of the multiple (A_{mult}) takes more complicated form, as it is also depends on the reflection coefficients at two points of reflection:

$$A_{direct} = A_0 D(d_{direct}); \quad A_{mult} = A_0 R_{btm} R_{srf} D(d_{mult}) \tag{6.7}$$

If the ratio of the two amplitudes is taken, the amplitude of the initial impulse is eliminated from the equation. The decay of the amplitude due to spherical spreading is corrected using a coefficient that depends on the distance travelled by the signal. Finally, the reflection from the sea surface is assumed to be perfect with a phase reversal, that is $R_{srf} = -1$. Thus, the reflection coefficient of the bottom can be found using the following expression:

$$R_{btm} = -\frac{\tilde{A}_{mult}}{\tilde{A}_{direct}} \tag{6.8}$$

where $\tilde{A}$ is an amplitude of the corresponding arrival corrected for the spreading loss.

It is obvious that to provide reliable results the amplitudes must not be clipped, and therefore only data from OBS F were suitable for these calculations.

For this analysis, individual data samples were used. The amplitudes for the direct water-wave and water column multiple were plotted against horizontal offset of the source from the receiver, and then the ratio of the amplitudes for each shot was calculated separately (Fig. 6.9)

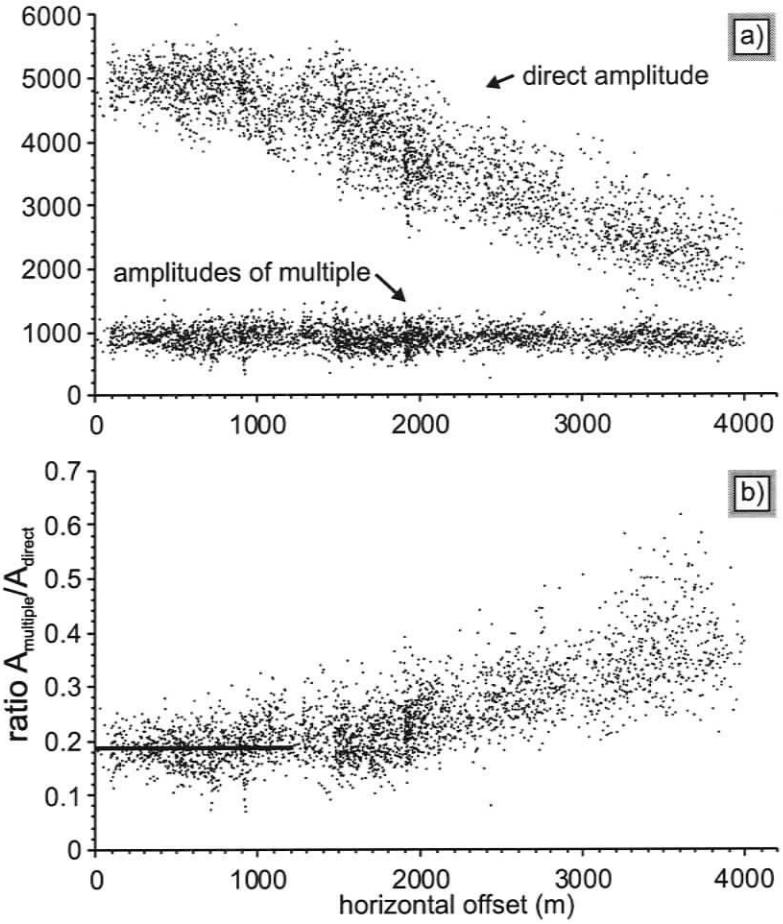

Figure 6.9: Amplitudes for the direct water-wave and water column multiple (corrected for spherical spreading).

The average value of the sea bottom reflection coefficient was estimated using information from the shots with horizontal offsets less than 1000 m. For the offset range chosen, the effect of the source directivity and AVA for the bottom reflection is negligible (less than uncertainty in the bin). The reflection coefficient was calculated to be 0.19 with a standard deviation of 0.035. This value is typical for the soft sea bottoms and corresponds well with previous studies of the site (Riedel, 2001).

The selected rays sampled the bottom in a circular area about OBS F with an approximate radius of 660 m (2/3 of 1000 m).

Table 6.3: Average amplitudes for the water column multiple (corrected) and scaling factors for each OBS.

OBS	average amplitude	scaling factor
A	51 844	$3.664 \cdot 10^{-6}$
B	51 844	$3.674 \cdot 10^{-6}$
C	14 321	$1.327 \cdot 10^{-5}$
E	56 172	$3.382 \cdot 10^{-6}$
F	910	$2.200 \cdot 10^{-4}$

6.4.2 Amplitude scaling and AVA curves

While it was not possible to perform the calculations of the bottom reflection coefficient for each OBS, the ability to do this for at least one was very helpful. The assumption was made that the average reflection coefficient for the seafloor in the vicinity of each OBS, after removing anomalous areas (discussed later), is the same. Therefore, the amplitudes for other OBSs can be scaled accordingly. Table 6.3 provides the calculated scaling factors for each OBS. The scaling factors are used to convert recorded amplitudes to reflection coefficients. Again, only shots with the horizontal offset less than 1000 m were used.

The scaling of amplitudes is very important, since it allows us to work not with some relative values, but in terms of the reflection coefficients. The amplitude samples for each OBS were scaled accordingly and the resultant AVA curves (with binning applied) are plotted for comparison in Fig. 6.10a.

As expected, the curves match each other very well since the reflection points cover the same area of the sea bottom. This fact supports the merging of the data from different OBSs as a legitimate step in data processing. Thus, a single average AVA curve for the site area was plotted using all samples from all five OBSs (Fig. 6.10b). This average curve represents an average response of the seafloor and its analysis can give average values for the properties of the bottom sediments. Furthermore, the comparison of individual data points with the average values helps in the identification of anomalous areas.

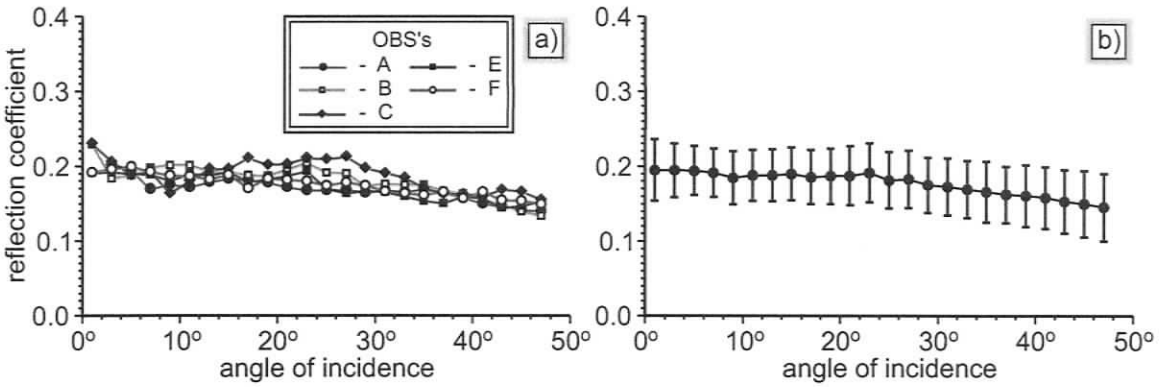

Figure 6.10: AVA curves for the sea bottom reflection in absolute values of reflection coefficient for each OBS separately (a) and averaged (b).

6.4.3 Reflection coefficient map

A map of reflection coefficients was created based on the individual amplitudes samples using data from all five OBSs. The positions of the reflection points for water column multiples were estimated using a ray tracing program with the actual bathymetry information (Fig. 6.11). The use of the ray tracing program allows more exact estimation of the bottom region sampled by the ray. It is especially true for the areas with variable bathymetry. By combining data for several receivers the density of the data points is increased, which, in turn, increases the reliability of the results and resolution.

The raw amplitudes of the multiples were transferred into reflection coefficients using the scaling factors (Table 6.3). In order to bring the amplitudes for the rays with different angles of incidence to normal incidence, the correction was made according to the average AVA curve for the seafloor reflection (Fig. 6.10b). The range of seafloor incidence angles used for the analysis is from 0° to 30°. For these angles the AVA function is relatively flat. The map is presented on the Figure 6.12a. It provides the distribution of normal incidence reflection coefficients over the site.

In order to help to distinguish the variation of the reflection coefficient due to changes in sediment properties from possible variation due to bathymetry features,

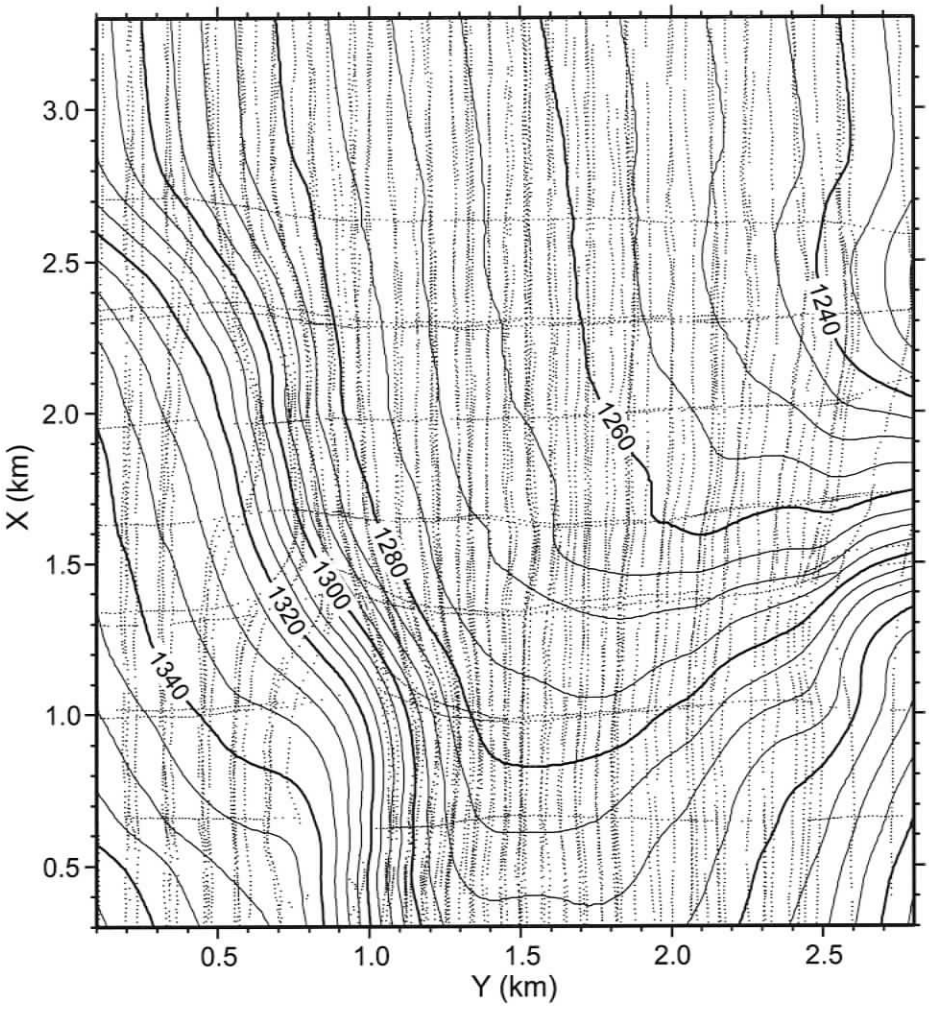

Figure 6.11: Reflection point positions for the data used in creation of the seafloor reflection coefficients map. Bathymetry is shown on background (in meters of water depth).

the same map was plotted over the bathymetry (Fig. 6.12b).

Based on the reflection coefficient, the seafloor around the site can be divided into

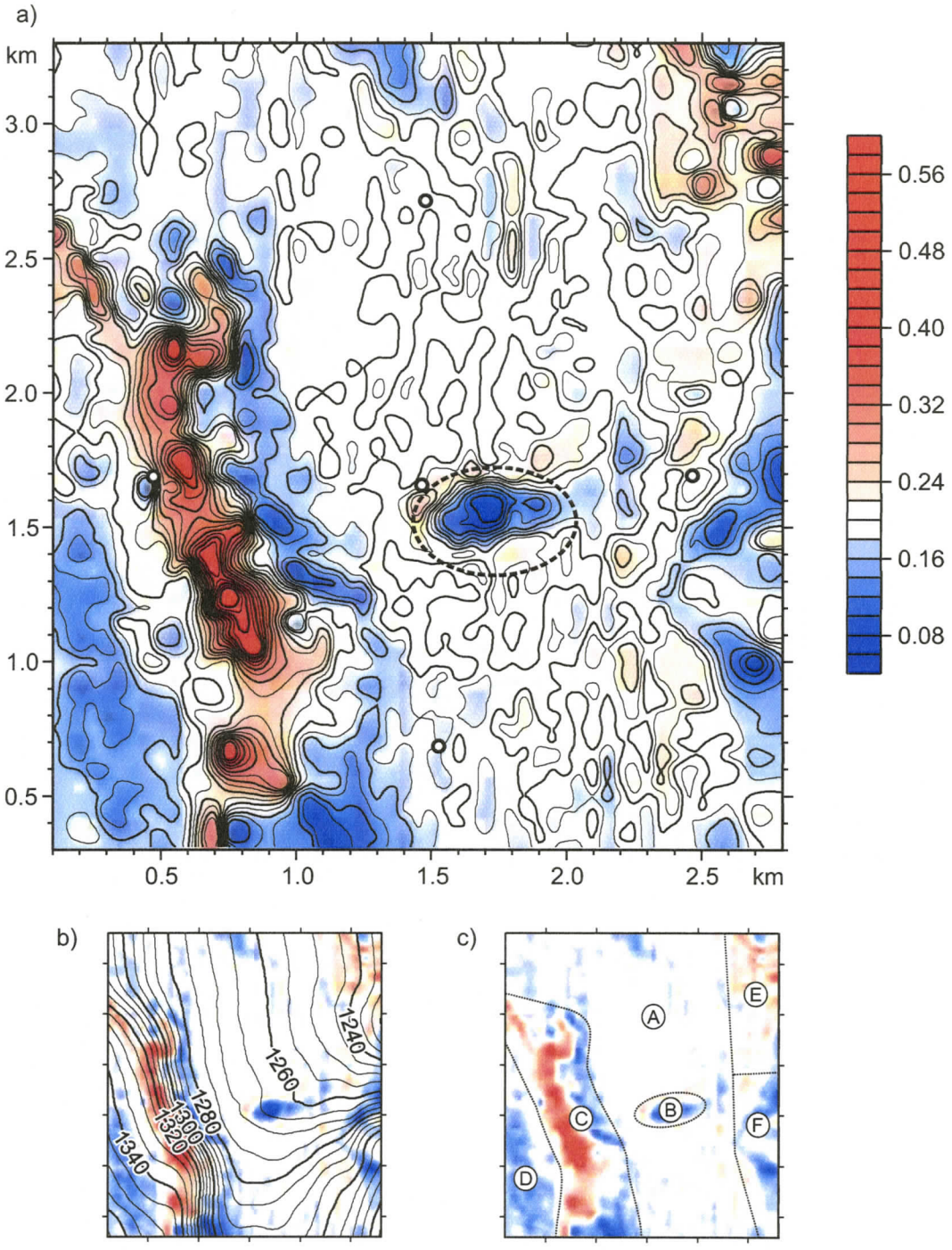

Figure 6.12: Seafloor reflection coefficients map (a) with OBS positions indicated (dashed line shows the limits of the Bullseye blank zone), same map over the bathymetry information (b) and zonation of the seafloor based on the reflection coefficient information (c).

6 regions (A to F) (Fig. 6.12c):

A. Uplifted sediment block (0.18–0.24)

B. Blank zone

C. High slope angle area

D. Depression (less than 0.20)

E. Topographic mound (0.20–0.28)

F. Edge of the slope (0.14–0.22)

The largest region (A) is characterized by the values of reflection coefficient in the range of 0.18–0.24. It is a nearly flat area with a small slope (less than 1.5°). The variation of the reflection coefficient is also small. Inside this area, there is an elliptical feature (B) associated with the blank zone. The central part of it is represented by a strong negative anomaly (up to 0.05). The margin of the negative anomaly coincides with the limits of the blank zone. The outer part is characterized by higher than average values for the reflection coefficient (0.20–0.26) forming a high amplitude rim (zoomed in map for zone B is shown in Fig. 7.8).

A highly anomalous region C is represented by strong positive and negative anomalies. Together with regions E and F, it is believed to be mostly an effect of bathymetry, due to focussing and defocussing of acoustic energy. The negative features are related to concave sections of the sea bottom, and positive features with convex parts of it.

Finally, region D shows lower values of reflection coefficient than in region A and is associated with a depressed area of the seafloor. Here, the reduced seafloor reflection coefficient most likely represents softer less compacted sediment material in the first few meters of the sediment columns, compared to elevated areas.

In general, the map provides greater details than the previous results for the site produced using the single channel seismic data (Riedel, 2001). Higher resolution is achieved due to more dense population of the data points and better localization with ray tracing. In particular, the low reflectivity anomaly is outlined better and a higher reflectivity rim is revealed around it.

6.5 AVA modelling

As discussed earlier, the AVA function depends on the properties of the media on both sides of the interfaces. Therefore, by modelling this curve it is possible to estimate P- and S-velocities and density of the sediments above and below the interface.

6.5.1 AVA inversion technique

The inversion of the AVA data is a non-linear and nonunique problem (Riedel et al., 2003). There are a number of different methods of modelling the amplitude data, including manual curve fitting, grid search over the range of the parameters, and linearized techniques. For this study a nonlinear Bayesian approach using Gibbs sampling procedure was chosen. This approach was implemented in the code written by Dr. Stan Dosso.

Bayesian inversion by Gibbs sampling is an efficient method for solving strongly non-linear inversion problems. It allows the user to include *a priori* information into the inversion (e.g., the expected range for the parameters). Finally, it provides the uncertainty values for the inverted parameters (Riedel et al., 2003).

The model parameters are treated as random variables for the Bayesian approach. All parameters are repeatedly and randomly perturbed, and a new model is subject to acceptance based on the specific rule that incorporates the data fit. Two independent populations of accepted models are collected. The difference between the cumulative marginal probability distributions for all parameters of this two populations is a criterion for the convergence. The union of the two independent samples is taken as a final result (Dosso, 2002).

The results of the inversion are usually presented as marginal probability distributions for each model parameter. The credibility intervals for the solution are determined by the boundaries of the narrowest window that incorporates 95% of all samples. If the distribution is asymmetric, so are the credibility intervals around the maximum a posteriori (MAP) value that represent the model with the best fit to the input data.

Inversion consideration

It is very important to consider the limitations of the inversion method in order to understand its ability to resolve specific parameters, and the quality of the results.

Numerous tests performed on synthetic data revealed that it is more practical to solve for the absolute value for a property in the upper media and for a contrast of that property at the interface, rather than for two absolute values for each half space. This follows from the fact that media velocity parameters are included into the Zoeppritz equations (6.4) as ratios in different combinations.

If the values are not held constant, the upper half space parameters, either P-wave velocity or density, usually are poorly constrained, due to the non-unique nature of the impedance problem. However, the tests showed that acceptable results can be achieved for S-wave velocity, since both the value in the upper half space and the contrast at the interface are fairly well resolved.

The value of the contrast for a property plays a significant role in the quality of the results. A larger P-velocity contrast decreases the value of the critical angle; therefore, even with the limited range of available angles of incidence, it is possible to reach the sub-critical angles which provide better constraints on the P-velocity contrast, which, in turn, gives better results for density contrast recovery. However, large contrasts are not expected when working inside uniform sediment section.

6.5.2 AVA inversion for the sea bottom interface

The strategy differs for the sea bottom interface, since the properties are well known for the upper media (water), compared to that for a boundary inside the sediment section, where properties of both half-spaces are unknown and have to be inverted.

The water velocity was fixed at 1481 m/s, according to the water velocity profile (Fig. 3.6). The density for the water was set at 1029 kg/m^3. No S-wave propagation was allowed in the water ($V_s = 0\ m/s$).

The results of Bayesian inversion for the average properties of the sea bottom at the site are presented on Figure 6.13 and Table 6.4

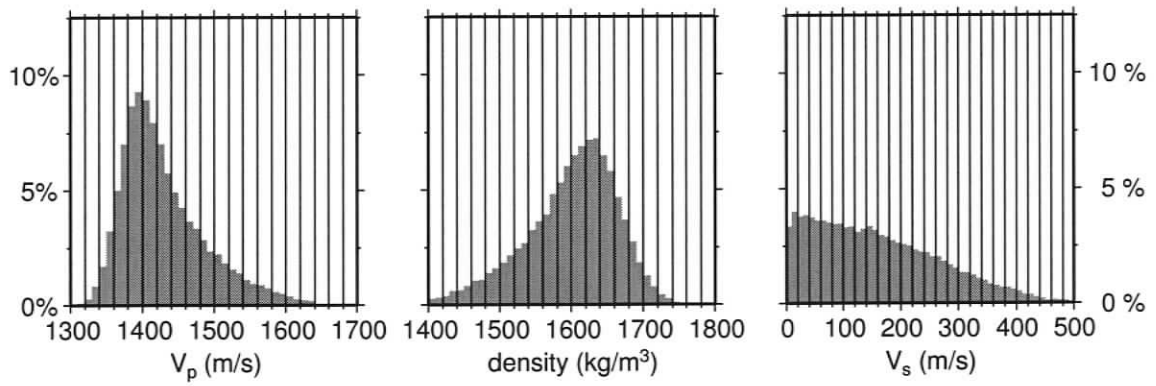

Figure 6.13: Marginal probability distributions from inversion of the AVA data for the sea bottom interface.

The probability distributions are asymmetrical with respect to their medians, and the distributions for P-wave velocity and density are mirror images symmetrical to a certain degree with respect to each other. The latter is the result of the inverse correlation between these two parameters in terms of the AVA curve modelling (discussed earlier). The S-wave velocity distribution has no well determined peak, although the tendency is for lower values.

Table 6.4: Prior bounds and inversion estimates with the 95% credibility intervals for the AVA sea bottom data.

	$V_P\ (m/s)$	$V_S\ (m/s)$	$\rho\ (kg/m^3)$
Lower bound	1300	0	1400
Upper bound	1700	500	1800
Results:			
MAP	1381^{+170}_{-40}	2^{+360}_{-1}	1650^{+60}_{-190}
Mean	1429 ± 116	158 ± 210	1600 ± 126

Both MAP and mean values for the P-wave velocity give a value that is lower than the P-wave velocity in the water. This can be explained by two reasons: (1) the uncertainty for the results of the method is large and the expected value for the the compressional wave velocity of the near bottom sediments still falls well inside the confidence interval for the results; (2) the compressional wave velocity in the sediments is lower than in the water due to high porosity.

The resultant density for the bottom sediments corresponds well with the direct measurements conducted on samples retrieved by piston cores at the site (Novosel, 2002). The density varies in the range from 1450 kg/m^3 to 1650 kg/m^3 for the samples from the top 5 m of the sediment column.

There are no previous measurements or estimates of shear-wave velocity available for the site, yet it is expected to be low as the sediments immediately below seafloor are not compacted enough to provide great shear strength. Reasonable values for shear-velocity for near bottom silty-clay and clay sediments are about 100–150 m/s (Hamilton, 1980) and the results of the inversion are consistent with the expected velocity range.

As an option, an attempt was made to do the inversion with fixed compressional wave speed for the sediments at 1485 m/s. This value was chosen according to the tomography results and also based on direct measurements from the sediment cores (Mi, 1998). The estimates for the shear wave velocity and density for this case are presented on Figure 6.14 and Table 6.5.

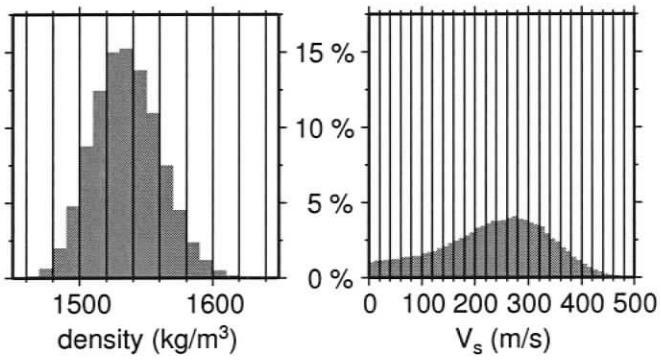

Figure 6.14: Marginal probability distributions from inversion of the AVA data for the sea bottom interface with P-wave velocity in the sediment fixed at 1485 m/s.

	V_S (m/s)	ρ (kg/m^3)
Results:		
MAP	270^{+122}_{-260}	1538^{+46}_{-52}
Mean	233 ± 202	1535 ± 50

Table 6.5: Inversion estimates for the AVA sea bottom data with P-wave velocity in the sediment fixed at 1485 m/s.

The estimate for density is lower, but still corresponds well with the results obtained by other methods. The S-wave velocity is higher than the expected values for this type of sediments (see above).

6.5.3 AVA inversion for the BSR

Inversion considerations

It is now widely accepted that the BSR is produced by a thin layer of definite thickness with a large negative gradient of P-wave velocity, rather than by a sharp change at the interface. The thickness of the BSR producing layer in the site area is estimated at 4–8 m (Chapman et al., 2002). It is from this fact the frequency dependence of the BSR response originates. It was noted in numerous studies that the BSR has higher amplitude and is more prominent on the seismic sections obtained using low frequency sources (40–50 Hz). For higher frequency sources (100–250 Hz), the BSR appears weaker and can almost disappear for even higher frequency sources (250–450 Hz) (Papenberg, 2004).

The higher frequency signal has higher vertical resolution, and hence it samples only a portion of the total velocity change at the BSR resulting in lower effective compressional wave velocity contrast. The maximum response is achieved when the layer thickness is equal to the tuning thickness or 1/4 of the dominant wavelength (Fig. 6.15).

For the data used in these studies the dominant frequency is 150 Hz, which gives a tuning thickness of 3 m. The expected amplitude of the BSR reflection, according to Figure 6.15, would be 30–80% of the maximum possible, because the seismic wave samples only a portion of the BSR producing layer.

The density of the medium at the BSR is not expected to change significantly. The density of pure gas hydrate is slightly less than water, and the presence of free gas below the BSR in small amounts cannot provide significant decrease in bulk density of the sediments. Therefore, during the inversion the density ratio was fixed at unity (no change).

In order to obtain reliable results, the modelling should be done using the amplitude data from the seismic sections where the BSR event does not interfere with other reflections. Accordingly the AVA inversion was performed only for the data recorded by OBSs A and C. In the vicinity of these stations the BSR lies inside the accreted

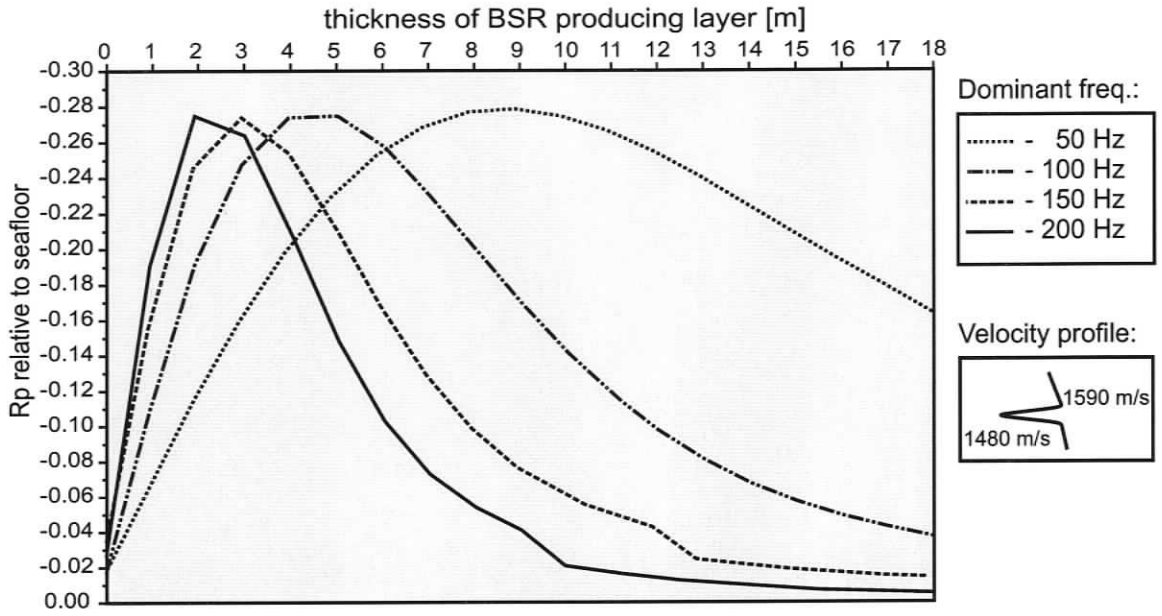

Figure 6.15: Dependence of reflection amplitude on the thickness of the BSR producing layer and the dominant frequency of the seismic source (after Papenberg, 2004).

sediments, and hence it is not affected by the reflections from the layered structure of slope sediment package.

Input data

Similar to the sea bottom modelling, data samples over the area around each station were used to form an AVA curve. Hence, two separate curves were obtained characterizing the BSR in the vicinity of the OBSs A and C. The raw amplitudes were scaled using the scaling factors in Table 6.3. In addition, the data were corrected for the energy loss due to reflections from the seafloor. The correction factor was calculated as the inverse square of the seafloor transmission coefficient, which is $(1 - R_{btm})$. The input data for the inversion are presented on Figure 6.16.

The P-wave velocity for the upper half space (sediments above BSR) was fixed at 1730 m/s. The value was taken from the results of the tomography studies as an average velocity at the BSR for the regions around the OBSs. The following three properties were inverted for: P-wave velocity contrast; S-wave velocity in the upper

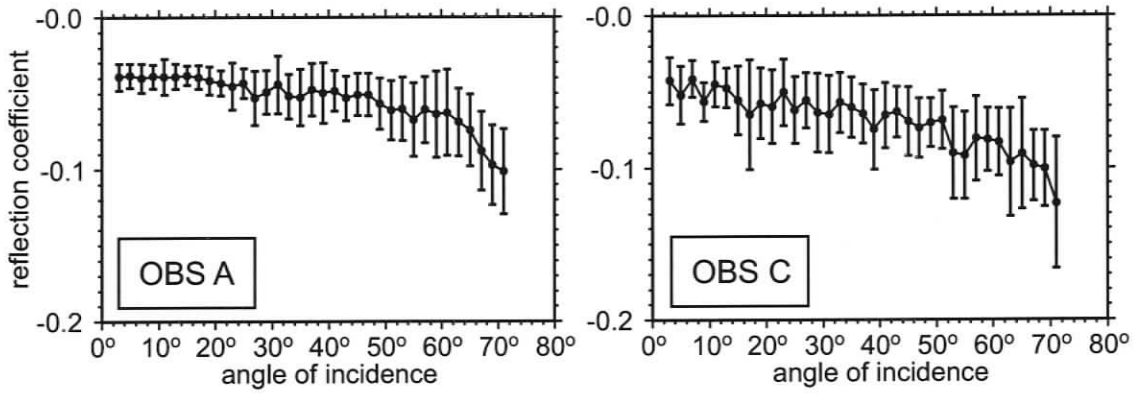

Figure 6.16: AVA curves used in the inversion for the BSR interface (correction and scaling applied). The uncertainties for the data points are also shown.

half space; S-wave velocity contrast.

Results

A map of the reflection coefficients for the BSR was created for the area in the vicinity of the two OBSs. The methodology was the same as for the map of the reflection coefficients for the seafloor, except that separate AVA curves were used for correction for the amplitude variation due to change of the incident angle. The map is presented on Figure 6.17.

The reflection coefficients for the BSR vary greatly inside the mapped area. Although it is difficult to draw any conclusions, as the data from only one station were used to create each piece of the map, a prediction can be made that the BSR strength is not constant over the area.

The results of the inversion of the two AVA curves for the BSR reflection constructed for OBS A and C are presented on Figure 6.18 and in Table 6.6.

The negative change of the P-wave velocity at the BSR, sensed by the seismic signal, is estimated at 100–150 m/s, depending on the region. Nevertheless, as discussed earlier, the resolved change in the velocity may not represent the total decrease below the BSR. According to the analysis, the actual decrease in the P-wave velocity below the BSR can be up to two times larger than that obtained with this data set. The

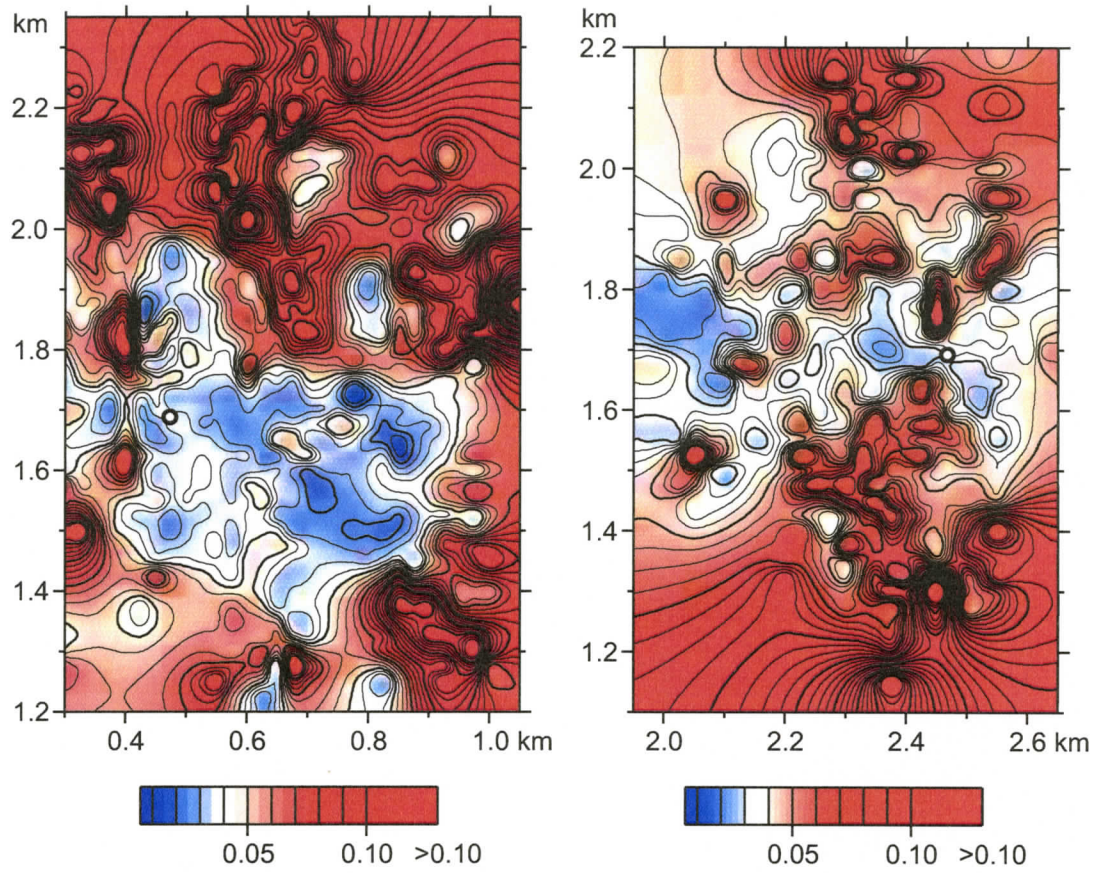

Figure 6.17: Map of the reflection coefficients of the BSR in the vicinity of the OBS A (left) and C (right). The positions of the OBSs are specified.

results from other studies predict the negative change in the P-wave velocity in the range from 250 to 350 m/s (Chapman et al., 2002; Yuan et al., 1999)

The shear wave velocity for the gas hydrate bearing sediments above the BSR is predicted to be in range from 300 to 800 m/s with slight preference for the lower end of the range. Hamilton (1980) predictions of the S-wave velocity for the non-gas hydrate bearing sediments are about 400–450 m/s for the similar type of sediments. That is, the influence of the gas hydrate on the shear strength of the matrix at the site seems to be small. The fact that the S-wave velocity decreases by 10–20% across the BSR also supports the idea that the gas hydrates mostly are formed in the pore space, rather than reinforcing the sediment matrix (Dvorkin et al., 2000).

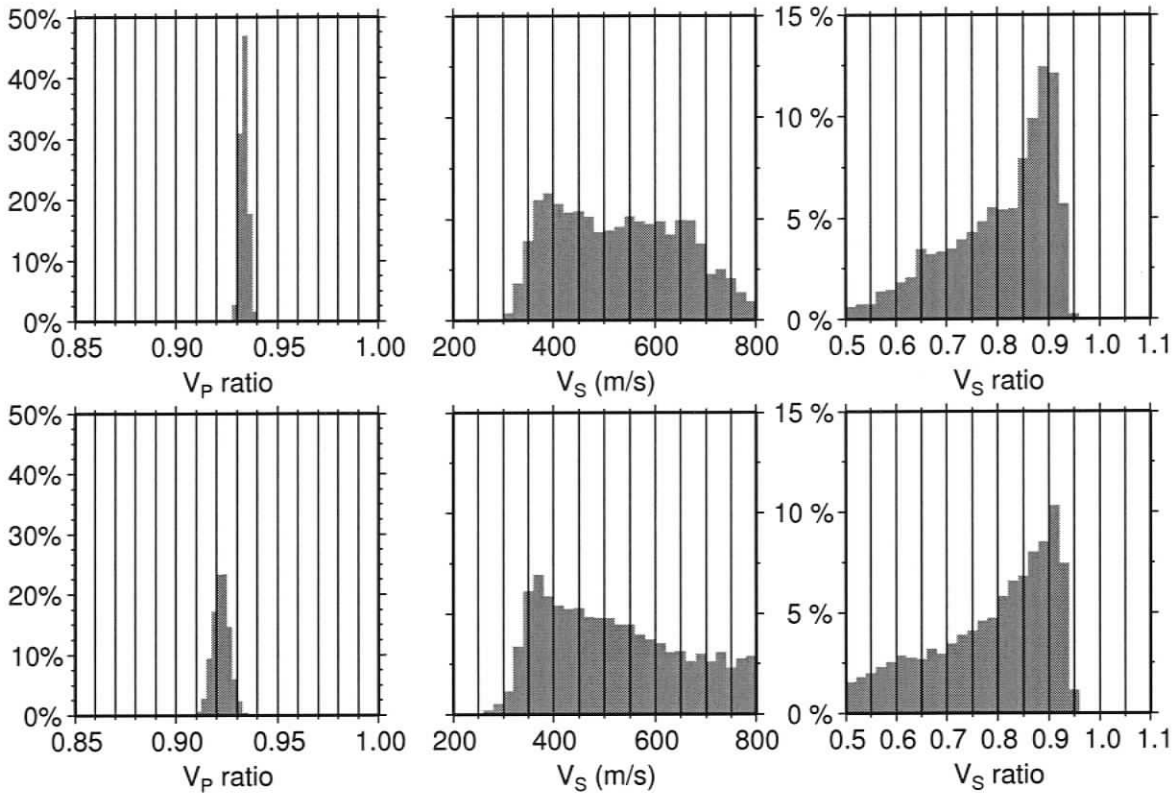

Figure 6.18: Marginal probability distributions from inversion of the AVA data for the BSR. Two separate inversions were performed on data from OBS A (upper row) and C (lower row). The density ratio was fixed at 1; P-wave velocity in the upper half space at 1730 m/s.

6.5.4 Conclusion

The amplitude analysis was complicated by the quality of the data, the insufficient dynamic range of the recording devices, and the lack of information on the initial impulse wavelet. Also some limitations were imposed by the frequency of the seismic source. Nevertheless, important results were achieved.

The map of the reflection coefficient was created with the grid size 50 $m \times 50$ m, which provided greater resolution than was available from previous studies. It accurately outlined not only the zone of low bottom reflectivity, associated with the blank zone, but also revealed a high reflectivity rim around it, most likely to be the carbonate outcrops.

Table 6.6: Inversion estimates with the 95% confidence intervals for the AVA BSR data.

	OBS A				
	V_P contrast	V_S (m/s) upper	V_S contrast	V_P (m/s) change	V_S (m/s) change
Results:					
MAP	$0.933^{+0.003}_{-0.004}$	690^{+52}_{-360}	$0.91^{+0.03}_{-0.32}$	-115^{+7}_{-5}	-62^{+280}_{-21}
Mean	0.933 ± 0.004	530 ± 240	0.80 ± 0.2	-115 ± 7	-110 ± 100
	OBS C				
Results:					
MAP	$0.92^{+0.006}_{-0.010}$	420^{+370}_{-90}	$0.74^{+0.20}_{-0.19}$	-140^{+18}_{-10}	-110^{+80}_{-85}
Mean	0.92 ± 0.008	520 ± 140	0.78 ± 0.24	-140 ± 14	-115 ± 125

The map of the reflection coefficients of the BSR displayed non-uniform nature of the BSR around the site. The size of the area, where the BSR may be considered uniform, can be as small as 200 $m \times 200$ m or even less.

The AVA analysis provides a means to probe the sediments below the BSR, and to estimate properties. The results were consistent with the previous studies conducted in this area, but also gave an insight on such an important property as shear wave velocity for both half spaces. The results showed that the S-wave velocity for the sediments immediately above the BSR is similar to the velocity of sediments that contain no hydrate. The decrease of the shear wave velocity below the BSR is not dramatic. Thus, the gas hydrate is more likely to be formed in the pore space, rather than as a part of the matrix; if hydrate were in the matrix, then the shear strength of the sediments would be affected more and the change in the S-wave velocity would be more significant.

In the current survey the dominant frequency of 150 Hz may not have sampled the full velocity contrast across the BSR. For future surveys, the most suitable seismic source for the BSR studies should have a dominant frequency in the range of 50–100 Hz.

Chapter 7

Results and Discussion

7.1 Modelled area

7.1.1 Seafloor morphology

The modelled area is located approximately between two local ridges. The water depth inside the area varies from 1250 m in the north corner of the model that catches the southern flank of the NE rise, to 1355 m in the south corner of the model, where a local depression is found. The major part of the model area is relatively flat and represents the local depression between the two highs. The heights are the topographic expression of a buried ridge structure that runs parallel to the deformation front, about 20 km landward from it. The ridge separates a nearly flat basin with water depths about 1400 m on the NE side from the seaward steep slope (Fig. 7.1).

The seafloor reflection coefficient, as defined from the OBS data analysis (Chapter 6), does not vary significantly over the area with the average value being about 0.2. Several localized reflection coefficient anomalies are believed to be connected with the seafloor curvature and do not represent the actual value for the interface. The lower reflection coefficients for the South corner of the model may represent younger and softer sediments accumulated in the depression in comparison to the sediments at the higher parts of the seafloor, where they are believed to be older as the possible water currents prevent the sediment accumulation.

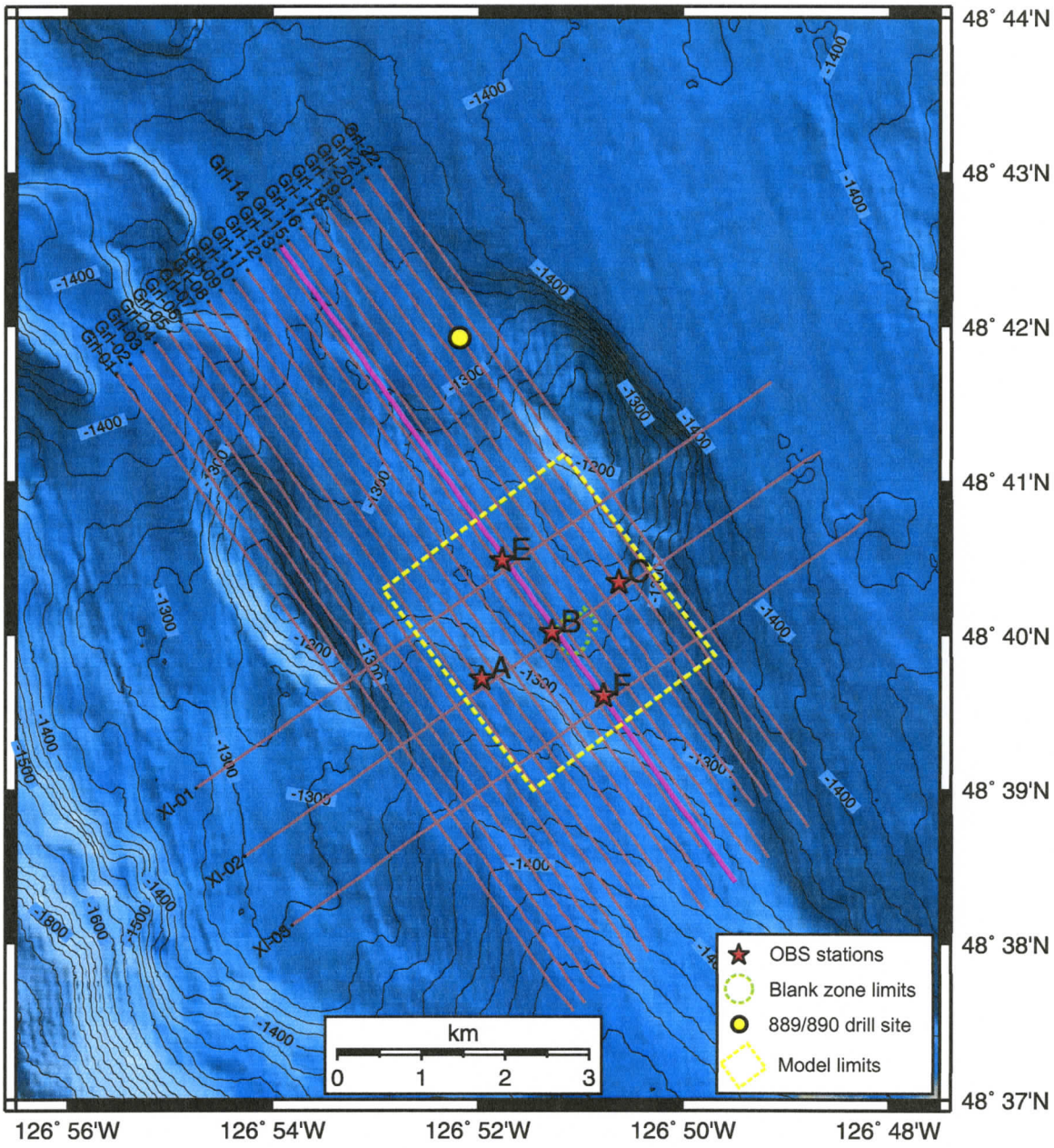

Figure 7.1: Bathymetry map around the site of interest.

7.1.2 Local lithological structure

Most of the available lithological information comes from the ODP 889 drill site, which is situated about 2 km north of the northern border of the area modelled in the travel time tomography study (Fig. 7.2). Considering the proximity of the site, the information obtained through the ODP well logging can be applied for the analysis of the area, although it requires certain adjustments for the depth.

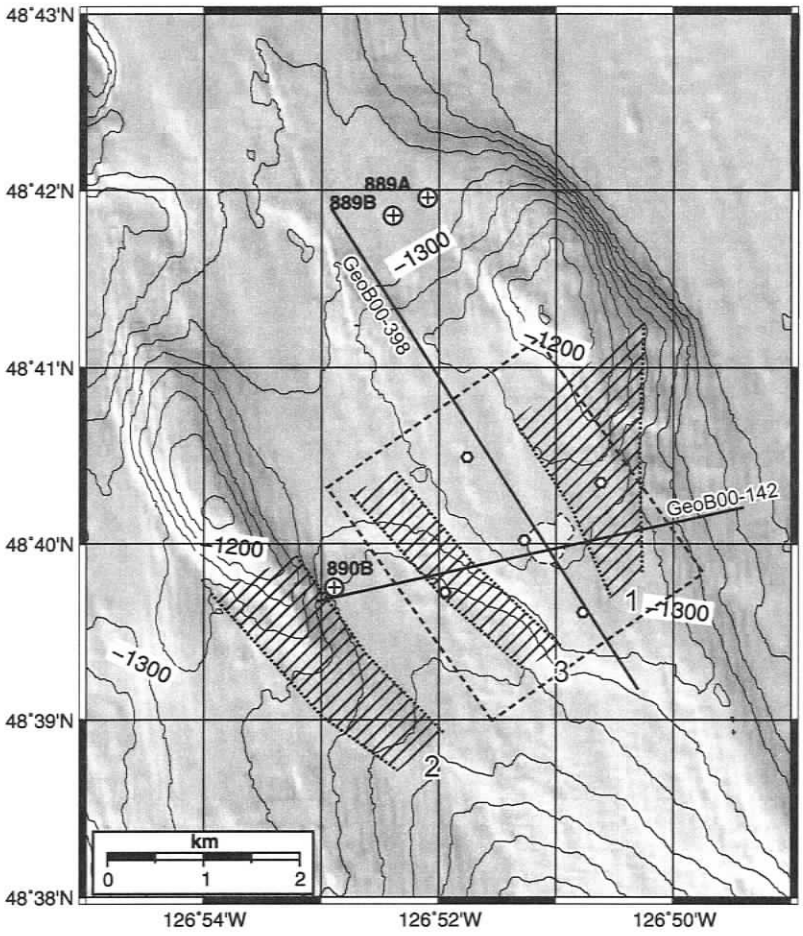

Figure 7.2: Position of the modelled area (thick dashed line) relative to the bathymetry and ODP drill sites. The position of two seismic lines from R/V Sonne Cruise SO 149 (Zühlsdorff and Spieß, 2004) are also shown together with the limits of the Bullseye blank zone. Hatched areas represent buried ridges of accreted sediment complex.

In the upper 300 m of the sediment section it is possible to separate two lithological units at the site using the 2-D and 3-D seismic data available. The first unit is characterized by the well-defined parallel bedding. It can be correlated with the Unit I at the 889 drill site as defined by Westbrook et al. (1994). The second unit with almost complete loss of coherency of the seismic signal can be attributed to the Unit III at the drill site.

The lower unit represents accreted sediments. According to the description of the core samples from the ODP 889 drill site, the sediments of this unit are more consolidated, but highly fractured compared to the undisturbed sediments of the upper unit.

The upper boundary of the accreted sediment complex is highly variable in terms of its depth below the seafloor. It is possible to outline three small well expressed ridge structures within the limits of the modelled area, using single channel seismic data from COAMS-99 data set. The ridges are superimposed on top of the regional ridge, and run almost parallel to each other in the same direction as the main ridge structure, SE–NW, i.e., parallel to the deformation front (Fig. 7.2). Two of them, landward and seaward (#1 and #2 in Fig. 7.2), have expressions on the seafloor in the form of topographic highs. The third, smaller ridge (#3) that lies approximately in the middle between the above mentioned pair does not correlate with any topographic mound.

The shape of the boundary between the accreted sediment complex and slope sediments can be approximately evaluated for the elevated areas by considering the shape of the layer 3 in the tomography model (see Fig. 5.16). The surface of layer 3 replicates the boundary within a few tens of metres for the top parts of the ridges. In contrast, in the depression between ridges, the top of the accreted sediments complex lies substantially deeper than layer 3. Its position can be as deep as 100 m below the BSR.

The landward ridge of accreted sediments can rise as close as a few tens of metres from the seafloor at the highest points of the topographic mounds. In the modelled area it generally stays at a depth of 100 $mbsf$. The ridge width changes from a few hundred metres at its SE end, where it is less prominent, to a maximum of about 2 km under the topographic high.

The middle ridge structure does not come up closer than 100 m to the seafloor, and its width is about 500 m. It is completely buried under the slope sediments.

The slope sediments were deposited on top of the accreted sediments. The bedding

of the unit is undisturbed and almost parallel at the top of the section. The thickness of the unit mostly depends on the configuration of the surface of the accreted sediment complex, rather than bathymetry. The thickness is greatest for the area associated with the depression between the two accreted sediment ridges and may reach 300 m, so that the bottom of the GHSZ lies inside the unit. The thickness of the slope sediments unit can be as small as 50 m in the northern corner of the modelled area.

The bedding of the slope sediment unit suggests normal depositional processes on top of the irregularly shaped surface. The layering repeats the shape of the base structure in the bottom part of the unit, gradually smoothing it upward and finally becoming almost horizontal.

Several faults were observed in the multichannel seismic sections that outline the elevated part of the seafloor. The observed faults are either thrust faults (at the landward side of NE mound and the seaward side of SW mound) (Riedel, 2001) or normal faults in the north corner of modelled area (see Fig. 7.3 – 'Fault zone') (Zühlsdorff and Spieß, 2004). Thrust faults suggest compressional forces and are common for the accretionary prism environment. The central seafloor block was uplifted along those faults. The faults penetrate several hundreds metres into the sediment section. At the top they reach the seafloor, which suggests that the uplifting process took place recently. The elevated position of the part of the seafloor may have led to extensive weathering of the top sediments layers. In contrast, the normal fault occurs only within the slope sediments, without penetrating deeper into accreted sediment section.

7.2 Gas hydrate distribution

The ultimate goal for most of the surveys targeting gas hydrate sites is to assess the quantity of hydrates in the sediments. Regardless of the purpose of the hydrate investigation, whether an expected energy source, storage of a greenhouse gas, or an agent of sediment property alteration, it is the amount of gas hydrates in a given volume that is important. No less important is the distribution of hydrate inside the

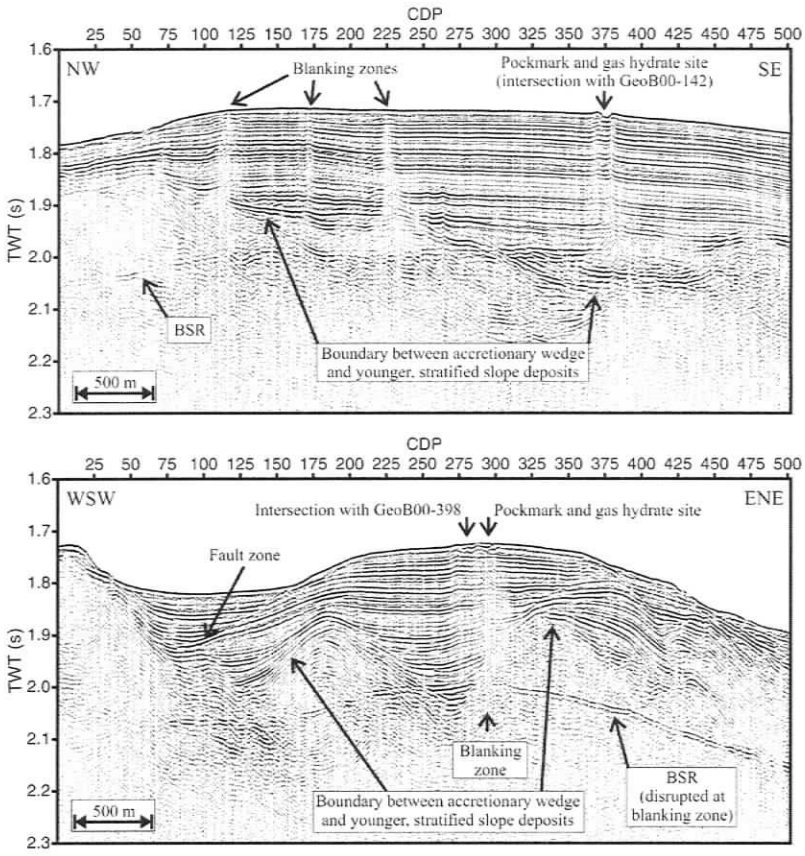

Figure 7.3: GeoB00-142 (bottom) and -398 (top) multichannel seismic lines from R/V Sonne Cruise SO 149 (Zühlsdorff and Spieß, 2004). Location of these profiles is found in Fig. 7.2

volume, both vertically and horizontally.

There are a number of methods for the remote detection of gas hydrates. Several of them were discussed in the previous chapters. Among them the detection of gas hydrates and estimation of their concentrations using seismic velocity information can be named as most cost-effective. The velocity information can be obtained routinely through processing of seismic information over a large volume. Other methods, such as electromagnetic, compliance, and well logging, are very costly and provide information only for a limited area.

The background no-hydrate reference velocity is a vital component for accurate estimation of gas hydrate content at the site through velocity information. Such a reference velocity can be obtained by different means. First of all it can be measured at a site in the same region where hydrates are believed to be absent. Also, the background velocity profile can be extrapolated from the deeper depths below the bottom of GHSZ, where the velocity were obtained using MCS interval velocity analysis. Fi-

nally, the velocity can be estimated using information about sediment grain content and porosity obtained from the nearby drill site by applying established formulae.

Velocity estimates by all the above mentioned methods are subject to a significant uncertainty. For instance, dispersion of MCS interval velocity can be up to 100 m/s in the depth range of just several tens of metres. The direct physical property measurements performed on core samples also provide very dispersed results for density, porosity, and velocity. The variation in the measured properties may reflect the actual variation due to sediment type change. In order to use these results to the full extent, the variations should be correlated with the observed strata, but this is usually impossible in practice.

An averaging approach over depth can be very useful in the case of dispersed data points. It can produce a reliable average trend of a property with depth, that can be used in subsequent calculations. The difference between measured velocity and the average velocity for a specific depth can be related to gas hydrate presence. Comparison of the average no-hydrate reference profile with the velocity profile obtained by tomography studies can provide an average concentration of gas hydrates inside a volume. The latter is more important for estimates of total gas hydrate amount at a specific site.

The increase in the velocity can be converted into gas hydrate concentrations in a number of ways (Lee and Collett, 2001). Some of these are based on complex theory of sound propagation that include a large number of parameters (e.g Helgerud et al., 1999). This approach can lead to large uncertainties, as the final uncertainty of the hydrate concentration estimate depends on the uncertainties of each model parameter.

A simpler method of estimating gas hydrate concentration utilizes the relation of sediment velocity and its porosity. The calculation proceeds by conversion of the background and anomalous velocities at specific depth into porosity estimates. The velocity-porosity conversion is carried out using time-average equation involving the velocity of the dry matrix, pore fluid, and pure gas hydrate (Lee et al., 1993). The

decrease in porosity implies an increase amount of gas hydrates occupying the pore space (Yuan et al., 1996).

Probably the best no-hydrate reference velocity profile for the sediment in the vicinity of the ODP 889 drill site (see Fig. 7.4) was provided by Yuan (1996). It takes into account the separation of the sediment section into two units based on the lithology. The velocities for the slope sediment unit are taken from the interval velocity analysis of the Cascadia basin sediments (Yuan et al., 1994).

The velocity profile starts with a value of 1495 m/s for the sediments immediately below the seafloor. It increases with the rate of 1.15 m/s *per* m reaching 1635 m/s at the bottom of the slope basin sediment unit (120 $mbsf$). Accreted sediments are assumed to have lower velocity at the same depth, only 1570 m/s. The accreted sediments, though more consolidated, are also more fractured and the decrease in velocity may reflect this difference. The background velocity trend for the accreted sediment unit was obtained using third-order polynomial fit of MCS data. In the upper few hundred metres of the unit the trend can be approximated with a straight line that has a slope 0.62 m/s per m.

It is believed that in the vicinity of the ODP 889 drill site gas hydrates are present in significant concentrations ($> 10\%$) only in the pore spaces of the accreted sediment unit, while the slope sediments may contain less than 5% of hydrates (Hyndman et al., 1999). The sonic log velocity profile, when averaged over 20 m depth intervals, matches the background profile in the 60–120 depth range very well suggesting no-hydrate sediments.

The absence (or extremely low amounts) of gas hydrates in the slope sediment unit can be explained by the fact that supply of methane in sufficient amounts gas is required for gas hydrate formation. It has to be brought into the stability field by fluid flow or by other means from below. Highly fractured accreted sediments have higher permeability than perfectly layered undisturbed slope sediments. The upward fluid flow inside the slope sediments would be difficult, prohibiting a large supply of methane for gas hydrate formation. That is, the lithology of the sediments is the

control factor of gas hydrate distribution.

If the lithology of the sediments is assumed to be the major factor that controls the distribution of gas hydrates, it is safe to suggest that inside the modelled area the volume of sediments favorable for the gas hydrate formation is small, as the slope sediments occupy most of the modelled volume.

Putting aside the velocity anomalies in the tomographic model near OBS A, the velocity field is quite uniform throughout the model. The maximum variation of velocity values for an equal subbottom depth is 40 m/s. Assuming that the change in the velocity occurs due to variation in the gas hydrate concentration, it can be concluded that if averaged over the volume of a model cell, the concentration does not vary greatly in the lateral direction over the modelled area.

In order to evaluate the quantity of gas hydrate at different parts of the modelled area, the tomography model velocities are compared to the velocity profile obtained at ODP 889 drill site (Fig. 7.4). The tomography model cube was sampled at three points, and a vertical velocity profile was plotted for each point. Profile A represents velocities revealed in the model at a local minimum on the horizontal plane, where the base of the GHSZ is above the surface of the accreted sediment complex. The position is approximately in the middle between OBS E and B. As can be seen, it follows the background profile for the slope sediments (Unit I) within a few m/s. This fact suggests virtually no presence of gas hydrates at the point. The velocity profile at this point can be used as a new background.

Velocity profile B is taken at a point associated with a local maximum. At this point, the sediments within the modelled thickness are represented exclusively by slope sediments. The increase in the velocity compared to profile A is minor. It is 20 m/s at the seafloor. The velocity difference increases down the sediment section to 40 m/s at the BSR depth. If the change in the velocity is completely attributed to the change in gas hydrate presence, these numbers correspond to 5–6% of pore space occupied by clathrates (or 2–4% of the sediment volume).

The results of the travel time tomography study argue in favour of no gas hydrates,

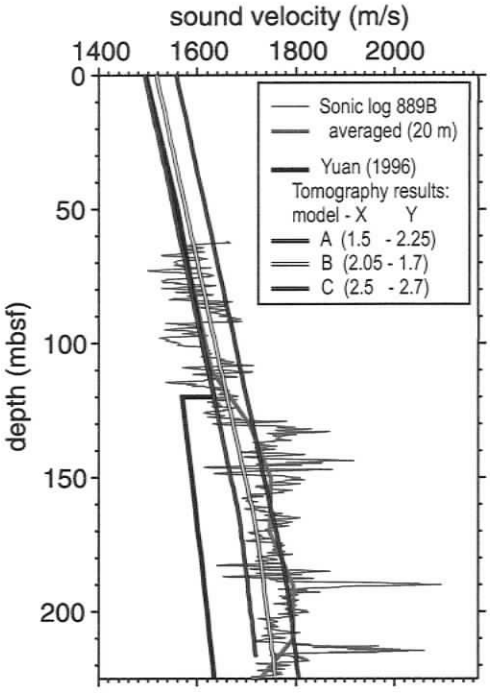

Figure 7.4: Travel time tomography results compared with background velocity for the site (Yuan et al., 1996) and sonic log measurements at ODP 889 drill site. Three vertical velocity profiles from the model are presented. Coordinates (East-North) at which they were retrieved are indicated.

or only a very small amount, present in the slope sediment unit. At the sampled points the section from the seafloor to the BSR is represented by slope sediments. The gas hydrates may be distributed evenly in the vertical direction or they can be localized in the thin layers of more porous sediments (e.g., Tréhu et al., 2004). The layers may be as thin as several tens of centimetres, which is impossible to resolve by means of the travel time tomography inversion.

The estimates of low concentrations of gas hydrates at the site (excluding the blank zones) are also supported by a recent controlled source electromagnetic (CSEM) study conducted in the vicinity of the Bullseye vent zone (Schwalenberg et al., 2005). The experiment consisted of one profile that runs through four blank zones. The position of the profile approximately corresponds to the GeoB00-398 seismic line (Fig. 7.2). An inline dipole-dipole array was used consisting of transmitter dipole and two receiver dipoles. With two preset transmitter-receiver distances, the array was most sensitive over the depth range of 0–90 $mbsf$ and 0–150 $mbsf$. The survey results reveal that the resistivity of the sediments outside of the anomalous blank zones is at a level of 1.2 to 1.3 Ωm and almost does not vary for the two different depths (Willoughby

et al., 2005). Marine sediments of similar type containing no gas hydrate are expected to have resistivity of 1.2 Ωm at 100 m depth (Hyndman et al., 1999).

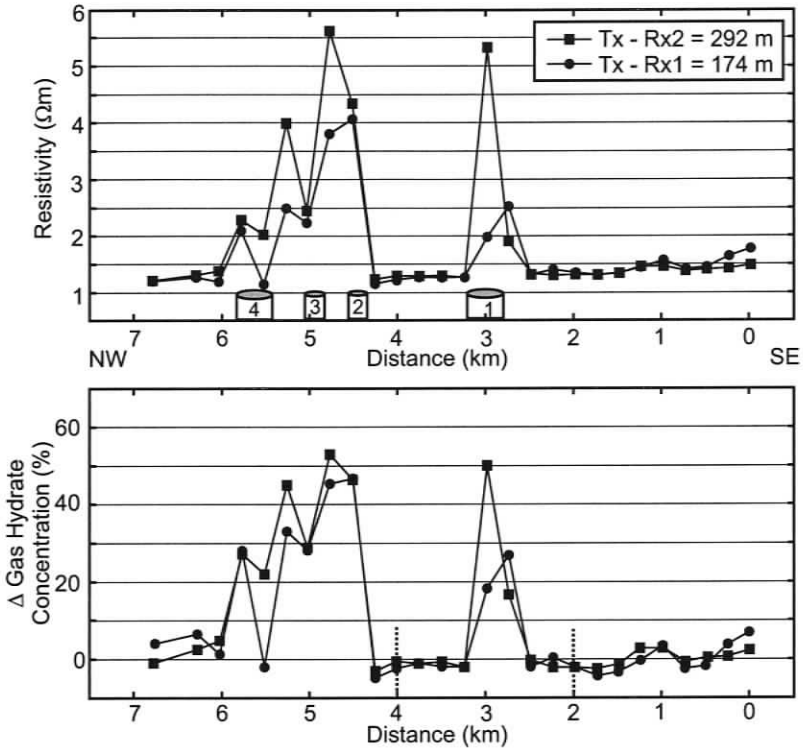

Figure 7.5: Results of CSEM experiment in the vicinity of Bullseye vent zone. Bulk resistivities (top) and corresponding difference in gas hydrate concentrations over a background value are shown. Positions of blank zones are indicated with numbered cylinders, the Bullseye corresponding to #1. The portion of the EM profile falling into the modelled area indicated with dotted lines. (after Schwalenberg et al., 2005).

The results of the CSEM experiment suggests the presence of small amounts of gas hydrate outside of the blank zones. Moreover, the concentration does not increase with depth.

Gas hydrates and accreted sediments

As indicated above, in the middle part of the modelled area the boundary between slope sediment unit and the accreted sediment unit lies below the BSR. That is, the GHSZ is entirely within the slope sediment sction. On the other hand, on the east and west flanks of the area, two local accreted sediment ridges come up close to the seafloor and accreted sediments enter the GHSZ. Accreted sediments, due to their lithological peculiarities such as higher permeability and the presence of small cracks, are better hosts for gas hydrate than are slope sediments.

It is possible to correlate spatially two positive velocity anomalies with the accreted sediment ridges. The two anomalies are located in the NE corner of the model and

in the SW quadrant. The increase in the velocity is up to 70 m/s over the minimum value for the constant depth below the seafloor. Profile C on Figure 7.4 represents the vertical velocity profile through the NE anomalous zone. It nicely matches the averaged sonic velocity profile for the part below 120 m. The recognized velocity increase translates into 10–12% of the pore space occupied by gas hydrates (or 5–7% of the total sediment volume).

7.2.1 BSR distribution and strength

BSR reflection coefficient

The presence of the bottom simulating reflector (BSR) on a seismic section is commonly connected to gas hydrate presence in the sediment. The BSR is believed to be associated with the bottom of the gas hydrate stability zone, outlining the depth above which gas hydrate can be formed in the pore space of the sediments. It is widely accepted that the BSR is produced by a combination of gas hydrates in the upper half space and free gas below. The actual importance of each phenomenon may vary from site to site and even around a single site. In addition, it was deduced that the BSR is produced by a layer of finite thickness over which the velocity decreases, rather than by a simple interface. This assumption was made after observing a strong frequency dependence of the BSR amplitude (Chapman et al., 2002).

The BSR presence and its effect on a seismic reflection for a given signal frequency depends mainly on three factors:(i) the concentration of gas hydrates above the boundary; (ii) the concentration of free gas below; and (iii) the thickness of the transition layer. Given that all three unknowns can vary simultaneously, it is impossible to calculate the effect of each of them separately by simply observing the amplitude of the BSR. However, the thickness of the transition layer can be estimated by comparing the reflection coefficient of the BSR for different frequencies (Papenberg, 2004).

The analysis of the multichannel COAMS-99 data (central frequency 100 Hz) for the area revealed a rather irregular distribution of the BSR (Riedel, 2001). It is clearly

visible in the areas where the bottom of GHSZ lies inside the accreted sediments and not observed where it is inside the slope sediments, though in the latter case it might be obscured by a layered structure of the host sediments. The average reflection coefficient for the BSR was estimated to be about -0.05. Several local BSR bright spots were also observed in close proximity of the Bullseye vent zone. The reflection coefficient of the BSR may be as much as -0.3 at such points.

Inside the modelled area the strongest BSR was observed under the local accreted sediment ridge on the east side (Fig. 7.2) (around the OBS C).

Two maps of BSR reflection coefficients were created using the OBS data (Fig. 6.17). They cover the areas in the vicinity of OBS A and C, as the BSR amplitude data were considered reliable only for these two stations. In the seismic sections for the three other OBSs, although the BSR could be identified as an event, its amplitude was contaminated by other reflections. In the vicinity of OBSs A and C the BSR occurs inside accreted sediments. Each map represents an area of approximately 0.7 km^2 each. The limits of the maps were defined by the span of the reflection points of the rays recorded by the OBSs.

The absolute average value for the BSR reflection coefficient is 0.07 near OBS C and 0.06 near OBS A. The absolute maximum value is about 0.22 and the minimum is about 0.005. As can be seen, the reflection coefficient varies greatly even around such a small area. The asymmetrical OBS geometry provides higher horizontal resolution than the conventional towed streamer due to smaller radius of the first Fresnel zone. With the reflection point being at the BSR, the radius of the zone is estimated to be two times smaller than for the COAMS data. For the normal incidence rays the radius of the first Fresnel zone is calculated to be about 55 m.

It is difficult to establish any correlation between the variation of the BSR reflection coefficient with other known features or the velocity field, as the coverage is very limited and does not allow the observation of larger scale trends in the BSR strength. Unfortunately, as deduced from the uncertainty analysis for the travel time tomography results, the velocity values immediately above the BSR are subject to large errors,

and thus the comparison of the BSR reflection coefficient with the tomography results would be not informative.

Previous studies by Hobro (1999) showed that in the vicinity of the ODP 889 drill site there is virtually no connection between the BSR strength and concentration of gas hydrate above the BSR. Similarly, at the site of interest, it can be suggested that the distribution of BSR reflection coefficients depends mostly on the distribution of free gas below the BSR. It is also worth noting that the thickness of the BSR producing layer may affect the strength of the BSR reflection for the middle range frequency signal. More conclusions can be made after comparison of maps of the BSR reflection coefficient over the same area produced using seismic sources with different frequency bands.

Depth to the BSR and heat flow

The depth of the bottom of the GHSZ and, subsequently, the depth of the BSR below the seafloor is defined mainly by the pressure and temperature conditions. The variation in the position of the BSR under the seafloor follows the variation in the local heat flow pattern. Under normal conditions of conductive heat transport and uniform thermal conductivity for the sediments, the variations of the temperature field depend mostly on the seafloor configuration. Heat flow is minimal at local convex features and greater at concave features.

The depth to the BSR from the tomography inversion was used to estimate the heat flow over the area (Fig. 7.6). The average value for the BSR depth in the middle part of the model is about 220 metres below the seafloor. The variation of the BSR depth is about 40 m over the modelled area. The BSR is closer to the seafloor in the SW corner of the model, where the water depth is greatest near a local seafloor depression. The largest values for the BSR depths are observed under the local seafloor highs in the NE corner. This general trend corresponds well with general expectations of the heat flow pattern.

Under the conditions of a linear temperature gradient and conductive heat trans-

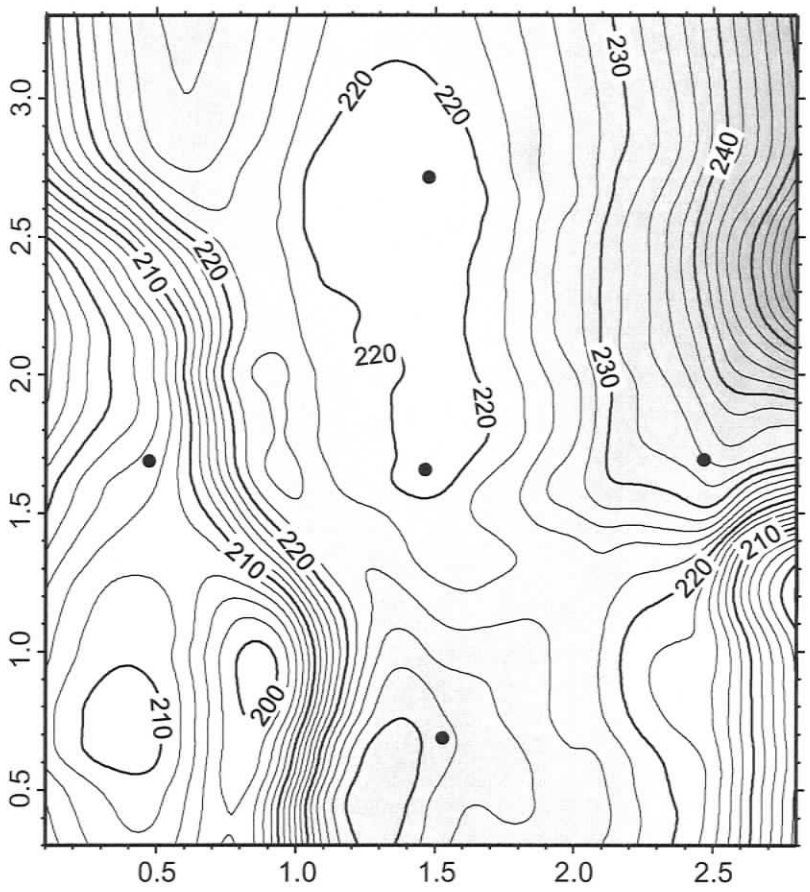

Figure 7.6: Map of the depth to the BSR below the seafloor. Positions of the OBSs are marked with black dots.

portation, heat flow (H) can be estimated by this simple equation:

$$H = k\frac{T_{BSR} - T_{sf}}{z_{BSR}}. \tag{7.1}$$

where k is the thermal conductivity, T_{BSR} and T_{sf} are temperature at the BSR and seafloor respectively, and z_{BSR} is the depth of the BSR below the seafloor.

Empirical dependence of the mean thermal conductivity coefficient on depth for the Northern Cascadia region was obtained by Davis et al. (1990) and is as follows:

$$k = 1.07 + 5.86 \cdot 10^{-4} \cdot z - 3.24 \cdot 10^{-7} \cdot z^2, \tag{7.2}$$

where k is in $W/m°C$ and z is in m.

The temperature at the BSR can be calculated by recalling that it is a phase boundary. The P-T curve for the pure methane-sea water system is defined by the following empirical relation (Bouriak et al., 2000):

$$\log P = 0.4684 + 0.0401 \cdot T + 0.0005 \cdot T^2, \tag{7.3}$$

where T is temperature in degrees Celsius and P is pressure in MPa. Equation 7.3 can be solved for T as a quadratic equation. Hydrostatic pressure at the BSR (Davis et al., 1990) was calculated as:

$$P = \rho \cdot 9.81 \cdot Z_{BSR}, \tag{7.4}$$

where ρ is sea water density (usually 1030 kg/m^3) and Z_{BSR} is the depth of the BSR below the sea surface. Finally, the temperature at the sea bottom was taken from measurements during the July/August 2000 cruise (Spence et al., 2000) to be $3.16°C$.

The results of the heat flow calculations are shown on Figure 7.7. The pattern follows the distribution of depth of the BSR. The highest values for the heat flow correspond to regions with minimal depths of the BSR below the seafloor, and vice versa.

For an independent check, the heat flow derived from the BSR depth was compared with the actual measurements with a heat probe during the July/August cruise (Spence et al., 2000). The measurements give values consistently lower than those estimated from the BSR depth, with the average discrepancy being 5–7 mW/m^2 (see histogram analysis on Figure 7.7).

There may be several sources for errors in the heat flow calculations. First of all, is the thermal conductivity approximation. Second, the temperature at the BSR might differ from that predicted from the laboratory measurements, as the natural environment is more complex system than a controlled experiment. Ganguly et al. (2000) estimated that the uncertainty for the heat flow values derived from the BSR depth can be as high as 20%.

Observations conducted during ODP Leg 146 showed that the actual temperature at the BSR was $1.5°C$ cooler than predicted from the phase diagram by Ganguly et al. (2000). If the temperature at the BSR is adjusted for this value, the heat flow estimations from the BSR depth would be 8 mW/m^2 smaller.

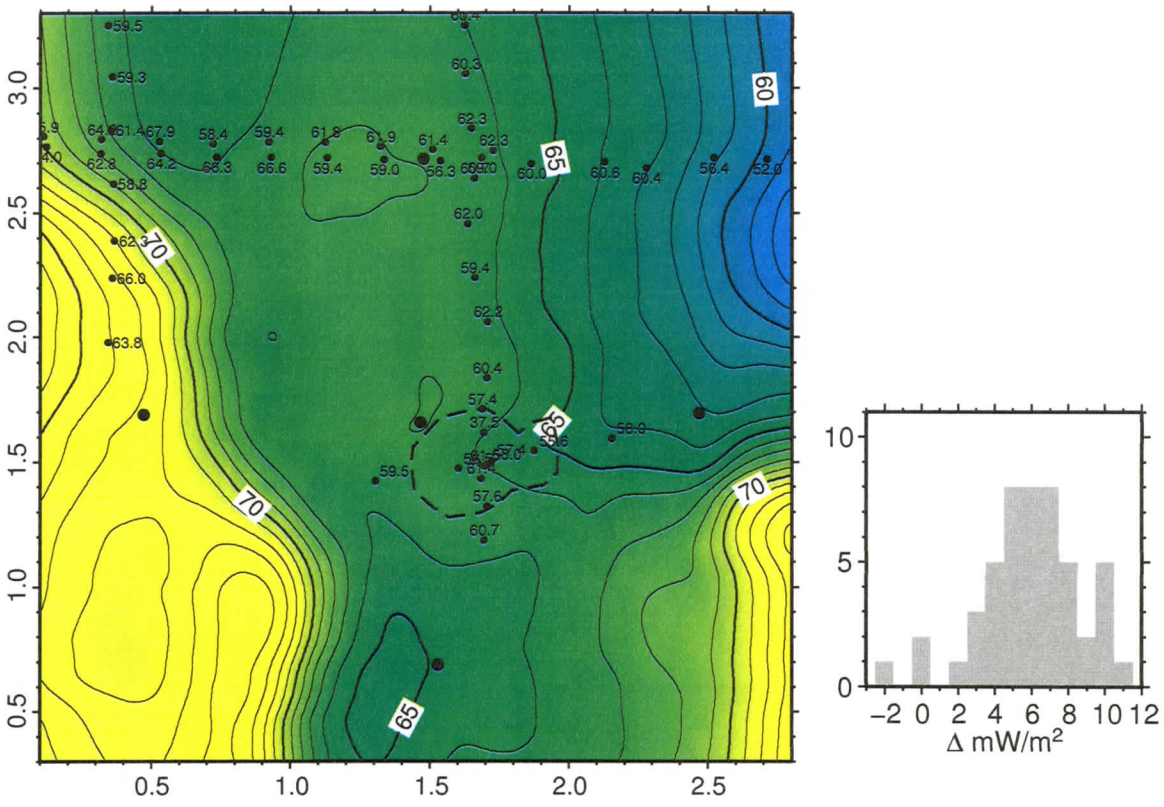

Figure 7.7: Map of the heat flow derived from the BSR depth distribution (left). Individual measurements of the heat flow at the sea bottom are also shown. Dashed contour outlines the limits of the Bullseye vent zone, large dots represent positions of the OBSs. Histogram analysis of the mismatch between *in situ* heat flow measurements and heat flow calculations from the BSR depth are shown on the right panel.

7.3 Bullseye vent zone

7.3.1 Seafloor reflection coefficient features at the vent zone and their connection with other observations

Ring structure

The study of the seafloor reflection coefficient (RC) distribution around the site revealed a negative anomaly associated with the vent zone (Fig. 6.12). With a smaller grid cell size (25 m), Figure 7.8 allows closer inspection of the zone and reveals more complex structure of the anomaly than simple oval-shaped area of low reflection co-

efficients.

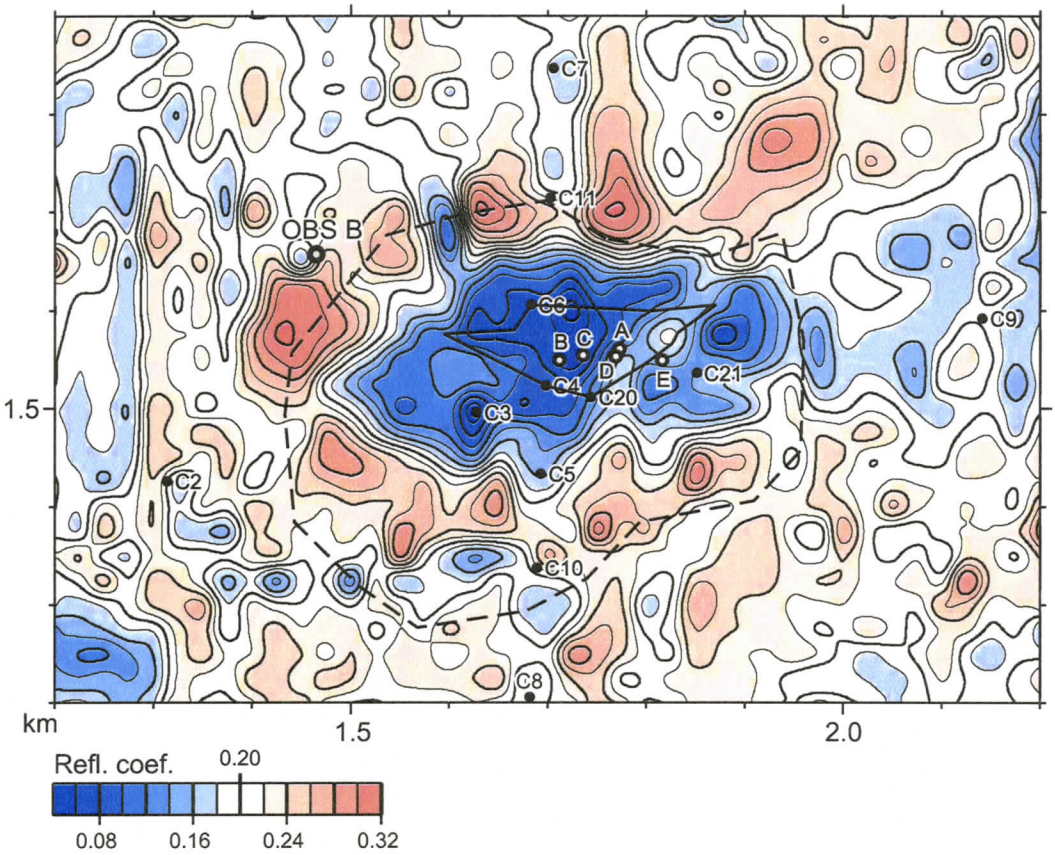

Figure 7.8: Seafloor reflection coefficient map at the Bullzeye vent zone. Dashed line denotes the limits of the blanking at depth according to the single channel Teledyne data. Solid line outlines the occurrence of massive gas hydrates at 6–8 m depth according to the piston core experiment. Solid dots indicate the positions of sediment piston cores collected in 2000 (Spence et al., 2000). Empty dots specify locations of the U1328x wells drilled during IODP 311 expedition (Expedition 311 Scientists, 2005).

The negative anomaly is 500 m long and 250 m wide; that is, it is almost as long as the limits of the blanking phenomena at depth associated with the vent zone, but significantly narrower than these limits. Its centre coincides with the centre of the occurrence of massive hydrates detected by piston coring. The lowest values for the RC inside the anomaly are in the range of 0.04–0.06 if individual data points are considered.

The negative anomaly is outlined by a ring-shaped area of higher than average

seafloor reflection coefficient. The average value for RC inside the 50–100 m wide ring is 0.275 with individual data points as high as 0.325, compared to the average of 0.2 over the entire study region; individual data points go as high as 0.325. The ring structure is not closed, but rather it is open at the NE end.

The overall anomalous structure is symmetrical relative to the zone of shallow massive gas hydrates occurrence, and displaced towards the NW side of the blanking feature.

The low RC zone determined from OBS seafloor reflection coefficients is comparable to that calculated from normal incidence reflection data (Riedel, 2001); however, the high RC ring structure was not observed in the earlier study. The low RC values at the seafloor contrast with the direct reflection coefficient calculations using physical properties of the sediments from the piston core samples (Novosel, 2002). Calculation using measured density and velocity of the sediments provide slightly higher reflection coefficient (0.24) inside the limits of the blank zone than outside of it (0.22). The explanation of this apparent inconsistency may be found in the different approaches: a seismic wave sampled sediment under *in situ* conditions and averaged the information over large vertical intervals of the sediment (4 m); physical property measurements were carried out on-board under normal conditions and provided data averaged over 10 cm intervals. In addition, the core sections affected by cracking due to gas expansion were excluded from the measurements, and that gas might have been responsible for an overall low reflection coefficient of the sediments inside the vent zone.

Zone of low magnetic susceptibility of the sediments

The studies on the magnetic susceptibility of the sediments by Novosel (2002) revealed a zone of low magnetic susceptibility (300–800·10^{-6} SI volume units) closely associated with the vent site. The measurements were conducted on sediment piston cores up to 8 m in length. Two piston core profiles across the vent site (Fig. 7.8) allowed mapping of the variation of the thickness of the zone. The zone extended from the seafloor to

the base of the core inside the zone of occurrence of shallow massive hydrates. Its thickness was reduced to several metres, occupying the middle part of the cores, at the points in close proximity. Finally, sediment samples obtained from outside the limits of the blanking feature showed no reduction in magnetic susceptibility (2500–$3000 \cdot 10^{-6}$ SI volume units) (Fig. 7.9).

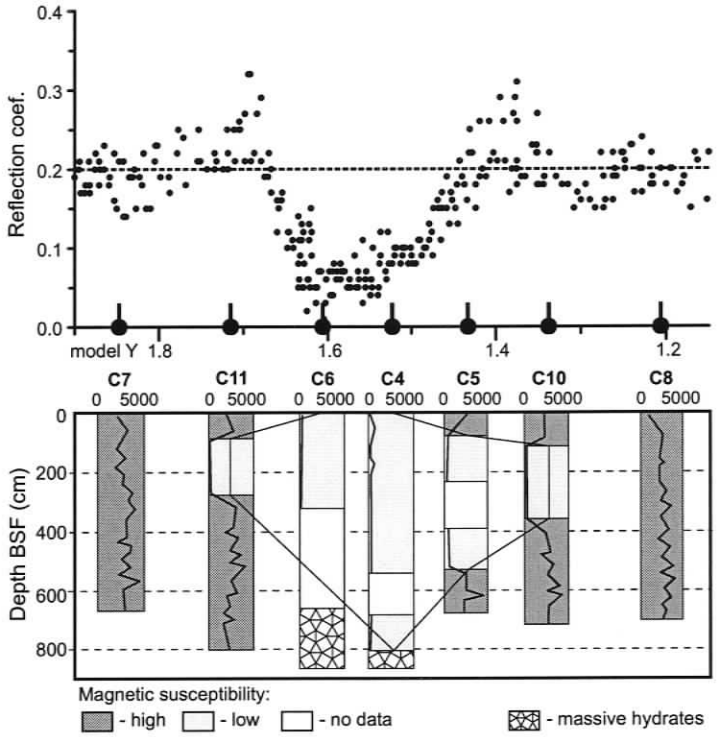

Figure 7.9: Comparison of the seafloor reflection coefficient values with magnetic susceptibilities. Individual data points for the RC are taken from the 100 m wide band along the coring transect. The bottom picture is modified from Novosel et al. (2005). The magnetic susceptibility is given in 10^{-6} SI volume units.

The high magnetic susceptibility of the sediments is primarily attributed to the presence of detrital magnetite (Fe_3O_4), highly magnetic mineral (Novosel, 2002). As a result of digenesis, magnetite can be transformed into another ferrous mineral, pyrite (FeS_2), which is not magnetic. It was found that in the sections of cores with low magnetic susceptibility, the pyrite was present instead of originally deposited magnetite (Novosel, 2002).

Canfield and Berner (1987) suggested that dissolution of magnetite and formation

of pyrite is assisted by biological sulfate-reduction process, which often occurs in methane rich environments. The microbially driven anaerobic methane oxidation reaction is $(SO_4^{2-} + CH_4 \longrightarrow HS^- + HCO_3^- + H_2O)$(Ritger et al., 1987). As can be seen, the reaction results in generation of two ions HS^- and HCO_3^-. The first ion forms hydrogen sulfide (H_2S), which reacts with magnetite ultimately producing pyrite. The second provides carbon material to form authigenic carbonates.

The complete transformation of the magnetite into pyrite can occur when sufficient amount of hydrogen sulfide is present in the system, which, in turn, is controlled by the amount of methane brought into the system by upward fluid flux. Thus, the distribution of the low magnetic susceptibility zone can be used as an indicator for the intensity of the methane flux (Novosel et al., 2005). This indicates that the methane flux is greatest in the centre of the seismic blanking feature. The flux decreases in the peripheral zones, and completely disappears outside of the limits of the vent zone.

Authigenic carbonates

The presence of authigenic carbonates is often associated with cold vent sites (e.g. Tréhu et al., 2003; Orphan et al., 2004; Formolo et al., 2004). The carbonate formation requires sufficient inflow of methane into the narrow zone near the sediment surface. In this zone, oxidation of methane by sulfate from the sea water is assisted by anaerobic bacteria, providing bicarbonate, which increases alkalinity and supports the precipitation of authigenic carbonates (Berner, 1980).

Carbonates are present in two different forms at the Bullseye vent site. According to the video observations, carbonates are abundantly present in the vicinity of the central part of the vent zone as sheets, 10–15 cm thick, covering substantial parts of the seafloor (10 m^2 per occurrence) (Riedel et al., 2006). Also, as concluded by Novosel (2002), the authigenic carbonates can be present in disseminated form inside the sediment, noticeably altering its physical properties such as density, P-wave velocity, and thermal conductivity.

Using numerical modelling, Luff et al. (2004) found that carbonate crust formation

occurs only over a rather narrow range of upward fluid flow (20–60 $cm\ a^{-1}$). Higher flow rates do not allow build-up of sufficient concentration of carbonate matter inside the sediment column, as the results of the methane oxidation process are washed away by the fluid flow. They also concluded that the formation of several centimetre thick carbonate crust takes only 100–500 years.

Compilation of the observations

In an attempt to combine observation on the thickness variation of the low magnetic susceptibility zone and the variation of the seafloor reflection coefficient, the available data were plotted along the same line (Fig. 7.9), core transect 1 (cores C7 – C11 – C6 – C4 – C5 – C10 – C8 in Fig. 7.8) through the vent zone. For better data quality, individual data points from the amplitude studies of OBS data were plotted. The data points were taken from the 100 m wide band along the core transect.

The following trend was observed. At the locations of cores which exhibited the low magnetic susceptibility zone extending from the sediment surface to the full length of the core (cores C4 and C6), the seafloor reflection coefficients also exhibited minimal values. Positions of cores that show reduced thickness of the low MS zone, which begins at depth (cores C5, C10, and C11), coincide with the high seafloor reflection coefficient ring. Finally, cores with no anomalous MS observations (cores C7 and C8) were taken where the seafloor reflection coefficient is also normal.

The increased reflection coefficient ring structure is believed to be connected with the occurrence of authigenic carbonates, whether in the form of pavement on the sediment surface or as inclusions in the sediment. However, visual observations with a remotely operated vehicle showed extensive occurrence of the carbonates on the seafloor, but poor navigation did not allow accurate localization for comparison.

Both phenomena, low magnetic susceptibility and seafloor reflection coefficient variations, support the hypothesis of differentiation of the fluid flow rates around the vent site with respect to the distance from the centre of the site. The highest fluid flow rates are expected in the central part. The rates decrease toward the peripheral

parts of the zone.

7.3.2 Seismic signatures of the Bullseye vent zone

The COAMS-99 cruise and, especially, the OBS experiment was focused on the Bullseye vent zone, associated with the largest and most prominent blanking feature observed on seismic sections.

Among the numerous surveys in the vicinity of ODP 889 drill site, a significant number were targeted specifically on the blank zone. Seismic experiments used a wide range of source frequencies and provided insight on the structure of the zone. Piston coring provided information on the lithology of the upper few metres at the site, as well as on the geochemistry. Direct video observations using an unmanned submersible vehicle allowed visual study the seafloor expression of the vent site.

However, despite these intensive studies the phenomenon of blanking still remains unresolved. Also, the major question on how the sediment properties are different inside the blank zone compared to those outside is still unanswered.

An analysis of the available high- and mid-frequency seismic data (Riedel, 2001; Riedel et al., 2002) is summarized below:

- High frequency echosounder data (12 kHz) with depth penetration of just 10 m shows that the blank zone has a bathymetrical expression. A mound structure is present at the top of the zone. The height of the mound varies in the range of 2 to 5 m. The reflection coefficient inside the limits of the elevated seafloor topography is reduced compared to the adjacent area.
- The Sonne Parasound system with 4 kHz acoustic source provided penetration up to 60 m into the the sediments. It also showed a distinctive surface expression of the Bullseye blank zone. The coherent signal outside the limits of the blank zone produced by the layered sediment structure is completely absent inside. That is, the blank zone is completely blank. The boundary of the blanked area is very close to a vertical line on the NW flank. The SE boundary is slightly tilted, so the width of the zone increases with depth due to expansion in the SE

direction.

- The DTAGS with the working frequency of 250–650 Hz provides deeper penetration of the signal down to the depth of the BSR. On the DTAGS seismic section, the blank zone is not completely transparent. Several prominent seismic events can be traced through it, though with highly reduced signal strength (Fig. 7.10). Also an inclined reflector is visible near the surface. It has depth of about 10 m in the centre of the blank zone and approaches the sea bottom towards the NE side of it. The blank zone itself has significant variability.

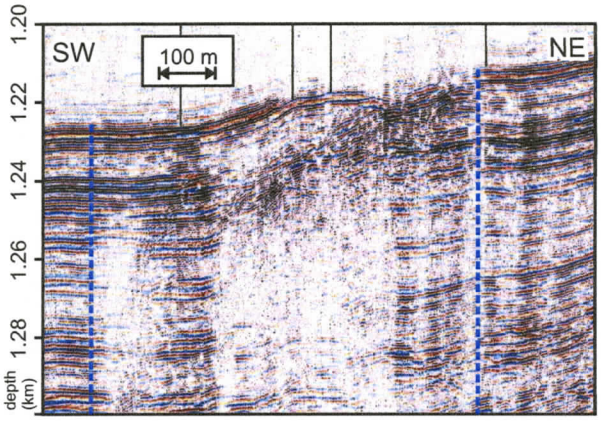

Figure 7.10: DTAGS seismic data over Bullseye blank zone (Gettrust et al., 2004). Dashed blue lines indicate the limits of the blank zone as seen on the conventional single channel seismic section.

The largest portion of the available seismic information over the site was acquired using a 40 in^3 air gun with central frequency of 150 Hz. It includes conventional multi- and single channel seismic data and OBS data. The resolution for these data, both vertical and horizontal, is lower compared to the higher frequency systems, due to increased wavelength and a larger Fresnel zone.

As the frequency is decreased, the degree of blanking also decreases. At a dominant frequency of 150 Hz, almost all reflection events can be traced through the blank zone (Fig. 7.11). Due to lower resolution it is hard to define clearly the vertical boundaries of the blank zone. In general it can be described as isometric, wider at the bottom than at the top (Zühlsdorff and Spieß, 2004; Riedel, 2001). Two features associated with the blank zone are obvious on the seismic section: a pull up of the reflection event inside the blank zone compared to the time of the same event outside of it; and diffractional features, more distinguishable at the top of the zone (see also Fig. 2.8).

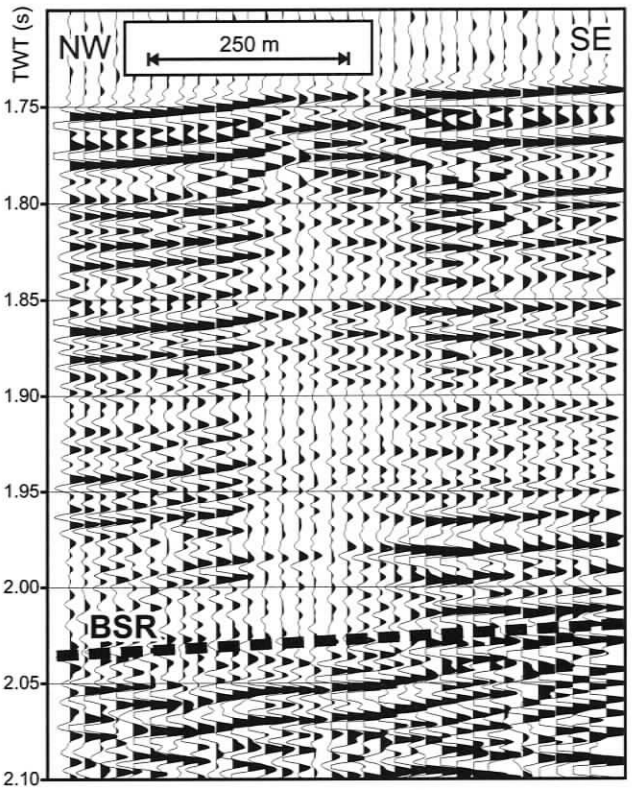

Figure 7.11: Crl-16 single channel seismic line over the Bullseye blank zone.

The pull up of the reflection from a flat reflector indicates that the seismic velocities inside the affected region are higher. The pull up is about 5 ms, and it affects the reflections as close as 20 ms two-way travel time from the seafloor. However, the pull up does not increase with depth and remains approximately the same all the way down to the BSR. This means that the high velocity zone is located close to the seafloor and it is relatively thin (few tens of metres). The velocities at deeper parts of the blank zone are approximately the same as the ones outside of it, since otherwise the pull up time would increase with depth.

Diffractional features occur on a seismic section when an object in the sediments is truncated laterally. The object has to differ from the surrounding material in terms of its acoustic properties, e.g., has higher impedance. This kind of diffractional feature can be observed throughout the entire vertical extent of the blank zone, the most prominent being at the top. The sources of the diffractions seem to be located approximately half the wavelength from the reflectors and in some instances the peak of the diffraction hyperbola can be mistaken with the pull up of the reflection event.

The two cases can be separated by observing the wings of the diffraction hyperbola.

The OBS seismic recordings have the same vertical resolution, since they used the same seismic source as the normal incidence data. However the horizontal resolution is better, as the receiver was placed closer to the reflection point, which leads to a smaller first Fresnel zone. For the reflection point at 200 m depth (approximate depth of the BSR), the estimated radius of the first Fresnel zone for the OBS geometry is as much as three times smaller than for the conventional seismic geometry (30 m vs. 86 m). Unfortunately, due to asymmetric geometry, the analysis of the OBS seismic section is difficult, especially when the station is offset from the shooting line. Nevertheless, it is possible to apply NMO corrections to such sections in order flatten the seismic events. The result can be used for qualitative assessment. The complex geometry has to be kept in mind during such evaluations. The shot offset information cannot be used directly for evaluation of the linear dimensions of the objects of interest.

Two seismic profiles recorded by OBS B were investigated (Fig. 7.12). The features in the data were the same as for the normal incidence seismic sections, except for the pull up of the seismic events inside the blank zone.

The blanking is clearly recognizable on the OBS seismic sections. Most of the seismic events can be traced through it, especially in the upper and lower parts. In the middle part (between 50 and 200 ms two-way travel time from the sea bottom), the recognition of the events is obstructed not only because of the reduced amplitude, but also due to disturbed linearity of the reflections.

The diffraction features are also more recognizable compared to the normal incidence data. In addition to the strong diffractions from the top of the blank zone and weaker diffractions in the middle part of it, diffraction hyperbolae can be recognized near the BSR. Due to the high horizontal resolution, it is now possible to estimate the width of the objects that cause the diffraction of the seismic signal. Their horizontal size is several times smaller than the width of the blank zone. It is worth noting that diffractions close to the BSR are stronger than those in the middle part of the blank

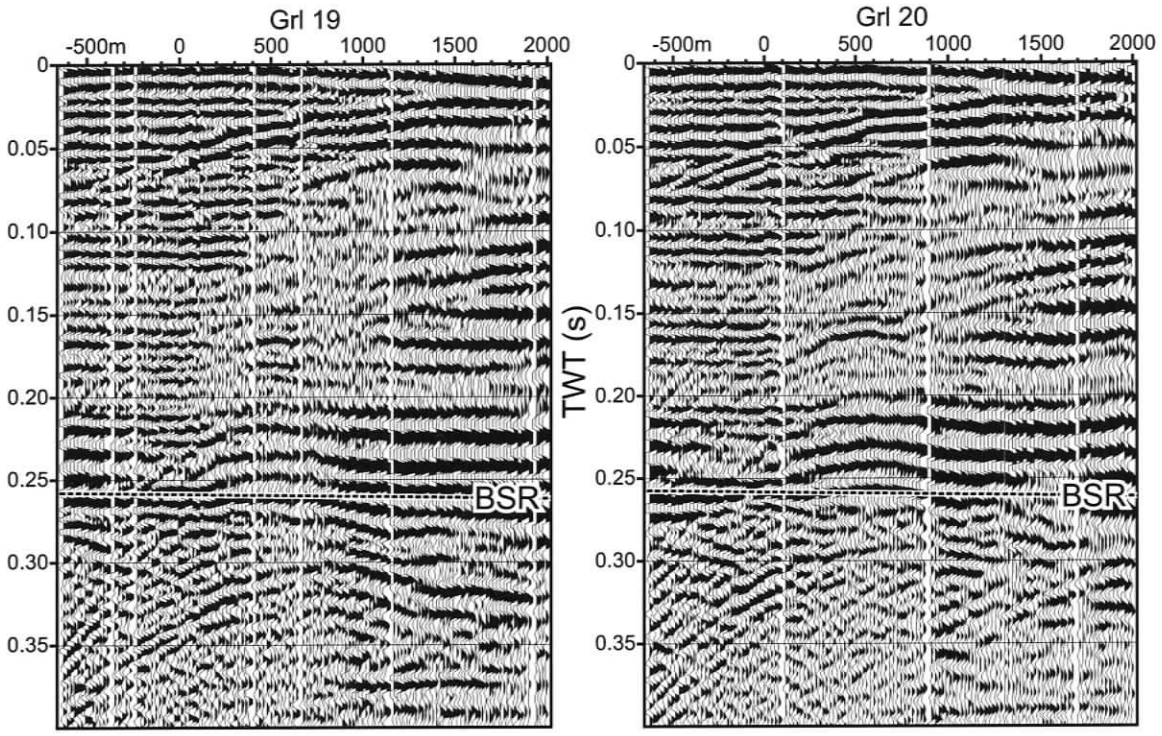

Figure 7.12: Grl-19 and Grl-20 profiles recorded on OBS B with NMO correction applied. Due to asymmetric geometry, the reflection points for a single trace are located on a tilted line. The reflections from the top of the blank zone are recognizable on traces with large offsets ($> 1500\ m$), deeper parts of the zone are represented on closer traces ($< 1000\ m$). Offset is calculated from the projection of the OBS position onto the profile. The horizontal distances from OBS B to Grl-19 and Grl-20 are 950 and 1130 m accordingly (see Fig. 3.2).

zone and almost of the same strength as at its top. In addition, the size of the objects that cause these diffractions can be estimated to be larger at the bottom than in the middle part, since the width of the vertex of the diffractional curve is larger compared to the diffractions in the middle of the zone.

The absence of pull up features for the deep reflectors supports the hypothesis that the high velocity zone is restricted to the top of the sediment section, rather than spread over the entire volume of blank zone. The rays reflected from the deeper parts of the blank zone have larger offsets and do not pass through the high velocity layers, and hence no pull up of the reflection events is observed.

7.3.3 Structural model of the vent zone

A model that helps to explain most of the observations at the vent site was suggested by Riedel et al. (2006) (Fig. 7.13a). The model assumes the presence of a hydrate lens at the top of the blank zone and thin layers of sediments with initially higher than average porosity, but at present time containing gas hydrates in small concentrations. The methane is delivered into localized hydrate formation areas through a network of thin channels in either a dissolved form or as a free gas. In addition, Zühlsdorff and Spieß (2004) suggested episodic focused fluid flow. The episodic nature of the phenomena is justified by the necessity to build up the pore fluid pressure high enough to push the fluids through the sediments from the BSR depth to the sea bottom.

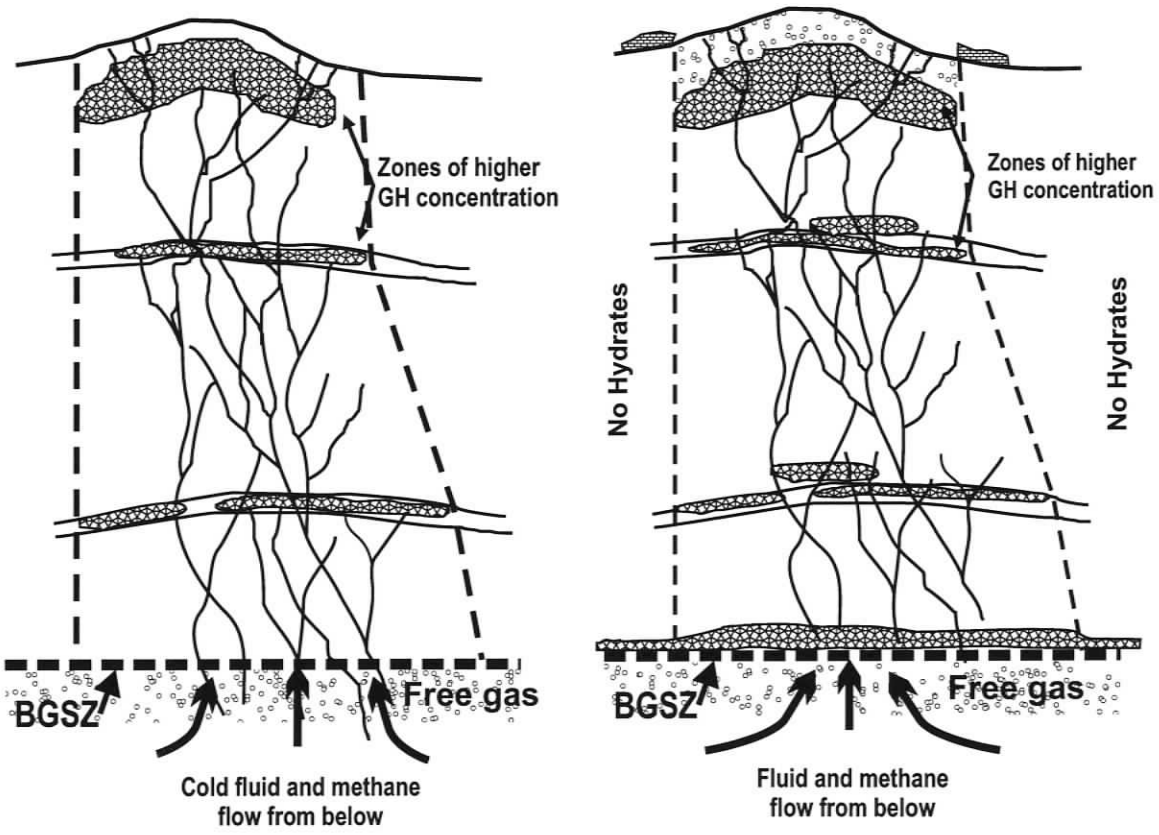

Figure 7.13: Suggested structure of the Bullseye vent zone based on seismic and other observations; a) – model by Riedel et al. (2006); b) – model produced using previous data and results of this study

While the above mentioned model satisfies most of the data for the Bullseye vent zone, there are still several questions that are unanswered. Within the framework of this study, this model was modified in order to comply better with the observations better.

As noted earlier, authigenic carbonates are present in the vicinity and the central part of the vent zone in the form of sheets that pave the sediment surface. Video data shows that some carbonate sheets were suspended over the sea bottom, with a water gap between the bottom side of the sheet and the top of the sediments. The suspended sheets of carbonate suggests extensive weathering of the sediments around them, as the carbonates can only be formed inside the sediments or in contact with them, since otherwise sufficient concentrations of ions needed for the carbonate formation cannot be achieved.

In places where the carbonate pavement is in contact with the seafloor, the seafloor reflection coefficient may increase over the average value. This occurred within the high reflection coefficient ring that surrounded the blank zone (Fig. 7.8).

The hydrate cap that consists of either layers with high hydrate concentration or dispersed hydrate chunks and lenses is responsible for the pull up of the travel time for the seismic events inside the blank zone. The hydrate cap also acts as a diffractor.

For a cap thickness of about 30 m, the observed pull up of 5 ms will be achieved if the velocity in the affected sediments are 200 m/s more than the velocity in the adjacent sediments. Such an increase of the velocity translates into gas hydrate concentrations of about 15–17% of total sediment volume.

However, the results of the travel time tomography (Figs. 5.10–5.14) do not reveal any significant velocity anomaly associated with the blank zone, which indicates that the bulk velocity increase within the zone is low. If a high velocity zone is present at the top of the blanking feature, the rest of the vent zone is represented by sediments with a seismic velocity similar to that of the sediments outside.

One of the most controversial facts is that on the single and multichannel seismic recordings (central frequency 150 Hz) a signal from below the BSR is received

(Fig. 7.11). The signal strength is comparable to that in the adjacent areas of the blank zone. This observation indicates that the blanking for this range of low frequencies cannot be caused either by high attenuation of the sediments inside the vent zone or by dispersion of the seismic energy. Signal from the deeper layers suggests penetration of the seismic energy through the blank zone. In this case, the logical explanation would be the seismic transparency of the sediments inside the vent zone. In contrast, almost absolute blanking for the higher frequency systems suggests that the seismic energy is either absorbed by the sediments or dispersed for those frequencies.

The inability to explain the blanking phenomena with one mechanism for different experiments leads to the conclusion that the blanking mechanism is different for different frequencies.

Blanking of the signal for high frequency systems and low seafloor reflection coefficients inside the limits of the blank zone for the COAMS and Teledyne systems most likely have the same cause. Both phenomena may be attributed to processes happening in the top few metres of the sediment section above the hydrate cap, such as free gas seepage or increased porosity.

As discussed before, the reflected seismic events in the slope sediment section in most cases are caused by thin layers of different lithology, e.g., silts with larger than average grain size, or sands. Selective formation of hydrates in specific layers rather than an even distribution over the sediment section would smooth the velocity profile, reducing the impedance contrast between the adjacent layers. That is, the blanking in the middle part of the vent zone for the 150 Hz systems is most likely caused not by attenuation or scattering of the seismic energy, but due to increased acoustic transparency of the sediments. This situation is similar to the observations at the Blake Ridge gas hydrate site (Lee and Dillon, 2001). The concentration of gas hydrate required to produce this type of blanking can be as low as a few percent (Lee and Dillon, 2001), which would not affect the bulk P-wave velocity of the sediments greatly.

The presence of the strong diffractions in close proximity to the BSR that are

observed on the seismic sections recorded by OBS B suggests a physical condition similar to the one at the top of the vent. A structure like the hydrate cap can be in place at the BSR inside the limits of the blank zone. These hydrates were most likely formed by to free gas entering the GHSZ from below.

Also, it is worth noting that the vertical axis of the blank zones goes through the intersection of the BSR and accreted sediment boundary (Fig. 7.14). The coincidence of these two boundaries may be the controlling factor for the blank zone location. The accreted sediments are more compacted than the slope sediments, and at the same time they are more permeable due to the presence of cracks. On the other hand, filling the cracks with gas hydrates can greatly reduce their permeability. That is, below the bottom of the GHSZ, accreted sediments are more permeable than slope sediments, and above this boundary the situation may reverse forcing the fluids to penetrate through the slope sediment section.

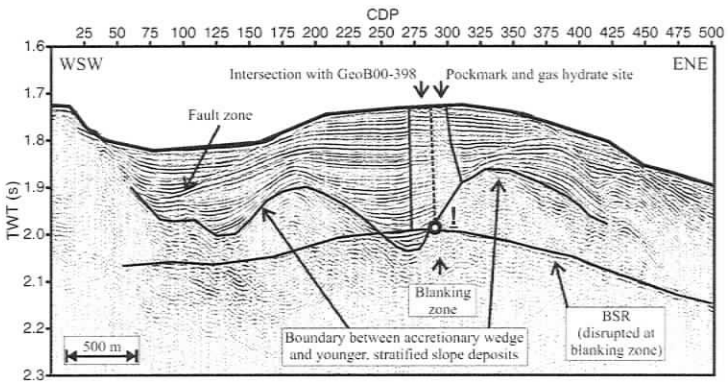

Figure 7.14: Blank zone central axis coincides with the intersection point of the BSR and boundary between accreted and slope sediments. Based on multichannel seismic data by (Zühlsdorff and Spieß, 2004).

7.3.4 Preliminary results of IODP 311 expedition

During the period from 28 August to 28 October of 2005 IODP 311 expedition targeted gas hydrates at Northern Cascadia (Expedition 311 Scientists, 2005). A total of five sites were successfully drilled, one of which (1328) was dedicated to the Bullseye vent. An extensive range of methods and tools were used during the study, including Logging While Drilling and Pressure Core Sampling. Some of the most important results on porosity, resistivity and chlorinity are presented on Figure 7.15.

The main findings relevant to this study can be summarized as follows:

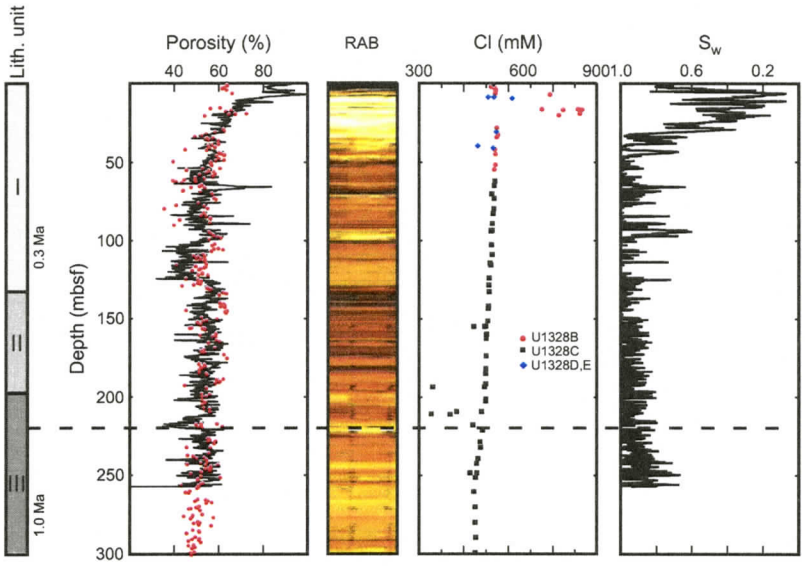

Figure 7.15: Summary of core and downhole logging data from Site U1328 IODP 311 Expedition (Expedition 311 Scientists, 2005). Shown are lithostratigraphic units subdivision, porosity from logging while drilling (LWD) analysis, resistivity-at-the-bit (RAB)image, pore water chlorinity, and pore water saturation (S_w) derived from LWD data using Archie's law.

1. Gas hydrates are localized to three places: (i) between the seafloor and 46 $mbsf$; (ii) at a depth of 160 $mbsf$; and (iii) in the interval 10 m thick above the BSR. Virtually no hydrate is present through the rest of the sediment section.
2. Occurrence of near sediment surface hydrates is associated with a strong positive chlorinity anomalies.
3. Concentration of gas hydrates from 0 to 46 $mbsf$ can be as high as 80% of pore space for certain layers, according to the resistivity measurements.
4. Dipping fractures were inferred from the RAB image, which can be interpreted as migration conduits for fluids that feed near seafloor gas hydrate accumulations.

In general, the new findings support the structure of the blank zone and the distribution of gas hydrates with depth proposed in this study based on the velocity model

from the tomographic inversion and analysis of the seismic data: a layer of several 10's of metres thick at the top of the sediment section; no presence of hydrates in significant concentrations below the layer to the BSR; and occurrence of gas hydrates just above the BSR.

Probably the most intriguing result is high chlorinity data for the pore water inside the top layer. The maximum values exceeded 850 mM, i.e. 50% larger than normal (560 mM) (Expedition 311 Scientists, 2005). Considering the usual freshening of the pore water due to hydrate dissociation, *in situ* values for chlorinity may be even greater. High chlorinity of pore waters was interpreted as the outcome of an ongoing process of hydrate formation, which results in salt exclusion from the water lattice structure (Expedition 311 Scientists, 2005). On one hand, under normal circumstances the excessive salt would be removed by advective or diffusive processes in a short period of time . Thus the formation of hydrates can be dated as very recent. On the other hand, evacuation of the brine can be significantly slowed by the sediment layers with hydrates occupying 80% of the pore space, which significantly reduces permeability.

7.3.5 Bullseye vent zone — extinct mud volcano? (Cold vent was hot in the past?)

While the model for the present structure of the blank zone is vital for the blanking phenomena explanation, a model for the evolution of the vent zone is no less important. Moreover, the information about what processes were taking place at the vent zone in the past may help in understanding its present structure.

The accretionary wedge is a dynamic environment. The accretionary prism lengthens as more material is introduced, and so, a site on the wedge moves further and further away from the deformation front. Together with the increasing distance, other conditions may change that depend on the proximity of the site to the deformation front. One such condition is pore fluid pressure, which can be related to the fluid flow.

The abundance of the carbonates around the Bullseye vent site, for which the methane was a source of carbon (Conly et al., 2005), suggests active venting in the past to supply the necessary amount of methane.

The hydrate occurrence zonation at the vent site is similar to that observed at some presently active mud volcanoes, e.g., Håkon Mosby mud volcano in Barents Sea (Ginsburg et al., 1999). Also the vertical distribution of gas hydrate, that is the hydrate lens at the top of the vent, is analogous to the above-mentioned mud volcano (Egorov, 2000). Presence of similar biota and carbonates at "Mound 11" mud volcano at Costa Rica forearc (Schmidt et al., 2005) helps to draw a parallel between that site and Bullseye vent zone. The seafloor expression of the Bullseye vent zone is also similar to the mounds observed on top of the mud volcanoes.

All the above mentioned facts lead to a logical conclusion that the Bullseye vent zone in the past may have been a mud volcano. At present, the supply of fluids has expired or has been greatly reduced, but the structure itself and, more importantly, the accumulation of gas hydrates and carbonates remain as a relict.

This assumption is consistent with the Wood et al. (2002) model (derived from modelling the heat and fluid flux) in which blanking is explained by hot venting and the resulting disturbed gas hydrate zone. While the present state of the vent zone is cold, in the past hotter fluid flux may have taken place. Such flux could be responsible for the large volumes of methane needed for the formation of the carbonates and hydrate lens at the top of the vent zone. The paleo conduit through which the fluids and methane were delivered to the sea bottom was responsible for the formation of the small hydrate bodies along it (Fig. 7.13b). These bodies now are imaged as the diffractional features on the seismic sections (see Fig. 7.12). Also, the active stage of the mud volcano led to the formation of the present system of thin conduits for the fluid flow through the hydraulic fracturing.

The current slow venting state prohibits the transportation of the methane in free gas form through the gas hydrate stability field, as the methane would be immediately converted into gas hydrates,since abundant water is available for the formation. The

free methane supplied from beneath the BSR is formed into gas hydrate upon entering the GHSZ, forming the relatively thin (few tens of metres) zone of higher hydrate concentration at that depth.

The hypothesis of a more active vent zone in the past requires the explanation of a possible mechanism. Two alternatives can be proposed. One deals with the distribution of the pore pressure with the distance from the deformation front, and the other takes into account local stress.

The process of scraping the sediments from the incoming plate leads to a thickening of the sedimentary layer at the accretionary prism. In this case underconsolidated sediments with high porosity can be found at a depth of several kilometers (Hyndman and Davis, 1992). The compression of the sediments under its own weight creates overpressure of the fluids in the pore space. The maximum pore pressure (80% of the lithostatic pressure) is achieved at about 15 km from the deformation front (Hyndman, 1995). After going through the maximum it decreases landward. The increased pore fluid pressure can be the driving force for an active fluid expulsion through such formations as mud volcanoes.

According to this model, the active phase of the Bullseye vent zone occurred at a time when it was closer to the deformation front, i.e., a few hundred thousand years ago. The current position of the site is about 22 km from the tip of the accretionary prism and the pore pressure in the underlying sediments is not high enough to provide the necessary high fluid flow rates.

An example of active venting behavior nearby is the Hydrate Ridge vent sites in the South Cascadia region. Currently, the ridge is a very active venting zone, as methane in free gas form is being expelled into the water column (Shipboard Scientific Party, 2003). Formation of carbonates and seafloor hydrate are also reported at this site. The distance of Hydrate Ridge from the deformation front is about 17 km, which is at the distance of the expected pore fluid pressure maximum. However, there is a distinction that separates the Hydrate Ridge site from the Bullseye vent. At Hydrate Ridge there is a fluid conduit system in place that facilitates the fluid supply to the

zone of unloading. In general, however, the Hydrate Ridge venting system might be considered as an example of an early stage of the development of the Bullseye vent site.

The active, mud-volcano-like venting at the Bullseye vent site can also be explained by local tectonic processes, such as an event causing the uplift of the seafloor block that hosts the vent field. The uplift was the result of stress that may have led to an increase of pore pressure. The location of a population of the blank zones, among which Bullseye is the largest, along the central elongated axis of the block supports this alternative.

After the inferred large methane flux event that was responsible for the formation of the massive hydrate at the top of the vent zone, smaller events followed, most likely as described by Zühlsdorff and Spieß (2004). In between the events the hydrate cap released methane in the dissolved form into the system in small amounts through hydrate dissociation process. Although hydrate is within its stability zone, hydrate dissociation can occur due to disequilibrium in the hydrate-water-free methane system, because the concentrations of methane in the pore water are so low.

Smaller blank zones located near the Bullseye vent, most of which do not reach the top of the sediment, can be interpreted as immature mud volcanoes, which stopped developing due to termination of the fluid supply in sufficiently large volumes.

In the current state, the supply of methane to the top of the sediment section occurs by fluid flow through the system of small cracks that penetrate through the GHSZ within the limits of the vent site, as suggested by (Riedel et al., 2006). This prevents the hydrate lens from being completely wasting away due to hydrate dissociation by supplying additional methane into the zone rejuvenating the accumulation. The release of methane into free gas occurs due to the decreasing methane solubility profile inside the GHSZ. Also, the presence of brines in the top 40 m of the sediment section provides an additional geochemical barrier for dissolved methane, forcing it to escape from the solution into the free gas state, as the increase in salinity decreases the solubility of methane.

Better understanding of the origin of the vent zone can be achieved through accurate dating of the events, such as time of carbonate formation, the age of the sediments at the top of the blank zone and deeper parts, as well as the timing of the recent local tectonic events.

7.3.6 Unresolved controversial issues

Major apparent contradictions in the existing model can be outlined as follows:

- Seafloor reflection coefficient inside the limits of the blank zone: studies of the reflection coefficient using single channel and OBS seismic data provide values up to two times lower for the inside blank zone area compared to those for outside; on the other hand, calculations of the reflection coefficient using physical properties measurements indicate the reverse pattern.
- Gas hydrate concentration inside the vent zone: the CSEM experiment (Schwalenberg et al., 2005) revealed anomalously high resistivity values for the sediments inside the Bullseye vent zone at depths of 90 m and 150 m, which were interpreted as a result of high hydrate concentrations in the sediments; neither the tomography velocity studies nor the IODP drilling showed any significant presence of hydrates for the depth intervals in question that can affect the resistivity of the sediments.

These controversial issues require further clarification and possible review of the models used for interpretation of the observations.

Chapter 8

Summary and Conclusions

8.1 New techniques

In the framework of this study of the COAMS-99 OBS experiment, several new techniques were developed and applied to the data.

A new method for localization of sources and receivers using the direct wave travel time information was developed based on previously available travel time inversion algorithms (Chapter 4). The method greatly improves the quality of localization. It allows the user to resolve the non-linear time drift experienced by clocks of autonomous recording stations using piecewise linear approximation. The method is most suitable for the application to the surveys with multiple lines which were shot in one sequence.

Amplitude analysis was applied to an unconventional data set obtained using OBSs. The complicating factors consisted of the common receiver geometry, and placement of the receivers on the seafloor. Maps of the reflection coefficient of the seafloor and the BSR proved that such a data set can be successfully used for the mapping of the reflection coefficient distribution along an interface, both at the seafloor and within the sediment section (Section 6.4). Also, OBS data can be used for the Amplitude Variation with Offset analysis to provide the information on the change of the acoustic properties at the interface (Section 6.5).

8.2 Scientific results

The available seismic data set recorded by five OBS stations was used in conjunction with conventional seismic data for the investigation of the structure of the Bullseye vent zone. A 3-D velocity model was obtained by means of travel time tomography for the region around the Bullseye vent site (Section 5.5). The model does not reveal any large velocity anomalies. The anomaly associated with the vent zone was found to be in the range of 25 m/s, which suggests no anomalous high gas hydrate concentration inside the blank zone. Unfortunately, higher resolution (vertically) of sediment volumes with anomalous velocities was not possible due to limitations of the experiment geometry. Nevertheless, a combination of the tomography results with available seismic and other information about the site suggests that a layer of high gas hydrate concentration (15% or more) is located at the top of the vent zone. The rest of the blank zone may contain local concentrations of hydrates in small amounts.

The average velocity profile for the site starts with compressional velocities close to those in the sea water, and increases virtually linearly reaching about 1750 m/s at the BSR. The velocity profile does not reveal any significant variations from the background no-hydrate velocity profile for the slope sediments, which suggests that slope sediments outside the blank zone contain no or very little gas hydrate down to the BSR.

A map of seafloor reflection coefficients was created from amplitude data using the sea surface multiple (Fig. 6.12). The positions of the reflection points on the seafloor were obtained using a ray tracing code, which provided high accuracy. The map revealed the presence of a low reflectivity zone with the limits matching the border of the blank zone inside the sediments. The low reflection coefficient zone is outlined by a higher than average reflectivity rim, which is believed to be a result of the presence of carbonate pavement.

By combining the results of this study with the previously known information, a probable model of the blank zone genesis can be suggested. There are strong indicators of a significantly higher methane flux in the past than it is observed now.

The suggestion was made that in the past there was a mud volcano, which died out due to decreased fluid supply.

The major points stated in this study on the structure of the Bullseye vent site and distribution of gas hydrates were supported by the preliminary results of the recent drilling at the site conducted during IODP 311 expedition.

8.3 Recommendation for future work

Sea bottom receiver stations are clearly suitable for the purposes of 3-D travel time tomography and amplitude inversions. However, for the recovery of the finer scale velocity structure that may be associated with the vent zone, a more dense distribution of stations is recommended. The most efficient geometry of the OBS for the purpose of the GHSZ study, considering the water depth and depth of the BSR at the site, would be with the maximum distance between the stations of about 250 m. In general, the distance between the stations should be no more than two times the depth of the interface being investigated. In this case the uncertainty of the final model will be in order of few tens of metres per second or better due to denser ray coverage of the studied volume. This would also create more reliable maps of the reflection coefficients for the interfaces inside the sediment column. The geometry of the shot lines with 200 m spacing for the OBS data set is thought to be a good choice, although the normal incidence data would require closer spacing. The length of the seismic lines should extend no less than 2 km away from the limits of the area under investigation. However, offsets greater than 3.5 km are redundant for the Bullseye vent study area.

The use of OBH-on-a-rope technique can be recommended, in which the anchor is attached to the station using an extension rope. By employing this technique, the recording station can be placed up to 100–200 m above the sea bottom. This geometry allows recording of the direct water wave arrival and sea bottom reflection separately. Also, a greater coverage of the near sea bottom interfaces can be achieved.

8.4 Importance of the study

Blank zones provide a promising focus of investigation of gas hydrate as future energy resource. The average outside vent zones, concentration of hydrates in the sediment column is low and tends to be focused closer to the BSR, i.e. at depth of several hundred metres. In contrast, inside the blank zones, gas hydrate can occur within a few metres of the sea bottom, and in this type of conditions clathrates tend to form massive bodies. Future harvesting of gas hydrates is more likely to be from massive aggregations, rather than from low hydrate concentrations in sediments.

Bibliography

Aki, K. and P.G. Richards (1980). *Quantitative Seismology: Theory and Methods*, volume I. W.H. Freeman and Co., 1980.

Bangs, N.L.B., R.J. Musgrave, and A.M. Tréhu (2005). Upward shifts in the southern Hydrate Ridge gas hydrate stability zone following postglacial warming, offshore Oregon. *Journal of Geophysical Research*, **110**(B3).

Barlee, M., S.E. Dosso, and P. Schey (2002). Array element localization of a bottom moored hydrophone array. *Canadian Acoustics*, **30**(4):3–11.

Berner, R.A. (1980). *Early diagenesis; a theoretical approach.* Princeton Univ. Press, 1980.

Booth, J.S., M.M. Rowe, and K.M. Fischer (1996). Offshore gas hydrate sample database with an overview and preliminary analysis. Open-File Report 96-272, U.S. Geological Survey, 1996.

Bouriak, S., M. Vanneste, and A. Saoutkine (2000). Inferred gas hydrates and clay diapirs near the Storegga Slide on the southern edge of the Vøring Plateau, offshore Norway. *Marine Geology*, **163**(1-4):125–148.

Brewer, P.G., M.O. Franklin, M. Orr, G. Friederich, K.A. Kvenvolden, and D.L. Orange (1998). Gas hydrate formation in the deep sea: In situ experiments with controlled release of methane, natural gas, and carbon dioxide. *Energy & Fuels*, **12**:183–188.

Buffett, B. and D. Archer (2004). Global inventory of methane clathrate: sensitivity to changes in the deep ocean. *Earth and Planetary Science Letters*, **227**(3-4): 185–199.

Canfield, D.E. and R.A. Berner (1987). Dissolution and pyritization of magnetite in anoxic marine sediments. *Geochimica et Cosmochimica Acta*, **51**(3):645–659.

Caulet, J.P. (1995). Radiolarians from the Cascadia margin, leg 146. *In:* B. Carson, G.M. Westbrook, R.J. Musgrave, and E. Suess (eds.), *Proceedings of the Ocean Drilling Program, Scientific Results*, volume 146, pages 47–61. College Station, TX (Ocean Drilling Program), 1995.

Chapman, N.R., J.F. Gettrust, R. Walia, D. Hannay, G.D. Spence, W.T. Wood, and R.D. Hyndman (2002). High-resolution, deep-towed, multichannel seismic survey of deep-sea gas hydrates off western canada. *Geophysics*, **67**(4):1038–1047.

Chapman, R., J. Pohlman, R. Coffin, J. Chanton, and L. Lapham (2004). Thermogenic gas hydrates in Northern Cascadia margin. *Eos Trans. AGU*, **85**(38).

Clennel, M.B., M. Hovland, J.S. Booth, P. Henry, and W.J. Winters (1999). Formation of natural gas hydrates in marine sediments 1. Conceptual model of gas hydrate growth conditioned by host sediment properties. *Journal of Geophysical Research*, **104**(B10):22985–23003.

Collett, T.S. (1993). Natural gas hydrates of the Prudhoe Bay – Kuparuk River area, North Slope, Alaska. *AAPG Bulletin*, **77**:793–812.

Collett, T.S. (2000). Natural gas hydrates: Resource of the 21^{st} century. WWW based publication, link: `http://emd.aapg.org/technical_areas/gas_hydrates/resource_toc.cfm`, 2000.

Conly, A.G., S.D. Scott, and M. Riedel (2005). Mineralogy and stable isotope compositions of carbonate and sulphide minerals of carbonate crusts associated with gas hydrate-forming cold vents from the ne pacific. *In: GAC-MAC-CSPG-CSSS Joint Meeting, Halifax, Nova Scotia, Abstracts*, volume 30, 2005.

Dallimore, S.R., T.S. Collett, T. Uchida, and M. Weber (2002). Overview of the 2002 mallik gas hydrate production research well program. *In: Proceedings of the 4th International Conference on Gas Hydrates*, pages 36–39. 2002.

Davie, M.K., O.Y. Zatsepina, and B.A. Buffett (2004). Methane solubility in marine hydrate environments. *Marine Geology*, **203**:177–184.

Davis, E.E. and R.D. Hyndman (1989). Accretion and recent deformation of sediments along the northern Cascadia subduction zone. *Geological Society of America Bulletin*, **101**(11):1465–1480.

Davis, E.E., R.D. Hyndman, and H. Villinger (1990). Rates of fluid expulsion across the Northern Cascadia accretionary prism: Constraints from new heat floe and multichannel seismic reflection data. *Journal of Geophysical Research*, **95**(B6): 8869–8889.

Degtyarev, B.V. (1969). *Bor'ba s gitratami pri ekspluatatsii gazovykh skvashin v rayonakh Severa, prakticheskoye rukovodstvo (The fight with hydrates during exploitation of gas wells in the northern regions. Practical handbook).* Nedra (Moskva), 1969.

Dillon, W.P. and M.D. Max (2000). Oceanic gas hydrates. *In:* M.D. Max (ed.), *Natural Gas Hydrate in Oceanic and Permafrost Environments*, pages 61–76. Kluwer Academic, 2000.

Dobrynin, V.M., Y.P. Korotayev, and D.V. Pluschev (1983). Gas hydrates — a possible energy resource. *In:* R.G. Meyer and J.C. Olson (eds.), *Long-term Energy Resources*, pages 727–729. Pitman, Boston, 1983.

Dosso, S.E. (2002). Quantifying uncertainties in geoacoustic inversion I: A fast Gibbs sampler approach. *J. Acoust. Soc. Am.*, **111**(1):129–142.

Dosso, S.E. and N.E. Collison (2001). Regularized inversion for towed-array shape estimation. *In:* M. Taroudakis and G. Makrakis (eds.), *Inverse Problems in Underwater Acoustics*, chapter 6, pages 77–103. Springer-Verlag, 2001.

Dosso, S.E., M.R. Fallat, B.J. Sotirin, and J.L. Newton (1998). Array element localization for horizontal arrays via Occam's inversion. *J. Acoust. Soc. Am.*, **104**(2 part 1):846–859.

Dosso, S.E. and B.J. Sotirin (1999). Optimal array element localization. *J. Acoust. Soc. Am.*, **106**(6):3445–3459.

Dvorkin, J., M.B. Helgerud, W.F. Waite, S.H. Kirby, and A. Nur (2000). Introduction to physical properties and elasticity models. *In:* M.D. Max (ed.), *Natural Gas Hydrate in Oceanic and Permafrost Environments*, pages 245–260. Kluwer Academic, 2000.

Egorov, A.V. (2000). Formation and dissociation of the seafloor gas hydrates. *In: Proceedings of Indo-Russian Joint Workshop on Gas Hydrates Under Iltp*, 2000.

Englezos, P. (1993). Clathrate hydrates. *Industrial & Engineering Chemistry Research*, **32**(7):1251–1274.

Evangelidis, C.P., T.A. Minshull, and T.J. Henstock (2004). Three-dimensional crustal structure of Ascension Island from active source seismic tomography. *Geophysical Journal International*, **159**(1):311–325.

Expedition 311 Scientists (2005). Cascadia margin gas hydrates. Iodp preliminary report, 2005.

R.W. Fairbridge (ed.). *The encyclopedia of oceanography; encyclopedia of earth sciences series, V. 1.* New York, Reinhold Publishing Corp., 1966.

Fink, C.R. and G.D. Spence (1999). Hydrate distribution off vancouver island from multifrequency single-channel seismic reflection data. *Journal of Geophysical Research*, **104**(B2):2909–2922.

Formolo, M.J., T.W. Lyons, C. Zhang, C. Kelley, R. Sassen, J. Horita, and D.R. Cole (2004). Quantifying carbon sources in the formation of authigenic carbonates at gas hydrate sites in the Gulf of Mexico. *Chemical Geology*, **205**(3-4):253–264. doi:10.1016/j.chemgeo.2003.12.021.

Foucher, J.P., H. Nouze, and P. Henry (2002). Observation and tentative interpretation of a double BSR on the Nankai Slope. *Marine Geology*, **187**(1-2):161–175.

Franzblau, A.M. (1958). *A Primer of Statistics for Non-Statisticians*. Harcourt and Brace, 1958.

Funck, T., K.E. Louden, R.J. Wardle, J. Hall, J.W. Hobro, M.H. Salisbury, and A. Muzzatti (2000). Three-dimensional structure of the torngat orogen (ne canada) from active seismic tomography. *Journal of Geophysical Research*, **105**(B10):23403–23420.

Ganguly, N., G.D. Spence, N.R. Chapman, and R.D. Hyndman (2000). Heta flow variations from bottom simulating reflectors on the Cascadia margin. *Marine Geology*, **164**(1-2):53–68.

Gettrust, J.F., W.T. Wood, and S.E. Spychalski (2004). High-resolution MCS in deep water. *The Leading Edge*, **23**(4):374–377.

Ginsburg, G.D., A.V. Milkov, V.A. Soloviev, A.V. Egorov, G.A. Cherdashev, P.R. Vogt, K. Crane, T.D. Lorenson, and M.D. Khutorskoy (1999). Gas hydrate accumulation at the Håkon-Mosby mud volcano. *Geo-Marine Letters*, **19**:57–67.

Ginsburg, G.D. and V.A. Soloviev (1998). *Submarine Gas Hydrates*. St.-Petersburg, 1998.

Hamilton, E.L. (1980). Geoacoustic modelling of the seafloor. *J. Acoust. Soc. Am.*, **68**(5):1313–1340.

Hammerschmidt, E.G. (1934). Formation of gas hydrates in natural gas transmission lines. *Industrial & Engineering Chemistry Research*, **26**(8):851–855.

Handa, Y.P. (1990). Effect of hydrostatic pressure and salinity on the stability of gas hydrates. *Journal of Physical Chemistry*, **94**:2652–2657.

Helgerud, M.B., J. Dvorkin, A. Nur, A. Sakai, and T. Collett (1999). Elastic-wave velocity in marine sediments with gas hydrates: Effective medium modelling. *Geophysical Research Letters*, **26**(13):2021–2024.

Hobro, J.W.D. (1999). *Three-dimensional tomographic inversion of combined reflection and refraction seismic travel-times data*. PhD thesis, University of Cambridge, 1999.

Hobro, J.W.D. (2000). Seismic travel-time tomography in three dimensions: Synthetic experiments and results obtained using jive3d. *In: LITHOS Science Report*, volume 2, pages 11–20. University of Cambridge, Department of Earth Sciences, 2000a.

Hobro, J.W.D., S.C. Singh, and T. A.Minshull (2003). Three-dimensional tomographic inversion of combined reflection and refraction seismic traveltime data. **152**(1):79–93.

Hobro, J.W.D. (2000). *Joint Interface and Velocity Estimation in Three Dimensions: Instructions for use, version 1.0*, March 2000b.

Holbrook, W.S. (2001). Seismic studies of the Blake Ridge: Implications for hydrate distribution, methane expulsion, and free gas dynamics. *In:* C.K. Paull and W.P. Dillon (eds.), *Natural Gas Hydrates: Occurrence, Distribution, and Detection*, pages 235–256. American Geophysical Union, Washington, DC, 2001.

Hovland, M. and O.T. Gudmestad (2001). Potential influence of gas hydrate on seabed installations. *In:* C.K. Paull and W.P. Dillon (eds.), *Natural Gas Hydrates: Occurrence, Distribution, and Detection*, pages 307–315. American Geophysical Union, Washington, DC, 2001.

Hyndman, R.D. (1992). Ïcëbeneath the deep sea; studies of methane hydrate layers beneath the continental slope off Vancouver Island. *Geoscience Canada*, **19**(1): 21–26.

Hyndman, R.D. (1994). Regional geophysics and structural framework of the Vancouver Island margin accretionary prism. *In: Proceedings of the Ocean Drilling Program, Part A: Initial Reports*, volume 146, pages 399–419. Texas A & M University, Ocean Drilling Program, College Station, TX, United States, 1994.

Hyndman, R.D. (1995). The Lithoprobe corridor across the Vancouver Island continental margin; the structural and tectonic consequences of subduction. *Canadian Journal of Earth Sciences*, **32**(10):1777–1802.

Hyndman, R.D. and E.E. Davis (1992). A mechanism for the formation of methane hydrate and seafloor bottom-simulating reflectors by vertical fluid expulsion. *Journal of Geophysical Research*, **97**(B5):7025–7041.

Hyndman, R.D. and G.D. Spence (1992). A seismic study of methane hydrate marine bottom simulating reflectors. *Journal of Geophysical Research*, **97**(B5):6683–6698.

Hyndman, R.D., G.D. Spence, R. Chapman, M. Riedel, and R.N. Edwards (2001). Geophysical studies of marine gas hydrate in Northern Cascadia. *In: Natural Gas Hydrates: Occurrence, Distribution, and Detection. Geophysical Monograph 124.* AGU, 2001.

Hyndman, R.D., T. Yuan, and K. Moran (1999). The concentration of deep sea gas hydrates from downhole electrical resistivity logs and laboratory data. *Earth and Planetary Science Letters*, **172**:167–177.

Kastner, M. (2001). Gas hydrates in convergent margins: Formation, occurrence, geochemistry, and global significance. *In:* C.K. Paull and W.P. Dillon (eds.), *Natural Gas Hydrates: Occurrence, Distribution, and Detection*, pages 67–86. American Geophysical Union, Washington, DC, 2001.

Kvenvolden, K.A. (1993). Gas hydrates — geological perspective and global change. *Reviews of Geophysics*, **31**(2):173–187.

Kvenvolden, K.A. (1998). A primer on the geological occurrence of gas hydrate. *In:* J.P. Henriet and J. Mienert (eds.), *Gas Hydrates: Relevance to World Margin Stability and Climate Change*, volume 137, pages 9–30. Geological Society, London, Special Publications, 1998.

Kvenvolden, K.A. (1999). Potential effects of gas hydrates on human welfare. *Proceedings of the National Academy of Science of the USA*, **96**(7):3420–3426.

Kvenvolden, K.A. and T.D. Lorenson (2001). The global occurrence of natural gas hydrates. *In:* C.K. Paull and W.P. Dillon (eds.), *Natural Gas Hydrates: Occurrence, Distribution, and Detection*, pages 3–18. American Geophysical Union, Washington, DC, 2001.

Lee, M.W. and T.S. Collett (2001). Comparison of elastic velocity models of gas-hydrate-bearing sediments. *In:* C.K. Paull and W.P. Dillon (eds.), *Natural Gas Hydrates: Occurrence, Distribution, and Detection*, pages 179–187. American Geophysical Union, Washington, DC, 2001.

Lee, M.W. and W.P. Dillon (2001). Amplitude blanking related to the pore-filling of gas hydrate in sediments. *Marine Geophysical Researches*, **22**(2):101–109.

Lee, M.W., D.R. Hutchinson, W.P. Dillon, J.J. Miller, W.F. Agena, and B.A. Swift (1993). Method of estimating the amount of *in situ* gas hydrate in deep marine sediments. *Marine and Petroleum Geology*, **10**(5):493–505.

Luff, R., K. Wallmann, and G. Aloisi (2004). Numerical modeling of carbonate crust formation at cold vent sites; significance for fluid and methane budgets and chemosynthetic biological communities. *Earth and Planetary Science Letters*, **221** (1-4):337–353. doi:10.1016/S0012-821X(04)00107-4.

MacDonald, J.G. (1990). Role of methane clathrates in past and future climates. *Climatic Change*, **16**:247–281.

Makogon, Y.F. (1984). Razrabotka gazogidratnoy zalezhi (gas production from the natural gas hydrate deposits). *Gazovaya Promishlennost*, **10**:24–26.

Markl, R.G., G.M. Bryan, and J.I. Ewing (1970). Structure of the Blake Bahama Outer Ridge. *Journal of Geophysical Research*, **75**:4539–4555.

McCaughey, M. and S.C. Singh (1997). Simultaneous velocity and interface tomography of normal-incidence and wide-aperture seismic traveltime data. *Geophys. J. Int.*, **131**(1):87–99.

McIver, R.D. (1977). Hydrates of natural gas; important agent in geologic processes. *Abstracts with Programs - Geological Society of America*, **9**(7):1089–1090.

Mi, Y. (1998). *Seafloor sediment coring and multichannel seismic studies of gas hydrate, offshore Vancover Island.* PhD thesis, University of Victoria, 1998.

Milkov, A.V. and R. Sassen (2002). Economic geology of offshore gas hydrate accumulations and provinces. **19**(1):1–11.

Nisbet, E.G. (2002). Have sudden large releases of methane from geological reservoirs occurred since the last glacial maximum, and could such releases occur again? *Philosophical Transactions: Mathematical, Physical and Engineering Sciences*, **160** (1793):581–607.

Novosel, I. (2002). Physical properties of gas hydrate related sediments, offshore vancouver island. Master's thesis, University of Victoria, 2002.

Novosel, I., G.D. Spence, and R.D. Hyndman (2005). Reduced magnetization produced by increased methane flux at a gas hydrate vent. *Marine Geology*, **216**(4): 265–274.

Orphan, V.J., W. Ussler, III, T.H. Naehr, C.H. House, K.U. Hinrichs, and C.K. Paull (2004). Geological, geochemical, and microbiological heterogeneity of the seafloor around methane vents in the Eel River Basin, offshore California. *Chemical Geology*, **205**(3-4):265–289. doi:10.1016/j.chemgeo.2003.12.035.

Papenberg, C. (2004). *Seismic Investigations of a Bottom Simulating Reflector: Implications on Gas Hydrate and Free Gas at Southern Hydrate Ridge.* PhD thesis, University of Kiel, Germany, 2004.

Paull, C.K., W. Ussler, and W.P. Dillon (1991). Is the extent of glaciation limited by marine gas-hydrates? *Geophysical Research Letters*, **18**(3):432–434.

Paull, C.K., W.U. Ussler, and W.S. Borowski (1994). Source of biogenic methane to form marine gas hydrates. *In: Annals of New York Academy of Science*, volume 715, pages 392–409. 1994.

Pellenbarg, R.E. and M.D. Max (2000). Introduction, physical properties and natural occurrences of hydrate. *In:* M.D. Max (ed.), *Natural Gas Hydrate in Oceanic and Permafrost Environments*, pages 1–8. Kluwer Academic, 2000.

Riddihough, R.P. (1984). Recent movements of the Juan de Fuca plate system. *Journal of Geophysical Research*, **89**(B8):6980–6994.

Riedel, M. (2001). *3-D seismic investigations of Northern Cascadia marine gas hydrates.* PhD thesis, University of Victoria, 2001.

Riedel, M., R. Chapman, and G. Spence (1999). Marine gas hydrates offshore Vancouver Island pseudo 3-D seismic survey near ODP drillsite 889b and ODP site survey. Technical Report 99-5, University of Victoria, CEOR, 1999.

Riedel, M., T.S. Collett, and R.D. Hyndman (2004). Gas hydrate concentrations on the northern cascadia margin - a revisit. Unpublished, 2004.

Riedel, M., S.E. Dosso, and L. Beran (2003). Uncertainty estimation for amplitude variation with offset (AVO) inversion. *Geophysics*, **68**(5):1485–1496.

Riedel, M., I. Novosel, G.D. Spence, R.D. Hyndman, R.N. Chapman, R.C. Solem, and T. Lewis (2006). Geophysical and geochemical signatures associted with gas hydrate related venting at the North Cascadia Margin. *Geological Society of America Bulletin*, **118**(1-2):23–38. doi:10.1130/B25720.1.

Riedel, M., G.D. Spence, N.R. Chapman, and R.D. Hyndman (2002). Seismice investigations of a vent field associated with gas hydrates, offshore Vancouver Island. *Journal of Geophysical Research*, **107**(B9).

Riedel, M. and Theilen (2001). AVO investigation of shallow marine sediments. *Geophysical Prospecting*, **49**:198–212.

Ritger, S., B. Carson, and E. Suess (1987). Methane-derived authigenic carbonates formed by subduction-induced pore-water expulsion along the Oregon/Washington margin. *Geological Society of America Bulletin*, **98**(2):147–156.

Sassen, R. and I.R. MacDonald (1994). Evidence of structure H hydrate, Gulf of Mexico continental slope. *Organic Geochemistry*, **22**(6):1029–1032.

Schmidt, M., C. Hensen, T. Mörz, C. Müller, I. Grevemeyer, K. Wallmann, S. Mau, and N. Kaul (2005). Methane hydrate accumulation in Mound 11mud volcano, Costa Rica forearc. *Marine Geology*, **216**(1-2):83–100.

Schwalenberg, K., E. Willoughby, R. Mir, and R.N. Edwards (2005). Marine gas hydrate electromagnetic signatures in Cascadia and their correlation with seismic blank zones. *First Break*, **23**(4):57–63.

Seo, Y. and H. Lee (2002). Hydration number and two-phase equilibria of CH_4 hydrate in the deep ocean sediments. *Geophysical Research Letters*, **29**(8):85–1 – 85–4.

Shine, K.P., R.G. Derwent, D.J. Wuebblesand, and J.J. Morcrette (1990). *In:* J.T. Houghton, G.J. Jenkins, and J.J. Ephraums (eds.), *Climate Change 1992. The Supplementary Report to the IPCC Scientific Assessment*, pages 41–68. Cambridge Univ. Press, New York, 1990.

Shipboard Scientific Party (1996). Site 997. *In:* R.A. Duncan, H.C. Larsen, and J.F. Allan (eds.), *Proceedings of the Ocean Drilling Program, Initial Reports*, volume 164, pages 277–336. College Station, TX (Ocean Drilling Program), 1996.

Shipboard Scientific Party (2003). Leg 204 summary. *In:* A.M. Tréhu, G. Bohrmann, F.R. Rack, and M.E. Torres (eds.), *Proceedings of the Ocean Drilling Program, Initial Reports*, volume 204. College Station, TX (Ocean Drilling Program), 2003.

Shoell, M. (1988). Multiple origins of methane on the Earth. *Chemical Geology*, **71**: 1–10.

Shuey, R.T. (1985). A simplification of the Zoeppritz equations. *Geophysics*, **50**: 609–614.

Sloan, E.D. (1998). *Clathrate hydrate of natural gases.* Marcel Decker. Inc, Publishers, New York, second edition, 1998a.

Sloan, E.D. (1998). Physical/chemical properties of gas hydrates and application to world margin stability and climate change. *In:* J.P. Henriet and J. Mienert (eds.), *Gas Hydrates: Relevance to World Margin Stability and Climate Change*, volume 137, pages 31–50. Geological Society, London, Special Publications, 1998b.

Spence, G., M. Riedel, and I. Novosel (2000). VENTFLUX: Piston coring and heat flow near vent sites associated with marine gas hydrates offshore Vancouver Island. Technical Report 2000-4, University of Victoria, 2000.

Spence, G.D., N.R. Chapman, R.D. Hyndman, and C. Clearly (2001). Fishing trawler nets massive "catch" of methane hydrates. *Eos Trans. AGU*, **82**(50):621.

Spence, G.D., T.A. Minshull, and C.R. Fink (1995). Seismic studies of methane hydrate offshore Vancouver Island. *In:* B. Carson, G.M. Westbrook, R.J. Musgrave, and E. Suess (eds.), *Proceedings of the Ocean Drilling Program, Scientific Results.* College Station, TX (Ocean Drilling Program), 1995.

Tinivella, U. and E. Lodolo (2000). The Blake Ridge bottom-simulating reflector transect: Tomographic velocity field and theoretical model to estimate methane hydrate quantities. *In:* C.K. Paull, R. Matsumoto, P.J. Wallace, and W.P. Dillon (eds.), *Proceedings of the Ocean Drilling Program, Scientific Results*, volume 164, pages 273–281. College Station, TX (Ocean Drilling Program), 2000.

Tréhu, A.M., P.E. Long, M.E. Torres, G. Bohrmann, F.R. Rack, T.S. Collett, D.S. Goldberg, A.V. Milkov, M. Riedel, P. Schultheiss, N.L. Bangs, S.R. Barr, W.S. Borowski, G.E. Claypool, M.E. Delwiche, G.R. Dickens, E. Gracia, G. Guerin, M. Holland, J.E. Johnson, Y.J. Lee, C.S. Liu, X. Su, B. Teichert, H. Tomaru, M. Vanneste, M. Watanabe, and J.L. Weinberger (2004). Three-dimensional distribution of gas hydrate beneath southern Hydrate Ridge: constraints from ODP Leg 204. *Earth and Planetary Science Letters*, **222**(3-4):845–862.

Tréhu, A.M., D.S. Stakes, C.D. Bartlett, J. Chevallier, R.A. Duncan, S.K. Goffredi, S.M. Potter, and K.A. Salamy (2003). Seismic and seafloor evidence for free gas, gas hydrates, and fluid seeps on the transform margin offshore Cape Mendocino. *Journal of Geophysical Research*, **108**(B5):19pp.

Trofimuk, A.A., Y.F. Makogon, and M.B. Tolkatchev (1983). Ob roli gazogidratov v protsesakh akumulatsii uglevodorodov i formirovanii ikh zalezhei (on the role of gas hydrates in the process of hydrocarbon accumulation and their fields formation). *Geologiia i Geofizika*, **6**:3–15.

Vasiliev, V.G., Y.F. Makogon, F.A. Trebin, A.A. Trofimuk, and N.V. Cherskiy (1970). Svoistvo prirodnykh gasov nakhodit'sya v Zemnoi kore v tvyordom sostoyanii i obrazovyvat' gazogidratnyie zalezhi. translated title: The property of natural gases to occur in the crust in solid state and to form gas-hydrateaccumulations. *In: Otkrytiya v SSSR, 1968-1969 (Discoveries in USSR in 1968-1969)*. TsNIIPI (Moscow), 1970.

Villinger, H.W. (1996). Bathymetriedaten der Reise SO111 des Forschungsschiffes SONNE. Technical report, Fachbereich Geowissenschaften der Universitat Bremen, Bremen, 1996.

Vincent, T.H. and S.L.J. Hu (1997). Geodetic position estimation of underwater acoustic sensors. *J. Acoust. Soc. Am.*, **102**(6):3099.

Webster, M. (1994). *Webster's Dictionary*. Houghton Miffin Co., 1994. 1536pp.

Westbrook, G.K. (1994). Growth of accretionary wedges off Vancouver Island and Oregon. *In:* G.M. Westbrook, B. Carson, and R.J. Musgrave (eds.), *Proceedings of the Ocean Drilling Program, Initial Reports*, volume 146, pages 381–388. College Station, TX (Ocean Drilling Program), 1994.

Westbrook, G.K., B. Carson, and Shipboard Scientific Party (1994). Summary of Cascadia drilling results. *In:* G.M. Westbrook, B. Carson, and R.J. Musgrave (eds.), *Proceedings of the Ocean Drilling Program, Initial Reports*, volume 146, pages 389–396. College Station, TX (Ocean Drilling Program), 1994.

Willoughby, E.C., K. Schwalenberg, R.N. Edwards, G.D. Spence, and R.D. Hyndman (2005). Assessment of marine gas hydrate deposits: a comparative study of seismic, electromagnetic and seafloor compliance methods. *In: Proceedings of the Fifth International Conference on Gas Hydrates*, volume 3, pages 8002 – 8011, Trondheim, Norway, June 2005.

Wood, W.T., J.F. Gettrust, N.R. Chapman, G.D. Spence, and R.D. Hyndman (2002). Decreased stability of methane hydrates in marine sediments owing to phase-boundary roughness. *Nature*, **420**(6916):656–660.

Yefremova, A.G. and B.P. Zhizhchenko (1974). Obnaruzhenie kristallogidratov v osadkakh sovremennykh akvatoiy translated title: Discovery of gas crystallhydrates in recent offshore sediments. *Doklady AN SSSR (Reports of Academy of Science of USSR)*, **214**(5):1179–1181.

Yilmaz, O. (2001). *Seismic Data Analysis: Possessing, Inversion, and Interpretation of Seismic Data*, volume II. SEG, 2001.

Yuan, J. and R.N. Edwards (2000). The assessment of marine gas hydrates through electrical remote sounding: Hydrate without BSR? *Geophysical Research Letters*, **27**(16):2397–2400.

Yuan, T. (1996). *Seismic Studies of the Northern Cascadia Accretionary Prism: Sediment Consolidation and Gas Hydrates.* PhD thesis, University of Victoria, 1996.

Yuan, T., R.D. Hyndman, G.D. Spence, and B. Desmos (1996). Seismic velocity increase and deep-sea gas hydrate concentration above a bottom-simulating reflector on the northern cascadia continental slope. *Journal of Geophysical Research*, **101** (B6):13,665–13,671.

Yuan, T., G.D. Spence, and R.D. Hyndman (1994). Seismic velocities and inferred porosities in the accretionary wedge sediments at the Cascadia margin. *Journal of Geophysical Research*, **99**(B3):4413–4427.

Yuan, T., G.D. Spence, R.D. Hyndman, T.A. Minshull, and S.C. Singh (1999). Seismic velocity studies of a gas hydrate bottom-simulating reflector on the Northern Cascadia continental margin: Amplitude modelling and full waveform inversion. *Journal of Geophysical Research*, **104**(B1):1179–1191.

Zelt, B.C., R.M. Ellis, R.M. Clowes, and J.A. Hole (1996). Inversion of three-dimensional wide-angle seismic data from the southwestern Canadian Cordillera. *Journal of Geophysical Research.*

Zelt, C.A. (1999). Modelling strategies and model assessment for wide-angle seismic traveltime data. *Geophysical Journal International*, **139**:183–204.

Zühlsdorff, L. and V. Spieß(2004). Three-dimensional seismic characterization of a venting site reveals compelling indications of natural hydraulic fracturing. *Geology*, **32**(2):101–104.

Appendix A

Used abbreviations

AVA - **A**mplitude **V**ariation with **A**ngle

AVO - **A**mplitude **V**ariation with **O**ffset

BSR - **B**ottom **S**imulating **R**eflector/**R**eflection

COAMS - **C**anadian **O**ceanographical **A**coustic **M**easurement **S**ystem

CSEM - **C**ontrolled **S**ource **Electrom**agnetic

DGPS - **D**ifferential **G**lobal **P**ositioning **S**ystem

DTAGS - **D**eep **T**ow **A**coustic **G**eophysics **S**ystem

GPS - **G**lobal **P**ositioning **S**ystem

GHSZ - **G**as **H**ydrate **S**tability **Z**one

IODP - **I**ntegrated **O**cean **D**rilling **P**rogram

LWD - **L**ogging **W**hile **D**rilling

MAP - **M**aximum **a** **P**osteriori

MCS - **M**ulti**c**hannel **S**eismic

OBS - **O**cean **B**ottom **S**eismometer

ODP - **O**cean **D**rilling **P**rogram

RC - **R**eflection **C**oefficient

RMS - **R**oot **M**ean **S**quare

SRL - **S**ources and **R**eceivers **L**ocalization

TWT - **T**wo-**w**ay **T**aveltime

UTM - **U**niversal **T**ransverse **M**ercator

VSP - **V**ertical **S**eismic **P**rofile

Appendix B

OBS hydrophone data example

The following pictures represent an example of the seismic data recorded by the hydrophone sensor of the 5 OBSs. Each seismic line is shown in three ways: top panel – raw, unprocessed data; middle panel – direct water wave arrival flattened (note strong contamination of the signal with the bubble pulse energy, wide horizontal bands); bottom panel – seismic data after application of the F-K filter (these data were used for the travel time picking). The direct water wave arrival was flattened to arrive at 100 ms for all traces.

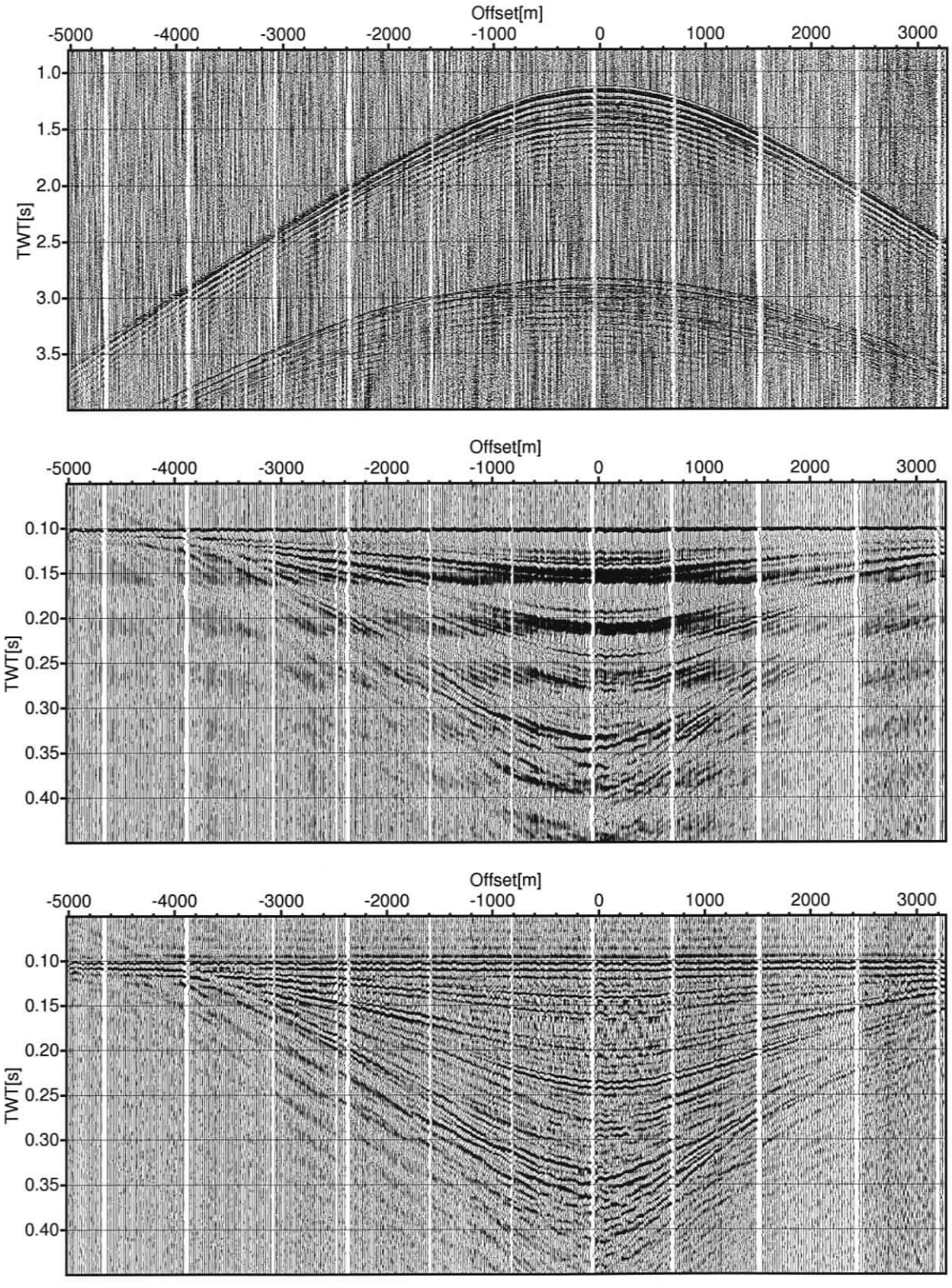

Figure B.1: OBS A (hydrophone), Grl-04

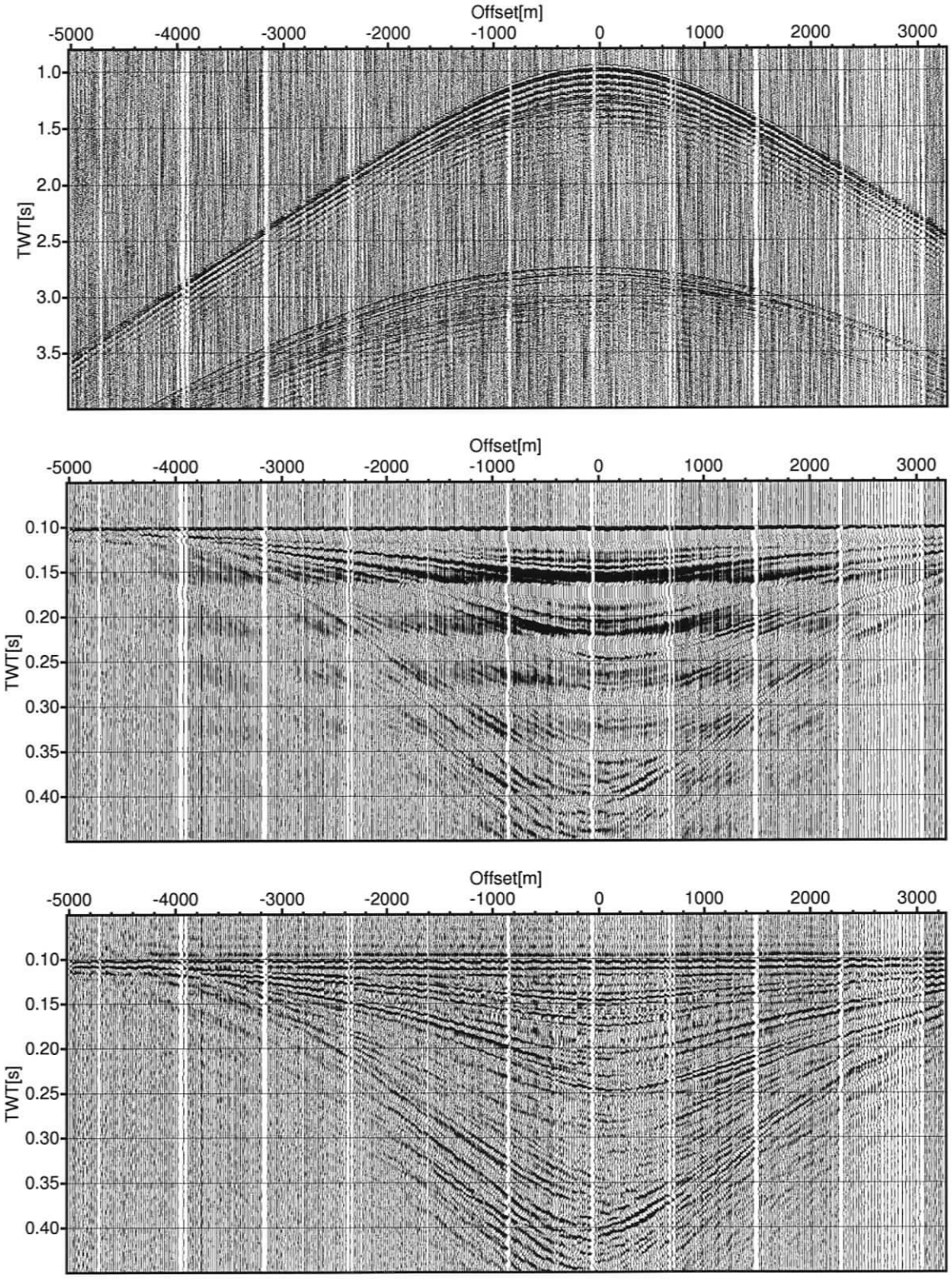

Figure B.2: OBS A (hydrophone), Grl-08

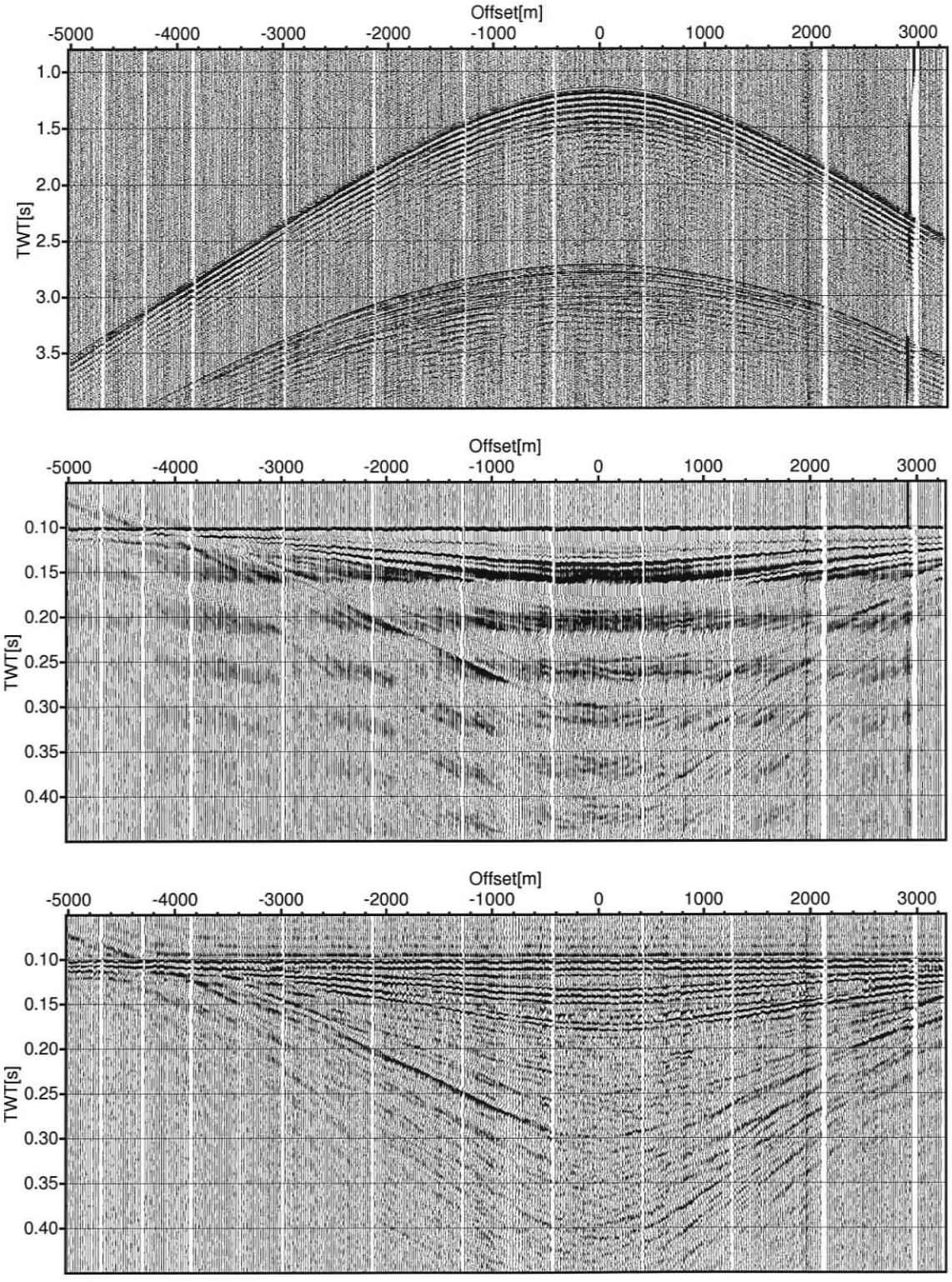

Figure B.3: OBS A (hydrophone), Grl-14

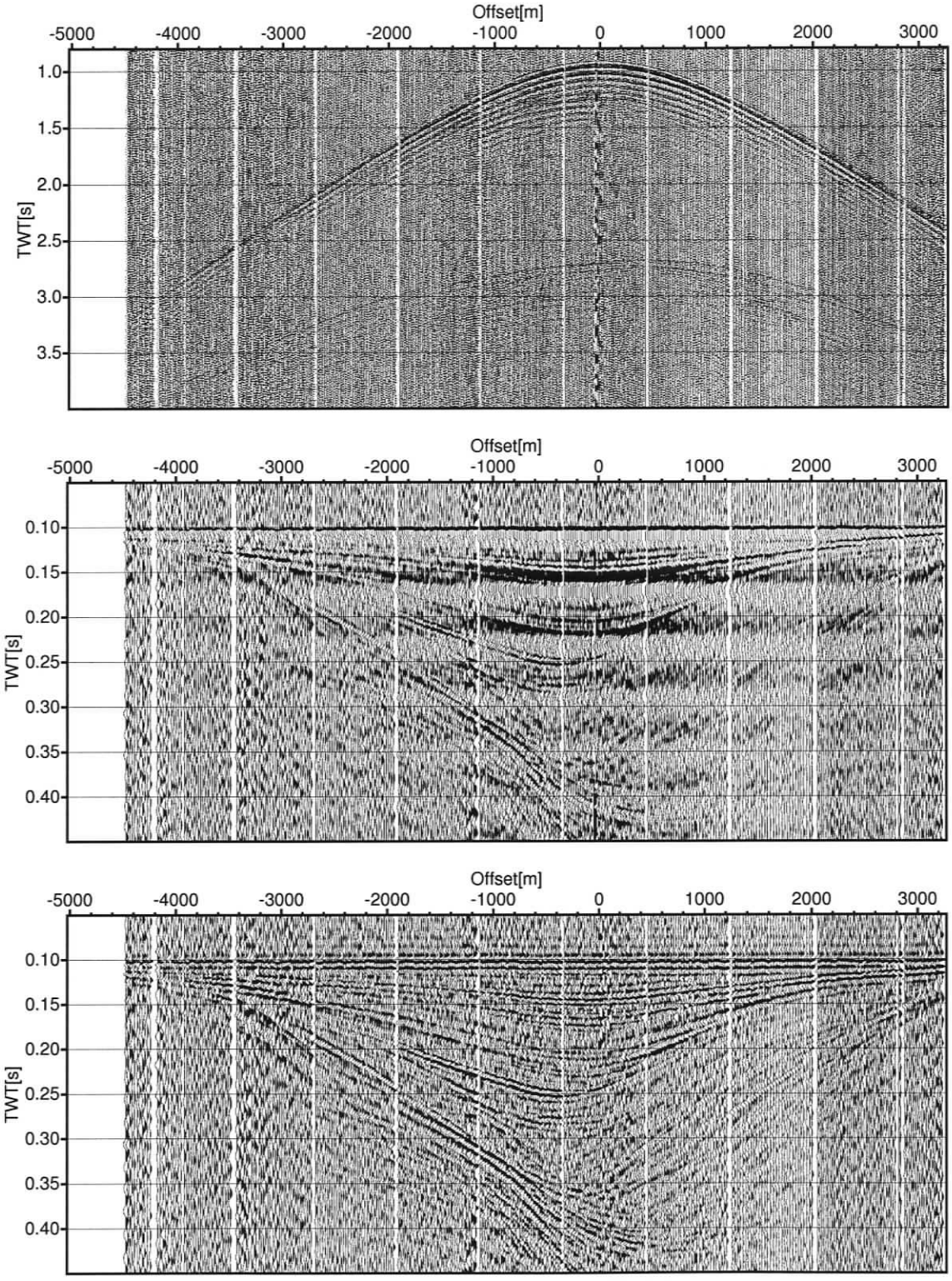

Figure B.4: OBS A (hydrophone), Xl-02

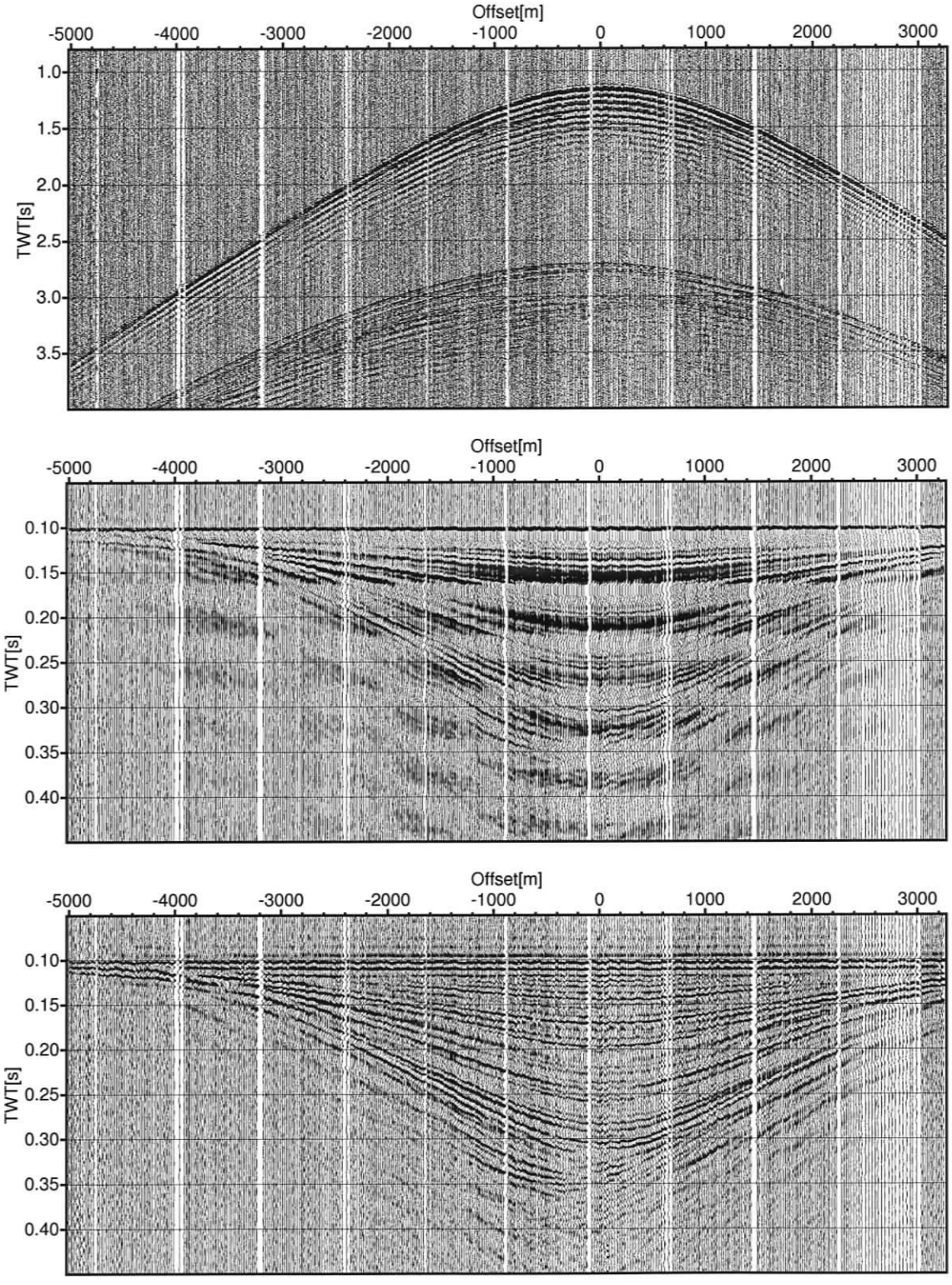

Figure B.5: OBS B (hydrophone), Grl-08

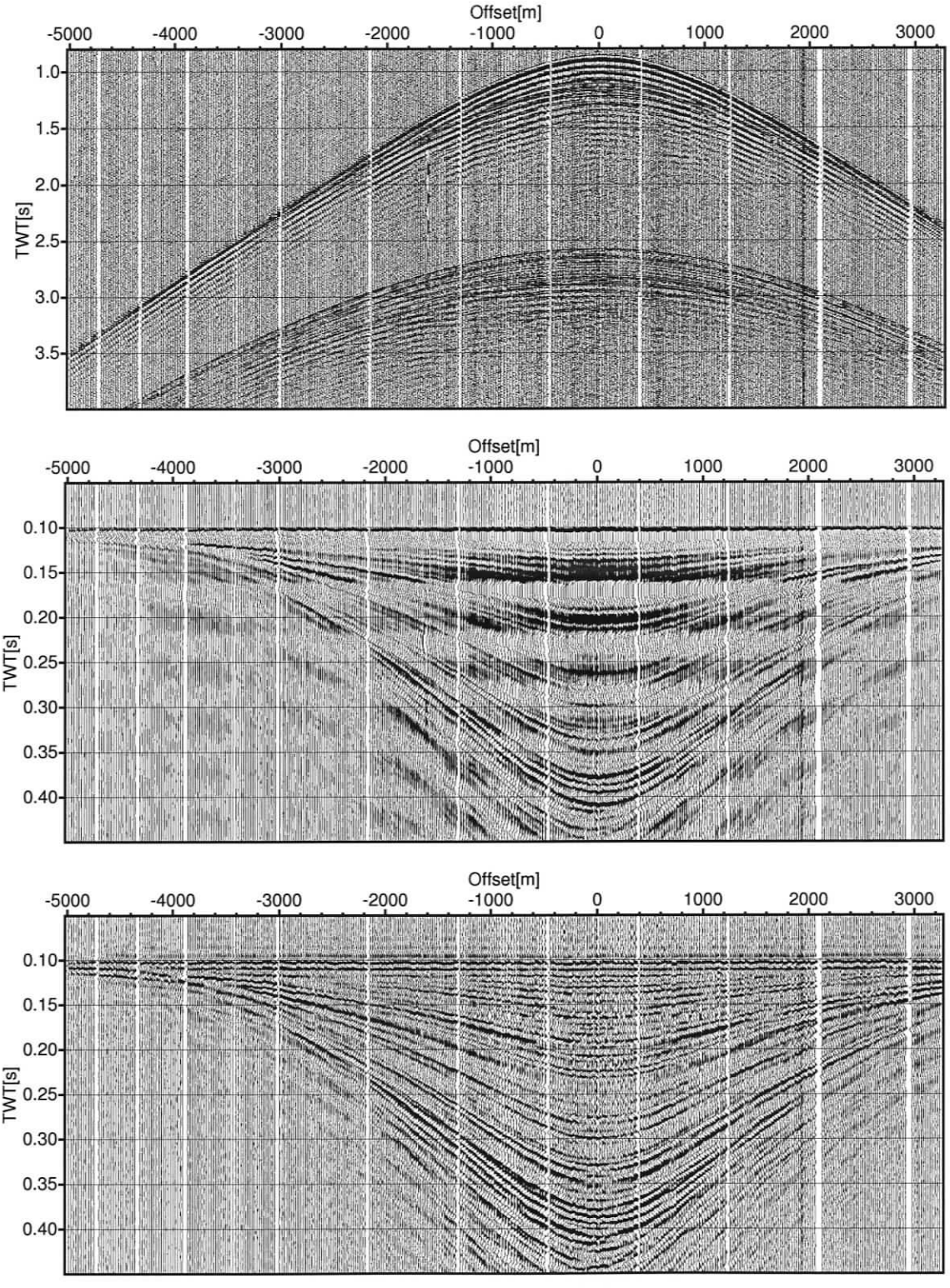

Figure B.6: OBS B (hydrophone), Grl-14

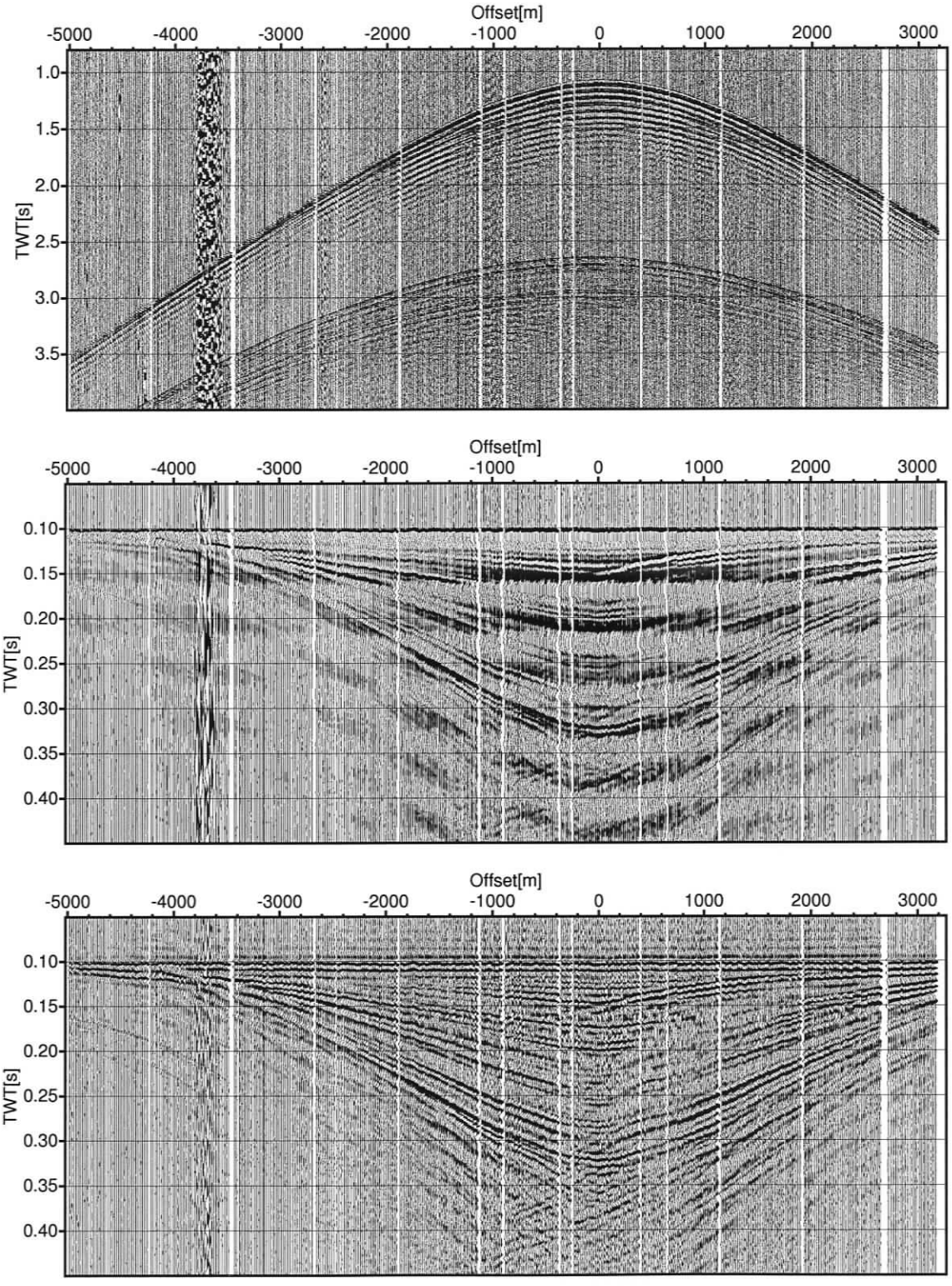

Figure B.7: OBS B (hydrophone), Grl-19

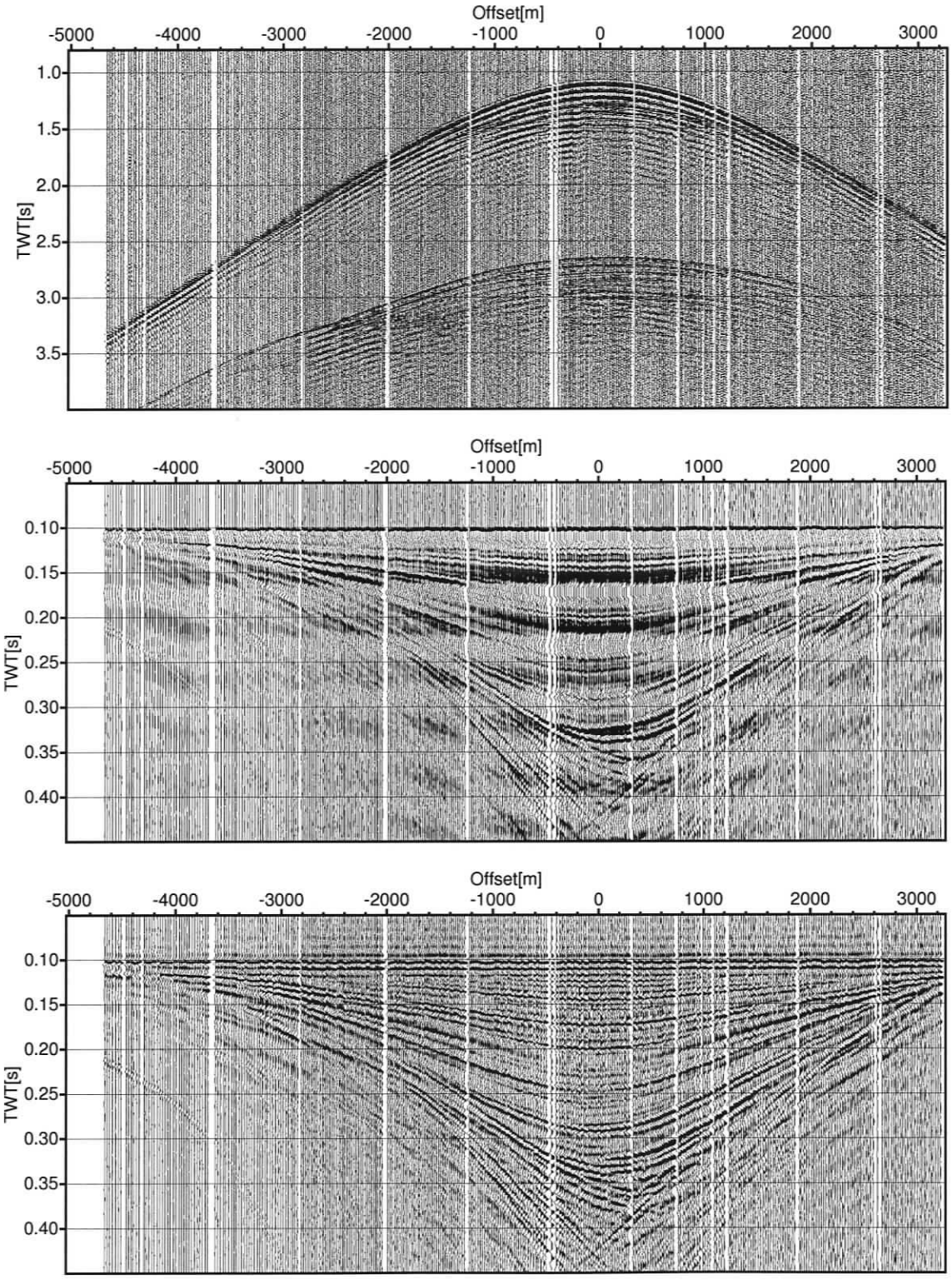

Figure B.8: OBS B (hydrophone), Xl-01

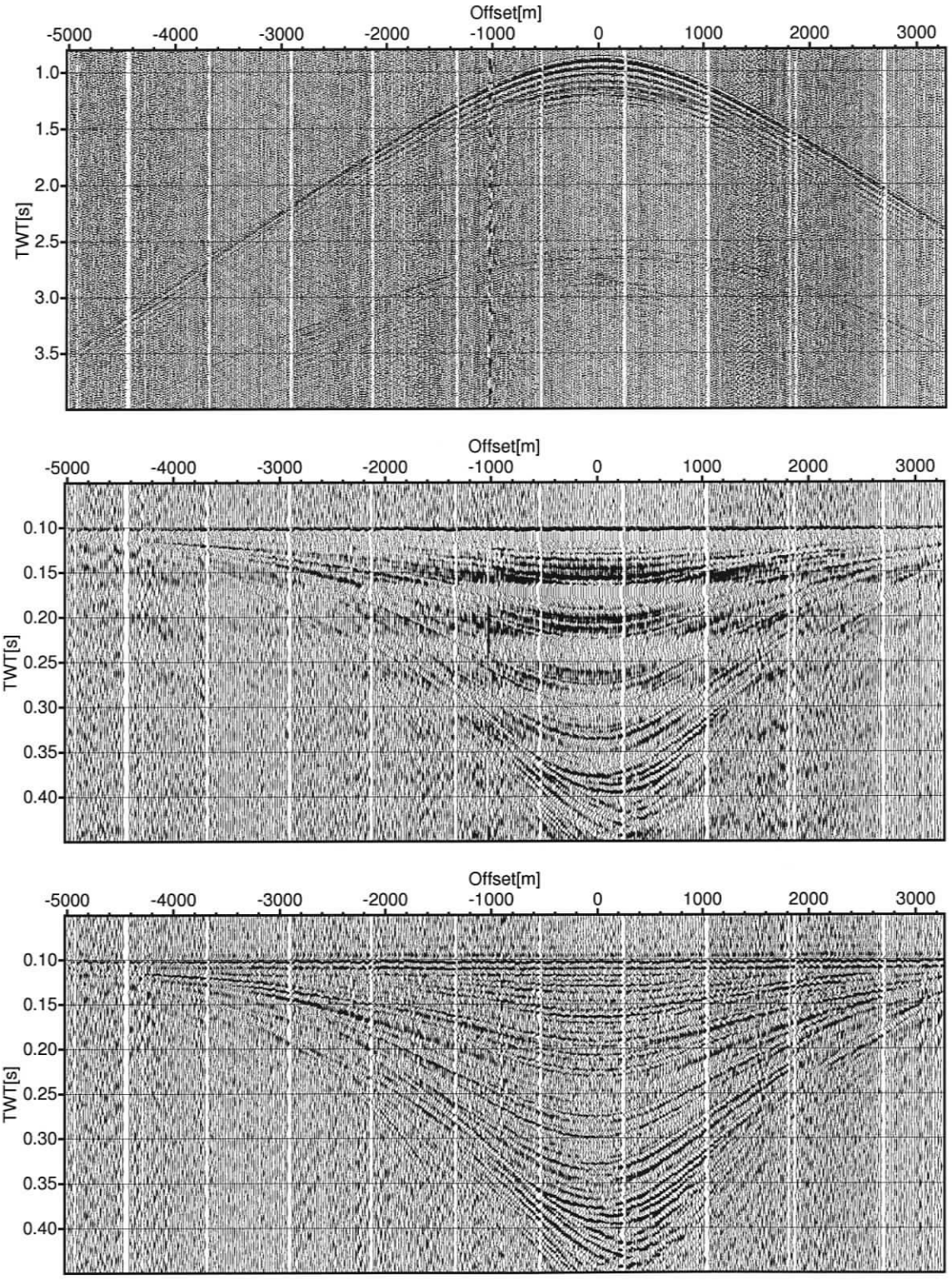

Figure B.9: OBS B (hydrophone), Xl-02

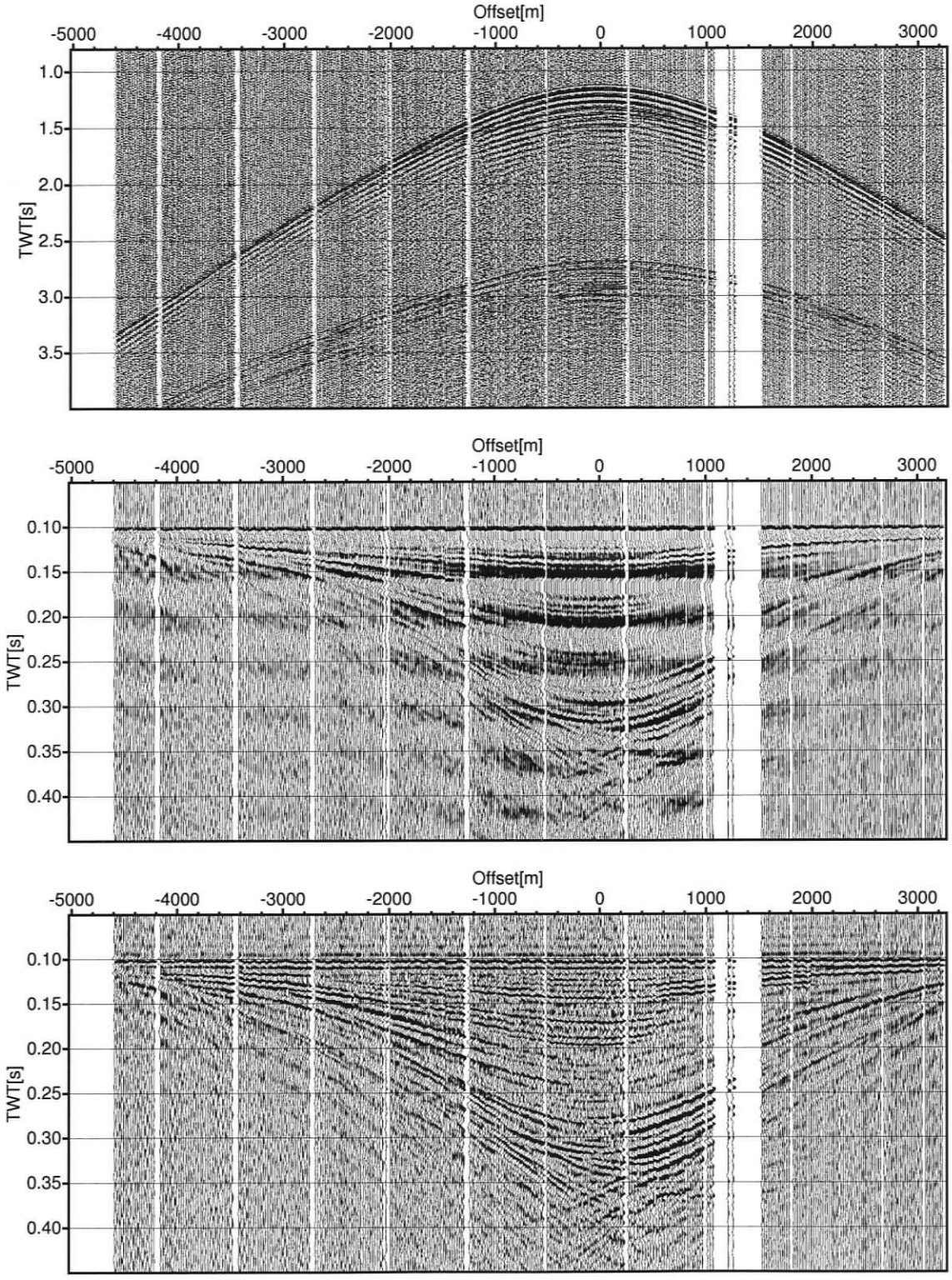

Figure B.10: OBS B (hydrophone), Xl-03

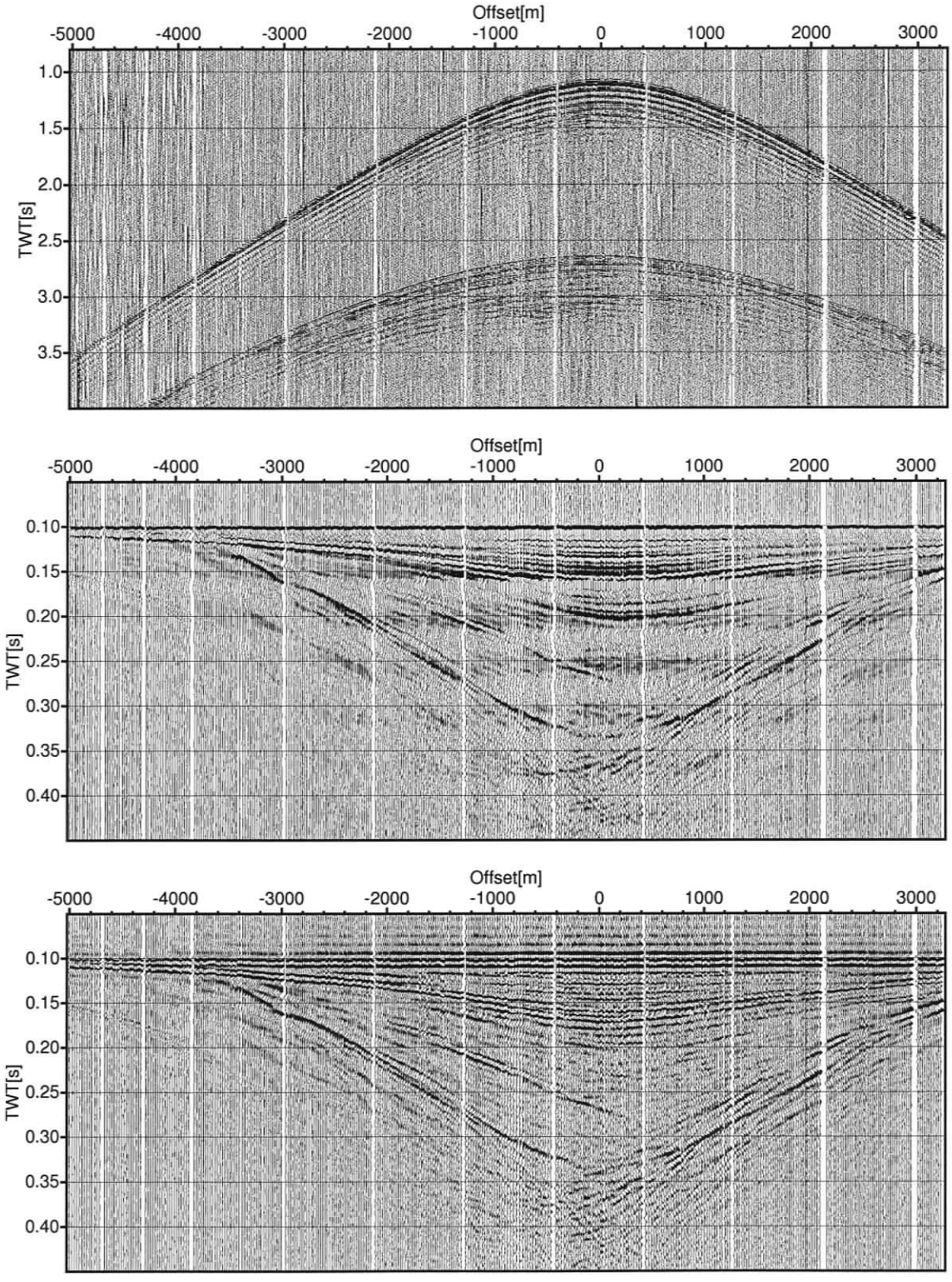

Figure B.11: OBS C (hydrophone), Grl-14

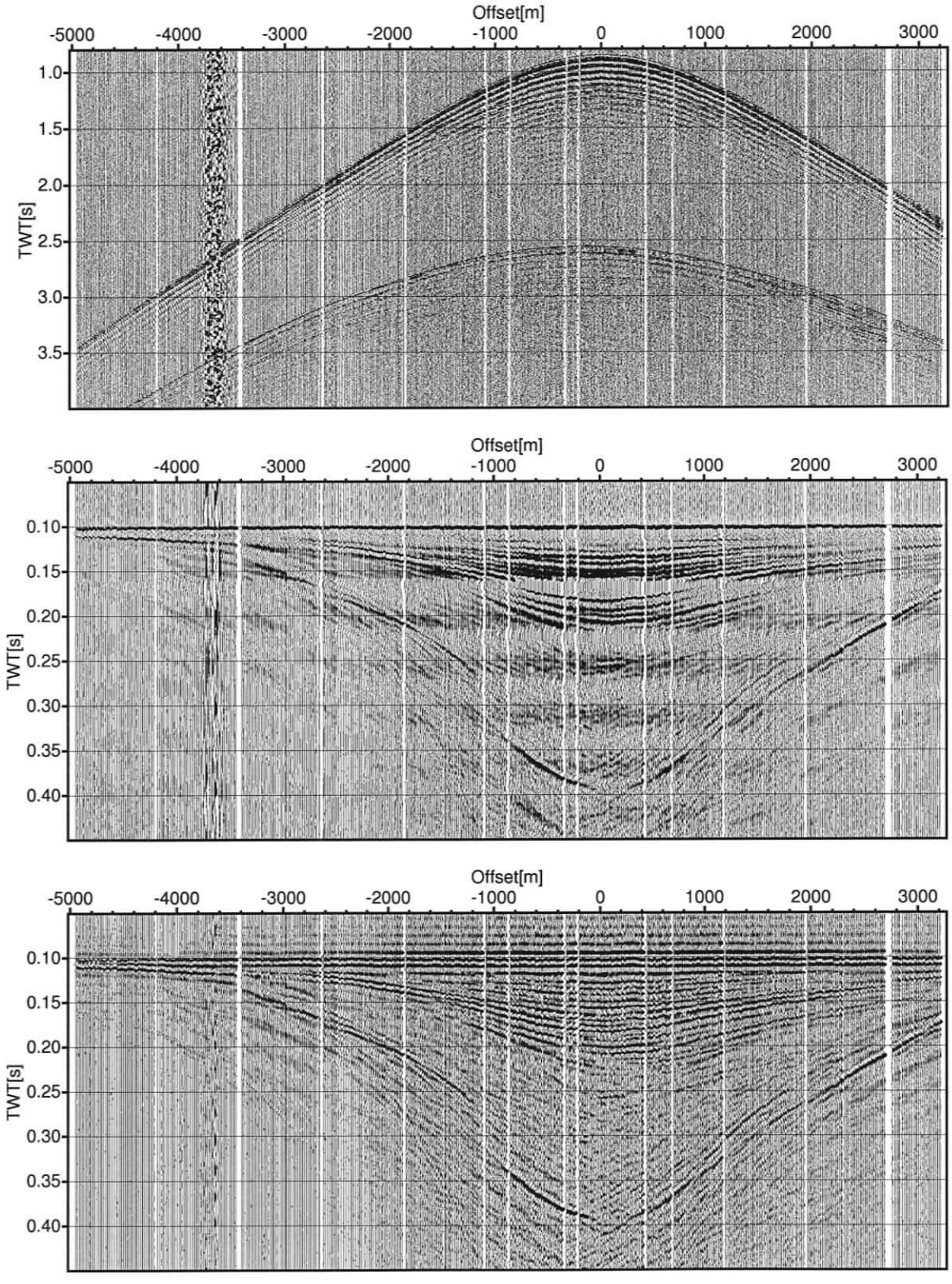

Figure B.12: OBS C (hydrophone), Grl-19

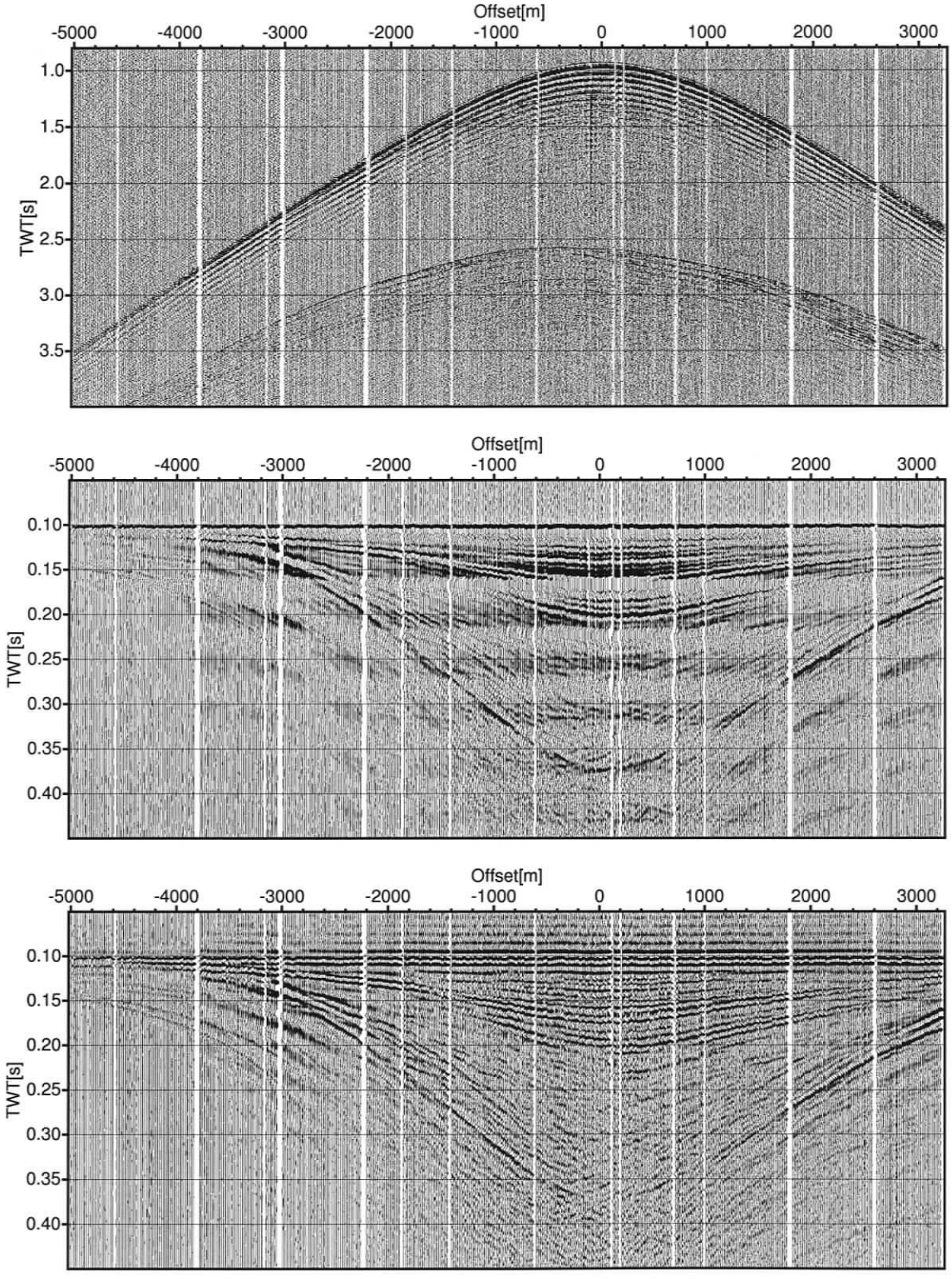

Figure B.13: OBS C (hydrophone), Grl-22

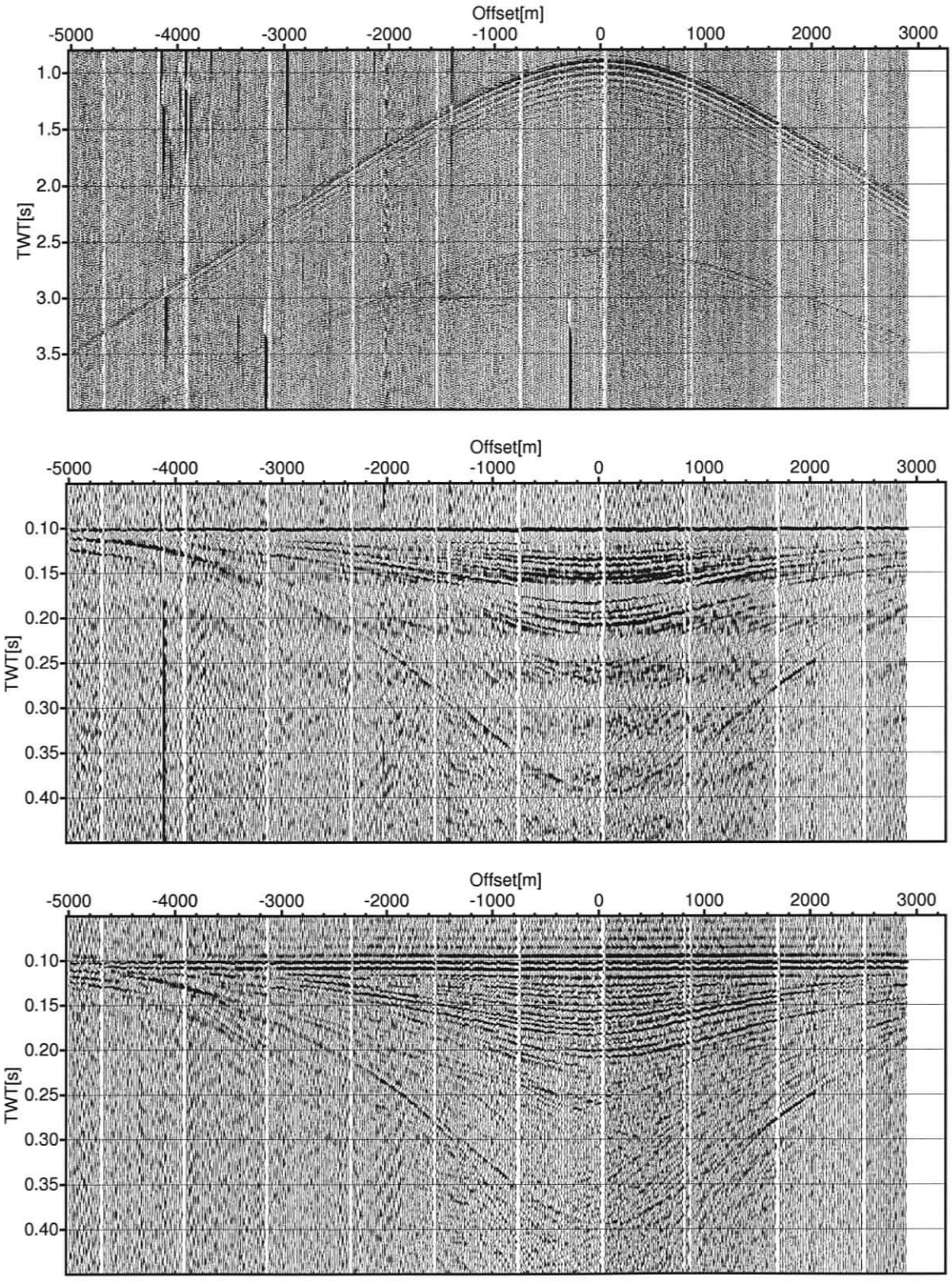

Figure B.14: OBS C (hydrophone), Xl-02

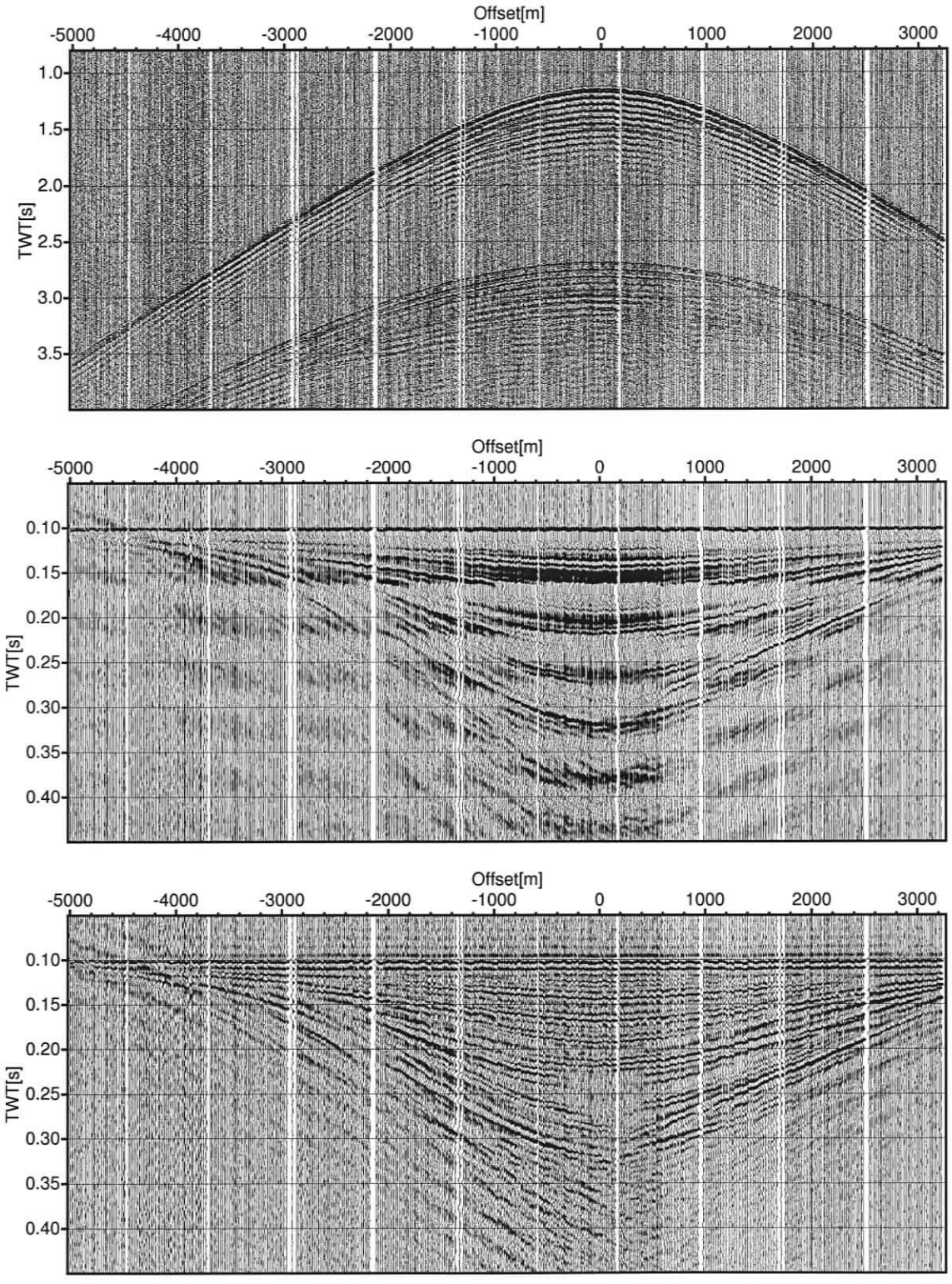

Figure B.15: OBS E (hydrophone), Grl-08

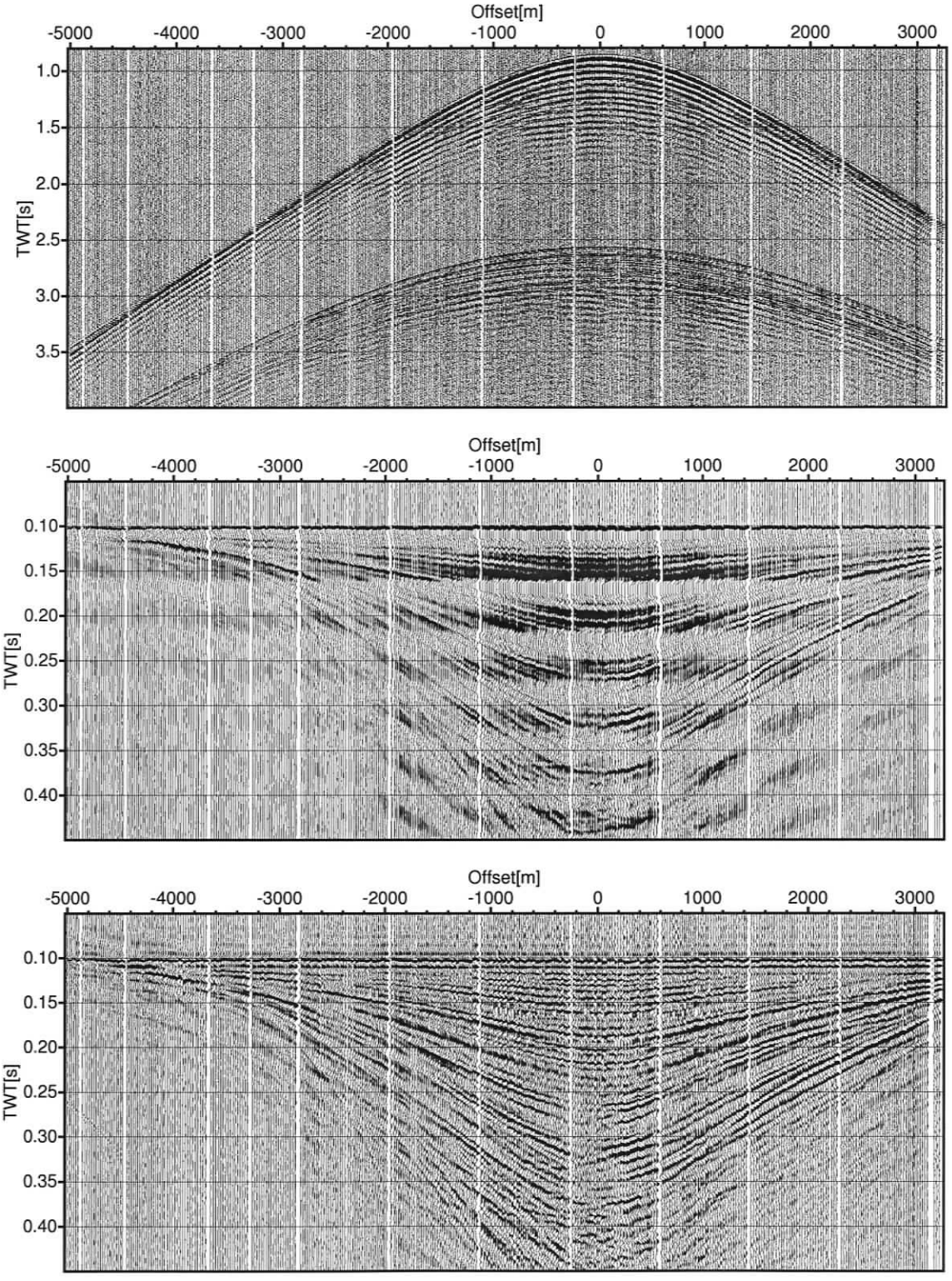

Figure B.16: OBS E (hydrophone), Grl-14

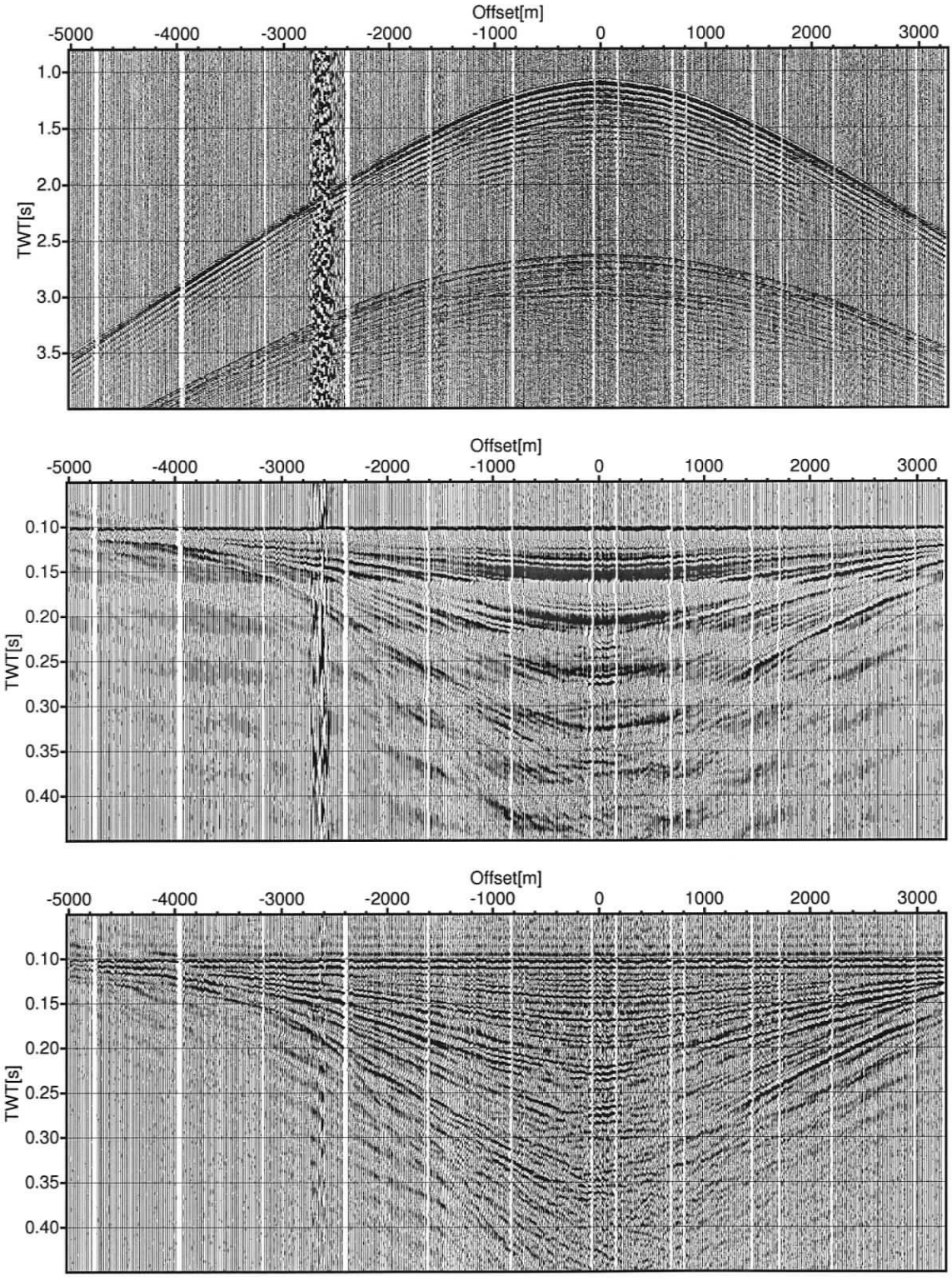

Figure B.17: OBS E (hydrophone), Grl-19

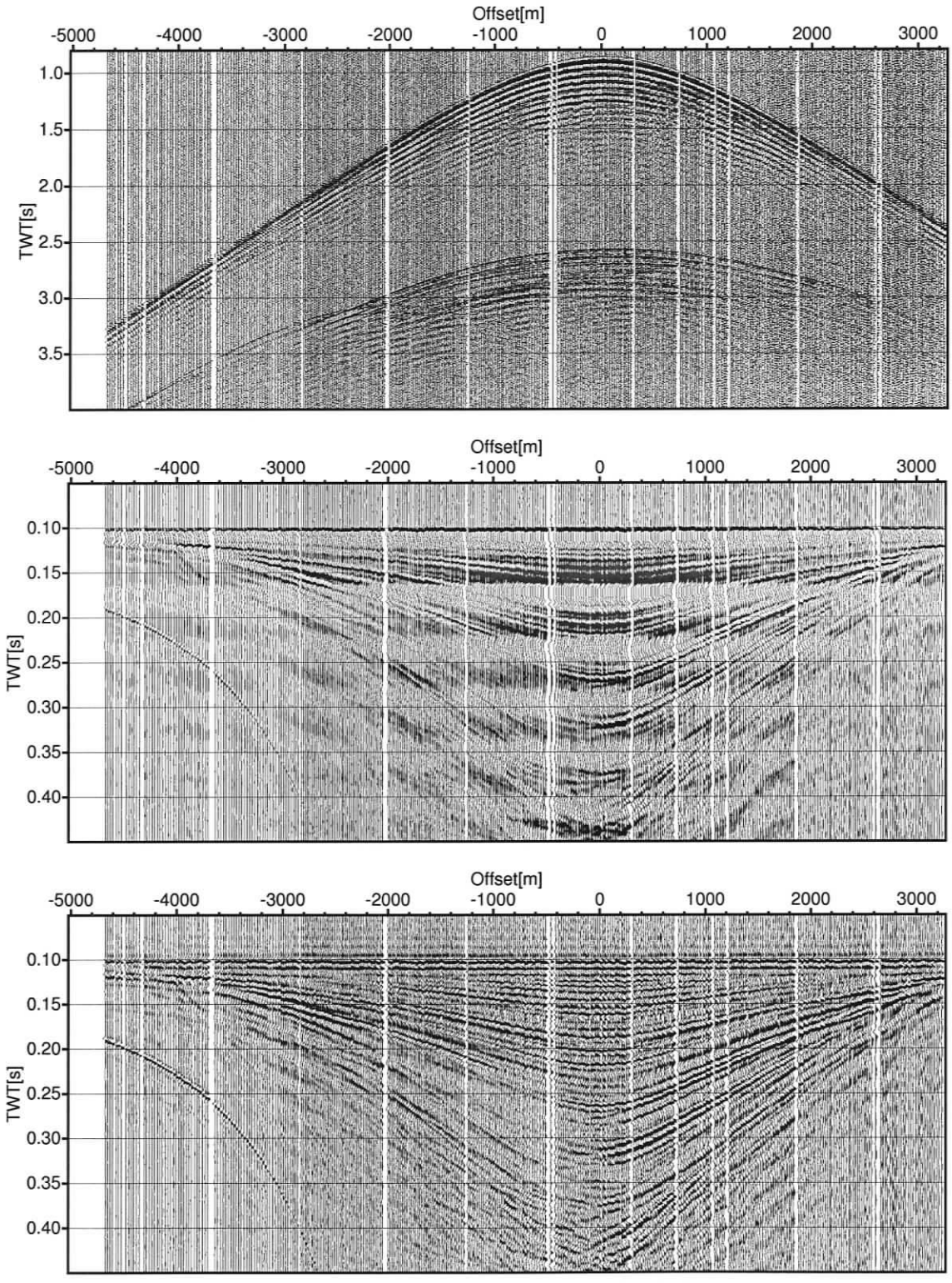

Figure B.18: OBS E (hydrophone), Xl-01

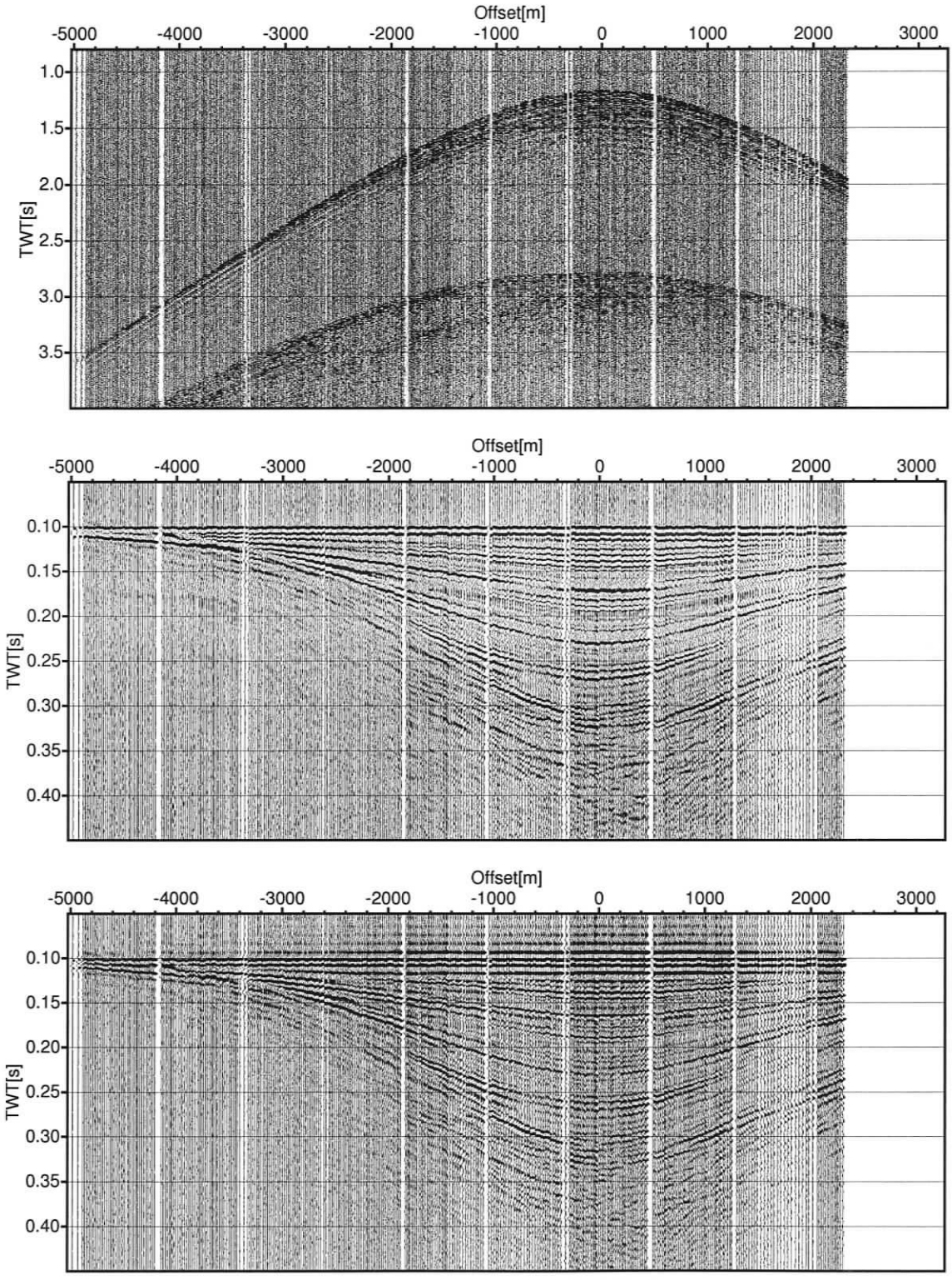

Figure B.19: OBS F (hydrophone), Grl-08

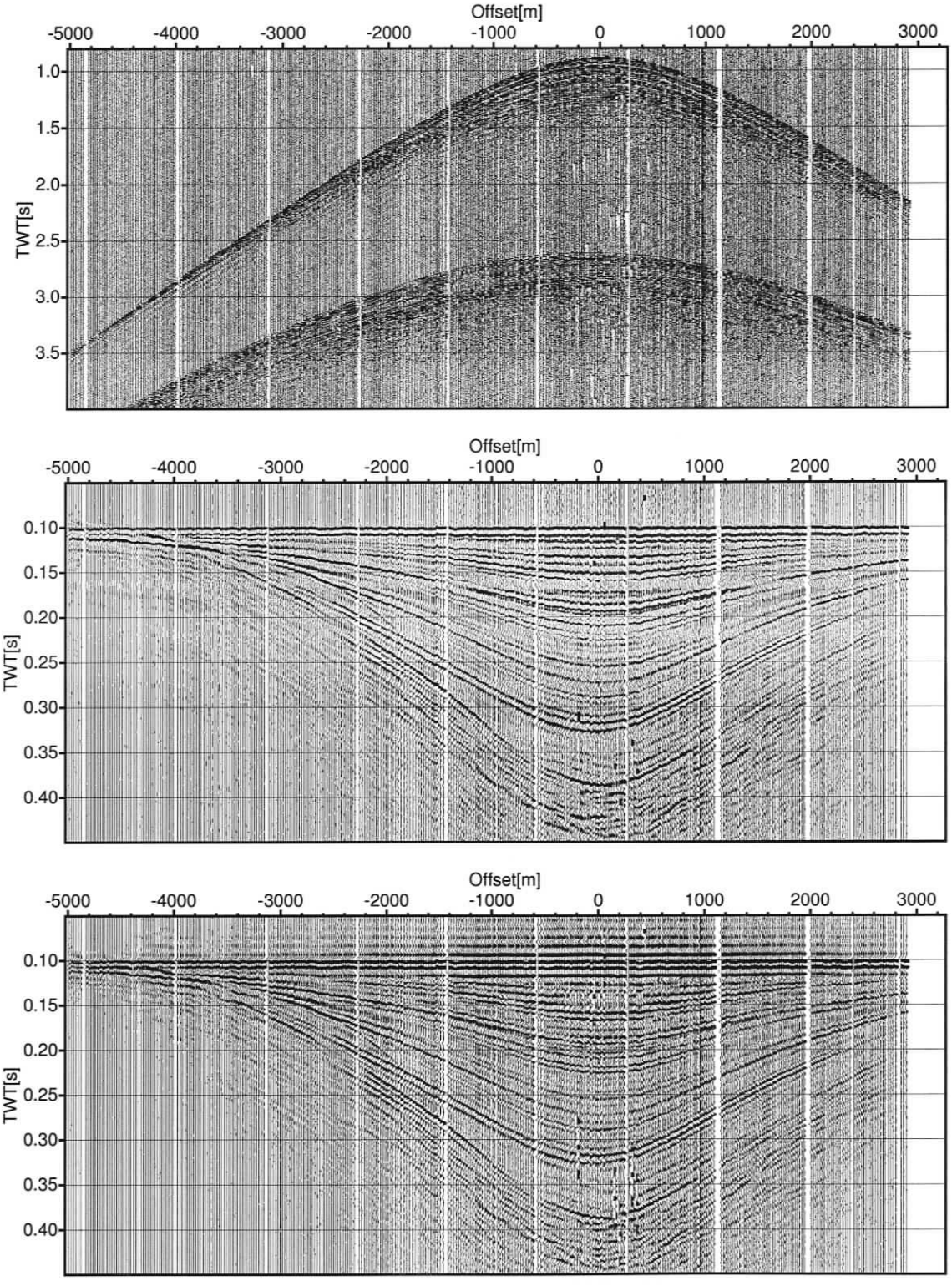

Figure B.20: OBS F (hydrophone), Grl-14

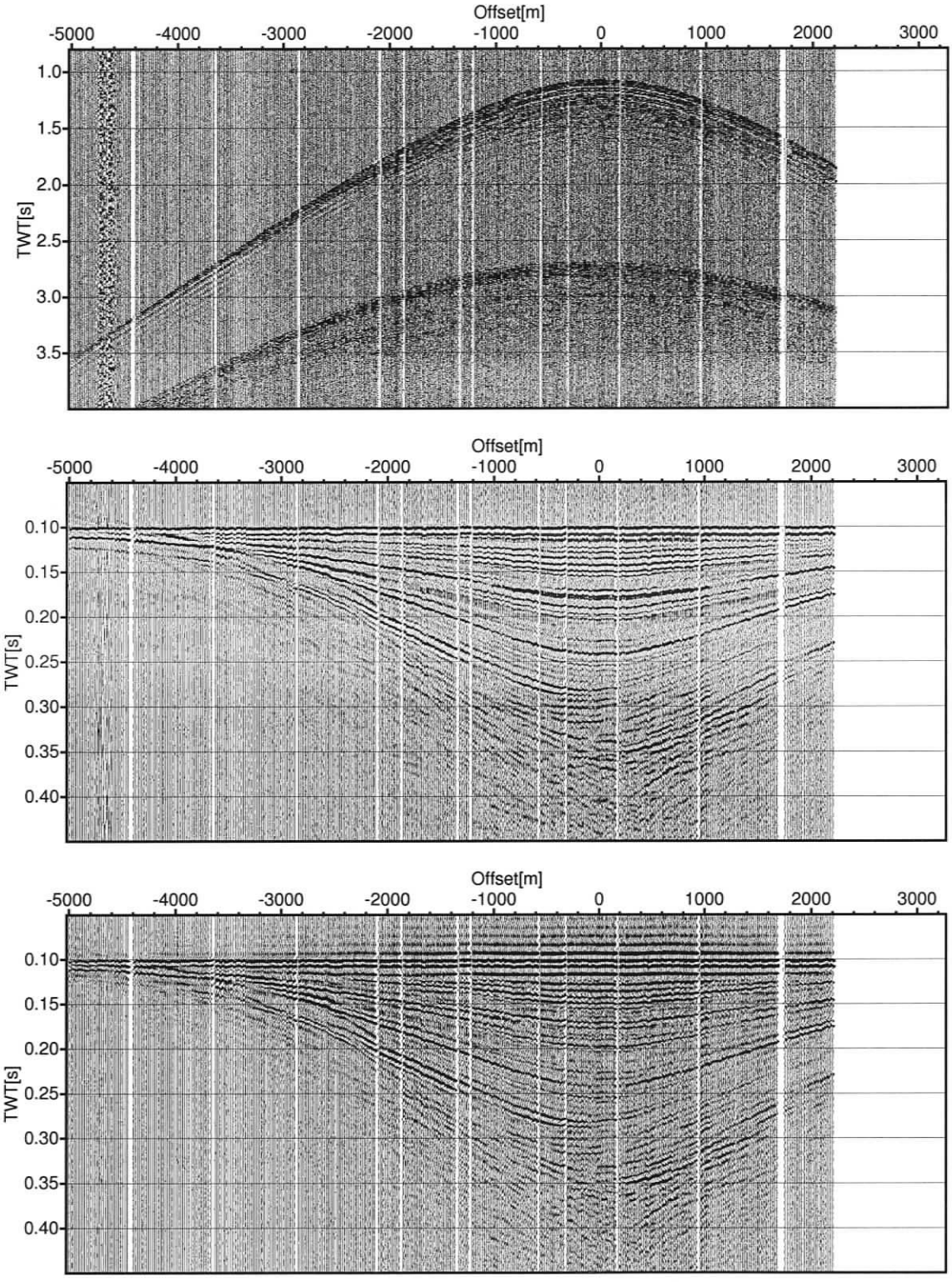

Figure B.21: OBS F (hydrophone), Grl-19

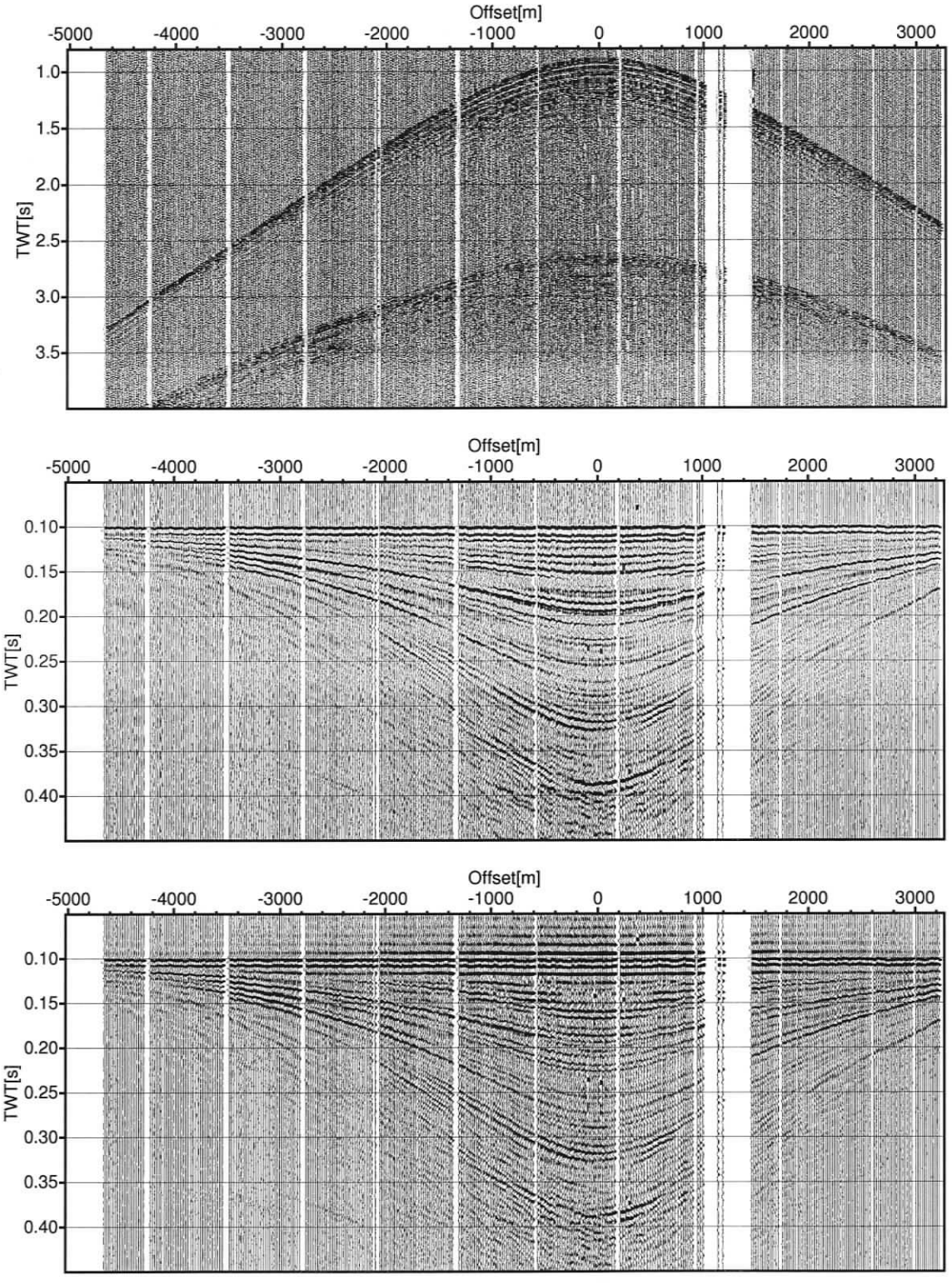

Figure B.22: OBS F (hydrophone), Xl-03